Pore morphology and the characterisation of North Sea sandstones

Thesis submitted for the degree of
Doctor of Philosophy
at the University of Leicester

by

Kate Louise Hatfield BSc (Leicester)
Department of Geology
University of Leicester

March 1999

Pore morphology and the characterisation of North Sea sandstones

Kate Louise Hatfield

Abstract

Within the oil and gas industry it is of the utmost importance to determine the value of a hydrocarbon accumulation. Key to this process is the prediction of reservoir flow and performance. Measurements on core are the main source of information that underpin this crucial prediction; however core is not always available and it is necessary to find another means to estimate the required flow properties.

Inspection of core data often reveals the presence of a simple relationship between the core porosity and the permeability to gas. Where this is the case, it is common practice to establish a relationship and then use estimates of porosity from wireline logs to predict permeability. However, for the reservoir examined in this thesis, like many others, this porosity–permeability relationship is neither linear, nor straight-forward.

A plug porosity–permeability relationship for this reservoir was derived from the analysis of 199 sandstone plugs. In addition 63 of these plugs have image analysis data; the end-trims of these plugs were impregnated, sectioned and polished. Back-scattered electron microscope images at both high (x150) and low (x30) magnifications were taken, captured as 256 grey scales and numerically analysed. This analysis enabled the pore geometry to be quantified.

The image data led to an improved understanding of the controls on permeability and porosity. This understanding was achieved by the demonstration that micro-porosity is an ineffective porosity in terms of fluid flow. Micro-porosity is identified as pores <13 μm^2 and mostly occurs within the *clay* (defined as the grey scale range 50-170 on the SEM images). Image porosity was calculated and observed to be less than plug porosity and has a stronger linear relationship with permeability; this is a result of micro-porosity being included in the measurement of plug porosity but not in the image porosity calculation. A non-linear relationship between gas permeability and mean pressure in the calculation of Klinkenberg permeability is present; a possible explanation for this observation is given.

To my mum, dad and

husband Lee

Contents

Acknowledgements

I would like to thank my supervisors, both official and unofficial. Firstly, Peter Whattler who initiated and nurtured the project - proving a constant source of moral and intellectual support. Peter unfortunately had to leave for Houston within the early stages of the project, leaving Jenny Garnham (the unofficial supervisor!) to oversee and offer guidance where needed and to remove the 'red-tape' often associated with the data. Jenny went far beyond what had been requested of her; giving time and effort in the final stages of writing-up which will always be sincerely appreciated. I would also like to thank Peter Harvey and Mike Lovell, my supervisors at Leicester University; especially Peter for our regular early morning discussions. There are many members of staff, both inside and out of the Geology department, who have been ready with time and advice; Tim Brewer's help in the last weeks is especially appreciated.

I would like to acknowledge Enterprise Oil plc. and Leicester University for funding this project and Enterprise for supplying the data. I would also like to thank Rick at Service Company 1 for taking all of the SEM images and always being there to answer my questions.

I would like to say a special 'thank you' to Caroline Bradley, Caroline Taylor and Joe Pedder, they are my oldest and *bestest* friends; who were supportive throughout. Many kind thanks are given to Gail Williamson and Trevor Williams, who were always around and ready for chats in the Coffee Shop, Snappers, Ratray or 'upstairs'. Roz White and Tiffany Barry are two special friends and fellow students of 1995-1999, with whom I have shared many experiences; including writing-up! Claire Thorpe is another close friend who has given much entertainment over the past three years!

My family have been (as always) 100% supportive in every way, and I hope they realise how much that support has been appreciated.

Lastly, I thank Lee; without exception he has been there in every possible way, and unlike my family and other friends, he had to live with me!!!

CHAPTER ONE

Introduction

1.1 Background

Core analysis is routinely performed on recovered material throughout the 'pay' zone within hydrocarbon reservoirs. Measurements are made on cylindrical plugs, taken perpendicular (horizontal plugs) or parallel (vertical plugs) to core length, if the bedding is assumed to be approximately horizontal. These horizontal and vertical plugs are commonly taken at a ratio of three:one respectively. The core plugs are cleaned prior to measurements. The routine measurements made on plugs are restricted to grain density, helium porosity and gas permeability. The pore fluids liberated by the cleaning process are used to derive fluid saturations. These data, combined with the downhole log data, enable the volume of *in situ* hydrocarbons to be estimated.

The relationship between permeability and porosity is commonly used to assist in the prediction of flow and reservoir performance. Great importance is attached to the permeability-porosity relationship, as porosity can be calculated from wireline log data, but permeability cannot. Therefore relationships between porosity and permeability derived from core can be used to infer permeability in uncored sections of a well. However, since this permeability-porosity relationship is rarely linear or straight-forward, in regions of greater commercial interest more laboratory measurements are acquired on the plugs. These are called Special Core Analysis Laboratory (SCAL) measurements.

SCAL measurements are generally routine core analysis measurements (grain density, bulk density, helium porosity, gas permeability and Dean & Stark analysis §5.3.2.1), plus brine permeability, Klinkenberg and relative permeability measurements, mercury injection, cation exchange capacity, resistivity index and capillary pressure curves, made on core plugs taken *parallel* to bedding. This Ph.D. study involves SCAL data from nine wells taken from a turbiditic sandstone reservoir.

Several plugs had, in addition to SCAL measurements, end-trims taken on each of which thirteen scanning electron microscope (SEM) images were made. A two-dimensional image porosity can be estimated from these images.

The combination of both the core plug and SEM data create an enormous data base from which several different lines of research could be followed; the permeability-porosity relationship was chosen. Initially, it was important to test or validate the core plug and image data sets. The data could then be plotted and interpreted with an understanding of the associated errors.

1.2 Thesis objectives

The aim of this study can be summarised as follows; *A simple, linear permeability-porosity relationship is often inaccurate, but the oil industry use it for the prediction of reservoir permeability from wireline logs. Can pore morphology data obtained from SEM images help to constrain this relationship? To answer this question requires a thorough assessment of the data and the techniques used to create it.*

The study can be split into two parts to fulfil these aims: *data validation (including software validation)* and *data assessment*. See Figure 1.1 for a flow chart of the aims of this study.

Data validation.

The image analysis software was tested to examine whether the numbers generated were both repeatable and represented the images correctly (§6.2.4.2). The image analysis data was then evaluated to assess if the data obtained really related to the mineralogy of the rock, and investigate what statistical definitions would represent the data in the best way (§6.3).

The core plug data needed to be tested in a similar manner as the image data, but due to time and facility limitations this was not possible. Therefore, it was necessary to examine potential errors from the literature, and use that knowledge in the data interpretation (§5.4). A number of interesting results have been observed within the Klinkenberg data plots during the assessment of the core plug data. These plots have been studied closely and the repeatability of the measurements assessed along with the curve shape which revealed an unexpected non-linear pattern (§5.3.6.2).

Data assessment.

The core plug data were investigated, specifically the permeability-porosity relationship. The data were examined to test whether the trends seen within the data were expected from theory and/or results published in the literature.

It is known that pore morphology controls a plug's response to many physical measurements, but an aim of this study is to examine which aspects control the physical properties of interest here (i.e. porosity and permeability). Would a qualitative analysis of the SEM images solve this problem (§6.4.2 and §7.4.1)?

Can the 2D SEM data be related to the 3D core plug data (Chapter 7)? Is there a direct relationship? If so, how can this be explained when the rocks being considered are heterogeneous?

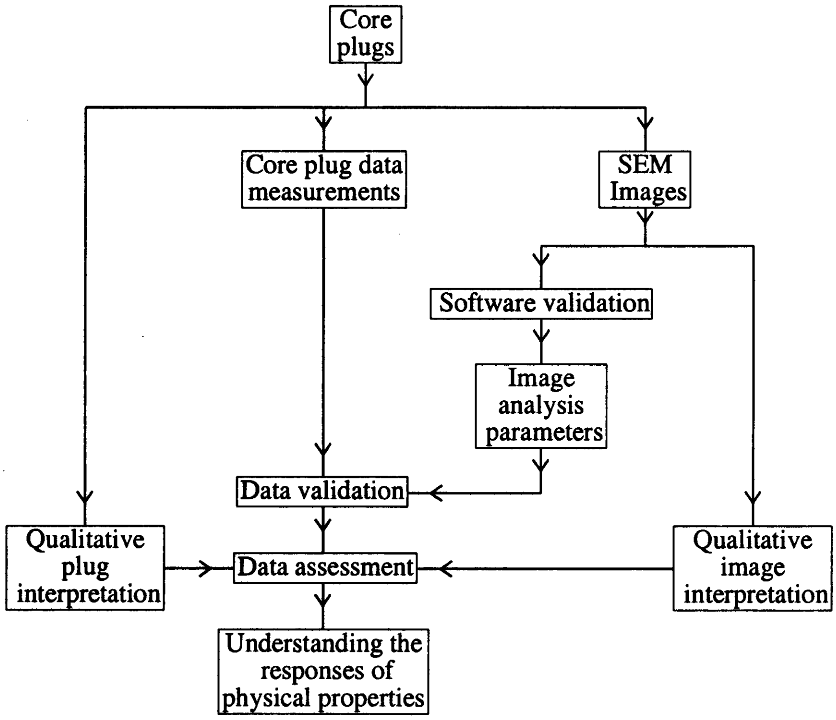

Figure 1.1. Flow chart showing the aims of this thesis

1.3 Thesis structure

This thesis is divided into eight chapters, where Chapters 1 to 4 explain the theoretical background of the thesis, the data used within the study, a critical literature review and the geological background respectively. Chapters 5 to 7 discuss the data, explaining both data errors and merits; it is within these chapters that hypotheses are stated and tested. Finally, Chapter 8 draws all the work together in a discussion making conclusions on how valuable the different data sets are to a petrophysicist, with suggestions for possible future studies.

1.3.1 Chapter content

- *Chapter 1;* Introduction. The introduction gives an outline to the thesis, including a short summary of the available data and an explanation of the overall thesis aims.
- *Chapter 2;* Literature review. A critical review of the literature. The chapter aims to demonstrate much of the confusion associated with core analysis measurements and standards used within the industry, along with definitions and explanations of petrophysical parameters.
- *Chapter 3;* A review of the data used in this study. Here a detailed account of the data available for this study is given.
- *Chapter 4;* Geological framework of the reservoir. This chapter is concerned with the geological setting of the reservoir, looking closely at facies and depositional environments.
- *Chapter 5;* Core plug data. The core plug data are assessed and a comparison between many of the physical parameters are made. A section is dedicated to understanding Klinkenberg data.
- *Chapter 6*; Scanning electron microscopy and image analysis. This chapter investigates the problems associated with image analysis and the positive and negative aspects of the data generated. The work in this chapter was both qualitative and quantitative.
- *Chapter 7*; A comparison of image analysis and core data. This chapter compares the image and core plug data sets and demonstrates the relationships between the 2D and 3D data.
- *Chapter 8*; Conclusions. The hypotheses and associated evidence are brought together and conclusions drawn from the previous chapters. Recommendations for further work are made.

CHAPTER TWO

Literature review

2.1 Introduction

'*No matter how thoroughly a single piece of rock is studied, even on a microscopic scale, it is not possible to predict the properties of a formation as a whole. This should not be taken to mean that fundamental research on a microscopic scale is not of great importance in the study of rock porosity*' (Archie, 1950).

This chapter is a review of papers, books and personal communications based on pore structure within geological situations and biased towards relationships with porosity and permeability. The review is selective due to the massive size of this interdisciplinary subject, which considers work from geological, engineering, petrophysical and geophysical fields. Definitions of pore structure parameters are given, and on occasions mathematical definitions of those parameters (nomenclature in Appendix A). Detailed experimental methods are not given in this chapter, as experiments associated with parameters used in this study are given in Chapters 5 and 6.

2.2 Macroscopic pore structure parameters

Dullien (1992) defines pore structure parameters as, 'those properties that are completely determined by the pore structure of the medium and do not depend on any other property.'

Pores are spaces between solid material and are not usually visible to the naked eye. The pore may be any shape and is able to contain a mixture of fluids. All macroscopic properties of porous media are influenced, to a greater or lesser degree, by the pore structure. Macroscopic pore structure parameters represent average behaviour of a sample containing many pores. Dullien (1992) states that the most important macroscopic pore structure parameters are: *(i)* porosity (§2.2.1), *(ii)* permeability (§2.2.2), *(iii)* specific surface area (§2.2.4), *(iv)* breakthrough (displacement) capillary pressure or bubbling pressure (§2.2.3) and *(v)*, formation resistivity factor (§2.5.1). The best way to determine pore distributions is by the measurement of all pores in a macroscopic sample, all other methods are indirect and require *a priori* information (Dullien, 1992). Archie (1950) had stated earlier that, 'if it were possible to measure the fundamental properties (exact size and fluid distribution) *in situ* of formations penetrated by the borehole, the volume of the hydrocarbon in place and productivity of the layer could be calculated.' Archie and Dullien both observe the importance of knowing the size and distribution of all pores within the rock, but to date there is no realistic method of measuring these exactly within the laboratory, although serial sectioning techniques (§2.3.5) do go some way towards this end result (X-ray tomography can be used on small 1cm^3 plugs), and certainly no methods for *in situ* measurements. Wissler (1987) noted that topological results for sandstones are not substantive and that complete topological mapping of the pore structure is not necessarily desirable. Wissler proposed that because of the variability of the structure and the difficulty of measurement, approaches such as stereological methods and metric measurements appear to be more promising.

Pore structures result from a wide variety of geologic processes including: *(i)* sedimentation with little alteration, *(ii)* alteration by solution, *(iii)* redeposition or cementation (Archie, 1950) to which can be added, *(iv)* fracturing and *(v)* compaction. Cade et al. (1994) also observed the effects of geologic processes on pore structures and note that minerals can precipitate as pore filling or as grain rimming deposits, Figure 2.1 simulates four geologic processes. The way in which sand grains are compacted and cemented together with or without clay infill has strong effects on many petrophysical measurements (see §2.4).

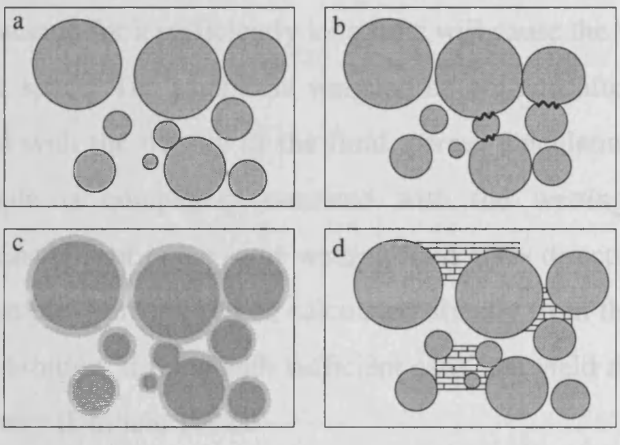

Figure 2.1. Numerical simulation of geological processes for equal spherical grains. (a) 2D slice through packing of equal spheres representing sediment of clean, well-sorted sand. (b) Compaction forces spheres closer together and inter-penetration occurs (pressure solution). (c) Quartz overgrowths cement the compacted packing together. (d) Pore-filling cement, (after Cade et al., 1994)

2.2.1 Porosity

Two main types of void space exist; interconnected or effective pore space and, non-interconnected or isolated pore space. The sum of interconnected and isolated pore space gives a total porosity which is the absolute fraction or percentage of pore space within a sample. Only interconnected, transport or effective pore space can contribute to the transport of matter through a porous medium. Dead-end or blind pores allow fluid in but not out; they are interconnected but have a negligible contribution to fluid transport (Dullien, 1992).

Porosity measurements

The various methods used to determine porosities have been discussed by Collins (1961) and subdivided into the following categories by Scheidegger (1974):

(i) Direct method. Bulk volume of a porous sample is measured and then somehow all the voids are destroyed and the volume of the solids alone is measured.

(ii) Optical methods. The porosity of a sample is equal to the 'areal porosity,' provided that the pore structure is 'random'. The areal porosity is determined on polished sections of the sample. It is often necessary to impregnate the pores with some material such as epoxy in order to make the pores more visible and/or to distinguish between interconnected and non-interconnected pores, as impregnating the sample from the outside will only penetrate the interconnected pores. Image porosity is considered in Section 2.3.1.

(iii) Imbibition method. Immersing the porous sample in a preferentially wetting fluid (§2.5.3) under vacuum for a sufficiently long time will cause the wetting fluid to imbibe into all the pore space. The sample is weighed before and after imbibition. The two weights, coupled with the density of the fluid, permit calculation of the pore volume. When the sample is completely saturated with the wetting fluid, a volumetric displacement measurement in the same wetting fluid gives directly the value of the bulk volume of the sample. Porosity can be calculated directly from the pore volume and the bulk volume. Imbibition, if done with sufficient care, can yield the most accurate value of effective porosity (Dullien, 1992).

(iv) Mercury injection method. The bulk volume of the sample is determined by immersion of the sample in mercury. Most materials are not wetted by mercury and therefore, the liquid will not penetrate into the pores. After evacuating the sample, the hydrostatic pressure of mercury in the chamber containing both the sample and the mercury, is

increased to a high value. As a result, the mercury will enter the pore space and, provided that the pressure is high enough, it will penetrate even into very small pores. Dullien (1992) states that the penetration is never quite complete because it takes infinite pressure to perfectly fill all the edges and corners of the pores; high pressures may cause changes in the pore structure of the sample.

(v) Gas expansion method (used in this study, Chapter 5, §5.3.3), this method measures the effective porosity. The sample is enclosed in a container of known volume, under known gas pressure, and is connected with an evacuated container of known volume. The valve between the two vessels is opened and the gas expands into the evacuated container decreasing the gas pressure. The effective pore volume V_p of the sample can be calculated by using the Boyle's law,

$$V_p = V_B - V_a - V_b\left[\frac{P_2}{(P_2 - P_1)}\right] \qquad [2.1]$$

where, V_B is the bulk volume of the sample, V_a the volume of the vessel containing the sample, V_b the volume of the evacuated vessel, P_1 the initial pressure, and P_2 the final pressure. Bulk volume is obtained separately.

(vi) Density methods. Density methods depend on determining the bulk density of the sample and the density of the solids in the sample. Since the mass of a porous medium resides entirely in the solids matrix, we have the following;

$$m = \rho_s V_s = \rho_B V_B \qquad [2.2]$$

where m is the mass of the sample, ρ_s the density of the solids in the sample, V_s the volume of the solids, and ρ_B the bulk density of the sample. It therefore follows from the definition of porosity ϕ, that,

$$\phi = 1 - (V_s / V_B) = 1 - (\rho_B / \rho_s) \qquad [2.3]$$

The density methods yield total porosity.

Porosity cannot only be measured from core samples but also estimated from relationships with sonic, formation density and neutron logs. Wyllie (1963), proposed the time-average equation for porosity from a sonic log,

$$\phi = \frac{\partial t - \partial t_{ma}}{\partial t_{liq} - \partial t_{ma}} \qquad [2.4]$$

where ∂t is the time for an acoustic wave to travel a given unit distance of formation along a path parallel to the borehole (measured by sonic tool), ∂t_{liq} and ∂t_{ma} correspond to transit times in the pore liquid and the rock matrix respectively. This relation is limited in its applications to clean, compacted formations of intergranular porosity, containing only liquids. Secondary porosity, such as vugs, presence of shale, fractures, or gas introduce errors.

Density logs emit medium-energy gamma rays into the formation from a radioactive source at the borehole wall, resulting in Compton scattering. The extent of which is directly related to the number of electrons per unit volume; the electron density of the formation. Electron density in turn is related to the true bulk density, determined by the density of the rock matrix, the porosity, and the density of the fluids filling the pores. The porosity is calculated from the formula (Rider, 1986),

$$\phi = \frac{\rho_{ma} - \rho_B}{\rho_{ma} - \rho_{liq}} \qquad [2.5]$$

where, ρ_B is the bulk density, ρ_{ma} is the matrix density and ρ_{liq} is the liquid density. The presence of shale or gas in the formation introduces error.

Neutron logs emit neutrons that collide with the nuclei of the atoms present in the formation, from radioactive sources mounted in a sonde. Neutrons colliding with hydrogen nuclei are slowed down more than those colliding with other nuclei. Those neutrons that have slowed to 'thermal' velocities may be captured by nuclei of other atoms, thus making it possible to count them with a detector. The counting rate at a fixed source-detector spacing may be used to measure the hydrogen concentration of the formation. Hydrogen is the most effective 'slowing down' nucleus but other nuclei (in the matrix and fluids) when present in sufficient quantities can introduce substantial errors, thus a matrix correction is required between limestone and sandstone. The neutron logs can give large errors in rocks with a high porosity and clay content.

'As the sonic, density, and neutron logs are affected to a different degree by the matrix composition and the presence of gas or light oils, a combination of several logs, usually in the form of cross plots will give better porosity results' (Schlumberger, 1972). This approach relies on the initial data being of high quality.

Porosity is also related to the formation resistivity factor F (§2.5.1) and can be estimated from resistivity logs in clean water-bearing formations using Archie's formula,

$$F \equiv \rho_o / \rho_b = \phi^{-m} \qquad [2.6]$$

where ρ_o is the resistivity of a non shaley formation sample 100% saturated with brine, ρ_b the resistivity of brine, Archie's m an empirical constant. The 'Humble' formula reviewed by Winsauer et al. (1952) develops a specific version of that suggested by Archie, based on the Humble River Formation; the multiplier is now 0.62 rather than the unity value chosen by Archie,

$$F = 0.62 / \phi^{\,2.15} \qquad [2.7]$$

The sonic, density and neutron logs make *in situ* estimations of porosity, but they are calibrated with core porosity measurements which are considered more reliable as they are actual porosity measurements. As core porosity measurements are not made *in situ* effects of core compaction must be accounted for in the laboratory. The core compaction correction is that factor by which ambient core porosities are multiplied to correct to reservoir condition porosities. Nieto et al. (1994) suggest that uniaxial compaction corrections should not be used in calculating core compaction factors. Instead, *in situ* stresses should be estimated using fracture gradient data. Pore volume compressibility is the measurement of pore volume reduction over a range of overburden pressures. The measurements are used in material balance calculations to accurately assess the amount of oil-in-place. As the pressure is depleted in a reservoir, the effective overburden pressure in the reservoir increases which causes a reduction in pore volume. Failure to take these factors into consideration can result in erroneous volume and production estimates (Basan et al., 1997).

To demonstrate the approximate limits of porosity, calculations on a cubic or wide-packed system of spherical grains gives a porosity of 47.6% (Figure 2.2a), and the rhombohedral or close-packed system has a porosity of 25.9% (Figure 2.2b). The porosity of such systems is independent of grain size (sphere diameter). However, if smaller spheres are mixed among the spheres of either system, the ratio of pore space to the solid framework becomes lower and porosity is reduced. Figure 2.2c shows three-grain-size cubic packing, the porosity of this cubic packing is now approximately 26.5% (Tiab and Donaldson, 1996). These examples assumed no cementation between the grains.

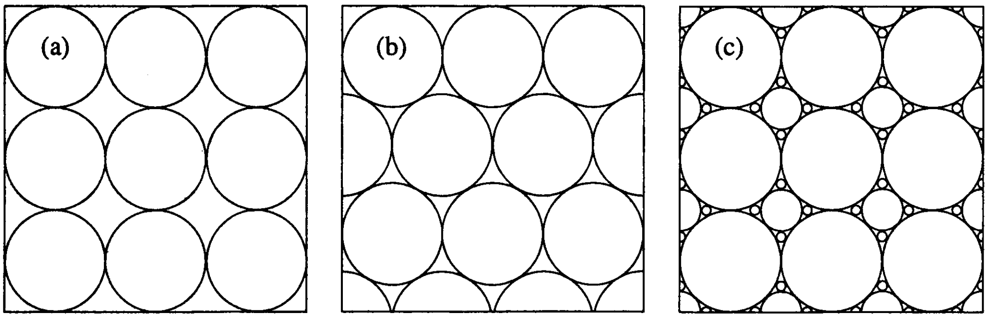

Figure 2.2. (a) cubic packing of single sized spheres, (b) rhombohedral packing of single sized spheres and (c) cubic packing of three-grain-sized spheres

The following section is adapted from Tiab and Donaldson (1996) and investigates the geological classification of porosity. As sediments were deposited in ancient seas, the first fluid that filled pore spaces in sand beds was sea water, generally referred to as connate water. A common method of classifying the porosity of petroleum reservoirs is based on whether pore spaces (in which oil and gas are found) originated when the sand beds were laid down (primary or matrix porosity), or if they were formed through subsequent diagenesis, catagenesis, earth stresses, or solution by water flowing through the rock (secondary or induced porosity). This general classification of porosity is adapted from Ellison (1958) and is based on the time of origin, mode of origin and distribution relationships of pore spaces.

Primary porosity

1. *Intercrystalline*; voids between cleavage planes of crystals, voids between individual crystals and voids in crystal lattices. Many of these voids are sub-capillary (i.e. pores less than 0.02 mm in diameter).
2. *Intergranular* or *interparticle*; voids between grains, i.e. interstitial voids of all kinds in all types of rocks. These openings range from sub-capillary through super-capillary size (voids greater than 0.5 mm in diameter).
3. *Bedding planes*; voids of many varieties are concentrated parallel to bedding planes. Differences of sediments deposited, or particle sizes and arrangements, and of the environments of deposition are causes of bedding plane voids.
4. *Miscellaneous sedimentary voids*: *(i)* voids resulting from the accumulation of detrital fragments of fossils, *(ii)* voids resulting from the packing of oolites, *(iii)* vuggy and cavernous voids of irregular and variable sizes formed at the time of deposition and *(iv)* voids created by living organisms at the time of deposition.

Secondary porosity

Secondary porosity is the result of geological processes (diagenesis and catagenesis) after the deposition of sediment. The magnitude, shape, size and interconnection of the pores may have no direct relation to the form of original sedimentary particles. Secondary porosity can be subdivided into three groups based on the most dominant geological processes:

1. *Solution porosity*: *(i)* channels due to the circulation of warm or hot solutions through the rocks, *(ii)* openings caused by weathering, such as enlarged joints and solution caverns and *(iii)*, voids caused by organisms and later enlarged by solution.
2. *Dolomitisation;* a process by which limestone is transformed into dolomite. If circulating fluids contain magnesium, the calcium ions can be exchanged for the smaller magnesium ions. Substantial replacement of calcium by magnesium can result in a 12-13% increase in porosity.
3. *Fracture porosity*; openings created by structural failure of the reservoir rocks under tension and shear caused by tectonic activities such as folding and faulting. These openings include joints, fissures, and fractures (Bergosh & Lord, 1987; Ostesen, 1983).
4. *Miscellaneous secondary voids*: *(i)* saddle reefs, which are openings at the crests of closely folded narrow anticlines, *(ii)* pitches and flats, openings formed by the parting of beds under gentle slumping and *(iii)*, voids caused by submarine slide breccias and conglomerates resulting from gravity movement of seafloor material after partial lithification.

In carbonate reservoirs, secondary porosity is much more important than primary porosity. However, it is important to emphasise that both types of porosity often occur in the same reservoir rock (Tiab and Donaldson, 1996).

The topic of correlation between porosity and permeability has been discussed for many years (Soeder & Randolph, 1987; Bloch, 1991; Bloch & Helmold, 1995; Liu et al., 1996). The main problem with the correlation is that it attempts to use total volume to predict the effective cross-sectional area for conducting fluids. However, total porosity is a static property related only to storage capacity, and not to the dynamic, flowing capacity of the pore system (e.g. Perez-Rosales, 1976; Katz and Thompson, 1986; Herrick and Kennedy 1994), and for this reason the permeability-porosity relationship can be poor. For example, a pumice has a very large porosity, but the effective porosity is nearly zero and there is no permeability. The reverse scenario is a microfractured carbonate rock which has a very low porosity and a high permeability. Serra (1984) stated that 'disconnected porosity is rarely found in most natural porous media. The clearest example of disconnected porosity is given by fluid inclusions in crystals. This disconnected porosity is often negligible in sedimentary rocks.' This may be the case, but it should be noted that not all interconnected pores create effective flow paths.

Beard and Weyl (1973) and Tiab and Donaldson (1996) discuss how textural properties are important to porosity and permeability values and can be expressed by: *(i)* sorting and *(ii)* grain size, which are of major importance to porosity and permeability, *(iii)* sphericity (shape) and *(iv)* roundness (angularity), which are of minor importance in lithified sediments to porosity and permeability and *(v)* packing, which is very difficult to measure. They state that well sorted sands have greater porosity than poorly sorted sands and that the porosity in well-sorted sands is independent of grain size (Figure 2.2a and b). Figure 2.3 (after Chilingarian, 1963; taken from Tiab and Donaldson, 1996) shows that the grain size of sandstones influences the relationship between permeability and porosity for these examples, and that as grain size increases so does permeability and porosity.

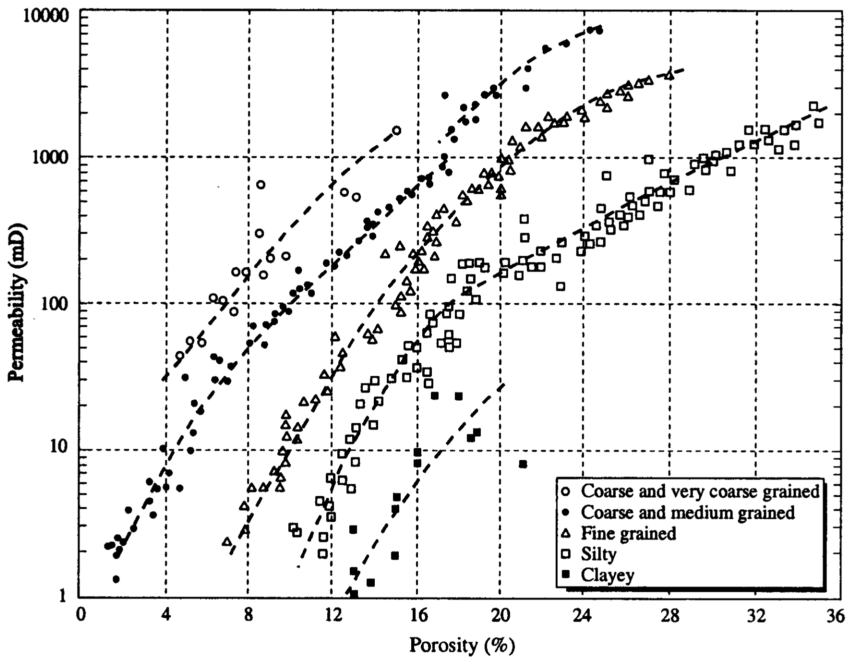

Figure 2.3. Influence of grain size on the relationship between permeability and porosity (after Chilingarian, 1963)

Dutton and Diggs (1992) observed that the decline of porosity and permeability with depth (between 1830-3050 m, with their samples from the lower Cretaceous Travis Peak Formation, East Texas) resulted from increasing quartz cement, decreasing secondary porosity and increasing overburden pressure that closes narrow pore throats (§2.3.2.3).

Figure 2.4 shows typical permeability and porosity trends for various rock types (after Tiab and Donaldson, 1996), and is useful as an aid in the understanding of fluid flow through lithified porous media and reference purposes.

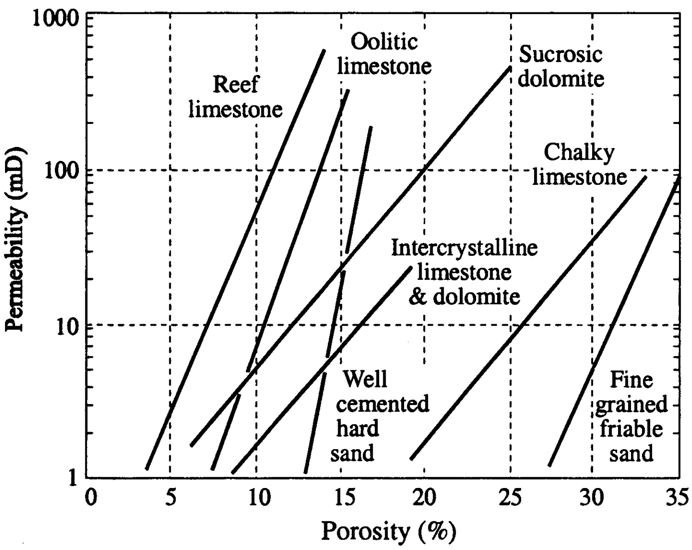

Figure 2.4. Typical permeability-porosity relationship for various rock types (after Tiab and Donaldson, 1996)

2.2.2 Permeability

Absolute permeability, k_A, is the conductivity of a porous medium with respect to permeation by Newtonian fluid. 'Permeability,' used in this general sense, is of limited use as its value in the same porous sample may vary with the properties of the permeating fluid, and the mechanism of permeation (i.e. confining pressure and flow rates). It is more useful to separate out the parameter that measures the contribution of the porous medium to the conductivity and is independent of both fluid properties and flow mechanisms. This quantity is the specific permeability, k_s, which is uniquely determined by the pore structure. In many papers permeability is not defined, so an assumption has to be made by the reader. In geological literature specific permeability is generally being considered, and in this thesis unless it is specified otherwise, 'permeability' is always the specific permeability. Permeability is described by Darcy's law (see Hubbert, 1956, for a discussion on Darcy's law).

Darcy (1856) performed a series of large scale experiments, to solve the problem of supplying water from a spring to the city of Dijon some 10 km away, solving this problem led to an empirical expression of the relationship among the variables involved in the flow of liquids through porous media. Darcy's law, as it is now known, showed that the volume rate of flow q of a liquid per unit cross-sectional area A, of a permeable medium was directly proportional to the pressure gradient ΔP and inversely proportional to the viscosity of the liquid μ, for a 'laminar flow' regime. Permeability k is the constant of proportionality in this equation. Summarising; Darcy's law relates pressure drop across a horizontal core sample, of length L, to the flow rate of fluid through the sample.

$$k = \frac{\mu\, qL}{A\Delta P} \qquad [2.8]$$

For Darcy's law to work there are five main assumptions:

(i) The saturating fluid is inert.

(ii) The permeability of the sample is essentially constant, and does not vary with the nature of the fluid, flow rate or pressure.

(iii) The flow through the sample is laminar (i.e. not turbulent or viscoinertial).

(iv) The fluid should completely saturate the porous media.

(v) The presence of other fluid phases will invalidate Darcy's law.

Darcy's Law can also be expressed by,

$$v = -\left(\frac{k}{\mu}\right)\Delta P \qquad [2.9]$$

where v is the fluid velocity and k the permeability.

Measurement of permeability (permeametry) is usually performed on cylindrically shaped core plug samples with either liquids or gases. However, liquids sometimes change the pore structure and therefore the permeability; due to movement of fines, swelling of certain materials (such as clays) in the pores and chemical reactions. Rock permeability is normally expressed in millidarcies (mD), or μm^2 in SI units. As permeability has the units of length squared, it depends not only on the porosity and pore tortuosity (§2.3.4), as does the electrical conductivity of a sample (§2.5), but also on the absolute length scales of the pores that govern fluid transport (Banavar & Johnson, 1987).

Muskat (1937) was one of the first to document discrepancies between permeability to air and permeability to water, where generally permeability to water was less than that to air. It was found that, for highly permeable media, the differences between permeability to water and air were less than for media with low permeability. Klinkenberg (1941) chose to investigate this discrepancy, as at this time it was assumed that the permeability constant of a porous medium was independent of the flowing fluid, so long as Darcy's law was obeyed. The investigation showed that the permeability constant of a porous medium to a gas is a function of the mean free path of the gas molecules and therefore depends on the pressure, temperature and the nature of the gas. It was from this conclusion that Klinkenberg (1941) introduced the idea that when the mean free path of gas molecules are small, the permeability to gas should be expected to approach that for liquids (§2.2.2.2).

Darcy's law must be modified for flow measurements with a gas, as gases are compressible. The equation for ideal horizontal flow of gas under steady-state conditions is,

$$k_g = \frac{1000(At.Pr.)q\mu L}{P_m(P_1 - P_2)A} \qquad [2.10]$$

where k_g is the gas permeability, q the flow rate, L the length, A the cross-sectional area, μ the gas viscosity, P_2 the downstream pressure, P_1 the upstream pressure, $At.\ Pr.$ is atmospheric pressure in atmospheres and P_m is mean pressure and equals $(P_1\text{-}P_2)/2$.

Consolidated sandstone and carbonate formations often give plots of log permeability against porosity which are linearly proportional, but these trends are not clearly understood. Differences in trends are attributed to differences in initial grain size and sorting, diagenetic history, and compaction history (Krumbein & Monk, 1942). Archie (1947) noted that the characteristics between rocks follow trends, not definite mathematical equations. The permeability of sands and sandstones will increase with increasing gravel and coarse grains, even while decreasing porosity. Permeability and porosity increase in unconsolidated sands with better sorting. Nelson (1994) stated that models to predict permeability from porosity and other measurable rock parameters fall into three classes based on either grain, surface area or pore dimension considerations. It is often found that the vertical permeability of a formation is several orders of magnitude less than the horizontal permeability (Dullien, 1992) which is evidence of the anisotropy associated with rocks, and an example of the difficulties in predicting permeability.

The single-phase permeability of a permeable medium is determined by both the bulk physical properties of the interconnected pore system (e.g. porosity and tortuosity) and the statistics of its particle-size distribution (Panda and Lake, 1994). Nelson (1994) stated that it is the dimension of connecting pores that determine permeability, not grain-size, sorting or porosity. However, grain size and sorting obviously do have an effect on the dimension of connecting pores.

2.2.2.1 Hagen-Poiseuille equation applied to gas flow in a capillary tube

The Hagen-Poiseuille equation, written for gas flow in a capillary tube is as follows,

$$G = \left(\frac{d^3\pi}{64\Re T}\right)\left[\pi\overline{U}_m + \left(\frac{dP_m}{2\mu}\right)\right]\left(\frac{\Delta P}{L}\right) \qquad [2.11]$$

where, G is the molar flow rate, d the diameter, $\Re$ the universal gas constant, T the absolute temperature, $\overline{U}_m$ the mean molecular speed, and $P_m = (P_1+P_2)/2$ (Dullien, 1992).

A plot of $G/\Delta P$ against P_m is expected to give a straight line, but at low ΔP, the line curves upwards giving a minimum at $D/\lambda = 0.4$ (Knudsen, 1909), where λ is the mean-free path of the gas. At $P_m = 0$ the experimental curve intercepts the ordinate axis at the specific flow rate corresponding to pore Knudsen flow, whether this minimum type behaviour actually exists is not proven. It has been suggested that the pore size distribution may be the factor that determines whether a minimum is observed or not.

2.2.2.2 Klinkenberg theory

This section is a summary of Klinkenberg's theory of slip. A complete derivation of the theory behind the Klinkenberg equation is given in Appendix C.

In gases, unlike liquids, the velocity at solid walls cannot, in general, be considered zero (Kundt and Warburg, 1875; Dawe, 1973), but a 'slip' or 'drift' velocity at the wall must be taken into account (Figure 2.5). This effect is significant when the mean-free path of the gas molecules is of a magnitude comparable to the pore size. The mean-free path is the average distance a molecule will travel before it collides with another. The distance between the molecules varies continuously, but the average distance between them is very much greater than the diameter of a pore, at normal temperature and pressure. At the lower pressures molecules will collide less frequently, the mean free path is larger and the slip effect is enhanced (i.e. the slip effect is not a constant for a sample but varies with pressure). Slippage is also affected by the molecular speed and weight (Figure 2.6).

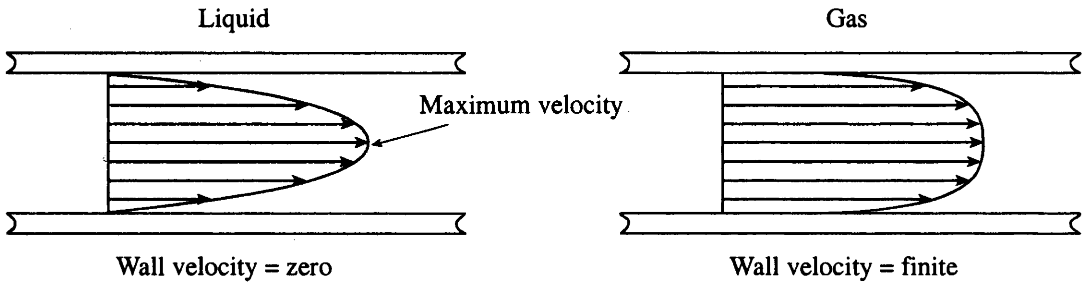

Figure 2.5. A figure to show the slip velocity at a pore wall for a liquid and gas

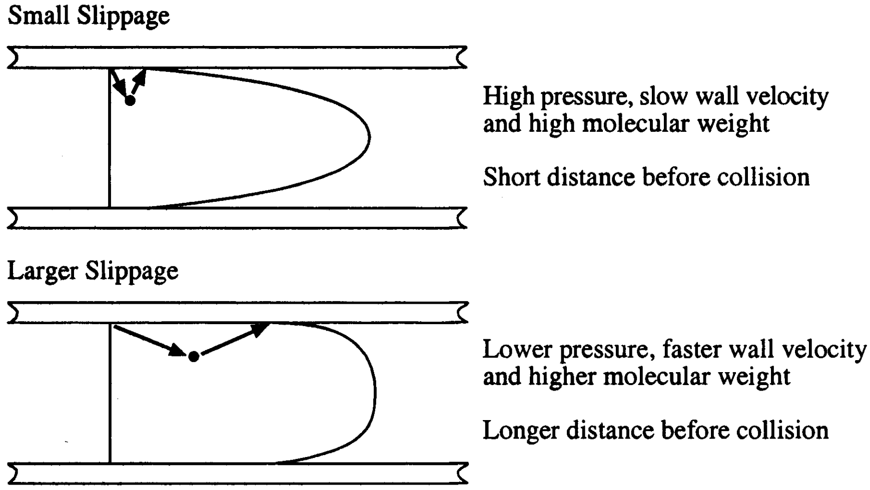

Figure 2.6. A figure to demonstrate effects on gas slippage

Another way of describing the slip effect is, as the mean-free path becomes an increasingly greater fraction of the capillary diameter, the 'wall velocity' increases in significance relative to the average velocity. When the mean-free path of the gas molecules is greater than the width and the length of the capillary, 'molecular streaming' or Knudsen flow is said to occur (i.e. diffusion is mainly due to the molecules colliding with the walls, rather than each other). In summary, when the gas is able to move freely at low pressures it moves more quickly due to the increased slip effect, therefore permeability of the plug appears to be that much higher. However, if the gas is under pressure the molecular collisions are more frequent and the slip effect is decreased and the gas permeability decreases and approaches that of a liquid.

Klinkenberg (1941) modified the Poiseuille equation, which describes flow through capillaries, to account for gas slippage at the capillary (pore) walls. He created a model that looked at gas flow through a bunch of randomly orientated straight capillaries and argued that the mean-free path of the gas is greater than or equal to the pore throat dimension and inversely proportional to the mean pressure giving,

$$\frac{4c\lambda}{r} = \frac{b}{P_m} \quad [2.12]$$

where λ is the mean-free path, P_m the mean pressure, c a constant ($\cong$ 1), where $c\lambda$ equals the average distance from the pore wall at which the last collision of the molecule took place. r is the mean pore throat radius, and b a constant called the 'slip-factor', which is characteristic of both the gas and the porous medium. Klinkenberg combined Poiseuille's law (modified for slip) with Darcy's law for gas flow and obtained,

$$k_g = k_l\left(1 + \frac{4c\lambda}{r}\right) \quad [2.13]$$

where k_g is the permeability to gas and k_l is the permeability to liquid. Combining Eq. 2.12 and 2.13 yields the familiar Klinkenberg equation,

$$k_g = k_l\left(1 + \frac{b}{P_m}\right) \quad [2.14]$$

Klinkenberg concluded that if the simplified considerations are not only valid for a system of straight capillaries, but also to porous media then according to Eq. 2.13 and 2.14:

(i) k_g is a linear function of $1/P_m$.

(ii) k_g is independent of differential pressure (and hence, flow rate), provided P_m is constant.

(iii) The slip-factor b is inversely proportional to r, therefore, b is small or negligible for high permeability samples.

(iv) At the same mean pressure, k_g is different for different gases, as their mean-free paths are different, but will be equal at infinite pressure, since mean-free paths are zero.

(v) k_g when extrapolated to infinite mean pressure ($1/P_m$= 0) should give the 'true' k_l.

Klinkenberg (1941) tested his ideas on porous media and found firstly, the assumption k_g being a linear function of $1/P_m$ is an approximation; showing that the value of the constant b increases with increasing pressure (the constant b is called the slip-factor which can cause confusion as *gas slippage* decreases with increasing pressure, Figure 2.6). An application of this is that Kundt and Warburg's (1875) theory of gas slip can only be applied when the mean free path is small compared to the capillary (i.e. deviations are expected at reduced pressures). Secondly, Klinkenberg validated that permeability does not depend on pressure difference (P_1-

P_2) as long as mean pressure is constant (i.e. permeability measured with upstream and downstream pressures of 8 and 10 psi will be the same as a permeability generated with pressure values of 4 and 14 psi). McPhee (1992) stated 'despite evidence to the contrary in the literature, in our view, we believe that the slip-factor has little physical significance, and at best should be viewed as a weak fitting parameter, until definitive test procedures can be better identified.' With the confusion which surrounds the slip-factor (b) and actual gas slippage this is sound advice from McPhee.

The Klinkenberg equation is used to express the effect of 'slip' in porous media gas flow,

$$\frac{v_2 P_2 L \mu}{\Delta P P_m} = k\left[1+\left(\frac{b}{P_m}\right)\right] \qquad [2.15]$$

where, v_2 is the volumetric flow rate divided by the cross-sectional area, P_2 the final pressure, P_m the mean pressure, L the length, μ the dynamic viscosity, ΔP the pressure gradient, and k is the permeability.

Klinkenberg data is interpreted in Chapter 5 (§5.3.6) and so it is important to note that interpretation of Klinkenberg data hinges on the assumption that the slip-factor is constant, and does not vary with mean pressure. Klinkenberg (1941) acknowledged that the value of the slip-factor b, increased with increasing pressure. This is a very significant statement which is often overlooked by analysts. Klinkenberg also convincingly argues that the concept of slippage was developed for gas flow in capillaries and is unlikely to be valid for flow in tortuous pore systems.

The Klinkenberg corrected permeability can be misunderstood; Luffel et al. (1989) state that all the permeability measurements in their paper are either corrected for the Klinkenberg effect or were conducted at high pore pressure to be equivalent to Klinkenberg corrected permeability. This is wrong, as by definition a Klinkenberg permeability would have to be measured at infinite gas pressure, which is not feasible. McPhee (1992) states that acceptable matches between liquid and Klinkenberg permeability are only found with inert media (e.g. glass filters) and refined mineral oils. Measured brine permeability in real reservoir rock, where the fluid can interact with the rock solid surfaces, are typically two to three times lower that the equivalent Klinkenberg permeability values.

2.2.2.3 Kozeny correlation

Kozeny (1927) derived one of the most fundamental and popular correlations expressing permeability as a function of porosity and specific surface area. The refined Carmen-Kozeny correlation has historically been used to explain the fundamental causes of permeability because it provides a link between media attributes and flow resistance (Panda and Lake, 1994). Derivation of the Kozeny correlation is given in full below and is used in Chapter 6 (§6.2.5.5) in the derivation of an image permeability.

Consider a porous rock sample of cross-sectional area A and length L as being made up of a number n, of straight capillary tubes in parallel, with the spaces between the tubes sealed by a non-porous cementing material. If the capillary tubes are all the same radius r and length, the flow rate q through this bundle of tubes according to Poiseuille's equation is (adapted from Tiab and Donaldson, 1996),

$$q = \left(\frac{n\pi r^4}{8\mu} \right) \frac{\Delta P}{L} \qquad [2.16]$$

where the pressure loss ΔP over length is expressed in dynes/cm^2.

The flow of fluids through these n capillaries can also be approximated by Darcy's law as,

$$q = \left(\frac{kA_c}{\mu} \right) \frac{\Delta P}{L} \qquad [2.17]$$

where A_c is the total cross-sectional area, including cemented zones, of this bundle of capillary tubes. Equating Eq. 2.16 and 2.17 and solving for k gives,

$$k = \left(\frac{n\pi r^4}{8A_c} \right) \qquad [2.18]$$

By definition, the porosity is,

$$\phi = \frac{V_P}{V_B} = \frac{n\pi r^2 L}{A_c L} = \frac{n\pi r^2}{A_c} \qquad [2.19]$$

Substituting $A_c = n\pi r^2/\phi$ from Eq. 2.19 provides the simplest relationship between the permeability and porosity for pores of the same size and radii equal to r,

$$k = \left(\frac{\phi r^2}{8} \right) \qquad [2.20]$$

where k is in cm^2 (1 cm^2 = 1.013x10^8 Darcys) or in μm^2 (1mD = 9.871 x 10^{-4} μm^2) and ϕ is a fraction.

Let S_{Vp} be the internal surface area per unit of pore volume, where the surface area A_s, for n capillary tubes is $n(2\pi rL)$ and the pore volume V_p is $n(\pi r^2 L)$. Therefore,

$$S_{Vp} = \frac{A_s}{V_p} = \frac{n(2\pi rL)}{n(\pi r^2 L)} = \frac{2}{r} \qquad [2.21]$$

Let S_{Vgr} be the specific surface area (§2.2.4) of a porous material of the total area exposed within the pore space per unit of grain volume. For a bundle of capillary tubes, the total area exposed to flow, is equivalent to the internal surface area A_a [$A_a = n(2\pi rL)$], and the grain volume V_{gr}, is equal to $A_c L(1-\phi)$. (From $\phi = \left(\frac{V_B - V_s}{V_B}\right) = \left(\frac{A_c L - V_s}{A_c L}\right)$), thus,

$$S_{Vgr} = \frac{n(2\pi rL)}{A_c L(1-\phi)} = \frac{2\pi rn}{A_c(1-\phi)} = \frac{n\pi r^2}{A_c}\left(\frac{2}{r}\right)\frac{1}{1-\phi} \qquad [2.22]$$

Combining Eq. 2.20, 2.21 and 2.22 gives,

$$S_{Vgr} = S_{Vp}\left(\frac{\phi}{1-\phi}\right) \qquad [2.23]$$

Eq. 2.20 can be expressed as,

$$k = \left(\frac{\phi}{2}\right)\frac{1}{(2/r)^2} = \left(\frac{1}{2S_{Vp}^{\;2}}\right)\phi \qquad [2.24]$$

Substituting for S_{Vp} from Eq. 2.23 yields,

$$k = \left(\frac{1}{2S_{Vgr}^{\;2}}\right)\frac{\phi^3}{(1-\phi)^2} \qquad [2.25]$$

Panda and Lake (1994) modified the Carman-Kozeny equation and concluded that above approximately 1 Darcy their model adequately predicts single-phase permeability; below 1 Darcy they attribute the failure of the model to 'blocked pore throats' which do not contribute to flow. The model was used to investigate the nature of the origin of variability in permeability and was used to explain facies-controlled differences in permeability.

Katz and Thompson (1987) state the possible relationship of absolute permeability k_A as,

$$k_A = c l_c^{\,2} \frac{\sigma}{\sigma_b} \qquad [2.26]$$

where, c is a constant (approximately 1/226), l_c the characteristic length, σ the rock conductivity and σ_b the conductivity of the brine in the pore spaces.

Hagiwara (1984), expresses rock permeability as,

$$k = c\phi^m r^2 \qquad [2.27]$$

where, c is a constant and r, is an average pore throat radius of the rock. The assumption was made by the reader that the rock permeability is equivalent to specific permeability k_s, as no detailed definition was offered. Eq. 2.27 is analogous to Archie's conductivity relationship for rocks saturated with brine (Eq. 2.6).

As permeability measurements and electrical conductivity measurements (§2.5) are both concerned with pore connectivity the two are frequently compared (Wyllie & Spangler, 1952; Patterson, 1983; Herrick, 1988; Kostek et al., 1992). Archie (1947) concludes that pore structure has a large bearing on the air permeability but does not greatly affect electrical conductivity. Hagiwara (1984) does not state the degree or effect of pore structure, rather that, 'permeability and electrical conductivity have identical tortuosity dependence.' This statement has been questioned as electrical and hydraulic tortuosity may be different (Clennell, 1997, §2.3.4). Doyen (1988) proposed that 'permeability and conductivity can be expressed in terms of the ratio of two characteristic lengths, which can be estimated directly from microsections.'

Doyen does accomplish this, but the repeated use of assumptions in his work needs to be considered if a geological application of his findings are to be considered. Also, the results are only meaningful in 2D. Doyen noted that, the inference of converting the 2D data into 3D would require unrealistic simplifying assumptions about the shape of the pore system, and no improvement in accuracy would be gained in the calculation of the flow parameters.

Wong et al. (1984) conclude that, 'the scaling behaviour of both the conductivity and the permeability of rocks is determined by the skewness of their pore-size distribution'. They state that permeability is more strongly dependent on the tube-size fluctuation than the electrical conductivity, but both quantities are in fact governed by the tube-size distribution and they can be simply related, at least in 1D.

The two main ways in which fluid flow through a porous media can be inhibited, and hence give reduced values of absolute permeability are: *(i)* mechanical entrapment of the fluid molecules during the flow through the porous media and, physical adsorption of the fluid onto rock surfaces; dynamic adsorption is less than static adsorption because of inaccessible pore volumes (Ali & Barrufet, 1995). *(ii)* A coating of the pore surfaces with discrete clay particles, which would cause a roughness, 'catching' the passing molecules and therefore reducing permeability. Ali and Barrufet (1995) state that pore throats can allow the flow of brine while restricting flow of the relatively larger polymer molecules. Smith (1970) found that calcium carbonates have a greater affinity for polymers than silica surfaces and Szabo (1975) observed that polymer adsorption increases as salt concentration increases.

2.2.2.4 Problems associated with gas permeability measurements

A viable direct method of predicting permeability requires both adequate theoretical underpinnings relating pore dimension to permeability, and experimental determination of the critical pore dimension parameters (Nelson, 1994). Permeability is usually measured with air at a mean pressure slightly above 1 atm; a rapid steady-state determination, which can lead to serious errors. Jones (1972) states that the low-pressure air permeability of tight core often differs from its permeability to liquid or high pressure gas measurements by 30-100% or more, which is due to gas slippage. These low-pressure errors are avoided by making measurements at several mean pressures and then extrapolating back to an infinite pressure, and obtaining a Klinkenberg corrected permeability (§2.2.2.2); relatively this is a slow procedure.

Applying a confining pressure is essential to reduce errors in permeability measurements. Gas bypass is a particular problem in low permeability samples, where high upstream pressures have to be applied to achieve a conveniently measurable gas flow rate. As the upstream pressure increases, with the confining pressure held constant, the effective sample confining pressure reduces and provides an opportunity for bypass (McPhee, 1992), a net confining pressure is recommended. Luffel et al. (1989) found a difference in permeability measurements made at net overburden pressure to those at ambient pressure, due to the presence of coring induced microcracks which had gone unnoticed during the analyses. If pressure was not applied to the cores during measurement excess permeability values were obtained. However, applying a confining pressure has the limitation that it may create an unrealistic crushing effect on the plugs.

2.2.2.5 Forchheimer (non-Darcy) flow analysis

Forchheimer (1901) observed that Darcy's law failed at high flow rate, underpredicting pressure drop. He showed that flow through a porous medium is represented by means of the quadratic equation,

$$-(\Delta P / \partial L) = (\mu v / k) + \beta \rho v^2 \qquad [2.28]$$

where $(\Delta P/\partial L)$ is the unit pressure drop across the core, L the length, v the flow rate/unit area (velocity), β the inertial resistance (Forchheimer) factor, ρ the gas density and k the permeability. As Eq. 2.28 includes permeability it allows the analyst to calculate permeability even if the data are within a non-laminar flow regime. The inertial term, ρv^2, becomes negligibly small at low fluid velocities and the Forchheimer equation approaches, but never equals, the Darcy equation. The non-Darcy flow coefficient is a property of the fluid as well as of the porous medium and increases with increasing effective stress, high temperatures and the presence of an immobile liquid saturation (Tiss and Evans, 1989).

2.2.3 Capillary pressure

Capillary pressure is used to study the behaviour of porous media containing two or more immiscible fluid phases; it relates the pressures in the two fluid phases (Dullien, 1992). 'A certain layer of rock will have a pore structure giving it a particular family of capillary pressure curves. The scattering of these curves will be large, but the only reason there is any correlation is because the measurements were made from a bed deposited under the same conditions,' (Archie, 1950). Archie is correct, as the capillary curves relate to the physical factors determined by diagenesis as well as the initial sediment deposition.

Archie (1950) showed that samples with an appreciable permeability exhibit a plateau or seat, and a steep slope in their capillary pressure curves. Examination of these curves show that two straight lines can be drawn to define the curve fairly well. The angle 'A' formed by the extension of these lines is used for interpretation; as 'A' increases the permeability of each type of rock decreases until one line appears and the plateau disappears (Figure 2.7). Katz and Thompson (1986) have interpreted the rapid rise in the mercury injection curve to occur when the intruded mercury initially forms a connected cluster that spans the sample. Archie (1950) concluded that 'rocks with high permeability for porosity exhibit much steeper 'steep slope' (Figure 2.7) due to less small pore space. Formations with comparatively low permeability for porosity however, exhibit a more gentle steep slope because of the many small pores.'

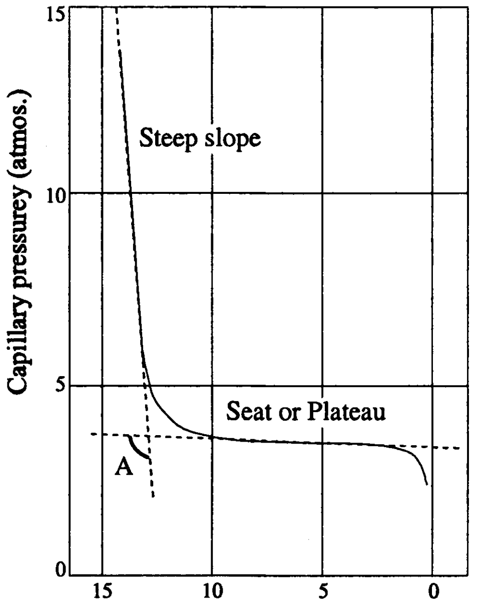

Figure 2.7. An idealised capillary pressure curve, which depict results obtained by injecting mercury into the cores. Two lines are constructed and an angle 'A' measured (after Archie, 1950)

The breakthrough capillary pressure or bubbling pressure P_{cb}, corresponds to the first appearance of the non-wetting (§2.5.3) phase on the outlet face of a plug sample. The reduced breakthrough capillary pressure P'_{cb} can be expressed as,

$$P'_{cb} = P_{cb} / 4\sigma_f \cos\theta \qquad [2.29]$$

where, σ_f is the surface tension and θ the contact angle (Dullien, 1992). P'_{cb} a characteristic of the pore structure of the sample, and is the minimum value of P_{cb} at which the penetrating fluid becomes hydraulically, or electrically (in the case of mercury), conductive in a macroscopic sample. Further reading on the application of capillary pressure curves can be found in Wardlaw & Taylor, 1976; Thompson et al., 1987; MacGowan, 1992; Ruth and Chen, 1995.

2.2.4 Specific surface area

Specific surface area of a porous material is defined as the interstitial surface area of the voids and pores either per unit mass (S) or per unit bulk volume (S_v) of the porous material. Specific surface based on the solids volume is denoted by S_o (Dullien, 1992). Ruzyla (1984) defined the specific surface as the ratio of area to volume, and its dimensions as $(\text{length})^{-1}$. Specific surface of a porous reservoir rock is an important parameter with regard to fluid flow, and it has long been known to be closely related to permeability (see Dullien, 1992, chapter 3 for examples). Laboratory studies show that NMR, gas adsorption and cation exchange capacity also serve as measures of surface area that can be correlated with permeability (Nelson, 1994).

2.3 Microscopic pore structure parameters

'The petrophysical system revolves mainly around pore-size distribution which defines the capillary pressure curve, permeability and porosity. The pore-size distribution does not necessarily define the type of rock, for actually several types of rock may have essentially the same pore-size distribution,' (Archie, 1950).

Permeability and formation factor are important properties in assessing hydrocarbon reservoirs. The two properties both require the existence of porosity, but the relationship of either to the amount of porosity is variable in type and quality. The patterns displayed on cross-plots of porosity and permeability commonly differ from formation to formation, and in single formations samples with similar porosity values can differ in permeability by several orders of magnitude. Such behaviour shows that the way in which the porosity is configured can be more important than the quantity of porosity. To understand this phenomenon, some knowledge of the porous microstructure is required (Burdine et al., 1950; Davies, 1990; Ehrlich et al., 1991a; Bowers et al., 1994; Lowden, 1994; Bliefnick & Kaldi, 1996; Dias & Jing, 1996;). Schlueter et al. (1991) stated the same point 'the macroscopic transport properties of porous and fractured media depend critically upon processes at the pore level, the connectivity and geometry of the pore space being most influential.'

2.3.1 Image porosity

Image porosity is defined as the area of detected pores divided by the image area, where for this study a pore space is any void which has been impregnated with epoxy (§6.2.5.1). Coskun and Wardlaw (1995) determined image porosity in the same way. The definition of the fraction of core porosity not accounted for by image analysis ϕ_{fc}, is,

$$\phi_{fc} = (\phi_c - \phi_{img}) / \phi_c \qquad [2.30]$$

where, ϕ_{img} is the image porosity and ϕ_c is the core measured porosity. ϕ_c is always greater than ϕ_i, and Coskun and Wardlaw (1995) conclude that this difference is due to the resolution in the calculation of ϕ_{img}, in effect small pores are not counted. Ehrlich et al (1991b) made similar conclusions and stated that the ratio of image pore pixels to total image pixels is called the total optical porosity (TOP). This is normally less than the physically measured porosity because some patches of porosity are too small to resolve. TOP is associated with effective porosity and the difference between TOP and physical porosity is usually attributed to immobile fluids.

There are different opinions on the validity of determining porosity from an image. Kendall and Moran (1963) state that porosity exposed on the surface of a section (point count porosity) equals the pore volume proportion under stereological assumptions. Ehrlich et al. (1991b) state that for transmitted light analysis porosity may be viewed beneath the surface of the section (viewed for instance, through an overlying transparent mineral) and therefore unbiased volumetric estimations are not possible. Ruzyla (1984) designed a quantitative image analysis system that is configured for characterising pore space and states that this quantity and quality of information is not obtainable using conventional thin-section point count techniques.

2.3.2 Feature analysis

Evidence from scanning electron microscopy (SEM) studies show that there are undoubtedly heterogeneities on a pore scale (e.g. microvariations in the distribution of clay minerals with the pores, Best & McCann 1995; Chapter 6). Several works have shown that 2D sections contain sufficient information to study relationships between 3D pore geometry and petrophysical properties (Etris, 1991; Ehrlich et al, 1991b; McCreesh et al, 1991; Nesbitt et al., 1991; Coskun et al., 1993).

An image feature is a closed region on the image with specific textural characteristics. The significance of individual feature parameters is poorly understood. Segmentation (§2.3.5) allows quantification of the relatively simple individual feature parameters. Manual segmenting is possible but slow and simple; non-subjective, automatic segmentation is preferable. Erosion and opening operations can be used for segmentation, these operations simplify features by removing irregularities of shape. Erosion operations cause the size of the feature to be reduced, whereas the opening operation keeps the size maintained but, is less effective at segmenting features. Rink and Schopper (1976) suggested a 'cutting' process is better than the erosion or opening operations, as it combines them both, but also uses logical binary combinations to simplify features.

2.3.2.1 Shape factor

Barrett (1980) presents a thorough and critical review of 2D shape descriptions used for geologic studies. He considers the shape of a particle to be expressed in terms of three independent properties: *(i)* the particles form (overall shape), *(ii)* roundness (large-scale smoothness) and *(iii)*, its surface texture. Form descriptors are mainly various ratios of principal axes. Roundness descriptors are mainly related to maximum or average curvature of the grain boundary. Barrett suggests specific shape measures for specific geologic application. Wadell (1935) showed these shape factor qualities to be logically independent. Ehrlich and Weinberg (1970) devised a technique that could yield a shape equation that estimates, and reproduce, 2D grain shapes as precisely as needed. Schwarcz and Shane (1969) did a study which based its definitions of shape properties as much as possible on objectively quantifiable measures of the whole particle. Wissler (1987) states that because pore features are representations on a plane and are *not* projections of particle outlines, shape measures do not appear to be particularly well-suited for describing pore structure.

Fourier methods of describing particle shape were first developed for sedimentology by Schwarcz and Shane (1969); Ehrlich and Weinberg (1970). Clark (1981) emphasises Fourier methods of shape description and presents nine desirable attributes of shape descriptors. Fourier coefficients are used to parameterise the profile curve of the particles. For a more complete summary see Boon et al. (1982).

Shape measure must be multivariate because the more a shape departs from simplicity, the more measurements are required to define it. The erosion/dilation pore processing procedure (Ehrlich, 1984) was designed to characterise precisely pores of varied and potentially complex geometries, and to provide optimal input into a pattern recognition/classification algorithm for deriving pore types from the pore size and shape distributions (Ehrlich et al., 1991a). A drawback in the classification by Ehrlich et al. is the same as all manual classification procedures in that they first require observation, then interpretation. A major problem concerns the penalty for error, bias or inconsistency, which is difficult to detect and once detected difficult to undo. Substituting electronic apparatus in place of the mind and eye of the observer for acquisition and storage of raw, un-interpreted imagery permits image acquisition to be distinctly separated from the process of classification (i.e. the images can be reprocessed as requirements change, Ehrlich et al., 1991b).

Figure 2.8 is a schematic showing the dependence of effective sampling area on feature size. The centre of the circular features must lie within the inner box to be counted (shaded features). The smaller circles (Figure 2.8a) can lie within a larger area, without touching the outer frame than the larger circles (Figure 2.8b). Thus, the smaller circles are sampled over a larger effective area. For simple features such as these, an analytic relation can be found to correct the sampling bias (Wissler, 1987).

(a) 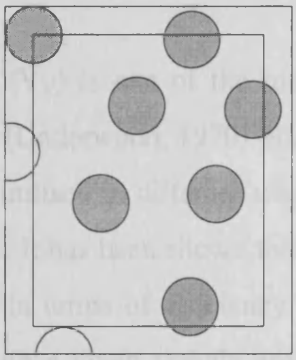 (b) 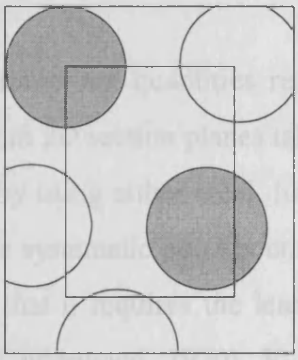

Figure 2.8. A schematic illustration of the dependence of effective sampling area on feature size, (after Wissler, 1987)

The Fisckmeister shape factor, *f*, (Fisckmeister, 1974) is calculated from consecutive parallel sections taken through a porous sample, close enough to allow each capillary branch to be followed from one section to the next, from this an irregular pore structure can be reconstructed. Wissler (1987) states that this shape factor is well-suited to the characterisation of pore space in sandstone, but only if properly computed.

Summarising; 'feature analysis is an important part of a comprehensive study of pore structure because it gives a measure of the variation in the structure. Stereological parameters determined from average feature parameters should agree with the values obtained by other stereological methods (e.g. point counting, lineal analysis, tangent counts)' (Wissler, 1987).

2.3.2.2 Stereology

The term stereology was coined about 20 years ago (Weibel, 1974) to describe a collection of mathematical methods which relate parameters defining 3D structures to measurements on 2D sections, and 'draws heavily on some fundamentals of geometrical probability' (Dullien, 1992). Quantitative stereology attempts to characterise numerically the geometrical aspects of those features of the microstructure that are of interest (Underwood, 1970). To make progress in the study of pore structure, it is assumed that the pore structure is sufficiently random to allow application of stereological methods. Quantitative stereology has several attributes which make it well suited to quantifying the pore structure in sandstone: *(i)* probabilistic foundation, *(ii)* direct geometric interpretation and *(iii)*, that small numbers of assumptions are typically required (Wissler, 1987). Ali and Barrufet (1995) state that results obtained from an environmental scanning electron microscope substantiate the results of Ali (1993); that 2D images can be used to formulate what the 3D object would look like from thin section analysis.

The volume fraction (V_V) is one of the most important quantities required in quantitative stereological analysis (Underwood, 1970). Random 2D section planes taken from the object to be observed, may be utilised in different ways, by using either areal, lineal or point counting analysis, to obtain V_V. It has been shown that the systematic point count is markedly superior to the other methods in terms of efficiency, in that it requires the least amount of effort to obtain an estimate with a given sample error (Underwood, 1970). V_V values are measured using the areal method in this study, and are used in the calculation of an image porosity from SEM images (Chapter 6).

2.3.2.3 Pore throats

Pore throats are often used in the literature as a description of when one pore narrows before it connects to another pore (Kopaska-Merkel, 1994; Luo & Machel, 1995). This relationship can often be observed in 2D but it is only a representation, as the relationship is only true in 3D. Dullien (1992) describes pore throats as where you find a local minimum of a void and place a boundary across that space. Modelling performed by Cade et al. (1994) provided a quantified understanding of how different styles of cement and compaction influence pores and pore-throats (Figure 2.1).

2.3.3 Image texture analysis

The relationship between image texture and rock texture (e.g. size, shape, sorting, orientation, and packing of grains) only exists for special cases (Blatt et al., 1972). Haralick and Shanmugam (1973) characterised the image texture of sandstone from the spatial grey tone (intensity) arrangement of digitised transmitted light photomicrographs. Haralick (1979) reviewed various approaches to the measurement of image texture and defined texture as 'an organised area phenomena which is constructed from tonal primitives with certain spatial organisation.' Wissler (1987) gives some limitations of image texture analysis by spectral results, 'spectral results do show some character of the image, but it is uncertain how to relate the data to geometrical aspects of the structure. Further, the spectra have not been shown to relate quantitatively to any physical properties. The local spatial relations of intensity variations probably carry no more useful information than the location of pore-grain and grain-grain boundaries.'

2.3.4 Tortuosity and connectivity

Tortuosity can have various meanings when used to describe different transport processes taking place in a porous material. Values for electrical, diffusional and hydraulic tortuosity may be, in general, different from one another (Clennell, 1997). Electrical tortuosity is defined in terms of conductivity (i.e. electrical current), whereas hydraulic tortuosity is defined geometrically (i.e. in terms of a static path length) and diffusional tortuosity is computed from temporal changes in concentration (i.e. flux of material). Hydraulic or pore tortuosity is a measure of how windy or tortuous a pore tube is. Pore tortuosity τ, is defined as,

$$\tau = \left(\frac{La}{L}\right)^2 \qquad [2.31]$$

where La is the length of the tube and L is the length of the rock (Figure 2.9). Tortuosity is an extensive and important subject (see Dullien, 1992; Clennell, 1997 for further reading).

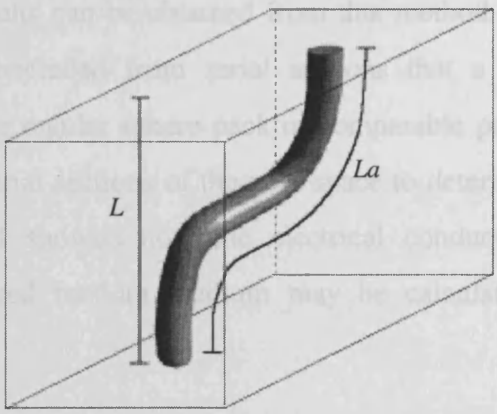

Figure 2.9. Diagrammatic representation of pore tortuosity.

Connectivity 'measures' the degree to which structure is multiply connected, and is a topological parameter. The genus G, is the largest number of cuts that can be made through parts of the shape without totally disconnecting any part from the rest. A general theorem of topology states;

$$G = C = b - n + N \qquad [2.32]$$

where, C is the connectivity, b the number of branches, n the number of nodes and N the number of separate networks. In real life 'serial sectioning' (§2.3.5) is the only method of assessing connectivity (Dullien, 1992).

Coskun and Wardlaw (1995) determined a connectivity indicator by calculating the smooth pore area, as the area in which approximately a circle will fit within a pore space, the rest of the pore area is called the rough pore area. Rough plus the smooth pore area is the total pore area which is used to calculate image porosity (§2.3.1), but the ratio of smooth to rough pore area S/R as a connectivity indicator. A high ratio indicating a reduction to spherical pores, which are probably poorly connected.

2.3.5 Serial sectioning and topology

de Hoff (1983) states, 'it is generally accepted that the connectivity of a phase in 3D, among other parameters, cannot be measured on a single 2D section.' Serial sectioning, where material is cut into wafers, is a method by which arbitrary objects and continuous phases may be traced. A rock sample for example, can have grains and pores mapped in 3D and the connectivity measured; results can be obtained from this method (Cooper & Hunter, 1995). Lin and Cohen (1982) concluded from serial sections that a sandstone sample is less connected than spheres in a regular sphere pack of comparable porosity and grain diameter. Koplik et al (1984) used serial sections of the pore space to determine an equivalent random network of cylinders, and showed how the electrical conductivity and the fluid flow permeability of a disordered random medium may be calculated from the microscopic geometry of pore space.

2.3.6 Pore geometry models

Pore geometry models must represent the rock but be simple to analyse; three example models follow:

(i) Bernabe (1991) model

Figure 2.10 shows tube-like and sheet-like throats in parallel, both forming connected sub-networks. Consequently, their contributions to hydraulic and electrical conduction are approximately additive. Whereas, the nodal pores are in series with the other pores and, therefore, are expected to contribute very little to permeability and electrical conduction.

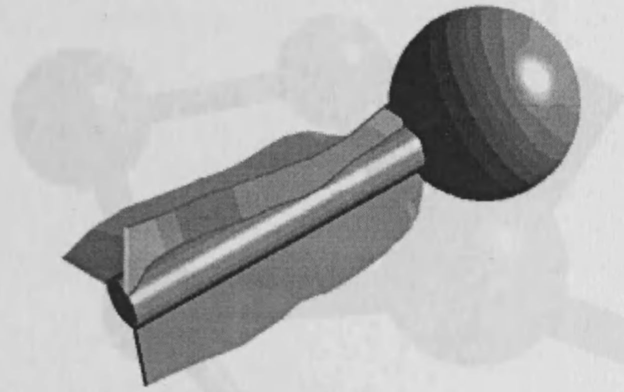

Figure 2.10. A schematic representation of the pore geometry of clean sandstones, showing a spherical nodal pore, a cylindrical throat and sheet like throats (after Bernabe, 1991)

Assuming the above model the permeability k, the inverse formation factor $1/F$ (effectively a conductivity formation factor), and the porosity ϕ can each be split into two terms, a pressure-dependent term associated with the sheet-like throats and a pressure-independent term associated with the tube-like throats and nodal pores,

$$k(p) = k_{tube} + k_{sheet}(p) \qquad [2.33]$$

$$1/F(p) = 1/F_{tube} + 1/F_{sheet}(p) \qquad [2.34]$$

$$\phi(p) = \phi_{node} + \phi_{tube} + \phi_{sheet}(p) \qquad [2.35]$$

where, p is the effective pressure.

(ii) Koplik et al. (1984) model

Koplik et al. show how the electrical conductivity and the permeability of a disordered random medium may be calculated from the microscopic geometry of the pore space. They used the model shown in Figure 2.11 and solved the equations of motion, the Stokes equations of low Reynolds number fluid flow in the pore space. This was done by dividing the network into pores and throats, solving the equations in each element, and matching the flow fields at the pore-throat boundaries. The velocity profile for the flow in the cylindrical throats is parabolic, with a linear relationship between flux Q_f and pressure drop ΔP,

$$Q_f = (g/\mu)\Delta P \qquad [2.36]$$

where g is the 'conductance' as a function of throat geometry alone. Eq. 2.36 is more complicated for an elliptical cylinder, but can still be solved. Transport coefficients of this network are related to the conductivity of an analogue random resistor network. The 'effective medium approximation' (given below) from solid state physics is used to average the probability distribution of conductances.

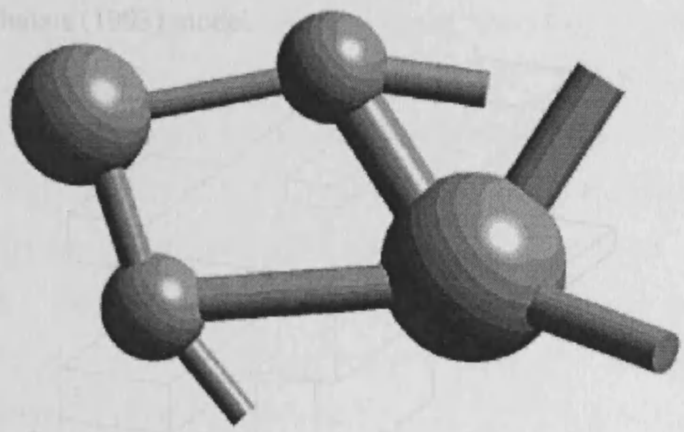

Figure 2.11. Model rock, consisting of spherical pores connected by elliptical cylindrical pore throats (after Koplik et al., 1984)

Koplik et al. compare their model to a random resistor network and state it would be possible to determine the permeability at this stage by taking a piece of real rock and setting up a cylinder model to solve Eq. 2.36 to determine the flux and pressure everywhere, and compute the permeability as,

$$k = \mu \frac{Q_{tot} / A}{\Delta P / L} \qquad [2.37]$$

where, Q_{tot} is the total flux, A the cross-sectional area, μ the viscosity and L the length.

Effective Medium Theory

The effective medium theory is known to give an accurate solution to the random-lattice problem even when the distribution of pores, pore throats or conductances are quite broad. Effective electrical conductance $g_e(d)$ and hydraulic conductance $g_h(d)$ of a pore of diameter d are given by,

$$g_e(d) = \frac{\pi d^2}{4 l_o} \sigma_f + \frac{\pi d \sum s}{l_o} \qquad [2.38]$$

$$g_h(d) = \frac{4 d^4}{128 l_o \mu} \qquad [2.39]$$

where, μ is the fluid viscosity, l_o the constant length of the pore, Σs the surface conductivity, and σ_f the pore fluid conductivity (after Banavar & Johnson, 1987).

(iii) Ioannidis and Chatzis (1993) model.

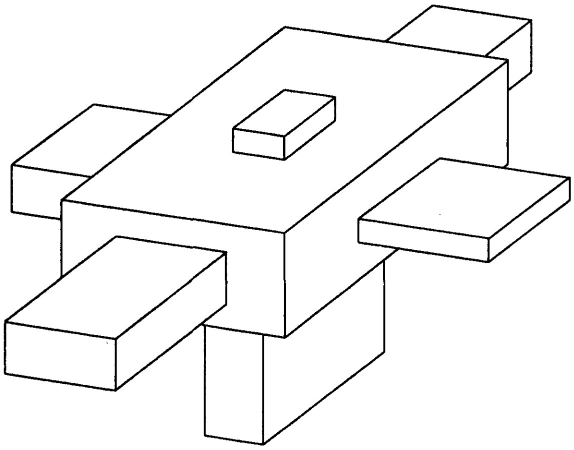

Figure 2.12. Schematic representation of the unit element of the network model (after Ioannidis & Chatzis, 1993)

In the model shown in Figure 2.12, the pore bodies and pore throats are assumed to be prisms of rectangular cross-section. This was considered a desirable assumption for it takes into account the angular cross-sectional shape of pores in reservoir rocks, thus allowing for late pore space filling during primary drainage, and it also allows for the existence of slit-shaped pore throats, in accordance with reservoir pore structures seen in pore casts.

Ioannidis and Chatzis (1993) consider the most realistic models for porous media as those which approximate to the pore space as a network of relatively large pores to small pore throats. They postulated that there is a similarity in the principal pore structures of all sandstones. Experimentally this was shown by drainage capillary curves (§2.2.3).

2.4 The effect of clay in sandstone reservoirs

There are two types of clay usually present within a non-aeolian sandstone reservoir, authigenic and detrital clay. Authigenic clays or clay minerals that are normally encountered in clastic sediments are a group of chemically related hydrous aluminium silicates, which generally occur as very small crystals, either platey or fibrous, and form in a rock during deposition and as an ongoing process after deposition. Detrital clays are small particles (<2 μm) which are formed as a result of erosion and/or weathering of any material.

2.4.1 Principal modes of occurrence of authigenic clays in sandstones

Shaw (1980) stated that pore-lining authigenic clays are composed of continuous thin (20-40 μm) coatings of clay minerals arranged tangentially or radially to the surface of the grains. Hawkins (1978) produces evidence of composite clay rims of tangentially arranged illite and radiating fibrous smectite; fibrous radiating pore-lining clays may extend outwards into the pore space to form pore-filling meshworks (Figure 2.14). Discrete-particle pore-filling authigenic clays are characteristically composed of kaolinite. Kaolinite is usually present as aggregates of euhedral pseudohexagonal platy crystals apparently randomly scattered throughout the pore space, rather than intergrowing on grain surfaces. Detrital micaceous minerals, muscovites, biotites and chlorites in sandstones may become deformed after deposition, showing alteration to various clay minerals along their cleavage planes. Hawkins (1978) reported radiating sheaves of kaolinite and fibrous illite growing between the split cleavage planes of muscovite. Authigenic clay assemblages tend to be dominated by one clay mineral phase and are often monomineralic.

2.4.2 The effects of clay minerals on the porosity and permeability of sandstones

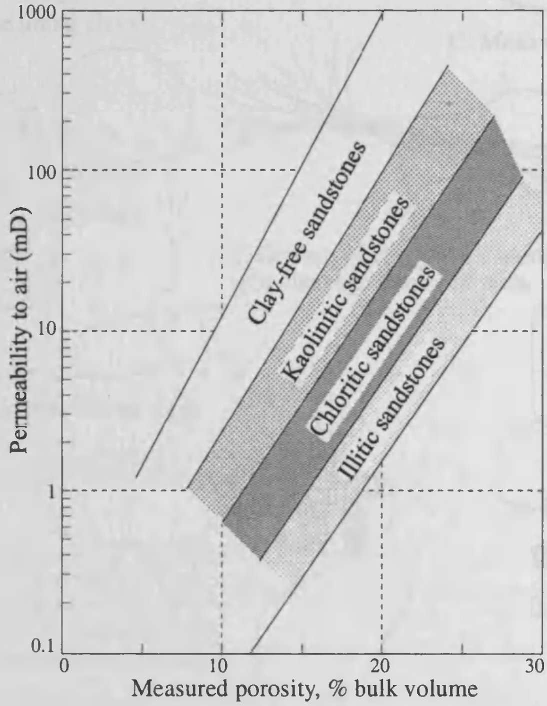

Figure 2.13. Permeability-porosity relationship in fine-grained, well-sorted sandstones as a function of various clay minerals (after Wilson, 1982, taken from Tiab and Donaldson, 1996)

The presence of clay minerals in sandstones is generally expected to reduce the porosity and permeability (Figure 2.13, Panda & Lake, 1995; Mowers & Budd, 1996). The manner in which authigenic clay minerals preferentially form by lining and infilling pore spaces means that they, rather than detrital clays, are more important in reducing porosity and permeability. Galloway (1979) estimated that a clay rim around a detrital grain would increase the grain radius by 1 to 6%. However, this relatively minor increase in the grain size reduces the pore throat passages by a much greater amount, in a fixed grain system. A 4% increase in grain diameter reduces the pore throat diameter by 26% and, as the permeability is approximately proportional to the square of the pore throat diameter (Eq. 2.20), the reduction in permeability is magnified further. The reduction in the permeability of sandstones due to the presence of authigenic clays is greater in fine-grained rather than coarser-grained sandstones because the initial small pore throat diameters.

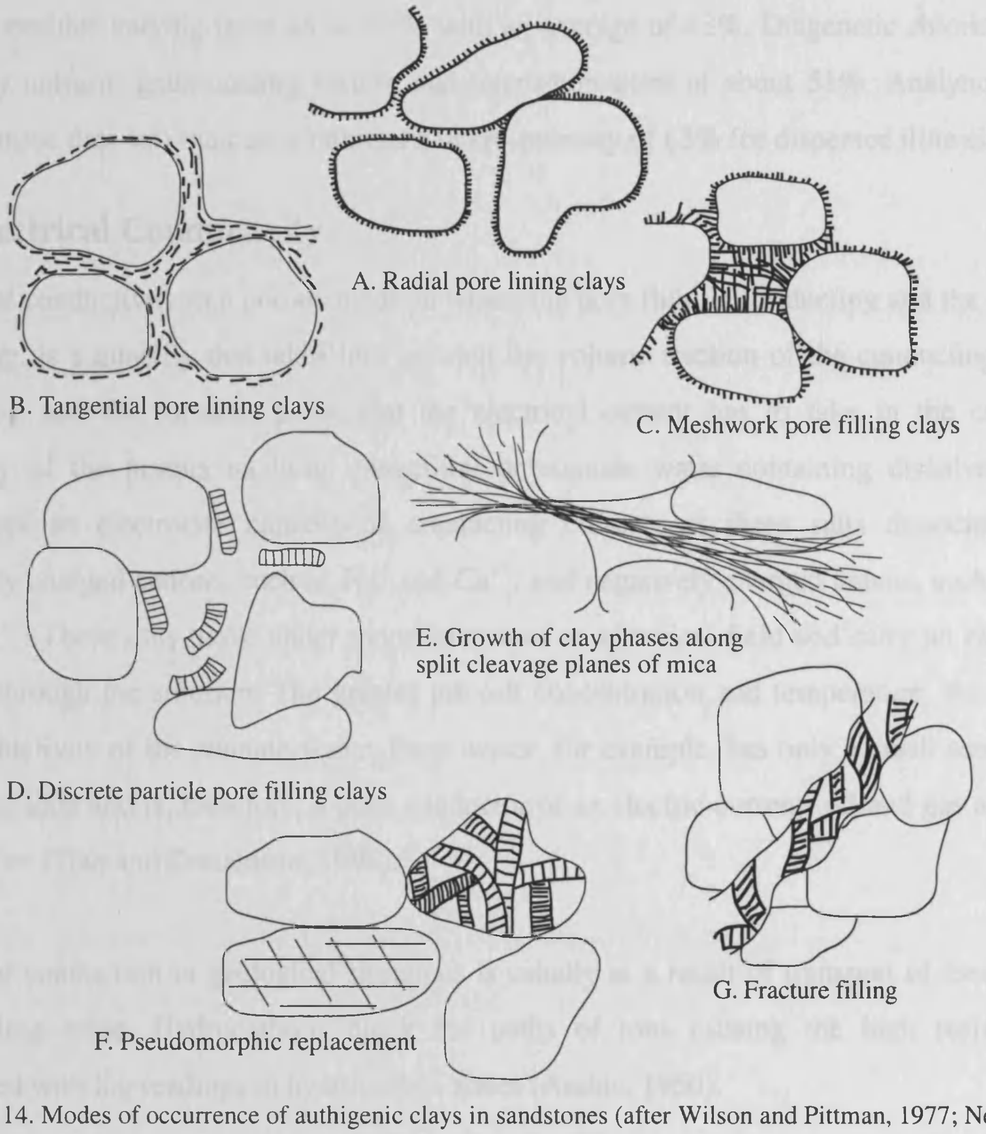

Figure 2.14. Modes of occurrence of authigenic clays in sandstones (after Wilson and Pittman, 1977; Neasham, 1977; and Hawkins 1978)

Hurst and Nadeau (1995) and others (Patchett, 1975; Frost and Fertl, 1981; Serra, 1984) found that smectite, and to a lesser extent illitic clay minerals, have a significant effect on formation conductivity and the water saturation of oil-bearing sandstones, whereas kaolinite and chlorite have relatively minor effects. The presence of clay in hydrocarbon reservoirs however, is not always negative. According to Wilson (1982) many of the largest petroleum reservoirs (North Sea, North slope of Alaska) have retained good porosity because of diagenetic clay coatings.

Nelson (1994) and Aase et al. (1996) found that these coatings reduce the forming of quartz overgrowths.

Hurst and Nadeau (1995) state that authigenic clay minerals from North Sea clastic reservoirs generally have higher micro-porosities than detrital clay minerals. Diagenetic kaolinite has micro-porosities varying from 25 to 50%, with an average of 43%. Diagenetic chlorite has a generally uniform grain-coating texture and micro-porosities of about 51%. Analytical data (for a limited data set) indicate a minimum micro-porosity of 63% for dispersed illite clays.

2.5 Electrical Conductivity

Electrical conductivity in a porous medium where the pore fluid is conducting and the solid is insulating, is a quantity that takes into account the volume fraction of the conducting phase (porosity), and the tortuous paths that the electrical current has to take in the complex geometry of the porous medium. Interstitial or connate water containing dissolved salts constitutes an electrolyte capable of conducting current, as these salts dissociate into positively charged cations, such as Na^+ and Ca^{++}, and negatively charged anions, such as Cl^- and SO_4^{--}. These ions move under the influence of an electrical field and carry an electrical current through the solution. The greater the salt concentration and temperature, the greater the conductivity of the connate water. Fresh water, for example, has only a small amount of dissolved salts and is, therefore, a poor conductor of an electric current; oil and gas are non-conductors (Tiab and Donaldson, 1996).

Electrical conduction in geological situations is usually as a result of transport of ions in the pore filling brine. Hydrocarbons block the paths of ions causing the high resistivities associated with log readings in hydrocarbon zones (Archie, 1950).

2.5.1 Formation Resistivity Factor

A rock that contains oil and/or gas will have a higher resistivity than the same rock completely saturated with formation water, and the greater the connate water saturation, the lower the formation resistivity. This relationship to saturation makes the formation resistivity factor (F), in conjunction with Archie's equation (Eq. 2.41) an excellent parameter for the detection of hydrocarbon zones. F is a function of many other properties including the presence or absence of clay species, type and character of a formations permeability and porosity.

Archie (1942) experimented with a suite of samples having a porosity range of 10-40%, and a range in electrolyte salinity, and proposed the following empirical relationship,

$$R_o = FR_w \qquad [2.40]$$

where, R_o is the resistivity of the rock when it is saturated with brine, F the formation resistivity factor and R_w the resistivity of the brine.

Archie (1942) then plotted F against porosity and permeability, and concluded that F is not only a function of the type and character of the formation, but varies with the porosity and permeability of the reservoir rock. He noted that many points deviated from the average line plotted for permeability and porosity against F and states that individual determinations from any particular core sample may deviate considerably from the average; this was particularly true for the relationship with permeability. The relationship of F with porosity for different groups of data may be widely different, but the character is quite consistent; the effect of variations in permeability on this factor is not so evident. Naturally the two relationships could not be held to apply with equal rigor because of the well established fact that permeability does not bear the same relation to porosity in all sands. F is found to be constant for many different saturated rocks, which is principally a consequence of the resitivity of the saturating fluid being several orders of magnitude lower than that of the rock matrix. After conducting the experiments on saturated sandstone core samples, Archie related F to porosity with what is now named the 'Archie equation',

$$F = \phi^{-m} \qquad [2.41]$$

where m is an empirical constant. Archie (1942) found the parameter m to take a value of about 1.3 for unconsolidated sand, increasing to around 1.8-2.0 with more consolidated sandstones.

Often a modified version of Eq. 2.41, first proposed by Winsauer et al. (1952), is used to obtain a better fit with certain data sets by the use of an empirical constant a,

$$F = a\phi^{-m} \qquad [2.42]$$

The resistivity is a function of the water saturation S_w (§2.5.2), in a formation containing oil and/or gas with a certain amount of water. The true resistivity, R_t, for the same porosity, of the formation is larger than R_o, because there is less available volume for the flow of electrical current. The ratio of R_t /R_o is commonly referred to as the resistivity index I_R. Archie determined the following relationship,

$$S_w = \left(\frac{R_o}{R_t}\right)^{1/n} = \left(\frac{FR_w}{R_t}\right)^{1/n} \qquad [2.43]$$

For a clean and uniformly water wet system the saturation exponent n, is equal to approximately two (Anderson, 1986). Baldwin (1994) states that the Gulf Coast shaley sandstone zones with 80% pore volume water, have high saturation exponents of $n>10$.

Substituting for F from Eq. 2.41 into Eq. 2.43 yields,

$$S_w = \left(\frac{R_w}{\phi^m R_t}\right)^{1/n} \qquad [2.44]$$

The relation in Eq. 2.44 is often referred to as 'Archie's law' (in some cases, Eq. 2.42 is included, adding the extra empirical constant multiplier a to the formula). Archie's law is invaluable in the hydrocarbon industry, where it is used routinely to estimate oil reserves in a given reservoir.

The relation between porosity and formation resistivity factor is significant because the average lines of formation resistivity factor versus porosity of consolidated rocks of different types are close together. Therefore, 'the porosity controls the formation resistivity factor and the pore structure or type of rock does not have a great effect' (Archie, 1947).

2.5.1.1 Charge Associated with the Rock

Clay minerals containing charged impurities are balanced by counter ions bound to their external surfaces and cling to the walls of the insulating grains. The hydrated counter ions, when such a rock is saturated with even mildly salty water, become mobile in a very thin layer surrounding the clay particles. This provides a surface conduction mechanism in addition to the usual bulk electrical conduction (Banavar & Johnson, 1987). The term 'diffuse' layer is used to describe a so-called 'ion-free' layer that extends from the clay-water interface (Berg, 1995).

2.5.2 Water saturation S_w

Water saturation S_w is the proportion of water that occupies the pore space, i.e. a rock which is completely saturated with water alone is said to have a water saturation of 1.00, or 100%.

Initial water saturation (S_{wi}) is the water saturation at an arbitrary pressure where saturation becomes relatively insensitive to further increases in capillary pressure (Coskun and Wardlaw, 1995). The pressure required to remove the water from a porous medium depends on the size of the pore throats within the medium.

An investigation by Coskun and Wardlaw (1995) of the relationships between 2D pore geometry data, from image analysis of thin sections, and initial water saturation, measured by conventional laboratory techniques on core plugs, reveals that the volumes of small pores within the pore space have strong influences on initial water saturation. Coskun and Wardlaw investigated two reservoirs and the models showed that 72% and 73% of the variance in initial water saturation can be explained by image data. Hurst and Nadeau (1995) found an evaluation of clay-bound water or irreducible water can be made using micro-porosity measurements.

Coskun and Wardlaw (1995) also showed that the negative relationship between permeability and initial water saturation, which commonly have been used for prediction of saturation, are not universal but depend on pore size variation. They postulated that the concept of hydraulically isolated 'irreducible' water saturation only applies for bead packs with smooth surfaces. Coskun and Wardlaw give an example of where relationships between porosity and S_{wi} are weak, and concluded it was due to the variation in porosity, which did not indicate the overall pore size differences or the degree of non-uniformity of pore systems among a suite of samples.

2.5.3 Wettability

The term 'wetting' in everyday language means that the liquid spreads over the solid surface (e.g. kerosene on a glass slide), and 'nonwetting' that the liquid tends to ball up and run off the surface (e.g. mercury on a glass slide).

Interfacial tension between the hydrocarbons and water (Figure 2.15) cause the hydrocarbons to assume outwardly curved shapes that resemble the grains more than the water. There are connections between the oil globules, and also connections between the matrix grains, but the water is the effective medium.

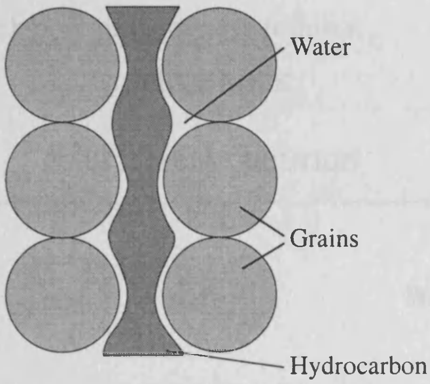

Figure 2.15. Schematic diagram showing how hydrocarbons are related to the matrix and water (after, Berg 1995)

Surface tension will keep a thin film of water, in a water-wet system, between the oil and the grains (exaggerated in Figure 2.15). The grains and hydrocarbon would appear to be 'floating' particles in a continuous water phase in an actual cross section, while in 3D space the hydrocarbon is like a mesh of interconnected globules, especially at lower S_w. This configuration is why resistors-in-parallel are a good approximation of the conductivity of the mixture of hydrocarbons and grains (Berg, 1995).

2.6 Summary

This chapter describes the fundamental macroscopic and microscopic parameters which are used to understand rock parameters, especially rock storage and flowing capacity i.e. porosity and permeability.

Particular points of interest which lead into a study of this nature are:

- Gas permeability can be an unreliable measurement which can give errors of 30-100% if not properly undertaken.
- Image porosity does not generally measure small pores which are associated with immobile water, and is therefore a closer measure of effective porosity; in 2D.
- The presence of clay within a rock is, in general, expected to decrease the porosity and permeability, especially authigenic clays.

Archie (1950) relates basic rock pore properties as follows;

TYPE OF ROCK

PORE SIZE DISTRIBUTION

POROSITY

WATER SATURATION

PERMEABILITY

CAPILLARY PRESSURE
(pore interconnection)

Type of rock, as referred to here, is a formation whose parts have been deposited under similar conditions and have undergone similar processes of later weathering, cementation or re-solution. The connecting lines are meant to portray the fact that a specific formation or rock type will have a certain pore-size distribution which will produce a particular family of capillary pressure curves. The pore-size distribution controls the porosity and is related to the permeability and water saturation. Further, a certain rock will exhibit a relation between porosity and permeability as well as permeability and water saturation. Pore-size distributions measured by image analysis provide the necessary information in this study and not capillary pressure curves.

CHAPTER THREE

A review of the data used in this study

3.1 Introduction

Enterprise Oil plc has collected a high resolution log and core data set from a hydrocarbon reservoir located in the North Sea. This chapter outlines the data sets used in this study and the location within this thesis of the data interpretation. Figure 3.1 is a flow diagram of the data available or generated within this study.

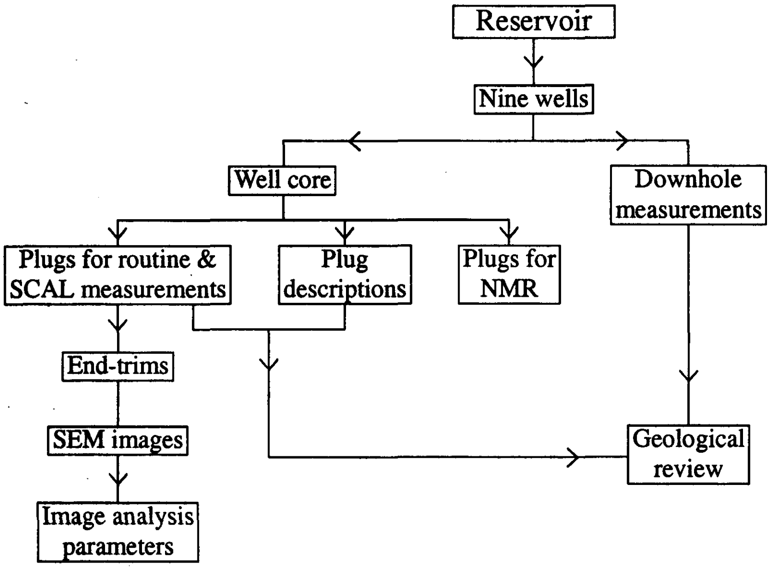

Figure 3.1. Flow diagram of the data available for this project

Routine, or conventional, core analysis was performed on plugs from each of the nine wells. In many cases special, or extra, core analysis laboratory (SCAL) measurements were made on the same plugs. Service Company 2 (SC2) performed all of the routine and special core analysis, dates of when the analysis was performed on each well are unavailable. Geological reports were made available, and have been summarised in Chapter 4.

Image analysis was performed on 819 images taken from sixty-three plugs. The image analysis process generated a series of image parameters which were hoped to be characteristic of the three-dimensional plug morphology. The intended purpose of this high resolution data set, of plug and image information, was to obtain a unique understanding of the relationships between the physical properties of the rock at different scales (i.e. the relationship between the whole core, the plugs and in turn the SEM images). Figure 3.2 demonstrates the relationship between the data sets.

The data used in this study have been put into a database (Access, Version 7) from where they can be extracted and assessed with relative ease and convenience.

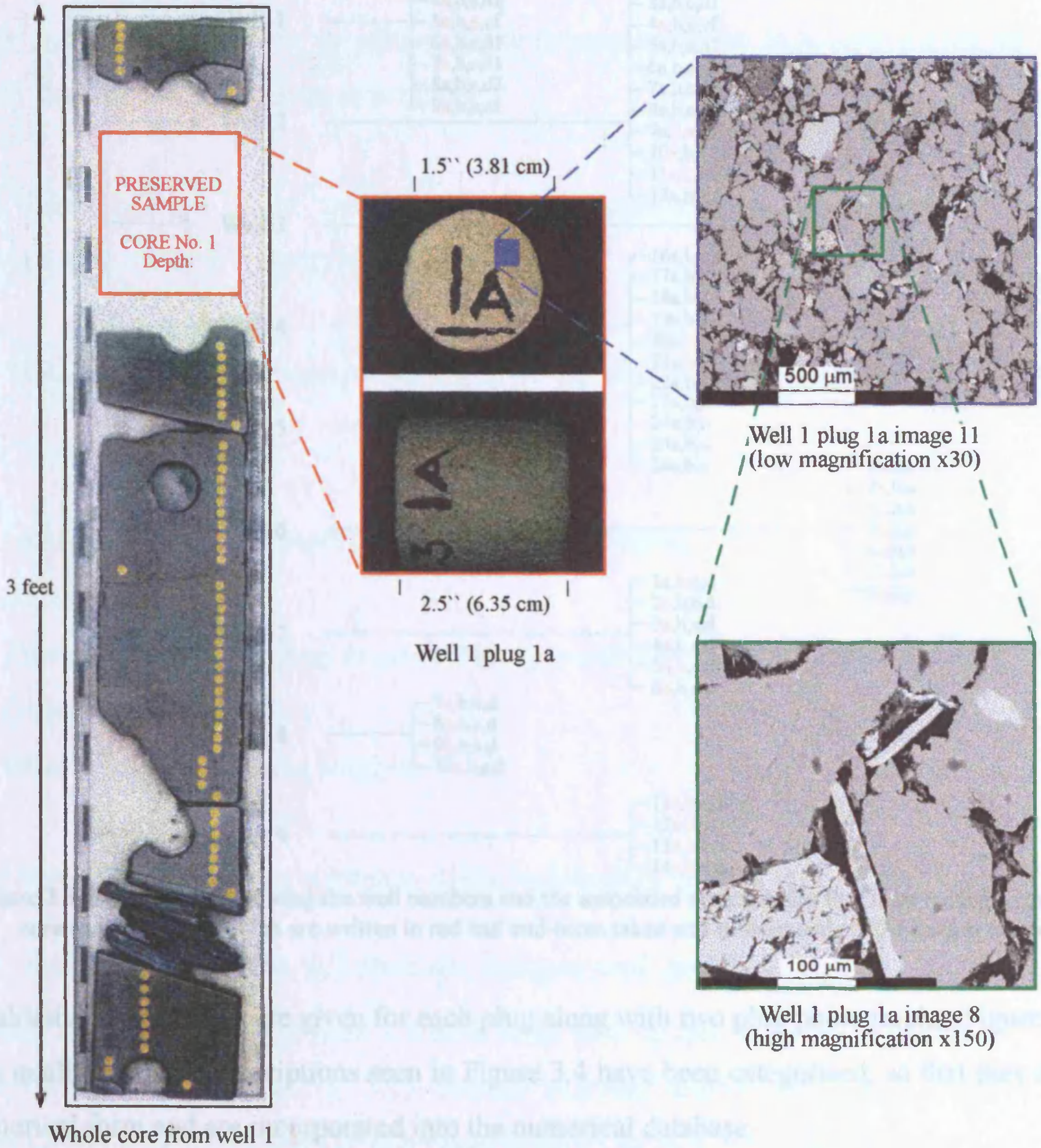

Figure 3.2. Relative location between core, plug and SEM images

3.2 Routine core analysis

Within the oil industry, routine core analysis measurements are made on plug samples taken from whole core. These measurements (grain density, bulk density, porosity, gas permeability and Dean & Stark analysis §5.3.2) are important because they are used to calibrate logs, estimate reserves and evaluate reservoir quality and description (Thomas and Pugh, 1989). Analyses were done on 206 plug samples from a total of nine wells (Figure 3.3). Details of selected experimental methods are given in Chapter 5.

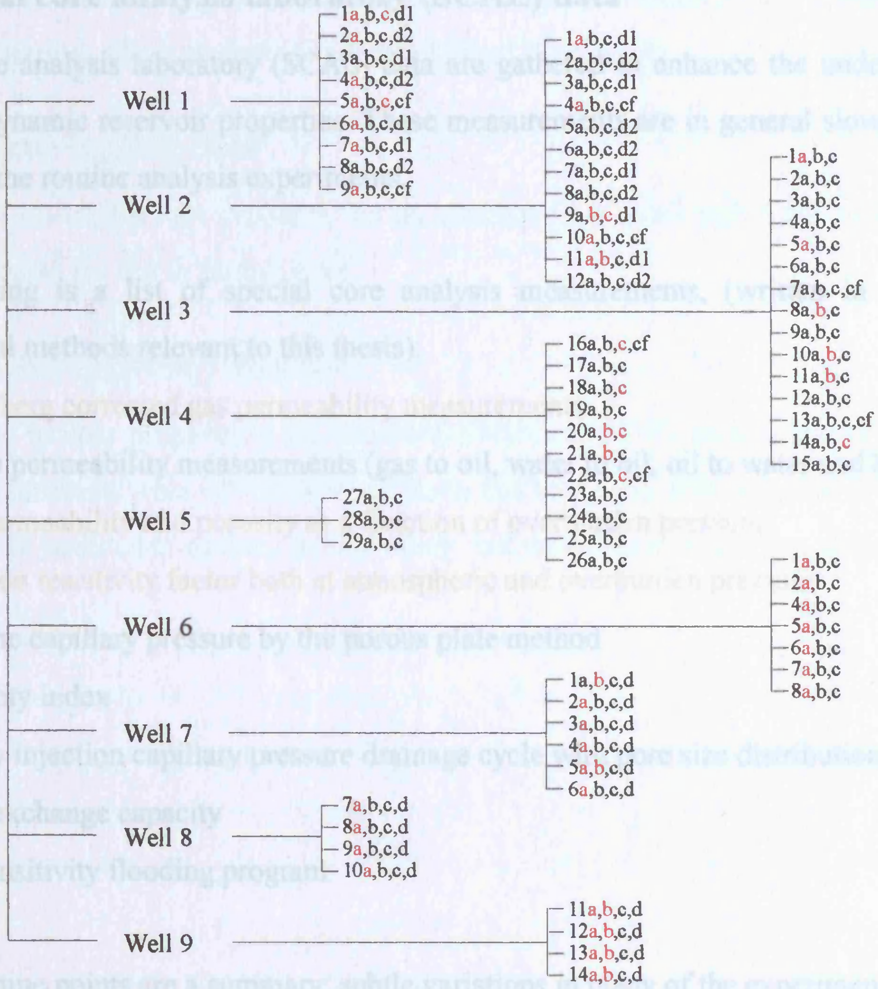

Figure 3.3. Tree diagram showing the well numbers and the associated core samples that have received routine core analysis. Plugs which are written in red had end-trims taken and subsequently SEM images taken

Qualitative descriptions are given for each plug along with two plug photographs (Figure 3.4). The qualitative plug descriptions seen in Figure 3.4 have been categorised, so that they are in numerical form and are incorporated into the numerical database.

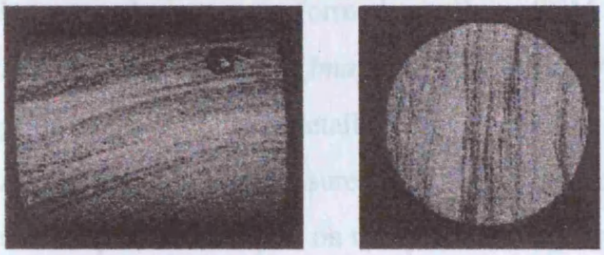

Lithological description
SANDSTONE: Grey, laminated, moderately well consolidated. Very fine to fine grained, moderately well sorted, subrounded. Common patchy calcareous cement (iron calcite?), common micas, trace disseminated pyrite. Silt laminae, trace white clays. Moderate visible porosity.

Figure 3.4. An example set of plug photographs and qualitative description as provided by SC2, for well 7 plug 5a.

3.3 Special core analysis laboratory (SCAL) data

Special core analysis laboratory (SCAL) data are gathered to enhance the understanding of static and dynamic reservoir properties. These measurements are in general slower and more costly than the routine analysis experiments.

The following is a list of special core analysis measurements, (written in red are the experimental methods relevant to this thesis):

- Klinkenberg corrected gas permeability measurements
- Relative permeability measurements (gas to oil, water to oil, oil to water and brine to oil)
- Brine permeability and porosity as a function of overburden pressure
- Formation resistivity factor both at atmospheric and overburden pressure
- Gas-brine capillary pressure by the porous plate method
- Resistivity index
- Mercury injection capillary pressure drainage cycle with pore size distribution
- Cation exchange capacity
- Fluid sensitivity flooding program

The above nine points are a summary; subtle variations in many of the experiments exist.

3.4 Scanning electron microscope images and image analysis

A total of sixty-three plugs from the nine wells used in this study had end-trims removed, after they had been cleaned (§5.3.2). Thirteen scanning electron microscope (SEM) images were taken on these end-trims at two magnifications by SC1. Five low magnification images at x30 and eight high magnification images at x150, resulting in a total of 819 images. Details on the image positioning and image interpretation are given in Chapter 6. Figure 3.3 shows from which wells and plugs the end-trims, and therefore SEM images, were taken.

Image analysis was performed on all the SEM images using a version of the Foster Findlay Associates Limited *PC_Image* for VGA and Windows software, adapted by SC1. Chapter 6 gives some technical detail and Appendix B a listing of the measurements made using *PC_Image*. All the measurements were made on pore space (the program could have been used to perform analysis on the quartz sand grains, or indeed on any particular grey scale).

3.5 Geological data

There were several geological reports available (Internal Reports* 1, 2 and 4) for this reservoir, these have been reviewed and summarised (Chapter 4).

3.6 Wireline logging data

Composite well-log data are available, but the data have not been used in this study, except for being referenced for use in further work.

3.7 Nuclear magnetic resonance

An extra set of core plugs were cut and both NMR and SCAL measurements made. These SCAL measurements were not made available to this study. As with the paper log data, NMR data have not been used directly in this study, but referenced in sections regarding further work.

* The internal reports are held at Enterprise Oil plc.

CHAPTER FOUR

Geological framework of the reservoir

4.1 Introduction

The sedimentological data and interpretations for this reservoir taken from Internal Reports* 1, 2 and 4, and augmented by staff at Enterprise Oil are reviewed in this chapter. The reservoir location, geological age and well depths are not important for this study. The facies codes used in Section 4.3 are the same as those in Chapters 5, 6 and 7, but a numerical code is used, Section 4.4 defines the relationship between these two codes. Section 4.5, petrography, is divided into detrital components and diagenesis. Core examples of where facies types and facies associations can be found are given (§4.3), note that the suffix d.d. is for driller's depth and for wireline measured depth the suffix is m.d; pseudo-depths are used.

4.2 Geology

Seven depositional phases have been recognised within the reservoir rock (Internal Report 1), which is bounded by a dark grey silty claystone. The majority of cores have been taken from the Upper unit of the reservoir which is the main reservoir sand body, mostly consisting of submarine channel systems. The Lower unit is dominated by extensive slump reworking of older lithologies. The division of the reservoir into Upper and Lower units reflects a large scale change in the sedimentological and lithological character of the sequence. The sandstone dominated lithologies of the reservoir are thought to be the products of a submarine turbidite depositional system, which has several phases of activity of both outbuilding and retreat.

* The internal reports are held at Enterprise Oil plc.

4.3 Sedimentology

4.3.1 Introduction

A hydrodynamic interpretation of features within the core has been used to interpret depositional environments and palaeogeography (Internal Report 1). A summary of the facies classification can be seen in Figures 4.1 and 4.2, which follows the classification of Mutti and Ricci-Lucchi (1972 and 1975). The identification of both specific facies type and recurring facies associations has been done through examining the core. Eleven main facies associations were recognised and are discussed below. These facies associations occur within one or more of the seven phases of deposition and are therefore not always restricted to a single place in the time record, these detailed facies descriptions are simplified in Section 4.4 and given a numerical facies code.

*(i) **Submarine fan channels and slumped channel sandstone***

The main reservoir sandbodies within the reservoir are the thick B1 Facies, associated with subordinate facies of Facies A1 and C. More rarely the basal units of some channels contain sandy debris between units of Facies A2. (e.g. well 7, 10912 ft - 10916 ft.d.d., well 9, 12229 ft - 12233.5 ft.d.d.).

*(ii) **Channel abandonment***

The sandstones in submarine channel abandonment units represent deposition from evolved, relatively low density turbidity currents. The mudrocks are mostly the products of turbid mud suspension fallout deposition. Channel abandonment units are characterised by the inter-bedding of the sands and the muds, D2 and D3, associated with the fining upward sequence of Facies C2, and commonly with the muddy flow of Facies F. These channels can be seen within Phase VI and VII channels (e.g. well 4, 9080 ft -9100 ft.d.d.). The channels can also be represented by muddy debris flows, (e.g. well 6, 7489 ft.d.d.).

*(iii) **Thicker bedded submarine sandlobe***

The thick bedded sandstone of Facies B1 are usually part of the sandlobe deposits, especially when associated with Facies C1.

*(v) **Slump sheets***

Slump sheets probably form the dominant non-reservoir facies within the main reservoir interval in the majority of wells. They are recorded in two main modes, (i) coherent slumps, including some larger slump sheets and (ii) as disarticulated and chaotic muddy and sandy debris flows as thin sheets. The thicker slump sheets contain deformed argillaceous intraclastic sandstone and brecciated claystones, usually Facies F (e.g. well 8, 1098 ft-1010 ft.d.d.). The coherent and larger slumps contain mixed dark grey, and grey green claystone lithologies (e.g. well 5, 7521 ft - 7532 ft.d.d., well 8, 10940 ft - 10945 ft.d.d.). The second type of slump sheet is found in thin discrete units (e.g. well 8, 10787 ft - 10989 ft.d.d.). The muddy debris flow units are the dominant slump type in the Upper unit, the debris contain intraformational large dark grey claystone clasts (e.g. well 8, 10710 ft and 10712 ft.d.d.). In the Lower unit these claystone clasts can also be dark green, and may be extraformational, (e.g. well 8, 10555 ft-10557 ft.d.d., well 7, 9284 ft - 9286 ft. d.d.).

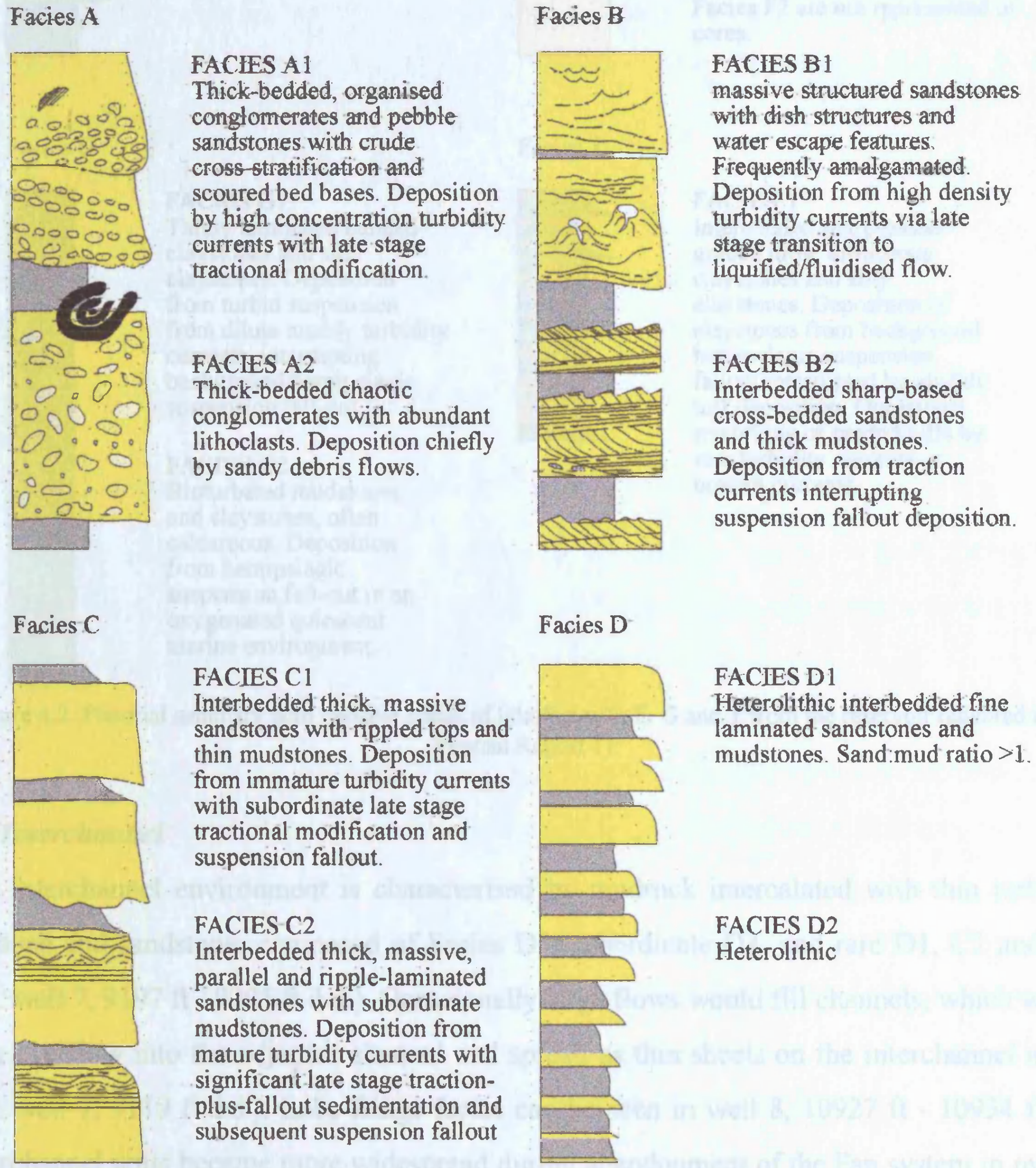

Figure 4.1. Pictorial summary with variable scales of lithofacies A, B, C and D from the reservoir (adapted from Internal Report 1)

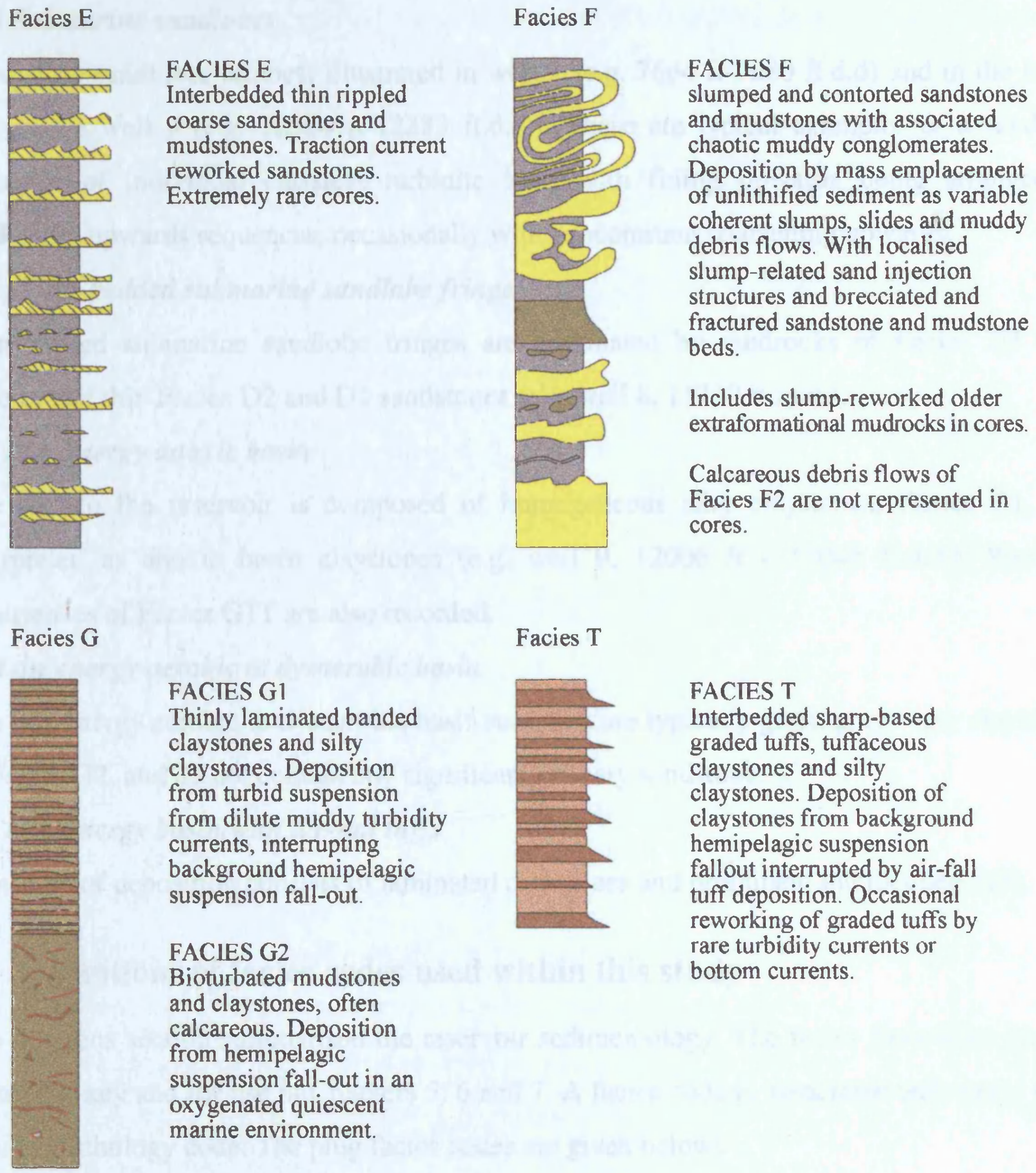

Figure 4.2. Pictorial summary with variable scales of lithofacies E, F, G and T from the reservoir (adapted from Internal Report 1)

(vi) Interchannel

The interchannel environment is characterised by mudrock intercalated with thin turbidite siltstone and sandstone, composed of Facies D3, subordinate D2, and rare D1, C2 and C1. (e.g. well 7, 9197 ft - 9205 ft.d.d.). Occasionally large flows would fill channels, which would then overflow into the adjacent channel and spread as thin sheets on the interchannel areas, (e.g. well 7, 9119 ft.d.d.). Lobe fringe facies can be seen in well 8, 10927 ft - 10934 ft.d.d. Interchannel units became more widespread during abandonment of the Fan system in overall fining-upwards sequences from interchannel to low energy basin.

(vii) ***Submarine sandlobes***

Submarine sandlobes are best illustrated in well 1 (e.g. 7664 ft-7680 ft.d.d) and in the lower part of the well 9 (e.g. 12364 ft-12383 ft.d.d.). These are typical examples of a sandlobe sequence of individual classical turbidite beds with fining upwards being arranged in thickening upwards sequences, occasionally with concomitant coarsening upwards.

(viii) ***Thin-bedded submarine sandlobe fringe***

Thin-bedded submarine sandlobe fringes are dominated by mudrocks of Facies D3 with subordinate thin Facies D2 and D1 sandstones (e.g. well 8, 11310 ft.m.d.).

(ix) ***Low energy anoxic basin***

The seal to the reservoir is composed of homogeneous silty claystones, Facies G1, and interpreted as anoxic basin claystones (e.g. well 9, 12006 ft - 12048 ft.d.d.). Sporadic occurrences of Facies G1T are also recorded.

(x) ***Low energy aerobic to dysaerobic basin***

The low energy aerobic to dysaerobic basin mudrock are typically green grey waxy claystones of Facies G2, and do not contain any significant primary sandstone.

(xi) ***Low energy basin with air-fall tuffs***

This style of deposition consists of laminated claystones and prominent interbedded tuffs.

4.4 Definitions of facies codes used within this study

The previous section summarised the reservoir sedimentology. The facies have been given a numerical key and for use in Chapters 5, 6 and 7. A facies code is associated with every plug, but not a lithology code. The plug facies codes are given below:

Facies 1 (B1) Thick-bedded massive sandstones with water escape structures; high density turbidity currents transitional to fluidise/liquified sediment gravity flows.

Facies 2 (B2) Cross-stratified sandstones with subordinate interbedded mudstones; current-deposited.

Facies 3 (C1) Massive sandstones with thin mudstone interbeds; classical turbidites.

Facies 4 (C2) Massive, parallel and ripple laminated sandstones with mudstones; classical turbidites.

Facies 5 (D1) Interbedded laminated sandstones and subordinate mudstones; classical turbidites.

Facies 6 (D2) Interbedded laminated sandstones and mudstones; classical turbidites.

Facies 7 (D3) Interbedded laminated mudstones with rare sands; classical muddy turbidites.

Facies 8 (F) Deformed, contorted, intercalated sandstones and mudstones; slumps, slides and debris flows.

Facies 9 (G) Mudstones and claystones; suspension deposited.

Well number	Facies group	Number of plugs	Total plugs for each well
1	1	12	
	3	10	
	6	3	
	8	4	29
2	1	32	
	3	3	
	8	3	38
3	1	31	
	6	11	
	8	3	45
4	1	27	
	3	3	
	6	3	33
5	1	9	9
6	1	6	
	2	9	15
7	1	4	
	3	4	
	6	4	12
8	1	6	
	3	2	8
9	1	6	
	3	2	8

Table 4.1. Facies group of the plugs from each well

Facies 1 through to 9 were deposited in depositional environments of decreasing energy. It is therefore expected that facies 1 would have the largest grains. A lithology consisting of grains such as these would be expected to have a large porosity and permeability. Facies 7 at the other end of the energy scale was deposited in a low energy environment and the grains are probably smaller. A lithology consisting of grains such as these would be expected to have a low porosity and permeability.

Each plug used in this study was given one of the above nine numerical plug codes for simplicity in computational purposes. Table 4.1 shows the facies group (using the plug codes) of the plugs from each well.

4.5 Petrography

Previous to the definition of facies given in Internal Report 1 (§4.3 and §4.4), Internal Report 4 had identified eight sedimentary facies within the Upper unit on the basis of macro-features, notably texture, bed character and sedimentary structures. Six of the facies consisted mainly of sandstones and therefore represented potential reservoir rocks, two of the facies consisted of non-reservoir mudstones.

A total of 124 thin sections and 30 combined SEM/XRD samples represent the petrographic data set and were taken from wells 1, 2, 3, 4, 5, 10 and 11. The samples are mostly fine grained, range from very fine to medium grained and are moderately or poorly sorted. Samples typically show similar grain contact and roundness characteristics throughout (Internal Report 4). The samples are biased towards facies group 2 and therefore, the conclusions provided by Service Company 4 (SC4) are not listed here.

There is no simple relationship between porosity, permeability and detrital clay or diagenetic minerals, but generally an increase in either of the latter will decrease the values of porosity and permeability. The porosity system of the samples used in this study is composed principally of primary intergranular macro-pores, with variable amounts of interclay micro-porosity. Feldspar dissolution contributes an average 2.2% to total macro-porosity.

4.5.1 Detrital components

The principal detrital components are monocrystalline quartz (24-62%) and feldspar (2-16%) which is represented by orthoclase, plagioclase and microcline. The feldspars have suffered variable degrees of dissolution to form secondary porosity. Lithic fragments (trace-26%) consist mainly of polycrystalline quartz, minor amounts of chert, sandstone, metamorphic granitic and volcanic rock fragments are also present. Detrital clays (0-32%) are concentrated in facies 1, and thin laminae in the more coherent, bedded facies. The indeterminate clay category included partly recrystallised and grain coating clay and possibly detrital clay. Much of the illitic clay, illite and interlayered illite/smectite detected by XRD analyses is probably detrital clay.

4.5.2 Diagenesis

The principal diagenetic minerals are kaolinite (0-9%), chlorite (identified by SEM and XRD), quartz overgrowths (0-12%), ferroan calcite (0-42%) and siderite (0-28%). The cements (chlorite, ferroan calcite and siderite) are preferentially developed in thin bedded sandstone facies which are associated with mudstones. Indeterminate authigenic clay content (<2 μm, mostly chlorite) is also preferentially developed in thin bedded facies, and facies associated with muddy sequences in general. Diagenetic minerals will tend to introduce micro-porosity into the rock structure. Micro-porosity does not contribute to permeability as much as macro-porosity and therefore the presence of diagenetic minerals are expected to decrease the rock permeability.

SC4 summarise the diagenetic history as:

- Early diagenesis, during which early grain coating clays, pyrite and feldspar overgrowths developed in reducing/alkaline (modified sea water) pore fluid, followed by siderite, ferroan calcite and chlorite precipitation and recrystallisation.
- Later diagenesis, during which mechanical compaction and quartz cementation began, feldspar grains began to dissolve and kaolinite was precipitated, possibly activated by influxes of acidic pore fluids.
- Following oil emplacement further chlorite precipitation and possible kaolinite dissolution occurred beneath the oil-water contact.

A comparison of the petrophysical properties of the different lithologies present within the reservoir is not possible, using the data set provided for this study, since 68% of the 197 plugs used are taken from the main sand body, facies 1. The image analysis results are similarly biased with 63% of the 54 image data sets taken from end-trims of plugs from facies 1. No plugs have been made available from facies 4, 5, 7 and 9.

CHAPTER FIVE

Core plug data

5.1 Introduction

There are nine wells from a single hydrocarbon reservoir included in this study, from which 251 plugs were taken. Forty-five plugs were put in storage, twenty-eight directly after being cut, the remaining seventeen after relative permeability measurements. The remaining 206 plugs received selected petrophysical measurements; forty-two were subsequently destroyed due to mercury contamination. Service Company 2 (SC2) performed most of these measurements, the exception being the extended Klinkenberg data set (§5.3.6) made by the author.

Chapter 5 is divided into five sections:

5.1 Introduction.
5.2 Errors associated with the core storage, preservation and sample preparation.
5.3 Experimental methods and associated errors. Including a substantial sub-section on an investigation into errors associated with Klinkenberg data.
5.4 Data interpretation.
5.5 Summary.

5.2 Core and plug damage before measurements are made

5.2.1 Core storage and preservation

Core storage and preservation is very important if measurements are to be made on fresh state (uncleaned) plugs. The speed and effectiveness with which the core is sealed can affect the results obtained from core plug measurements, since alteration of a core's wettability may occur from exposure to air (§2.5.3). The oxidation of crude oil in water-wet cores, can lead to a general movement towards an oil-wet preference (Cornwall, 1990), but it is also known that the reverse trend can occur (Chilingar and Yen, 1983; Mungan, 1966). In this study core plug measurements were made after the plugs had been cleaned (§5.3.2), therefore preservation is not a concern.

5.2.2 Sample preparation

All core handling, cleaning, drying, preparation and analysis procedures can, if incorrectly performed, be a source of laboratory induced damage, especially on core from formations with delicate mineralogy, fabric, cementation or friability (API recommended practice, 1998). Grain loss can be a problem (especially in friable rock) as core plugs are subjected to a considerable amount of handling during test procedures. If grain loss is unrecognised, and therefore unaccounted for, measurements which involve plug weight, will have associated uncertainties (pers. comm., Garnham, 1999). Care must be taken whilst drilling the plug samples, as use of a non-compatible plug drilling fluid may cause damage to the plug by a reaction between the drilling fluid and the rock, or between the drilling fluid and the *in situ* fluid (Sinclair and Duguid, 1990). A base oil (generally kerosene) was used as the core plug drilling fluid in this reservoir and the core was often invaded by the core drilling mud. Therefore, fluid-rock reactions are not considered a problem in this reservoir.

Toluene has been boiled through most of the plugs used in this study to drive-off the pore water, and to extract the residual hydrocarbon content. There are several recognised problems with the use of methanol and toluene solvents in plug cleaning (§5.3.2):

(i) The relatively high boiling points can cause clay dehydration.

(ii) Naturally occurring halite can be removed from the rock matrix causing subsequently erroneous pore volume determinations.

(iii) Toluene is not an effective solvent for removing heavy hydrocarbons, therefore heavy ends are left deposited on grain surfaces, making the sample oil wet or partially oil wet (Sinclair and Duguid, 1990).

Halite and heavy hydrocarbons are not present in the studied reservoir, and therefore not a problem. Clay dehydration may have occurred which would increase the value of plug porosity (§5.3.3). An attempt was made to preserve clay bound water, by drying the plugs in a humidity oven at 60°C and 40% humidity, rather than using a hot oven (105°C).

5.3 Experimental and analytical methods

The nine wells can be split into two groups of associated measurements (Table 5.1), based upon variations in experimental procedures (well 6 occasionally has a different procedure to wells 7, 8 and 9). The methods highlighted in red are utilised in this study.

	Experiments or methods Group:	A					B			
	Well:	1	2	3	4	5	6	7	8	9
1	Dean & Stark analysis (plug cleaning)	✓	✓	✓	✓	✓	✓	✓	✓	✓
2	Porosity (gas expansion porosity)	✓	✓	✓	✓	✓	✓	✓	✓	✓
3	Grain density	✓	✓	✓	✓	✓	✓	✓	✓	✓
4	Klinkenberg corrected gas permeability.	✓	✓	✓	✓	✓	✓	✓	✓	✓
5	Gas-oil relative permeability. Unsteady state condition flood	✓	✓	✓	✓	✓	✓			
6	Water-oil relative permeability. Unsteady state condition flood	✓	✓	✓	✓	✓				
7	Oil-water relative permeability. Unsteady state condition flood						✓			
8	Brine permeability at residual oil saturation, with end point plug conductivity determination						✓	✓	✓	✓
9	Brine permeability, forward and reverse directions						✓	✓	✓	✓
10	Brine permeability and porosity as a function of overburden pressure						✓	✓	✓	✓
11	Brine permeability versus throughput						✓			
12	Formation resistivity factor (F) - at room conditions	✓	✓	✓	✓	✓	✓	✓	✓	✓
13	F as a function of overburden pressure	✓	✓	✓	✓	✓	✓	✓	✓	✓
14	Gas-brine Capillary Pressure (CP) by the porous plate method.	✓	✓	✓	✓	✓	✓	✓	✓	✓
15	Resistivity index	✓	✓	✓	✓	✓	✓	✓	✓	✓
16	Mercury injection capillary pressure drainage cycle with pore size distribution. (Drainage and imbibition)		✓	✓	✓	✓	✓	✓	✓	✓
17	Cation exchange capacity	✓	✓	✓	✓	✓	✓	✓	✓	✓
18	Fluid sensitivity flooding program	✓	✓							

5.1. Summary of analyses performed on each well; the methods highlighted in red are utilised in this study

5.2.3 Drilling plugs from whole core

The plugs of approximately one and a half inch diameter by two and a half inches length, were taken from the whole core parallel to the apparent bedding. A bit lubricant of base oil was used to cut the plugs, trim their ends and used as the fluid while the ends were lightly brushed to remove any fines induced by the trimming. All the plugs were stored in glass containers and immersed in base oil pending analysis. The friable nature of selected sandstone plugs from Group B led to them being mounted in a protective and supportive heat shrink Teflon sleeve, which covered the length of the plugs but not the ends. A quality control check was performed by SC2 on the samples with sleeves; however, details are not given.

Samples designated for clean state testing (those considered in this study) had residual pore fluids removed by two separate methods (§5.2.4):

(i) Samples scheduled for basic electrical properties and relative permeabilities were cleaned by the Dean & Stark extraction technique.

(ii) Samples scheduled for formation resistivity factor measurements at overburden pressure, were cleaned in refluxing soxhlet extractors.

5.3.2 Plug cleaning

5.3.2.1 Dean & Stark Analysis

Dean & Stark Analysis is primarily for the purpose of cleaning core plugs, prior to the measurement of fluid saturations. De-watered toluene is boiled over samples raising the temperature to drive-off the pore water and to extract the residual hydrocarbon content. The process is continued until water production ceases and the samples show no fluorescence under ultra violet light. It was specified that for Group B samples, the cycle be continued for three days. The values of the initial water, oil and gas saturations were calculated as a percentage of the plugs pore space by volumetric and gravimetric material balance. The samples were then dried in the humidity oven, returned to the apparatus, and methanol used to remove residual salts. Finally, the samples were returned to the humidity oven, a final extracted weight taken, then placed in a desiccator partially filled with silica gel and allowed to attain thermal equilibrium. Porosity and gas permeability were determined when thermal equilibrium had been reached.

5.3.2.2 Solvent flushing

The technique of solvent flushing employed the same solvent as the Dean & Stark samples for continuity. The method involves the continuous flowing of a solvent through the plugs, until all original pore fluids are removed.

5.3.3 Helium porosity measurement

The gas expansion porosity (GEX ϕ) method is a means of obtaining the effective (connected) porosity of a sample (see §2.2.1 for porosity definitions). The Helium Porosimeter operates on the principle of Boyle's law, which states; *'for an ideal gas, assuming constant temperature, the product of the pressure and volume, in a closed system, remain constant'*. The error quoted by SC2 is ± 0.2 porosity percent.

The sample is enclosed in a container of known volume, under known gas pressure, and connected with an evacuated container of known volume. When the valve between the two vessels is opened, the gas expands into the evacuated container and the gas pressure decreases. The effective pore volume V_p of the sample can be calculated by using the Boyle's law,

$$V_p = V_B - V_a - V_b\left[\frac{P_2}{(P_2 - P_1)}\right] \qquad [5.1]$$

where, V_B is the bulk volume, V_a the volume of the vessel containing the sample, V_b the volume of the evacuated vessel, P_1 the initial pressure, and P_2 the final pressure (nomenclature given in Appendix A).

The bulk volume of the sample is determined by brine saturation and immersion under brine; not by the standard mercury displacement technique. This was at the request of Enterprise Oil plc, and the main advantage is that plug contamination is avoided. The accuracy is within 0.01 cm^3 (bulk volume), which is equivalent to the mercury displacement technique, assuming the pump is calibrated and is zeroed for each sample. However, the brine method is not as rapid as mercury displacement (API Recommended Practice, 1998). Amoco performed a quality assurance test and found that bulk volume measurement errors are one of the most common errors due to capillary pressure effects. A bulk volume method in which no capillary pressure effects occur would be ideal, but practically impossible! (Thomas and Pugh, 1989).

5.3.4 Brine permeability

5.3.4.1 Brine permeability in forward and reverse directions

Samples (from Group B) were evacuated and then saturated with simulated formation brine. The samples were subjected to a confining pressure of 200 psig, and when a steady flow and differential pressure regime were established, the permeability to brine for each sample was measured. The flow was then reversed, and the brine permeability re-measured (results, §5.4.1).

5.3.4.2 Brine permeability versus throughput

Subsequent to the measurement of formation resistivity factor (*F*) seven samples from well 6 were loaded into individual hydrostatic core holders, with a net confining pressure of 200 psig applied. The original brine (well 12 type) was displaced by simulated formation brine (well 4 type) at a constant flow-rate (see Appendix E for brine concentrations). The injection was continued for at least 200 pore volumes and at pre-determined points the brine permeability was measured in order to monitor any reactions taking place. The flow was reversed on completion of the forward flood, and brine permeability re-measured (results in §5.4.1).

5.3.5 Gas permeability

Porosity and other base parameters (sample length, bulk volume, and cross-sectional area) were measured on clean dry samples, which were then placed in a Hassler (hydrostatic) cell and a confining pressure (overburden) applied. A confining pressure of 200 psig was applied to samples with permeabilities greater than 10 mD and 400 psig on samples with a permeability less than 10 mD. The purpose of using these confining pressures was to prevent gas bypass. Thomas and Pugh (1989) state that confining pressures less than 500 psig, can cause errors by gas bypassing around the plug. Gas bypass is the action of gas passing between the core plug and the rubber core holder, therefore increasing the apparent value of permeability. In low permeability plugs a higher mean pressure is required to measure permeability and for this reason a larger confining pressure is required to prevent gas bypass. A confining pressure selected, nitrogen is forced through the individual samples, with the upstream, downstream and flow rates recorded, permeability was then calculated using,

$$k_g = \frac{2000\left(\frac{Bp}{760}\right)q\mu L}{\left[\left(\frac{P_1}{14.696}+\frac{Bp}{760}\right)^2-\left(\frac{P_2}{10332.203}+\frac{Bp}{760}\right)^2\right]A} \qquad [5.2]$$

where, k_g is the gas permeability, q the flow rate (cm^3/sec), L the length of the plug (cm), A the cross-sectional area of the plug (cm^2), μ the gas viscosity, P_2 the downstream pressure, P_1 the upstream pressure and Bp the atmospheric pressure (mmHg). Therefore, $Bp/760$ is converting the atmospheric pressure in mmHg into atmospheres, 1 atmosphere is equal to 14.6959 psia, therefore the $P_1/14.696$ is converting the upstream pressure in psig into atmospheres, and P_2 /10332.203 is converting the downstream pressure in mmH_2O into atmospheres.

The most common problem with gas permeability measurements are system leaks that affect the differential pressure measurement of the gas flow rate. Other problems are improper calibration or damage to the orifice used for gas flow rate calculations, correcting values for gas slippage (especially low permeability plugs) and high flow rates causing reduced permeability (due to turbulent flow). The main advantages of gas permeability measurements are the ease with which they are made. The gas is non-reactive with the rock, less corrosive to the equipment, less prone than liquid to mobilising fines in the rock sample and does not support microbial growth (Sinclair and Duguid, 1990; API recommended practice, 1998).

The value of permeability can change as the value of the mean pressure applied across the plug changes, permeability decreases as mean pressure increases. A normalised and consistent set of permeability measurements can be generated using the Klinkenberg method.

5.3.6 Klinkenberg permeability

Following an initial qualitative assessment of the Klinkenberg data (§5.3.6.2), it was found that the data did not give the expected linear trend and so it was decided to investigate the Klinkenberg data further. Two extra sets of measurements were collected on a selection of the plugs used for the initial measurements, giving three Klinkenberg data sets (KDS) in total:

KDS1, Original data provided by SC2 at the start of this study.

KDS2, Measurements collected at Service Company 3 (SC3) by the author in early 1997.

KDS3, Measurements collected at SC2 by the author in early 1997.

Klinkenberg (1941) showed that by taking several measurements of gas permeability over a range of pore pressures, and extrapolating the regressed data to infinite mean pressure, the core permeability to an *inert* liquid could be predicted within experimental error. This was a significant breakthrough in the hydrocarbon industry, since the gas permeability measurements were faster than liquid permeability measurements. A value of liquid permeability is required for reservoir characterisation models.

Klinkenberg measurements are faster than liquid permeability measures, but slow compared to a single gas permeability measurement. In the past the Klinkenberg value was sometimes calculated from a single gas permeability measurement using a correlation factor, in the interest of time and money. Accuracy suffered with this method as permeability correlations are empirically developed for specific sample sets, and cannot be considered transferable for all porous media. It is now the industry standard to measure the Klinkenberg value, at least for a subset of any group of data.

To generate a Klinkenberg corrected gas permeability the plug permeability values were measured using a gas permeameter (Figure 5.1), at four different mean pressures for Group A and six mean pressures for Group B, with the pressure differences across the core kept at a constant reading.

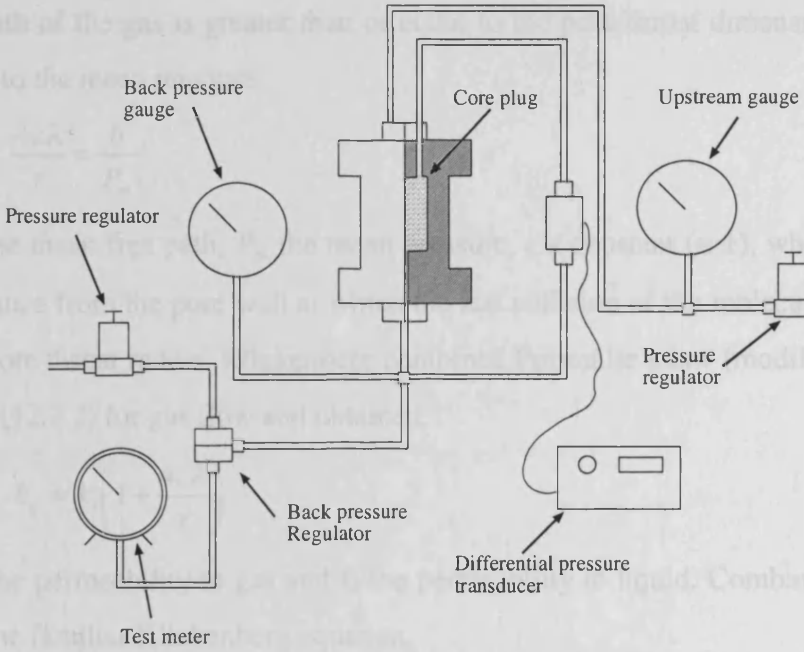

Figure 5.1. Schematic of the apparatus used to measure Klinkenberg corrected permeability

To prevent gas bypass a confining pressure of 200 psig was used for samples with a permeability greater than 10 mD and 400 psig for plugs with a permeability less than 10 mD. All the samples provided by SC2 for further tests, had original measurements made with an effective confining pressure (as upstream pressures are incrementally increased so is the confining pressure, keeping the total confining pressure constant) of 200 psig. A linear regression was carried out on the (inverse mean pressure, permeability) co-ordinate pairs and the extrapolated permeability at zero inverse mean pressure was calculated. This value is the reported Klinkenberg corrected permeability. The line was then extrapolated to an inverse mean pressure of 1 atm, the value of permeability at 1 atm^{-1} and 0 atm^{-1} were used to calculate the *b*-factor using the formula,

$$b = \frac{k_1 - k_0}{k_0} \qquad [5.3]$$

where, k_1 is the permeability at a mean pressure of 1 atm^{-1} and k_0 the permeability at zero inverse mean pressure. The *b*-factor (§5.3.6.1) was defined by Klinkenberg (1941), and is also called the 'slip-factor', which is characteristic of both the gas and the porous media.

The following section on Klinkenberg theory is summarised from Chapter 2 (§2.2.2.2). Klinkenberg modified the Poiseuille equation, which describes flow through capillaries, to account for gas slippage at the capillary (pore) walls. Klinkenberg created a model that looked at gas flow through a bunch of randomly orientated straight capillaries, and argued that the mean-free path of the gas is greater than or equal to the pore throat dimension and inversely proportional to the mean pressure;

$$\frac{4c\lambda}{r}=\frac{b}{P_m} \qquad [2.12]$$

where λ is the mean-free path, P_m the mean pressure, c a constant ($\cong$ 1), where $c\lambda$ equals the average distance from the pore wall at which the last collision of the molecule took place and r the mean pore throat radius. Klinkenberg combined Poiseuille's law (modified for slip) with Darcy's law (§2.2.2) for gas flow and obtained,

$$k_g = k_l\left(1+\frac{4c\lambda}{r}\right) \qquad [2.13]$$

where k_g is the permeability to gas and k_l the permeability to liquid. Combining Eq. 2.12 and 2.13 yields the familiar Klinkenberg equation,

$$k_g = k_l\left(1+\frac{b}{P_m}\right) \qquad [2.14]$$

Klinkenberg concluded that if the simplified considerations are not only valid for a system of straight capillaries, but also to porous media then according to Eq. 2.13 and 2.14:

(i) k_g is a linear function of $1/P_m$.

(ii) k_g is independent of differential pressure (and hence flow rate) provided P_m is constant.

(iii) The slip-factor is inversely proportional to r. Therefore, b is small or negligible for high permeability samples.

(iv) At the same mean pressure, k_g is different for different gases, since their mean-free paths are different, but will be equal at infinite pressure, as mean-free paths are zero.

(v) k_g when extrapolated to infinite mean pressure ($1/P_m$= 0) should give the 'true' k_l.

Permeability errors are difficult to quantify. SC2 estimate the Klinkenberg permeability error as ± 1.51%, in this study the gas permeability error has been calculated as ± 3.27% (Appendix C), but the Klinkenberg permeability error was not estimated. SC6 state that the gas permeability error can be as much as ±20%, especially in low permeability plugs.

It is important to note that in the interpretation of Klinkenberg data an assumption is made that the slip-factor is constant, and does not vary with mean pressure; in fact Klinkenberg (1941) acknowledges that the value of the b-factor, increases with increasing pressure.

Klinkenberg also argues that the concept of slippage is unlikely to be valid for flow in tortuous pore systems.

5.3.6.1 *b*-factor

The Klinkenberg *b*-factor is a function of the gradient of the line generated from a plot of gas permeability versus inverse mean pressure. The gradient of this line equals the *b*-factor multiplied by the extrapolated Klinkenberg permeability value (Figure 5.2, Eq. 2.14). It is therefore not surprising that people have reported that as Klinkenberg permeability increases so does the gradient of the line (Sampath and Keighin, 1982).

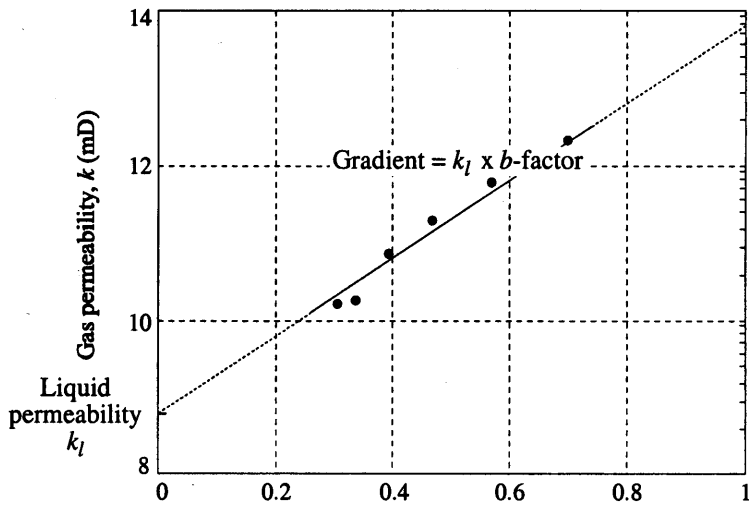

Figure 5.2. Gas permeability against inverse mean pressure to demonstrate the *b*-factor

A plot of Klinkenberg permeability against the actual *b*-factor, (i.e. the gradient of the Klinkenberg plot divided by the extrapolated Klinkenberg value for permeability) gives the significant* correlation seen in Figure 5.3. Figure 5.3 shows that as the permeability of a plug increases the *b*-factor decreases (r=-0.80, in linear space with permeability logged). This is expected as the higher the plug permeability, the higher the Klinkenberg permeability value is, and therefore the gradient divided by this Klinkenberg permeability is less. This occurs although the gradients of the plots increase with increasing permeability (Figure 5.9). Porosity and the *b*-factor show no significant correlation, (r=-0.34, Figure 5.4).

* Unless otherwise stated the significance of the correlation coefficient r, has been tested at a probability level of 0.05.

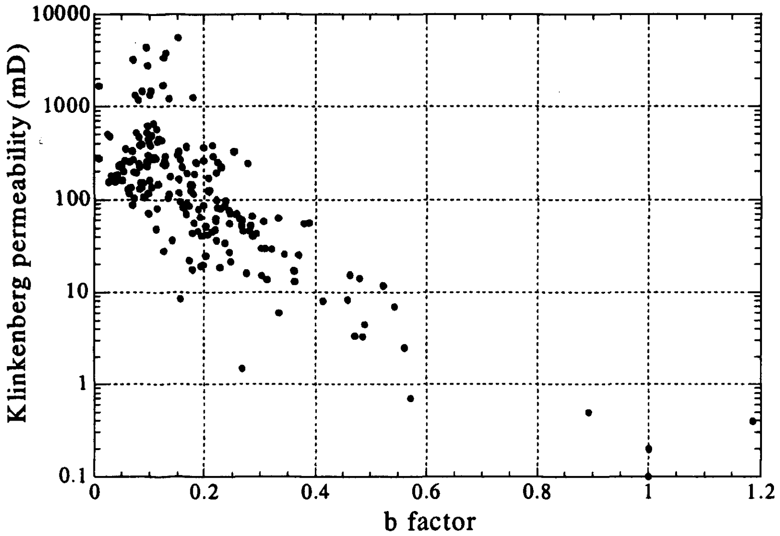

Figure 5.3. Klinkenberg permeability versus the *b*-factor

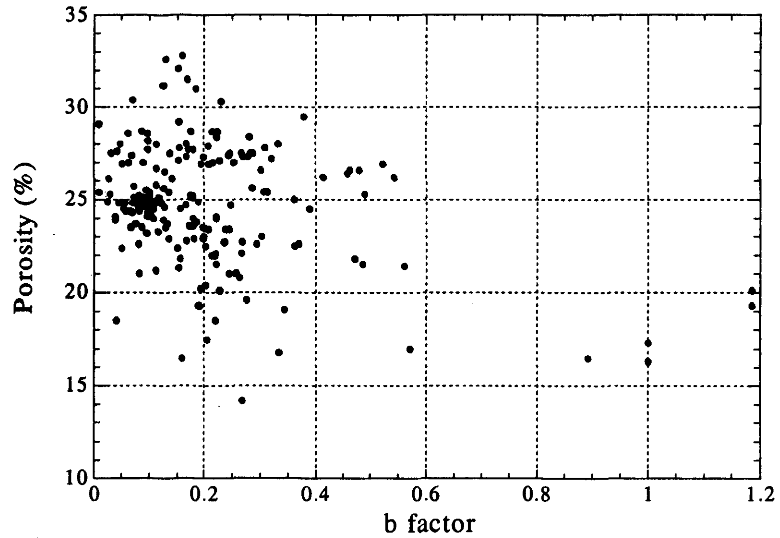

Figure 5.4. Plug porosity versus *b*-factor

5.3.6.2 A qualitative review of the Klinkenberg plots

Klinkenberg permeability measurements were made on 112 plugs. Forty-two of these data sets were plotted, examined qualitatively and divided into nine curve types (Figure 5.5, Table 5.2), following work done by Henderson (pers. comm., 1995). Curve types one to nine, show that a step or kink in the centre of the plots is the most prominent feature. One hypothesis was that the kink is caused by a movement of pore fines, either increasing the permeability by unblocking flow paths, or by decreasing the permeability by blocking previously free paths. The movement of fines was considered a possible explanation, as the methods of cleaning plugs (§5.3.2) do not require the cleaning fluid to be forced through under pressure. Therefore subsequent Klinkenberg measures may cause disturbance to the fines. To test this hypothesis repeated measurements were required.

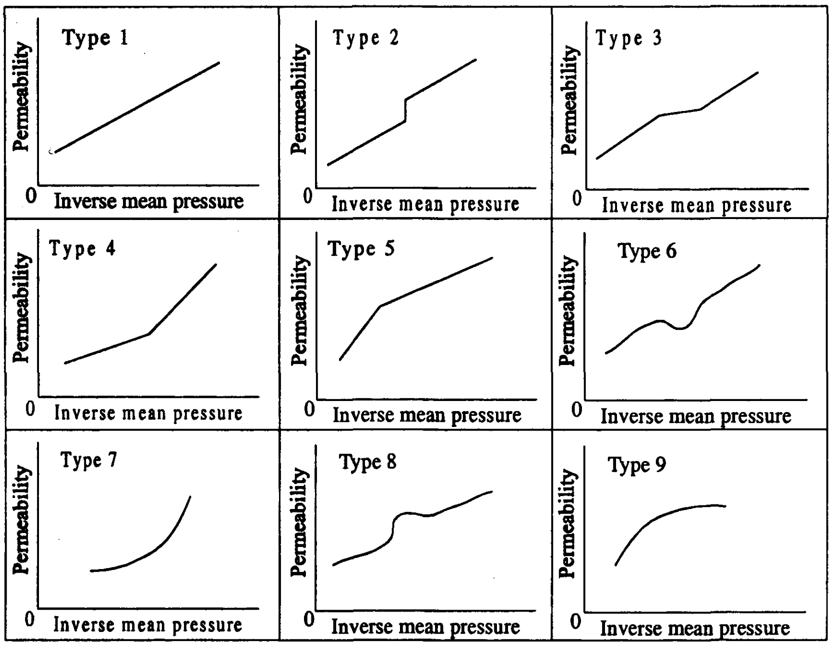

Figure 5.5. The nine curve types of best fit, for the Klinkenberg data versus inverse mean pressure plots

Figure 5.6 below is a typical example of a Klinkenberg data set; not perfectly linear but showing a linear trend, with a slight kink in the central region.

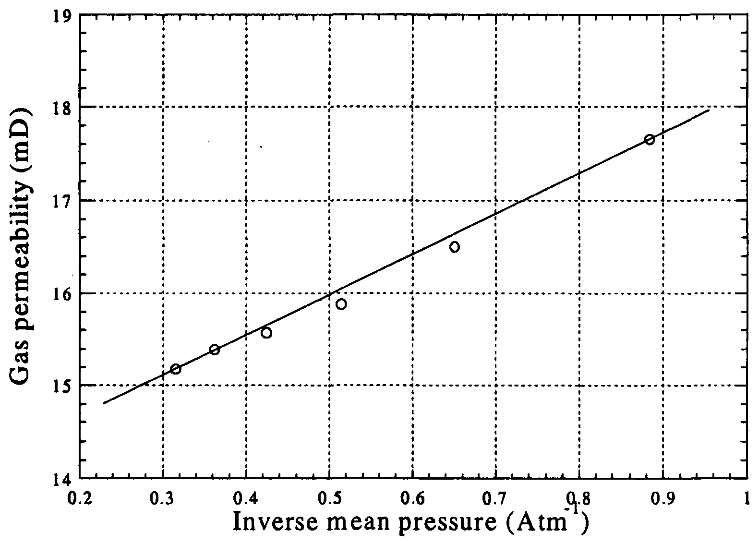

Figure 5.6. Gas permeability verses inverse mean pressure (well 6 plug 8c). The line is to demonstrate the kink in the curve and is not a line of best fit

SC2 quoted an error associated with the Klinkenberg permeability measurements of 1.51% which would, in the majority of cases, remove the kink in the curves. However, the kink was seen in over 50% of the forty-two randomly chosen plugs and can therefore not be ignored.

Permeability was plotted against porosity distinguishing curve type (Figure 5.7). Examination of the plot reveals that curve type 3 is associated with a narrow band of permeabilities and curve type 4 has a significant relationship (r=0.76, log:lin space).

Well/plug	Curve type	Porosity (%)	Permeability (mD)
7/1b	1	25.3	6.96
7/5a	1	26.6	36.7
4/21b	1	23	19.1
1/1a	1	27.4	92.7
1/1c	1	27	60
1/5a	1	22.6	505
1/5c	1	24	728
1/7a	1	26.7	91.9
2/4a	1	25.1	491
2/9b	1	27.7	1477
2/9c	1	27.7	490
2/10a	1	24.2	1638
2/11b	1	23.4	113
9/11a	1	21	82.4
9/11b	1	21.3	132
9/12a	1	27.1	347
9/12b	1	26.5	317
9/13a	1	21	65.9
9/13b	1	20.8	76.3
7/4a	2	28.7	294
3/1a	2	27.8	112
7/2a	3	29.2	189
7/3a	3	23.7	226
7/5b	3	28	78.7
3/8b	3	24.2	344.3
4/18c	3	19.3	97.4
8/7a	4	22	56
8/8a	4	24.6	1280
8/10a	4	25.2	168
3/10b	4	22.1	73.1
3/11b	4	24.2	180.8
3/14c	4	25.1	162.2
4/20c	4	28.7	1742
3/5a	5	25.3	489.4
4/16c	5	28	251
1/2a	6	21.4	3.79
1/4a	6	26.2	11.5
1/9a	6	23.6	162
2/1a	6	26.9	17.9
9/14a	6	23	400
1/6a	8	23.9	263
9/14b	8	22.4	337

Table 5.2. Plugs with their curve type number, and respective plug porosity and gas permeability values

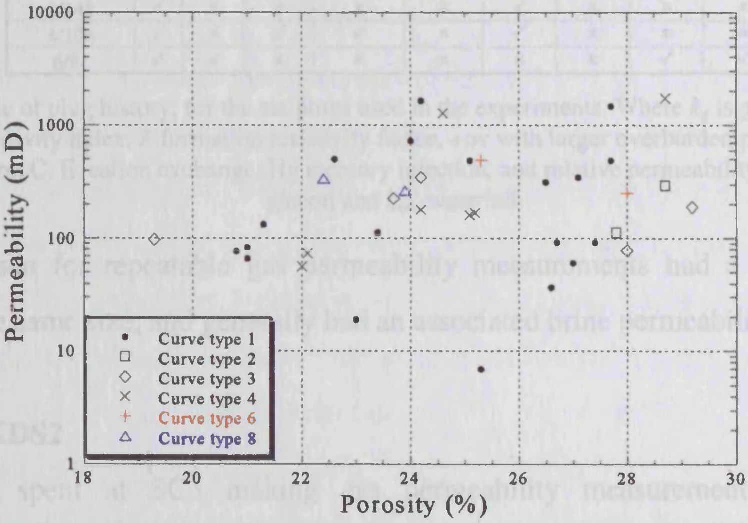

Figure 5.7. Gas permeability against plug porosity, with Klinkenberg curve type distinguished

5.3.6.3 Data collected at Service Company 3 (KDS2)

The qualitative curve shapes (§5.3.6.2) needed to be verified before their cause could be investigated. Therefore, the Klinkenberg measurements had to be tested for repeatability. This was performed using the permeameters at SC2 and SC3 on a selection of plugs supplied by SC2, which had already undergone Klinkenberg measurements. Table 5.3 lists the twelve plugs supplied by SC2, and also which plugs were then used for further permeability tests. All the plugs were visually intact, but it must be noted that measurements, possibly damaging the plugs, had already been made on these plugs (Table 5.4).

Well/plug	KDS1			KDS2	KDS3
	Porosity	Calculated k_{Klink}	k_{Brine}		
3/1b	27.7	85.7	74.11	✓	✓
3/9b	23.6	22.2	14.52	✓	✓
3/3c	25.2	17.5	11.3		✓
3/14b	24.6	136.6	108.6		✓
4/23b	25.6	28	✗		
4/17b	23.1	161	145.2	✓	✓
4/18a	17.5	42	✗		
6/1c	32.9	1342.9	✗		
6/2c	26.9	126.5	✗		
6/5c	31.5	191.5	✗		
6/7c	27.1	80.9	✗		
6/8c	25.4	13.8	✗	✓	✓

Table 5.3. Table showing available plugs, and whether those plugs have had repeated measurements taken

	Experiments								
Well/plug number	k_g	I_R	F	F +ov	Cap. Pr.	C. E.	Hg	$k_{g/o}$	$k_{w/o}$
3/1b	✓	✗	✓	✓	✗	✓	✗	✗	✗
3/9b	✓	✗	✓	✓	✗	✗	✗	✗	✗
3/3c	✓	✗	✓	✓	✗	✗	✗	✗	✗
3/14b	✓	✗	✗	✗	✗	✓	✗	✗	✗
4/17b	✓	✗	✓	✓	✗	✓	✗	✗	✗
6/8c	✓	✗	✗	✗	✗	✗	✗	✓	✓

Table 5.4. Table of plug history, for the six plugs used in the experiments. Where k_g is gas permeability, I_R formation resistivity index, F formation resistivity factor, +ov with larger overburden pressures, Cap. Pr. capillary pressure, C. E. cation exchange, Hg mercury injection, and relative permeability measurements $k_{g/o}$ gas:oil and $k_{w/o}$ water:oil

The plugs chosen for repeatable gas permeability measurements had a range of porosity values, were the same size, and generally had an associated brine permeability value.

Results from KDS2

One day was spent at SC3 making gas permeability measurements. Three sets of measurements were made on each plug over a range of mean pressures (Figure 5.8), the experimental procedure and table of results are given in Appendix C.

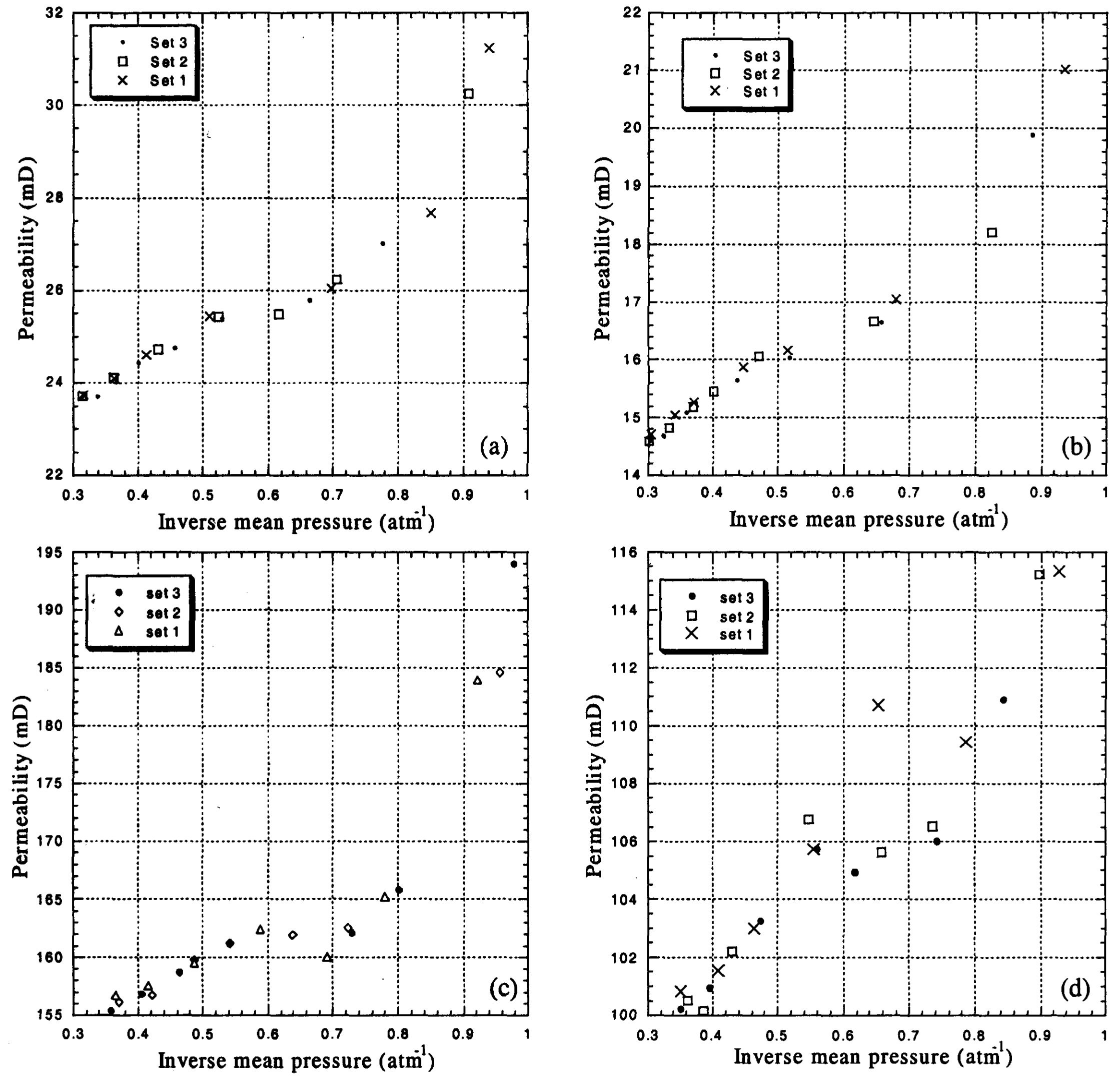

Figure 5.8. Gas permeability verses inverse mean pressure for; (a) well 3 plug 9b, (b) well 6 plug 8c, (c) well 4 plug 17*b*-and (d), well 3 plug 1b. KDS2 (note the linear gas permeability scale)

Observations from the data can be summarised as follows:

(i) The measurements were highly repeatable.

(ii) The data plots had a distinct curvature. A flat central part (in the region of inverse mean pressure range of 0.5 to 0.70 atm^{-1}) with an increase in gradient on either side.

(iii) One of the four plugs (plug 3/1b) gave less repeatable measurements (Figures 5.8d); this may be an indication of multiple pore sizes not allowing the gas pressure to stabilise within the measurement period of the test.

Possible reasons for these curve shapes are:

(i) At the higher mean pressures turbulent flow could occur causing a decrease in the permeability. Tiss and Evans (1989) observed that the lower the permeability of the core the lower the flow rate at which nitrogen flow achieves the non-Darcy flow regime. According to these findings, it should be expected that if the kink in the Klinkenberg

curves is due to non-Darcy flow, the kink will occur at higher inverse mean pressures in low permeability plugs than in high permeability plugs. Figure 5.8 shows that there is a shift in the kink towards higher inverse mean pressures with an increase in permeability.

(ii) Norman and Kalam (1990) observed a decrease in permeability with an increase in flow rate and attributed it to the gas slippage effect becoming important at the lower flow rate.

(iii) Perhaps the slip effect was greatest at the pressures associated with the flattened part of the curve, and therefore temporarily inhibited the decrease of the permeability values with the increase in inverse mean pressure.

(iv) The suggestion of movement of fines through the plug (§5.3.6.1) as the cause of disturbance to the expected linear trend in the plots can now be conclusively dismissed due to the repeatability of the curves.

(v) The shape is an artefact of errors in the measuring equipment at SC3, as the shape is not as pronounced in KDS1. It would have to be a stable error in the equipment due to the repeatability of the measurements.

(vi) There is a secondary porosity or micro-porosity which is opened at the higher pressures, preventing the steady decrease of permeability with increasing pressure in the plateau region. This possibility would have to occur regardless of the constant confining pressure, and be elastic due to the repeatability.

It is apparent from the results given in Figure 5.8 that depending at what inverse mean pressure the permeability was measured, different values of Klinkenberg permeability would be calculated. Therefore a large error is associated with the measurements. If high inverse mean pressures were used, negative values of permeability would be calculated. The Klinkenberg permeability calculated from points taken on the plateau region of the curve is approximately 9-17% higher than the permeability calculated on points taken from the low inverse mean pressure values.

To compare the gradients of the data from the four plugs, each set of plugs have been linearly shifted to have a permeability value of zero mD at 0.3 atm^{-1} (Figure 5.9). As the permeability of the plugs increases, so do the gradients of the curves, a point also noticed in KDS1. However, as the gradient of the slope is equal to the Klinkenberg permeability multiplied by the *b*-factor (Eq. 2.14), this result is expected. Therefore, as Klinkenberg permeability increases, so will the gradient. The same Klinkenberg value can have varying curve gradients, and hence a varying *b*-factor, therefore this is a general rule.

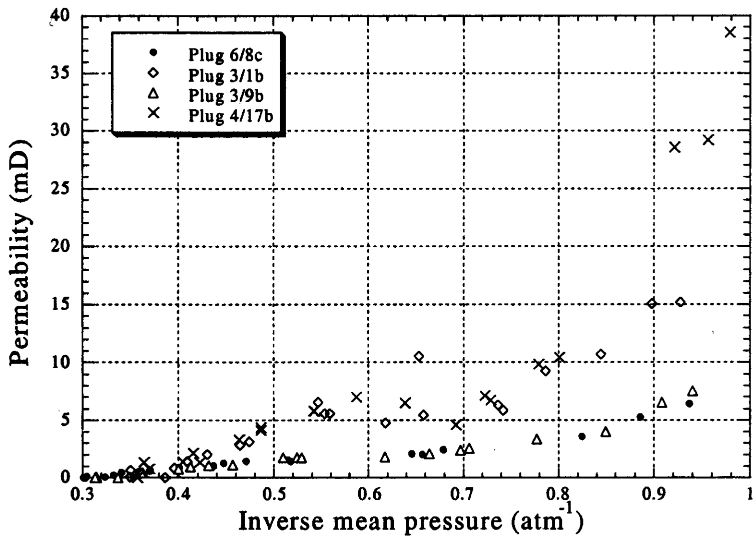

Figure 5.9. Gas permeability against inverse mean pressure, with the permeability values shift to a permeability value of zero mD at a 0.3 atm^{-1} (for the four tested plugs)

Sampath and Keighin (1982) proposed that the slope of the straight line relating apparent gas permeability to reciprocal mean pore pressure, decreased with increasing net confining pressure. However, they did not comment that an increase in confining pressure would decrease the permeability. Furthermore, a decrease in permeability gives a decrease in the gradient of the curve, such is the nature of their relationship, (these are the same results as seen in Figure 5.9).

5.3.6.4 Data collected at Service Company 2 (KDS3)

The details of the experimental method and full results are given in Appendix C. It was established through personal correspondence with SC2 that the KDS3 results were measured in the same manner as KDS1. Apart from the KDS1 measurements were made on plugs which had been dried in a humidity oven and then placed in a desiccator with silica gel prior to permeability measurement, and the KDS2 and KDS3 measurements were made on plugs taken from storage in a cardboard box.

Four fundamental differences exist between the permeameters at SC2 and SC3:

(i) The SC2 permeameter has a selection of orifices, which were used to try and keep laminar flow within the plugs and did not require *a priori* information of the plug permeability. At SC3, the approximate range of permeabilities of the plugs was

known and the permeameter was set up accordingly, with the most suitably sized orifice.

(ii) The permeameter at SC3 had a back pressure regulator which enabled a range of mean pressures to be obtained keeping a low flow rate but there was no back pressure adjuster, or upstream pressure regulator. Therefore this back pressure could not be controlled and the pressure difference across the plug could not be adjusted to get the exact required pressure difference. At SC2, however, the back pressure could be adjusted so that every successive measurement in each set of measurements could have the same pressure difference.

(iii) The confining pressure was a net effective pressure at SC2 unlike at SC3 where it was constant.

(iv) SC2 used a 2 mm thick Nitrile core holder, and a given specification of 70 IRHD. SC3 used a 3 mm thick Nitrile (high) core holder, and a given hardness specification of 75, ± 5 IRHD.

Results from KDS3

Twenty-five sets of measurements make up KDS3, and have been used to test:

(i) Measurement repeatability.

(ii) Effects of confining pressure.

(iii) Effects of different mean pressures.

(iv) Effects of no applied back pressure.

(v) Effects of using different orifices.

Additionally,

(vi) Effects of time have been investigated, but not with data from KDS3.

Table 5.5 shows the different measurements made on each plug.

Well / plug number	Run number	Pressure difference	Plug number written: Upstream	Plug number written: Downstream	Confining pressure (psig)	Orifice used
3/1b	1	3.5	✓		250	1
3/1b	2	3		✓	250	1
3/3c	1	NBP *	✓		250	3
3/3c	2	NBP	✓		250	2
3/3c	3	NBP	✓		250	1
3/3c	4	3	✓		250	2
3/3c	5	2.5	✓		250	2
3/9b	1	11	✓		250	1
3/9b	2	1	✓		250	2
3/9b	3	1	✓		250	2
3/9b	4	10.5		✓	250	1
3/9b	5	2	✓		450	2
3/14b	1	2	✓		250	1
3/14b	2	2.5	✓		250	1
3/14b	3	2		✓	250	1
4/17b	1	2	✓		250	1
4/17b	2	2	✓		250	1
4/17b	3	2		✓	250	1
4/17b	4	2		✓	400	1
4/17b	5	NBP		✓	250	1
6/8c	1	2.5	✓		250	2
6/8c	2	NBP	✓		250	2
6/8c	3	2.5	✓		250	2
6/8c	4	2		✓	250	2
6/8c	5	NBP		✓	250	1

* NBP = No back pressure applied

Table 5.5. Table showing various measurements made on the six plugs at SC2.

(i) Repeatability

Plugs 8c and 17b (Figure 5.10) each had measurements repeated on them under identical conditions, but only Plug 8c produced repeatable curves. The results of runs 1 and 2 for plug 17b did not give identical curves. The outcome of run 3 however, when 17b plug was reversed but measured under the same conditions, gave a similar curve to run 2. The familiar curve shape of run 1 (plug 17b) to those seen in KDS2, suggest that the same instability existed in this run.

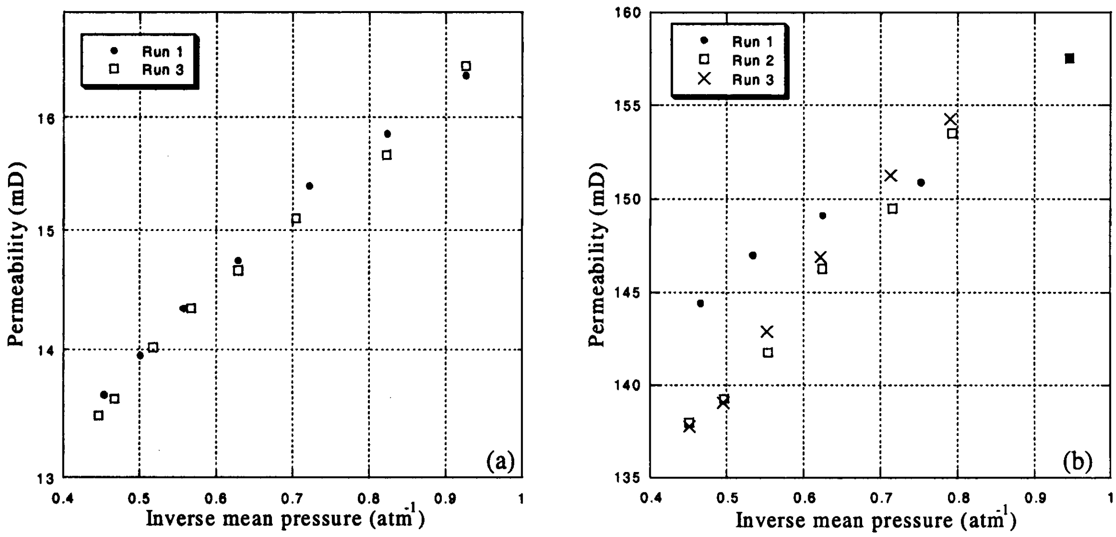

Figure 5.10. Gas permeability versus inverse mean pressure for (a) runs 1 and 3 on plug 8c (b) runs 1, 2 and 3 on plug 17b. See Table 5.5 for details of settings for each run. (KDS3)

(ii) Confining pressure

Plugs 9b and 17b had measurements taken at a confining pressure of 250 psig and a second pressure of 450 and 400 psig respectively. The outcome for both plugs 9b and 17b, show a decrease in permeability with the increase in confining pressure (run 5 Figure 5.11a, and run 4 Figure 5.11b). The decrease in plug 9b may be due to the changing pressure differences between the two runs as a small pressure difference can give unstable results. In the literature (API recommended practice, 1998) it is generally agreed that an increase in confining pressure will decrease the permeability due to a crushing effect on the plug. Luffel et al (1989) found extreme differences in permeability with increased overburden pressure, due to the presence of coring induced micro-cracks.

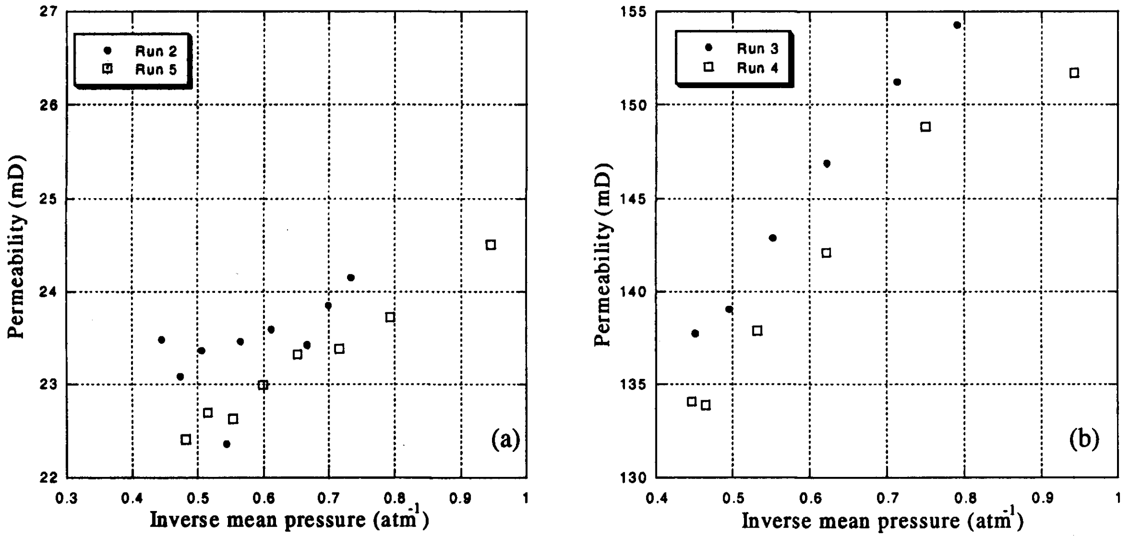

Figure 5.11. A plot of gas permeability versus inverse mean pressure for (a) runs 2 and 5 on plug 9b (b) runs 3 and 4 on plug 17b. See Table 5.5 for details of settings for each run. (KDS3)

(iii) Difference in the upstream and back pressure (mean pressures)

Plugs 9b, 8c, 1b, 14b and 3c give examples of a change in the difference between the upstream and the back pressure, (i.e. a change in pressure separation). The change in plug 9b in pressure difference is seen to have a dramatic effect (Figure 5.12a), where the two sets of measurements associated with the largest pressure difference (runs 1 and 4) are also associated with the higher permeability values and show a curve pattern similar to KDS2 (Figure 5.8a). It was also noticed in a comparison of all the curves for each plug, that in plugs 1b, 14b and 8c an increase in the separation created a plateauing effect (however slight) in the central part of the curve. (Compare run 1 with run 2 which has a larger separation, Figure 5.12b).

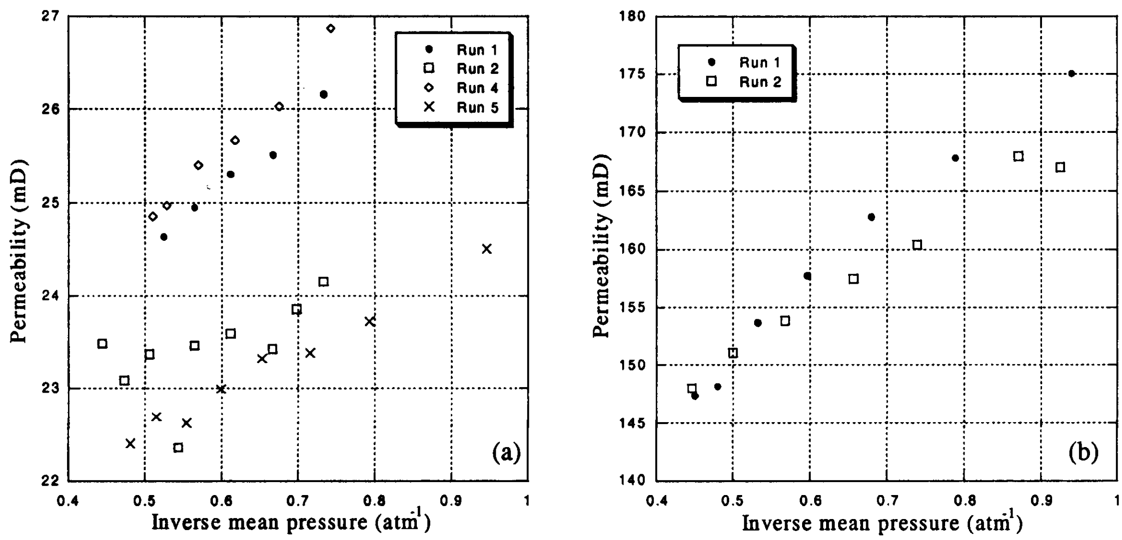

Figure 5.12. A plot of gas permeability versus inverse mean pressure for (a) runs 1, 2, 4 and 5 on plug 9b (b) runs 1 and 2 on plug 14b. See Table 5.5 for details of settings for each run. (KDS3)

(iv) Applying no back pressure

Some permeameter designs allow measurements to be made under back pressure conditions. The effect being to extend the mean pressure range, whilst maintaining the flow rate within a laminar regime. In atmospheric outlet pressure flow mode (i.e. no back pressure applied), the only way of increasing the mean pressure is to increase the flow rate, which brings with it the danger of inducing non-laminar flow in the sample. The method of applying no back pressure was tried to test if the increased difference in back pressure and upstream pressure, (which could be assumed on occasions for KDS2, where there was no choice of orifice) was the cause of the distinct curvature seen in the plots of KDS2. It has already been proposed in point *(iii)* that a large separation does emphasise the pattern. However, it is not possible to draw strict conclusions from these measurements as it is unknown if the curves are repeatable.

Figure 5.13 reveals for run 5 of plug 17b where no back pressure was applied, a smooth but unexpected curve shape. It was initially thought that gas bypass might be the cause, but this was not substantiated as gas bypass is a particular problem in low permeability samples (Thomas and Pugh, 1989) and when confining pressures are held constant (as in KDS2); neither of which are the case.

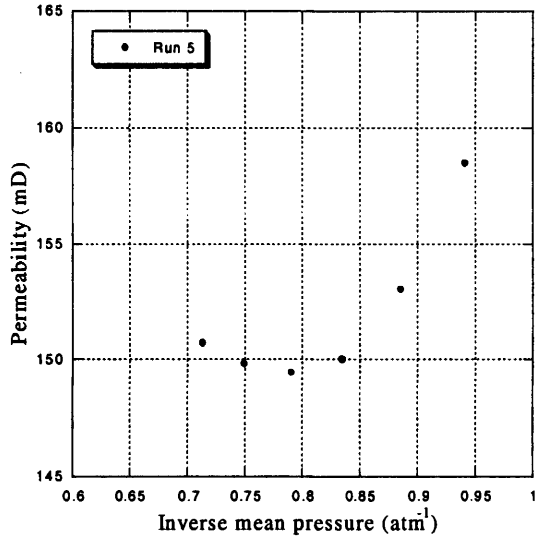

Figure 5.13. A plot of gas permeability versus inverse mean pressure for run 5 on plug 17b. See Table 5.5 for details of settings for this run. (KDS3)

(v) Use of different orifices

Multiple measurements have been made on plugs 3c and 8c using different orifices. The tests on plug 8c showed that as the size of the orifice increases (size increases from run 2 to run 5) the permeability at a given value of inverse mean pressure decreases (Figure 5.14a). The tests performed on plug 3c show the same outcome (Figure 5.14b) where run 3 uses the largest orifice, 2 an intermediate and run 1 the smallest. The tests were performed without applying back pressure, and therefore only the restriction of flow due to the orifices is being observed. The results seen in Figure 5.14 were also found by Sinclair and Duguid (1990) who state that, 'high flow rates in laboratory tests can cause reduced permeability due to either turbulent flow, movement of fines or *excessive confining pressure at the downstream end of the sample.*'

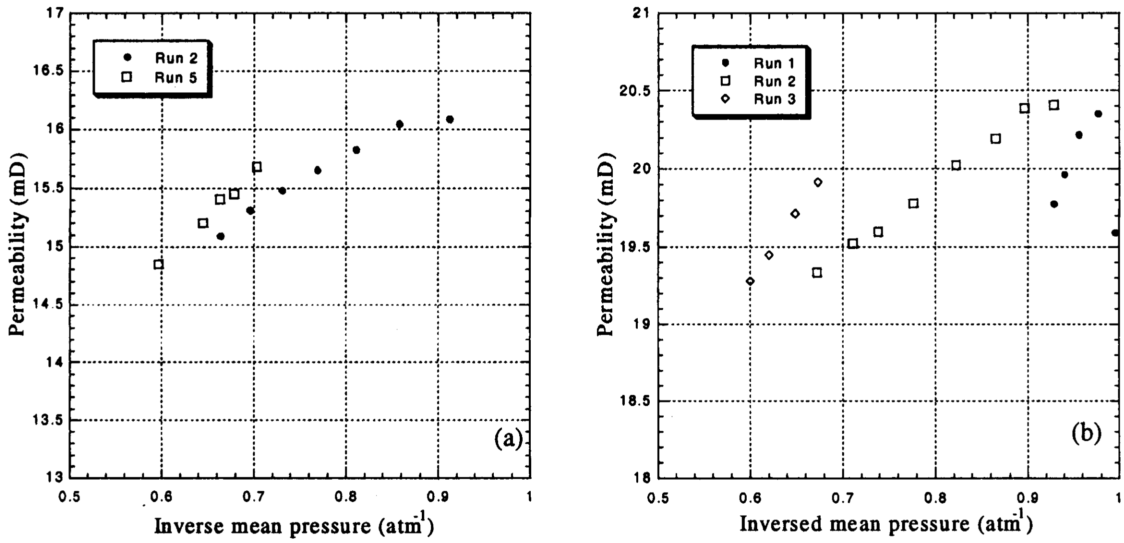

Figure 5.14. A plot of gas permeability versus inverse mean pressure for (a) runs 2 and 5 on plug 8c (b) runs 1, 2 and 3 on plug 3c. See Table 5.5 for details of settings for each run. (KDS3)

(vi) Effect of time

It has been noticed in the majority of plots for all three Klinkenberg data sets that, even for those which do not show repeatability, the curves are very smooth. It is suggested that this smoothness (even Figure 5.13) can be explained by the time required for the gas flow to stabilise. It is proposed that each point on each of the plots shows a higher permeability than is real and this error is carried through at each incremental mean pressure increase, creating results where each point is related to the point before and so forth, leading to a smoothness in the curve. McPhee (1992) showed the dependence of gas permeability measurements on time and confining pressure (Figure 5.15). It can be seen from the plot that in the lower confining pressures (<225 psi) the gas permeability takes five to ten minutes to stabilise.

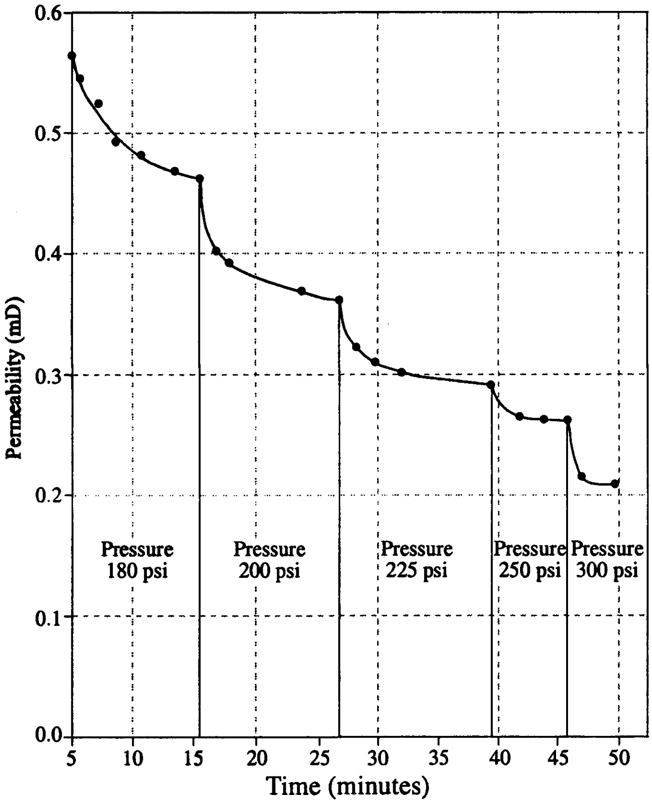

Figure 5.15. Effect of pressure and time on gas permeability measurements (after McPhee, 1992)

5.3.6.5 Comparison between the three data sets

McPhee and Arther (1991) confirmed that conventionally derived Klinkenberg parameters obtained on core plugs over a wide range of permeabilities, are sensitive to the methods, procedures and techniques used to acquire and analyse the data. It therefore comes as no surprise that the three Klinkenberg data sets give different results, but exactly why they are different is yet to be understood. In plugs 8c, 9b and 17b, KDS1 is well matched in position (i.e. the permeability distribution is similar) with KDS2, so although plugs 9b and 17b were probably salt contaminated, from the brine permeability measurements, it would appear that this has had little or no effect on the position of the curves. The three sets of Klinkenberg data have been compared more closely using selected data from plugs 8c and 1b (Figure 5.16). The data selected from 8c were the repeated curves shown in Figure 5.10a.

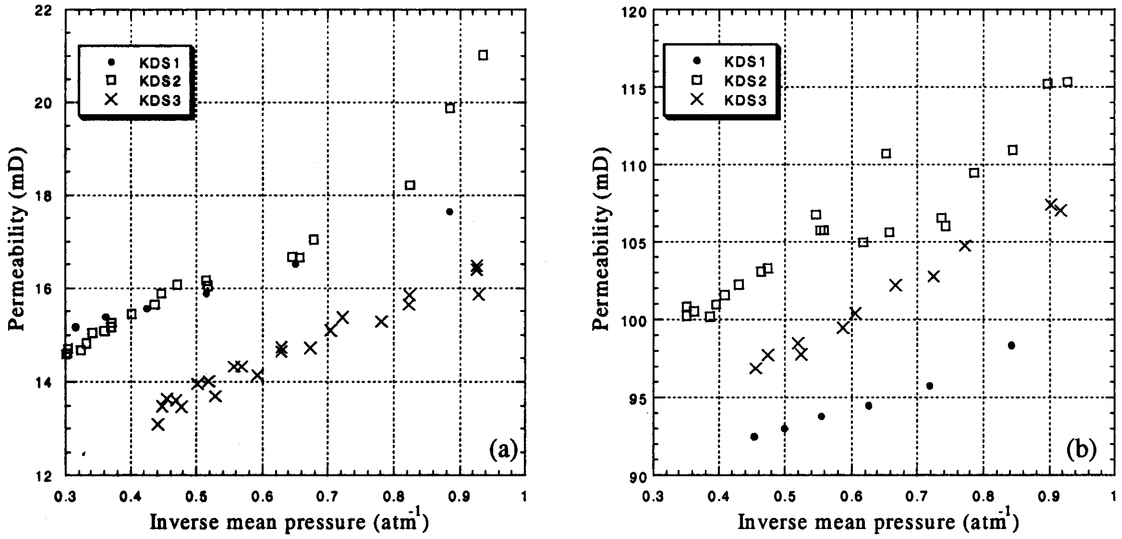

Figure 5.16. (a) A plot of gas permeability versus inverse mean pressure for comparison of the data supplied by SC2 (KDS1) and the two sets of data collected by the author at SC3 (KDS2) and SC2 (KDS3) on two plugs (a) is data for plug 8c and (b) data for plug 1b

Plug 1b produced the most unstable results (Figure 5.16b), with each of the three data sets giving a different trend. Plug 8c shows a good correlation between KDS1 and KDS2, in the central portion of the curve, but the curvature of the plot seen in KDS2 is not present in KDS1. The three sets of data for each of the four plugs did not match exactly, with either extrapolated Klinkenberg permeability value or curve shape. The majority of curves if seen in a laboratory environment, however, would look convincing due to their smoothness which may lead to the assumption of accuracy to the analysts.

5.3.6.6 Summary of Klinkenberg results

The most important result from the data sets is the non-linear relationship between gas permeability and inverse mean pressure. Especially KDS2 where attempts to find a Klinkenberg permeability by linear extrapolation methods would be highly inaccurate. If high inverse mean pressures were used, negative values of permeability would be calculated. The Klinkenberg permeability calculated from points taken on the plateau region of the curve is approximately 9-17% higher than the permeability calculated on points taken from the low inverse mean pressure values. It would also be difficult to select a suitable inverse mean pressure range from which to estimate Klinkenberg permeability.

It is concluded that permeameters that cannot offer back pressure control other than orifice size for the measurements (SC3) are not reliable for Klinkenberg permeability calculations and give the curvature seen in KDS2. It is also concluded that measurements should be repeated until stable results are given, confining pressure must be noted especially when plugs are to be compared, and small pressure differences can make measurements unstable.

5.3.7 Other core plug measurements

5.3.7.1 Formation resistivity factor (*F*) at ambient pressure

The brine concentrations for each well are listed in Appendix E. The samples were placed in a stainless steel saturator and evacuated over an extended period. Simulated formation brine was introduced at the end of this period, followed by pressurisation at 1000 psig for Group A samples and 2000 psig for Group B samples, to assist penetration. Gravimetric checks were made to ensure complete saturation of the pore space had been achieved. The fully brine saturated plugs were placed in turn between electrodes and their electrical resistance measured (Figure 5.17). The resistivity is calculated using the equation,

$$\rho = \frac{RA}{L} \qquad [5.4]$$

where ρ is the resistivity, R the plug resistance, L its length and A the cross-sectional area. The formation factor was obtained subsequently by the division of the plug resistivity by the resistivity of the brine at the test temperature. F is commonly used to generate Archie's exponent 'm' (see Chapter 2, §2.5.1 for more detail) from the equation,

$$F = \frac{a}{\phi^m} \qquad [5.5]$$

where ϕ is the porosity and m and a are empirical constants.

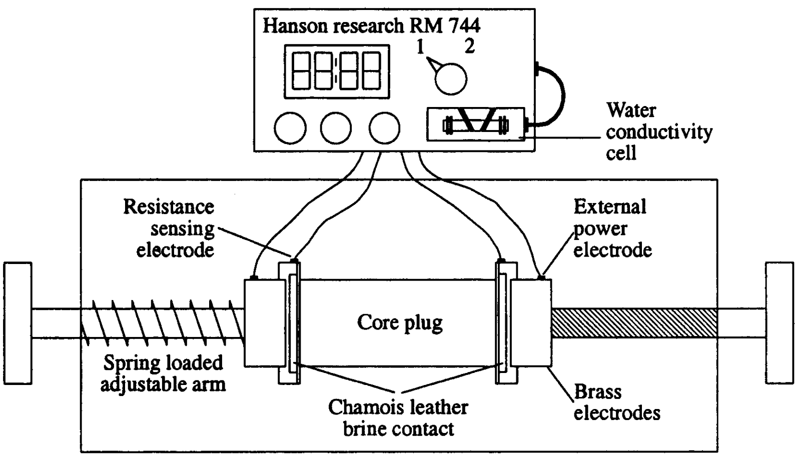

Figure 5.17. A schematic of apparatus used to measure resistivity, using the Hanson resistivity meter RM 774

5.3.7.2 Mercury injection capillary pressure drainage and imbibition

Clean, dry samples were placed in the mercury injection apparatus, evacuated and then completely immersed in mercury. Gas was admitted to the surface of the mercury at a number of pre-determined pressures, promoting mercury to be injected into the sample. The volume injected was corrected to allow for the expansion of the sample chamber and the compressibility of the mercury. On completion of the injection cycle, the procedure was reversed to facilitate the measurement of the imbibition curve. All mercury contaminated plugs were destroyed.

5.3.7.3 Cation exchange capacity

Clean, dry samples were gently disaggregated and passed through a 500 μm sieve. The cation exchange sites were saturated with sodium ions by immersing the samples in sodium acetate, buffered to a pH of 7, for a 15 hour period. The excess sodium acetate was removed by washing the samples in methanol. Potassium chloride was introduced to displace sodium ions by leaching. The amount of sodium displaced was measured by atomic absorption spectrophotometry. The cation exchange capacity, expressed as meq/100g, was used in conjunction with the pore volume and weight of the plug prior to disaggregation, to express the cation exchange capacity as meq/cc pore volume.

5.4 Interpretation of the core plug data

Core plug data acquisition and associated errors are discussed in Section 5.3 along with interpretation of Klinkenberg data (§5.3.6). Section 5.4 aims to interpret these data and investigate how various plug measures relate to each other, with interpretation concentrated on porosity and permeability. Further emphasis is placed on the permeability-porosity relationship and how best to understand this empirical relationship using all of the core plug data. The formation resistivity factor is discussed in Section 5.4.4, with the work biased towards understanding the permeability and porosity parameters. The results and interpretations obtained within Section 5.4 are referenced to published petrophysical results.

5.4.1 Permeability

Four types of permeability measurement are used in this study, brine permeability (§5.3.4), gas permeability (§5.3.5), Klinkenberg permeability (§5.3.6) and image permeability (§6.2.5.5). The three permeabilities investigated in this chapter are measures of transport properties, but all will give different values of plug permeability as they are different experiments. However, Figure 5.18, 5.19 and 5.20 have significant relationships demonstrating that the three permeability measurements are comparable.

(i) Gas permeability compared with brine permeability

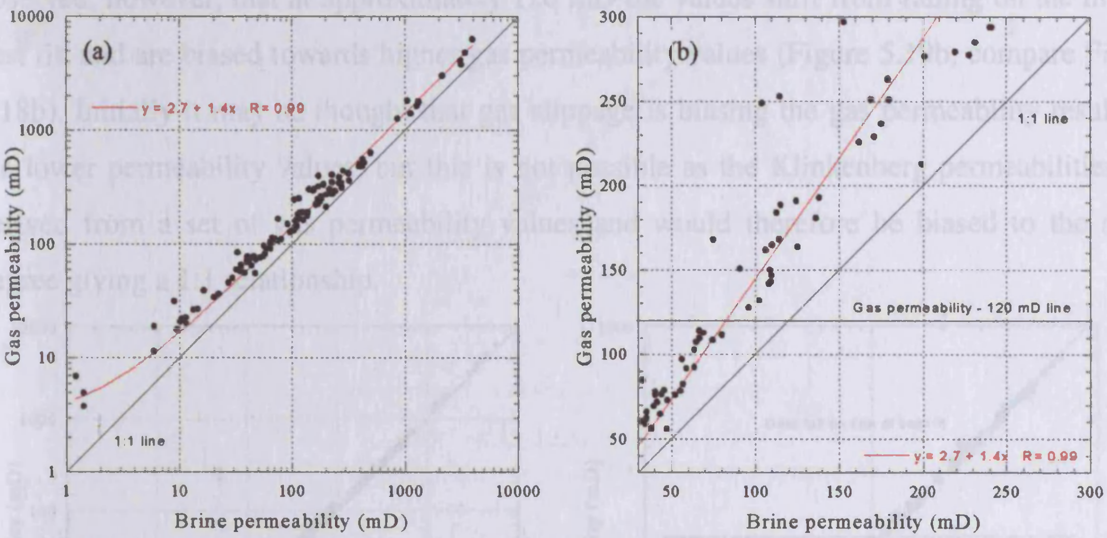

Figure 5.18. Gas permeability versus brine permeability (a) for the entire data set (b) for a section of permeability values between 30-300 mD, to demonstrate the apparent shift in the data

Gas permeability is expected to be larger than liquid permeability, especially at low permeabilities due to the ease of gas flow through an irregularly surfaced tortuous path, compared to a liquid. Figure 5.18a demonstrates this fact and the existence of a significant relationship between the gas and brine permeability measures. The line of best fit for this data gives an estimation of the difference in values between the two permeabilities. Gas permeability is approximately 1.4 times greater than brine permeability, which could have large effects on reservoir model calculations. It is observed by comparison of a portion of the data with the 1:1 line that the data does not have a linear relationship (Figure 5.18b). At an approximate gas permeability of 120 mD there is a step in the data, above this step the line of best fit has the same gradient of 1.4, but below 120 mD the points fall away from the 1:1 line so that all the gas permeability values are larger comparatively ($k_{gas} = 1.4k_{brine} + 8.5$) than above the line ($k_{gas} = 1.4k_{brine} + 3.9$). A similar result was observed by Muskat (1937) and investigated by Klinkenberg (1941). The result is thought to be due to gas slippage (§2.2.2.2) playing a significant role in the low permeability plugs.

(ii) Gas permeability compared with Klinkenberg permeability

Klinkenberg permeability is generated from a series of gas permeability measurements made at increasing mean pressures (§5.3.6). Permeability decreases with every increase in mean pressure (§2.2.2.2), and extrapolation of the data to infinite mean pressure gives the Klinkenberg or 'liquid' permeability. It is therefore no surprise that the gas permeability values are greater than the Klinkenberg permeability values (Figure 5.19a). It is again observed, however, that at approximately 120 mD the values shift from falling on the line of best fit, and are biased towards higher gas permeability values (Figure 5.19b, compare Figure 5.18b). Initially it may be thought that gas slippage is biasing the gas permeability results at the lower permeability values, but this is not possible as the Klinkenberg permeabilities are derived from a set of gas permeability values and would therefore be biased to the same degree giving a 1:1 relationship.

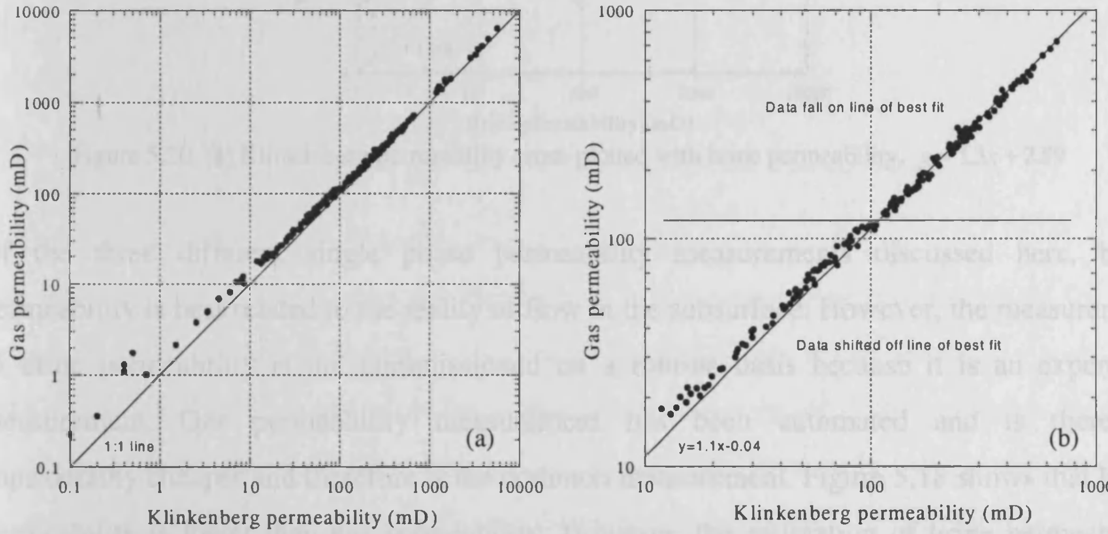

Figure 5.19. Gas permeability cross-plotted with Klinkenberg permeability for, (a) the entire data set and (b) to demonstrate the shift in the data at approximately 120 mD, $y = 1.1x - 0.04$

(iii) Klinkenberg permeability compared with brine permeability

Klinkenberg permeability is in theory the equivalent of an inert liquid permeability. In a comparison of Klinkenberg permeability with brine permeability, the brine permeability value is expected to be less. The result is as expected (Figure 5.20), because an inert fluid by definition will have no interaction with the core plug, whereas brine may experience a number of flow disturbances such as friction, turbulent flow and fluid-rock reactions, all decreasing the permeability of the plug to brine. The Klinkenberg permeability is approximately 1.3 times greater than the brine permeability value, where again the difference in permeability is larger in the low permeability plugs. Sinclair and Duguid (1990) found similar results to those shown in Figure 5.20, and state that acceptable matches between liquid and Klinkenberg permeability are only found with inert media (e.g. glass filters) and refined mineral oils. They found that measured brine permeability in real reservoir rock, where the fluid can interact with the rock solid surfaces, are typically two to three times lower than the equivalent Klinkenberg data.

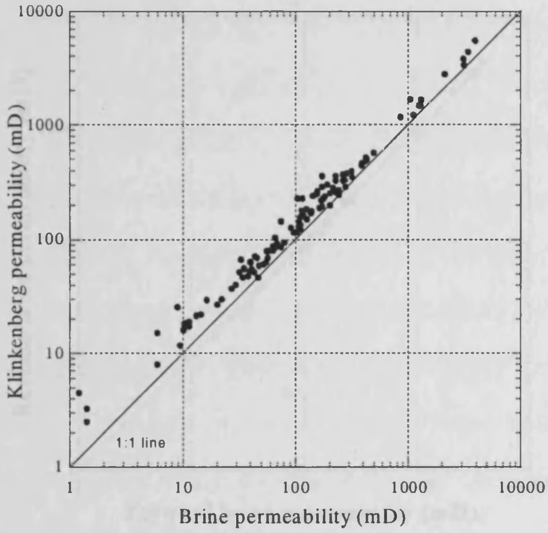

Figure 5.20. (a) Klinkenberg permeability cross-plotted with brine permeability, $y = 1.3x + 2.89$

Of the three different single phase permeability measurements discussed here, brine permeability is best related to the reality of flow in the subsurface. However, the measurement of brine permeability is not commissioned on a routine basis because it is an expensive measurement. Gas permeability measurement has been automated and is therefore considerably cheaper and therefore is the common measurement. Figure 5.18 shows that brine permeability is lower than gas permeability. However, the estimation of brine permeability from gas permeability is not recommended due to the scatter in the data. The same can be said for prediction of brine permeability from Klinkenberg permeability.

Inspection of these three data sets and the foregoing discussion demonstrates the difficulties of estimating a reservoirs capacity to flow fluids and thereby generate revenue for the owners. This work is restricted to considerations of single phase flow yet it is acknowledged that in the subsurface the fluid flow is occurring in the presence of multiple fluids. Although there is multi fluid data in the data set it was deemed inappropriate to study this before an insight into the single phase problem had been achieved.

(iv) Reverse brine permeability compared with forward brine permeability

Figure 5.21 is a plot of the forward and reverse brine measurement (§5.3.4.1). The 42 plugs give a correlation coefficient of 1.00 and from this it is concluded that the measurements are repeatable; average percentage error difference is ± 2.8%. More importantly, the data show that there is no significant effect due to mobile fines within the plugs, which would have become apparent from varying flow properties revealed in the forward and reverse directions.

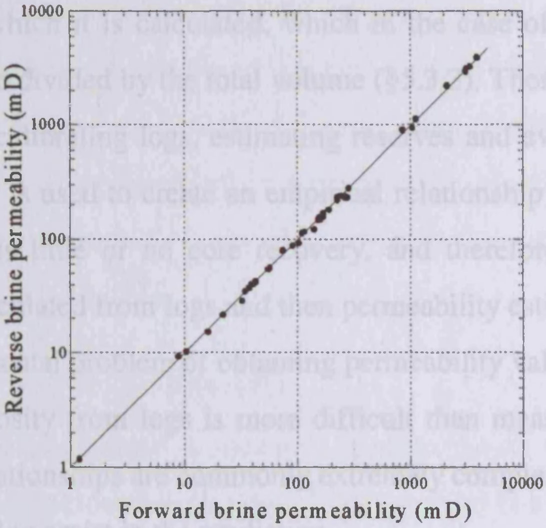

Figure 5.21. Reverse brine permeability against forward brine permeability

(v) Brine permeability versus throughput in forward and reverse directions

Forward and reverse brine permeabilities (§5.3.4.2) are plotted against throughput for two typical plugs from well 6 (Figure 5.22). The permeability values are seen to decrease and stabilise with throughput, and when the measurements are reversed there is either a decrease or increase in the value of permeability, which does not have to be within the range of permeability values for the initial forward throughput measurements. It is unclear from these results whether there is a reaction occurring between the two brines, or whether the variation in permeability values is due to the fluid flow stabilising with throughput. The movement of fines is dismissed as the cause of permeability variation in reverse flow from the results obtained in *(iv)* above.

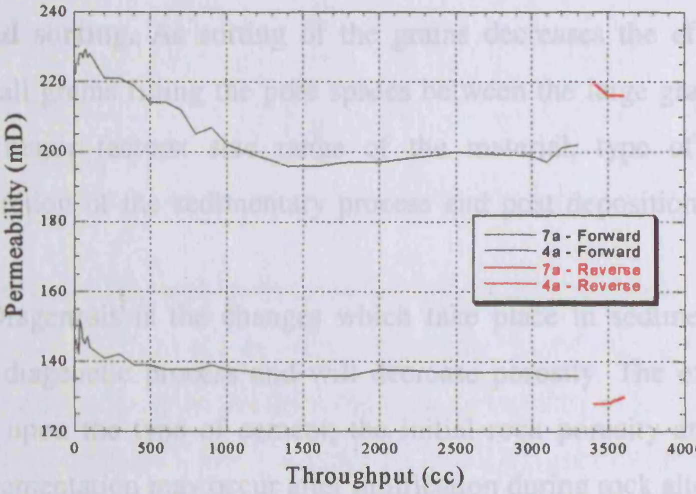

Figure 5.22. Brine permeability against versus throughput for both forward and reverse directions, plugs 4a and 7a from well 6

5.4.2 Porosity

Porosity is defined as pore volume divided by total plug volume. Specifically, it is defined by the measurement from which it is calculated, which in the case of this study is the area of interconnected pore space divided by the total volume (§5.3.3). Thomas and Pugh (1989) note the uses of porosity for calibrating logs, estimating reserves and evaluating reservoir quality and description. Porosity is used to create an empirical relationship with permeability so that in regions where there is little or no core recovery, and therefore permeability cannot be measured, porosity is calculated from logs and then permeability estimated from the empirical relationship. The fundamental problem of obtaining permeability values by this method is that calculating effective porosity from logs is more difficult than measuring it with core. Also, porosity-permeability relationships are commonly extremely complex and it is often necessary to develop a facies model to assist in the prediction.

Fraser and Graton (1935) studied the limits of porosity values using sphere packs. The porosity of an unrealistic system of a cubic sphere pack is 47.6%, and the rhomobohedral system, has a porosity of 25.9%, both are independent of bead size. So in theory a fine, well sorted, rounded sandstone, will have the same porosity as a coarse, well sorted, rounded sandstone. The porosity of reservoirs can be highly variable, Tiab and Donaldson (1996) state that the porosities of petroleum reservoirs range from 5% to 40% but most frequently are between 10% to 20%. The porosity data used in this study have an average value of 24.7%.

Three factors governing the magnitude of porosity in clastic sediments are distinguished below (adapted from Tiab and Donaldson, 1996):

(i) **Grain size and sorting.** As sorting of the grains decreases the effective porosity will decrease, with small grains filling the pore spaces between the large grains. Sorting depends on at least five major factors: size range of the material, type of deposition, current characteristics, duration of the sedimentary process and post depositional re-working of the rock.

(ii) **Diagenesis.** Diagenesis is the changes which take place in sediments after deposition. Cementation is a diagenetic process and will decrease porosity. The extent of the porosity decrease depends upon the type of cement, the initial rock porosity and the particle shape (Dullien, 1992). Cementation may occur after lithification during rock alteration by circulating groundwater.

(iii) **Compaction.** Compaction tends to close voids and squeeze fluid out to bring the mineral particles closer together, especially in the finer-grained sedimentary rocks. Compaction is also a function of packing. With increasing overburden pressure, poorly sorted angular sand grains show a progressive change from random packing to a closer packing. Some crushing and plastic deformation of the sand particles may occur, thus decreasing porosity. Tiab and Donaldson (1996) state that compaction is negligible in closely packed sandstones or conglomerates, but in general porosity is lower in deeper, older rocks, but exceptions to this basic trend are common.

5.4.3 The permeability-porosity relationship

The permeability-porosity relationship is very important and needs to be well understood and defined for use in the prediction of permeability from log data. The gas permeability-porosity relationship for this reservoir (Figure 5.23a) has a correlation coefficient is 0.32 which although is significant at a probability level of 0.01, any value of porosity could have an associated permeability value over an order of two magnitudes; this is poor for permeability prediction purposes. Figure 5.23b is a plot of Klinkenberg permeability against porosity which is just as poor for prediction purposes.

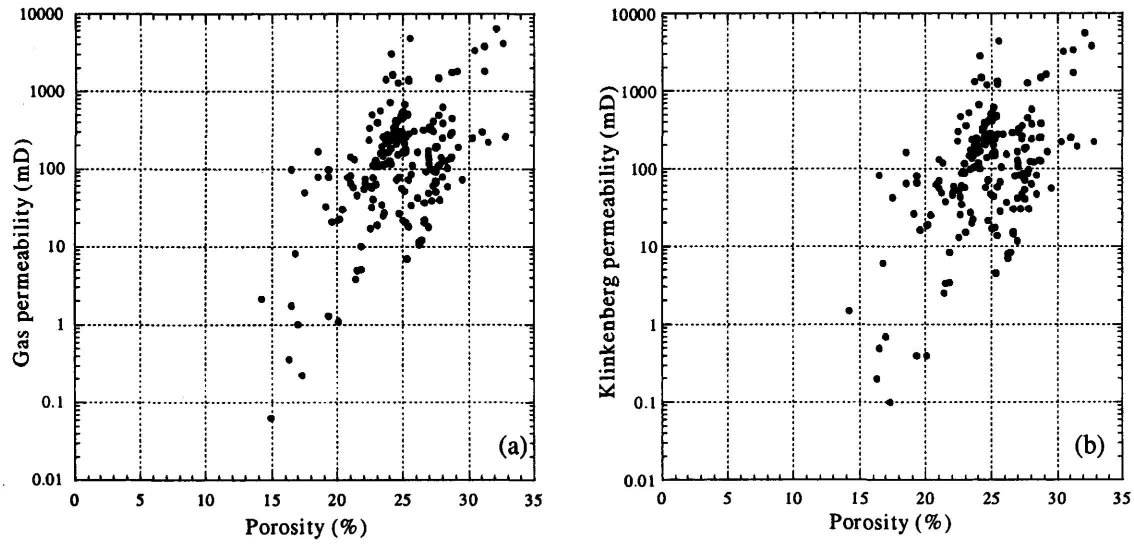

Figure 5.23. (a) Gas permeability against plug porosity, (b) Klinkenberg permeability against plug porosity

Utilising the correlation between permeability and porosity requires the plug volume to predict the effective cross-sectional area for conducting fluids. Porosity, however, is related only to storage capacity, and not to the dynamic flowing capacity of the pore system (Katz and Thompson, 1986). Therefore, the permeability-porosity relationship can be poor for permeability prediction as in the case of this reservoir. Basan et al. (1997) state that the permeability-porosity relationship is only good when pore throat size approaches the pore body size, as in the case of capillary models.

Klinkenberg permeability has been plotted against plug porosity, with plug lithological descriptors as defined in Section 3.2 distinguished on the plots. These plug descriptions are qualitative, with words such as 'common' and 'abundant' used to quantify the amount of minerals present in a plug. Reference is also made to published petrophysical results. The permeability-porosity relationship of this reservoir is investigated here under a series of headings; *(i)* location, *(ii)* facies, *(iii)* grain size and *(iv)* grain shape.

(i) Location

Archie (1950) wrote; 'The scattering is great, [with regards to the permeability-porosity relationship for some reservoirs] but it must be remembered that the only reason a trend exists at all is that the formation as a whole was deposited under a similar environment; individual parts (local environment) may differ from the whole.' Adapting Archie's statement, the permeability-porosity plot for this reservoir was grouped according to position (i.e. by well, Figure 5.24), this model makes the large assumption that the depositional environment varies only laterally and not vertically in terms of local environment, and so is not necessarily realistic. Groups do occur within the data (e.g. wells 5 and 9) but no linear permeability-porosity trends.

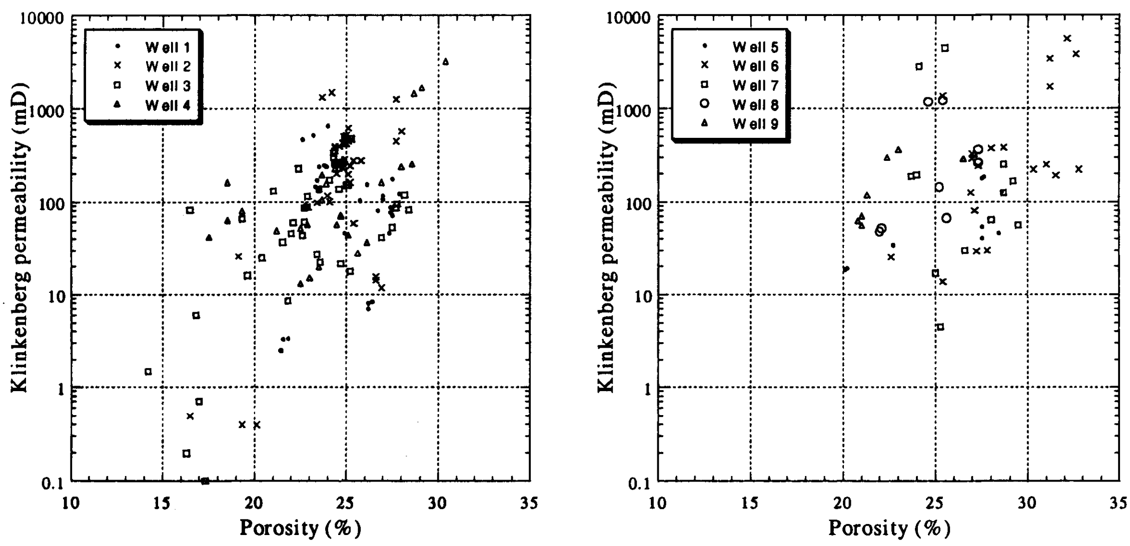

Figure 5.24. Klinkenberg permeability versus plug porosity with wells distinguished

(ii) Facies

The facies used in Figure 5.25 are those defined in Internal Report 1 (§4.4) and represent a depositional environment within the deep water turbidite channel/fan system. The facies groups are mostly restricted to bands of permeability and/or porosity, but none of the facies produce a strong trend for permeability prediction. SC4 also investigated lithological facies within the reservoir, using a total of 124 thin sections and 30 combined SEM/XRD samples to represent the petrographic data set from wells 1, 2, 3, 4, 5, 10 and 11. A series of conclusions were drawn from this data which are used in this section as a starting point for investigations. A problem associated with using these results and conclusions is that they are classified in terms of SC4 facies, and not the facies defined in Internal Report 1*.

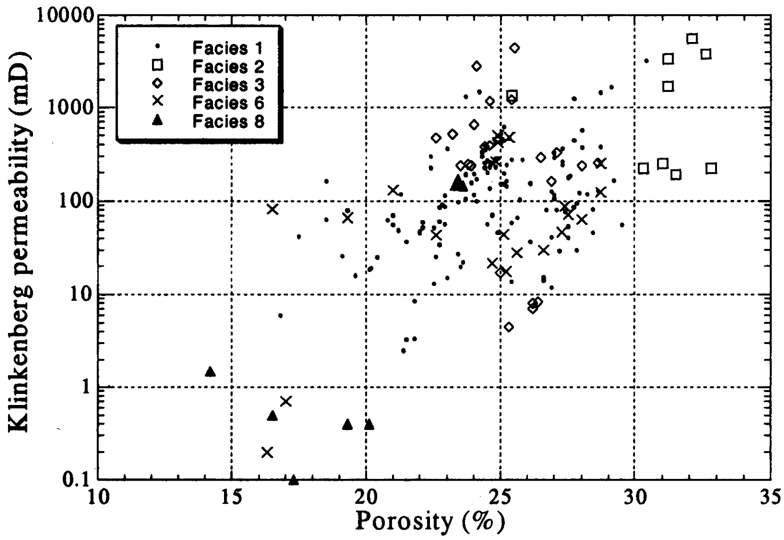

Figure 5.25. Klinkenberg permeability versus plug porosity, with facies defined

SC4 studied controls on permeability and porosity, concluding that, 'Field wide permeability [statistical] means show a close relationship with facies and therefore primary textural characteristics (detrital mud, grain size and sorting).' Figure 5.25 uses facies (defined in Internal Report 1) to constrain the permeability-porosity relationship for this reservoir, they offer none of the constraint which was presumably revealed by SC4 facies. SC4 also concluded that in clean reservoir sands, authigenic clay content (particularly indeterminate clays determined mainly as chlorite in XRD) is the main control on permeability distribution. Chlorite is more common in the bedded facies associated with mudstones and in the facies with higher primary detrital clay contents. These conclusions are supported by the Internal Report 1 facies used in Figure 5.25. Facies, 1 and 2 are not associated with mudstone and show relatively high permeability values as does facies 3. Facies 3 is a massive sandstone with thin mudstone beds, and so it is assumed the mudstone has not been sampled from this facies group. Facies 6 is interbedded laminated sandstones and mudstones, and so it is suggested that

* The internal reports are held at Enterprise Oil plc.

the two low permeability plugs shown in the facies group are taken from nearer the mudstone end member, the others are all from more sandstone rich samples of this facies. Similarly, with facies 8 (deformed intercalated sandstone and mudstones), the five low permeability plugs are expected to be closer to mudstone, and the three high permeability plugs sandstone.

The core plug photographs and descriptions provided by SC2 were used to verify the assumptions on mudstone content in facies 6. All of the facies 6 plugs were described as sandstone, with no added mention of mudstone in the low permeability plugs. However, the low permeability plugs were associated with "common clay" in the plug description and the high permeability associated with "pore lining clay". Different types of clay are looked at briefly in Chapter 2 (§2.4.2) and Chapter 6 (§6.4.1). A likely explanation is that the pore lining clay is less obstructive to fluid flow than pore filling clay.

(iii) Grain size

Chilingarian (1963) showed that the grain size of sandstones influences the relationship between permeability and porosity, for the rock samples used in his study (Chapter 2, Figure 2.3). The permeability-porosity distribution obtained from this reservoir for sandstone with different grain sizes reveal similar results to those of Chilingarian (1963) but are not as constrained. Figure 5.26 shows that the large grains are associated with higher permeabilities, which is expected and logical as medium to coarse grains will have larger pores and therefore normally higher permeability than very fine to fine grains.

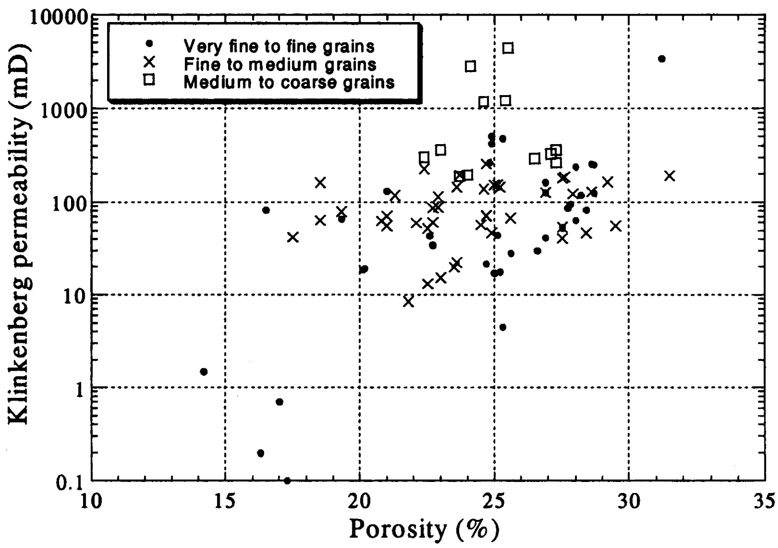

Figure 5.26. Klinkenberg permeability versus plug porosity, with grain sizes defined (89 points on this plot)

It is likely that the additional variable of sorting would further refine the relationships seen in Figure 5.26 (Pettijohn, 1975). Figure 5.27 gives a summary of the effects of grain size and sorting on porosity and permeability, further explanation is given in Chapter 2 (§2.2.1 and 2.2.2).

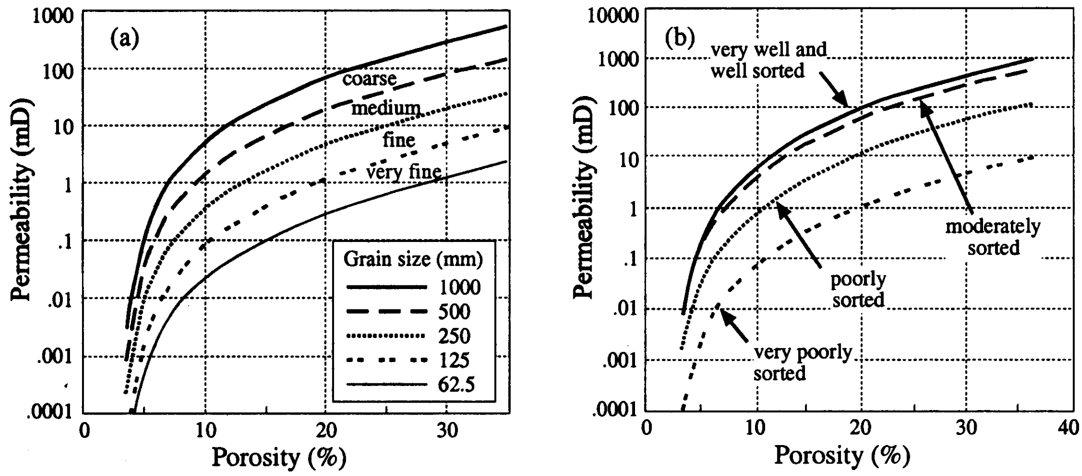

Figure 5.27. (a) The effect of grain size and sorting variation on model-derived porosity-permeability trends and calculated trends for different grain sizes: (b) empirically-derived trends for different sorting classes, (after Cade et al., 1994)

An extended set of grain size ranges is examined in Figure 5.28. It was expected that as the range of pore sizes increased (i.e. sorting decreased) the porosity would decrease due to pores being in-filled with more grains, such a result is not apparent in this figure. Figure 5.30 shows similar data with similar results, but here it is coarse grained matrix being infilled.

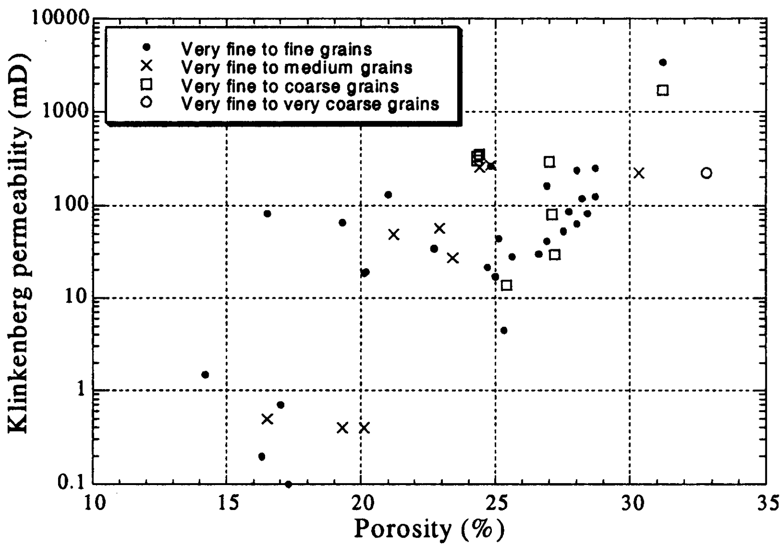

Figure 5.28. Klinkenberg permeability versus plug porosity, with grain sizes defined (46 points in this plot)

Figure 5.29 is similar in type to that of Figure 5.28 but the given grain size ranges are smaller, The fine to medium grained plugs are observed to have permeability values constrained to an order of magnitude.

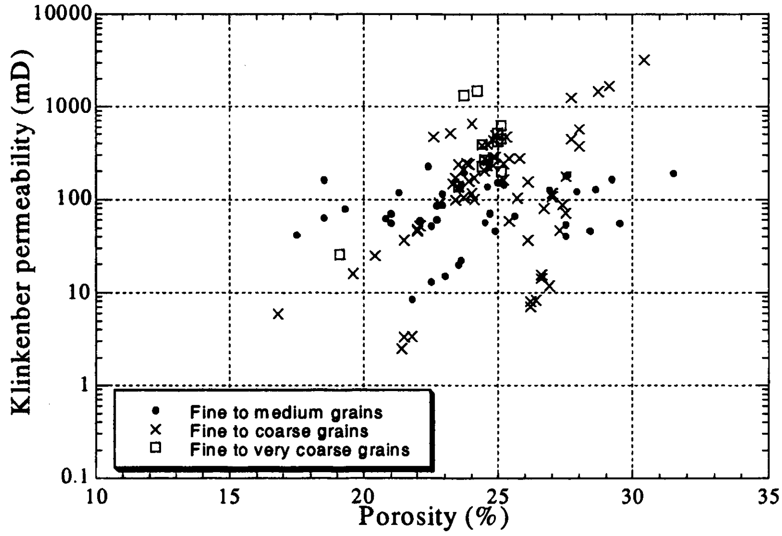

Figure 5.29. Klinkenberg permeability versus plug porosity, with grain sizes defined

Anomalies away from a trend could be due to secondary porosity development or overprint of authigenic minerals.

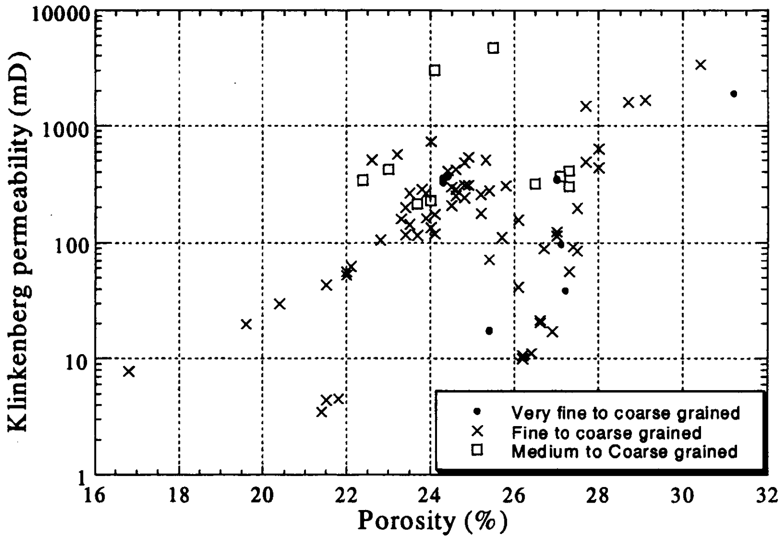

Figure 5.30. Klinkenberg permeability versus plug porosity, with grain sizes defined

Grain sorting data (Figure 5.31) were adapted directly from the core plug descriptions and are comparable to the grain size ranges used in Figures 5.28 through 5.30. Figure 5.31 contains three points of very well sorted data plotted together, however from the data base it was discovered that points are from the same depth in the same well, and so no conclusions can be drawn from them.

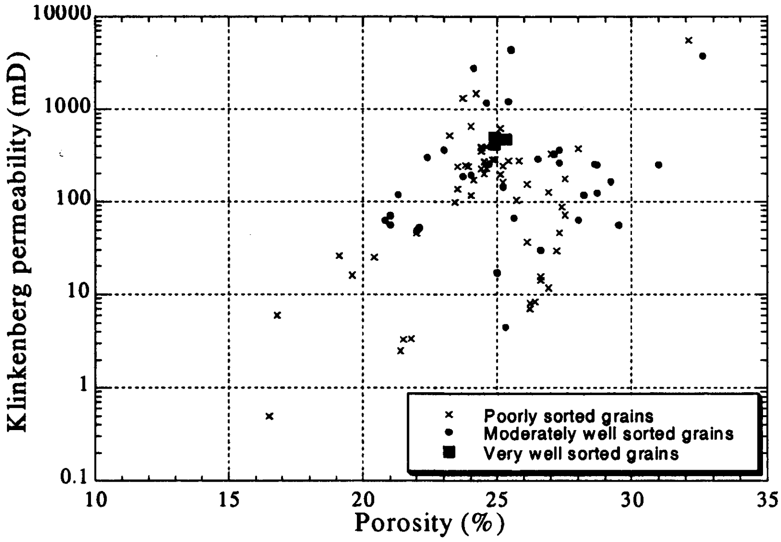

Figure 5.31. Klinkenberg permeability against plug porosity, with grain sorting defined (98 points)

(iv) Grain shape

Figure 5.32 looks at grain shape, and it is observed that if the four low permeability plugs are excluded from the interpretation there is no obvious relationship.

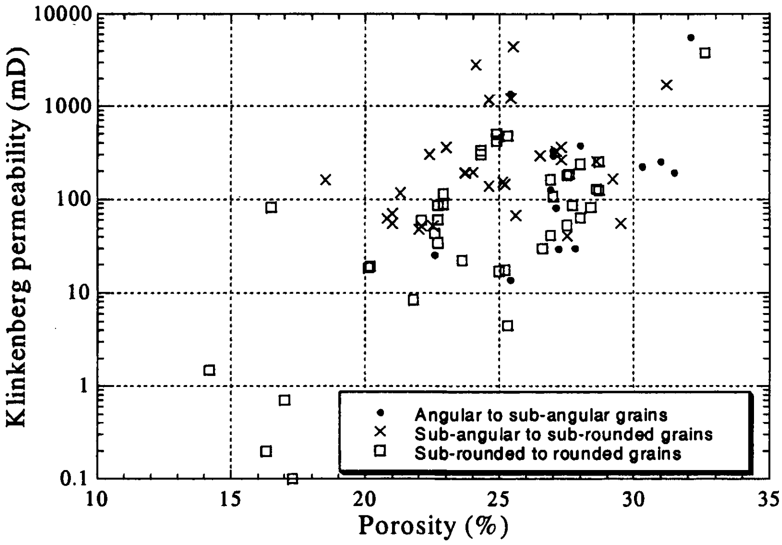

Figure 5.32. Klinkenberg permeability versus plug porosity, with grain shape defined (83 points)

Figure 5.33 examines grain shape ranges, and maybe shows that the larger the grain shape range the higher the porosity and permeability, a possible explanation for this observation is that poorly sorted grain shapes find it more difficult to compact and 'fit' together. Figure 5.34 demonstrates this theory pictorially.

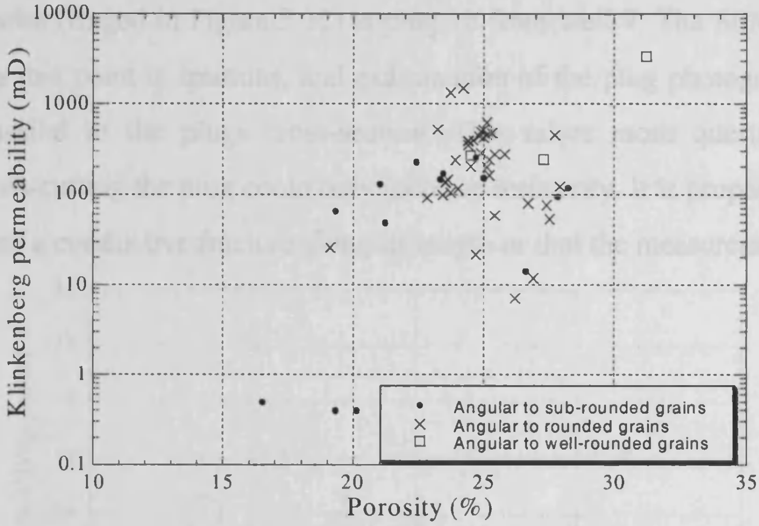

Figure 5.33. Klinkenberg permeability versus plug porosity, with grain shape defined (71 points)

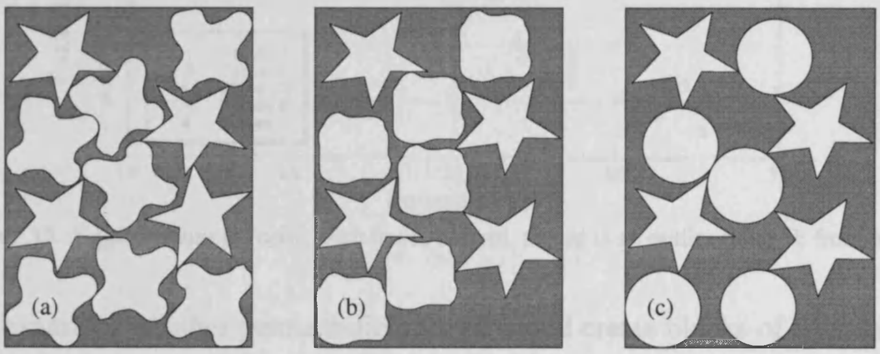

Figure 5.34. A pictorial representation of grain shape ranges. (a) Angular to sub-rounded grains, (b) angular to rounded grains and (c) angular to well-rounded grains.

5.4.4 Formation resistivity factor

Formation resistivity factor (*F*) is a dimensionless quantity which is defined only for porous matrices of negligible electrical conductivity. 'In the absence of surface conduction its value is uniquely determined by pore geometry. The influence of pore structure on the electrical conductivity may be divided into two contributions: the reduction of the cross section available for conduction and the orientation and topography of the conduction pores' (Dullien, 1992).

A plot of *F* against plug porosity was examined with facies distinguished (Figure 5.35), and it was observed that there is a significant trend between *F* and porosity (r=-0.91) which is stronger than the relationship between permeability and porosity. It is proposed that this is due to electrical conductivity using a wider range of pore spaces than permeability, suggesting a greater insensitivity to pore morphology than that of permeability. Facies 2 (cross stratified sandstone) are observed to be conductive plugs, and may therefore have high permeabilities, Figure 5.36 proves this to be the case with four of the six plugs.

The spurious point (ringed in Figure 5.35) is plug 1b from well 7. The SEM images gave no clues as to why this point is spurious, and examination of the plug photograph revealed fine laminations parallel to the plugs cross-section. This raises more questions however, as laminations cross-cutting the plug could only increase resistivity. It is proposed therefore, that the plug contains a conductive fracture along its length or that the measurement is erroneous.

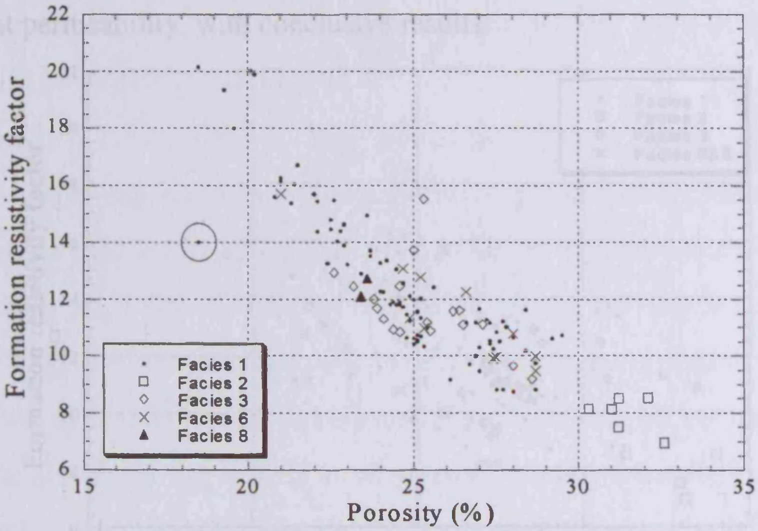

Figure 5.35. F against plug porosity, with facies defined, ringed is an outlier (plug 1b from well 7)

Figure 5.36 examines whether permeability ranges would create blocks of data within the F-porosity plot. It is observed that the F-porosity plot is split into a series of crude bands for different permeability ranges, demonstrating the relationship between the three parameters.

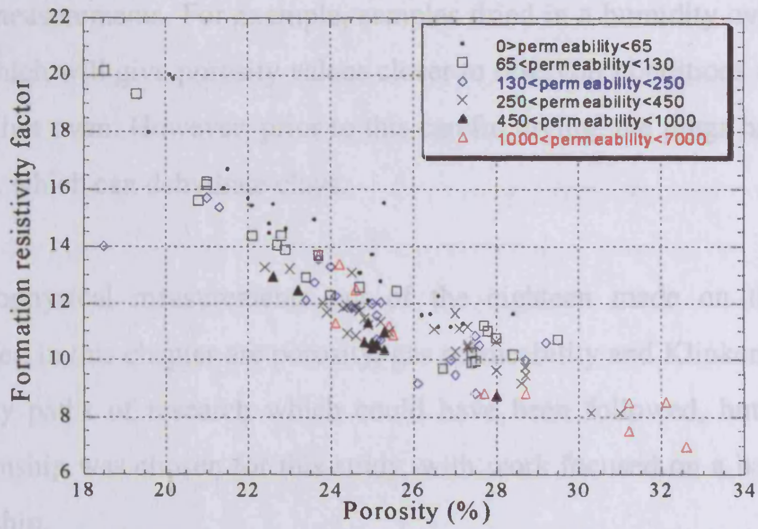

Figure 5.36. F versus plug porosity, with gas permeability ranges defined

Figure 5.37 examines F against gas permeability and there is a significant correlation between the two parameters (r=-0.55 for 122 points), facies is also distinguished. There are no significant relationships between F and permeability for facies 1, 2, 3, and 6&8, r=-0.34,

-0.15, -0.19 and -0.25 respectively. It was hoped that this plot could be used as a descriptive factor, and may even categorise the F and permeability plot, this was not the case as the data were not constrained by facies. It is concluded that facies defined in Internal Report 1 are of very limited use in characterising the permeability, porosity or F. In Chapter 7 (§7.4.5.1) the more specific descriptor of area *clay* (defined by image analysis) is used to characterise this plot of F against permeability, with conclusive results.

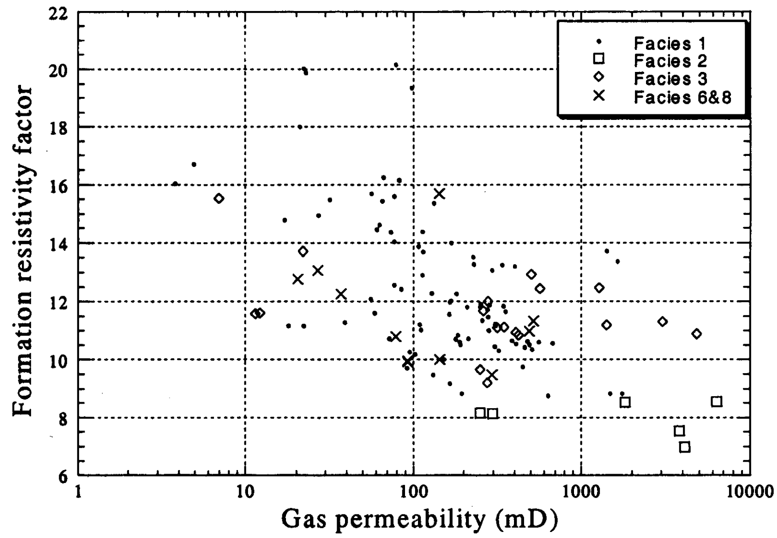

Figure 5.37. F against gas permeability with facies distinguished

5.5 Summary

Core plug sample preparation is discussed and how these preparations play a role in petrophysical measurements. For example, samples dried in a humidity oven may retain clay bound water which will give porosity values closer to reservoir conditions than plugs dried in a conventional hot oven. However, prior to this careful drying, the plugs had been cleaned in boiling toluene, which can dehydrate clays.

The only petrophysical measurements out of the eighteen made on the plugs that are significantly used in this chapter are porosity, gas permeability and Klinkenberg permeability. There are many paths of research which could have been followed, but the permeability-porosity relationship was chosen for this study, with work focused on a better understanding of this relationship.

The permeability-porosity (k-ϕ) relationship for this reservoir is very weak for use in the prediction of permeability from logs, as each value of porosity has at least two orders of magnitude of permeability associated with it. To try and improve the k-ϕ relationship for permeability prediction purposes four constraining parameters were introduced, *location, facies, grain size,* and *grain shape*. Within this reservoir grain size splits the data set into permeability bands, with large grains being associated with large permeabilities and small grains with lower permeabilities. Grain shape and grain size ranges (sorting) gave no strict conclusions, but generally the more sorted a sandstone the higher its permeability and/or porosity. It is concluded that facies defined in Internal Report 1 are of very limited use in characterising the permeability, porosity or F.

Three sets of Klinkenberg permeability data were compared. On examination of these three data sets it can be concluded that the kink in the curves is real, although more pronounced in the data collected at SC3 (KDS2). The results of this study are important, as the non-linear relationship between gas permeability and inverse mean pressure means that calculation of Klinkenberg permeability by linear extrapolation methods can be inaccurate, especially in KDS2. It is concluded that the lack of back pressure control other than orifice size for the measurements made at SC3 are responsible for the extreme curvature seen in KDS2. It is also concluded that all Klinkenberg measurements should be repeated until stable results are given, confining pressure must be noted especially when plugs are to be compared, and small pressure differences can make measurements unstable. The curve shape was not due to the movement of pore fines as the results were repeatable.

None of the three data sets matched in terms of either extrapolated Klinkenberg permeability value or curve shape. The majority of curves if seen in isolation, however, would look convincing due to their smoothness; this is suspected as being the result of insufficient time being allowed for gas flow to stabilise. The gradients of the curves increase with the permeability of the plugs. This result is expected as the gradients of the slope are equal to the Klinkenberg permeability multiplied by the *b*-factor (Eq. 2.14), and so as Klinkenberg permeability increases so will the gradient. However, this is a general rule, as the same Klinkenberg value can have varying curve gradients and therefore a varying *b*-factor.

Brine permeability is closer to *in situ* reservoir permeability than gas permeability, and is repeatable (§5.4.1). However, gas permeability measures are taken routinely and brine are not, for the simple reason that the gas measurement is easier. Gas, brine and Klinkenberg permeabilities have been compared. Gas permeability, as expected, is larger than brine permeability, due to the relative ease of gas flow through an irregular surfaced tortuous path, compared to a liquid. At low permeabilities this is especially true which is thought to be due to gas slippage (§2.2.2.2) playing a significant role. As Klinkenberg permeability is an extrapolated value from a series of decreasing gas permeability measurements made at increasing mean pressures (§5.3.6), gas permeability values are greater than Klinkenberg permeability values.

Brine permeability as expected is less than Klinkenberg permeability. Klinkenberg permeability is the equivalent of an inert fluid permeability, which by definition will have no interaction with the core plug, whereas brine may experience a number of flow disturbances such as friction, turbulent flow and fluid-rock reactions, all decreasing the permeability of the plug to brine. An experiment of brine versus throughput for two brine solutions was made, but it is unclear whether there is a reaction occurring between the two brines, or whether flow is just stabilising with time.

The comparison of the three permeability measurements demonstrates the difficulties associated with measuring a permeability which is representative of the reservoir, and this is without the complications of multiple fluids, which is recommended for further work as the next step in this interpretation.

Formation resistivity factor (F) and plug porosity have a stronger relationship than the relationship between permeability and porosity. It is proposed that this is due to electrical conductivity using a wider range of pore spaces than permeability, suggesting a greater insensitivity to pore morphology than permeability.

CHAPTER SIX

Scanning electron microscopy and image analysis

6.1 Introduction

Thirteen SEM images were collected on each of sixty-three end-trims taken from the core plugs whose porosity and permeability measurements are discussed in Chapter 5. A key to understanding reservoir behaviour is through the study of microscopic pore structure. The practicalities of collecting image analysis data are examined initially in this chapter, including an investigation of errors within the software and in capturing SEM images (§6.2). Section 6.3 discusses consequences of condensing and averaging the image data which is required to generate single values for the image parameters. A qualitative investigation is undertaken on the SEM images (§6.4), prior to a quantitative approach using the image analysis parameters (§6.5).

The term *clay* for the purposes of this study is defined as a specific grey scale range (50-170) on the SEM images, it includes detrital and diagenetic clays, as well as software artefacts such as grain edge effects (§6.2.4.2).

6.2 SEM images and image parameters

A fundamental requirement for quantitative optical microscopy is the production of an image that can be segmented into pore and grain phases (Ehrlich et al., 1991b.) There must be adequate intensity contrast between the pore and grain phases to practically achieve this.

6.2.1 Measuring back scattered scanning electron microscope (SEM) images

Back scattered scanning electron microscope (SEM) images were measured by Service Company 1 (SC1), using a 25 kV focused electron beam. Any SEM image is a function of the specimens atomic number contrast, and results are displayed as photographs, which can be quantified using 256 grey scale increments. Black is a grey scale of zero and is associated with low atomic numbers, whereas 255 is white and associated with high atomic numbers (Figure 6.1).

G

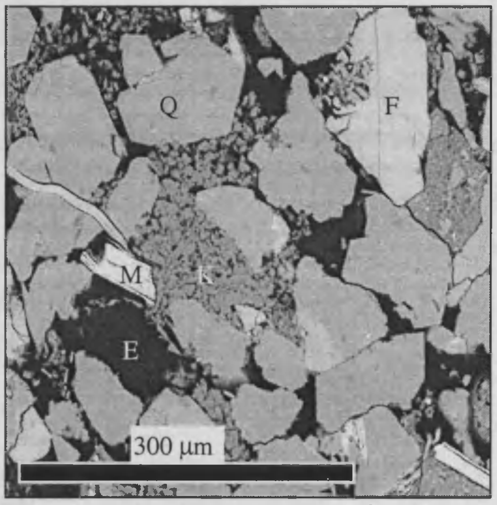

Figure 6.1. Example SEM image to demonstrate the quantification of minerals into grey scales. Key: Q = quartz, E = epoxy (pore space), F = feldspar, K = kaolinite and M = mica

Prior to measurement, the magnification and number of views to be digitised per section must be decided upon, since the higher the magnification, the higher the resolution (i.e. smaller pixel size) but the smaller the field of view (Ehrlich et al., 1991b; Ruzyla, 1984). The choice of magnification made by SC1 was x30 and x150, which strikes a balance between data resolution and data volume (i.e. cost). The grey scale is calibrated for each mineral using a set of mineral standards supplied by the Natural History Museum, London. SC1 noted that this type of methodology provides an estimation of mineralogy, and that the peaks of different minerals in the histogram can be very close to each other and on occasions difficult to differentiate.

6.2.2 Arrangement of SEM images

Thirteen images were measured on each core plug end-trim, eight high magnification images at x150 magnification and five low magnification images at x30. These constitute an image library of 2,662,400 pixels of information to describe the character of a single core plug. The grid used for the position of the images is shown in Figure 6.2.

The grid shown in Figure 6.2 was not strictly adhered to if the section of end-trim which lay in the region to be taken was not showing suitable properties. For example, if the image location was in a region of an excessively large mineral grain, pore space or gas bubble, the image would be moved to another position to avoid these potentially problematic images. Data acquisition was only truly random when the images were not moved away from the fixed grid.

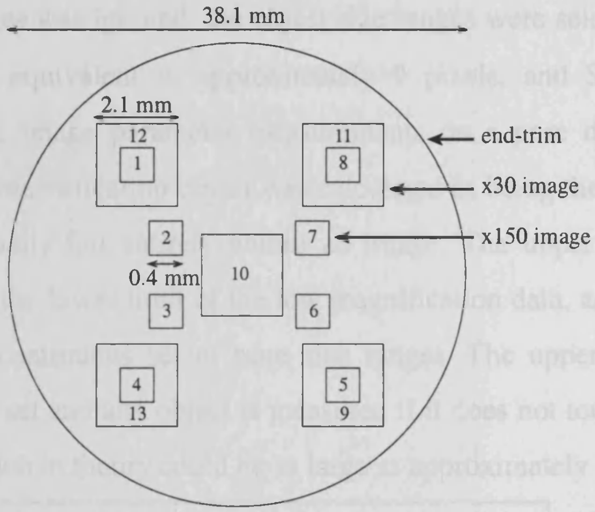

Figure 6.2. Diagrammatic representation of the position of the thirteen images (5 low and 8 high magnification) on the end-trim section of a plug

6.2.3 The image analysis package

Analysis of the SEM images was performed using software from Foster Findlay Associates*, called PC_Image - image analysis and petrophysical pore analysis for Windows and VGA. The software was modified by SC1 for this study. Image analysis, here, is the process in which 2D pictures (SEM images) are analysed by counting the number of pixels within different grey scale ranges. Errors and uncertainties have been found associated with the software package.

The image analysis package calculates descriptors such as length and perimeter of any 2D object, within the chosen grey scale range, these are called the image parameters throughout this study. The pore spaces, which are impregnated with epoxy during sample preparation, are considered the measurable object for the purpose of this project. The epoxy has a low atomic number, and an approximate grey scale value of 39. A selected object (pore) has 64 vectors distributed radially within it to calculate the descriptors (pers. comm., SC1). Table 6.1 shows the grey scale ranges assigned by SC1 to various mineralogical phases within the SEM images. The grey scale 51-170 is called *clay*, this range includes detrital and diagenetic clay as well as artefacts of the software such as grain edge effects (§6.2.4.2). The majority of clay present within the images falls within this range, but not all.

The high magnification data contains information from objects (pores) within a size range of 13-1334 μm^2, while in the low magnification images the object must be >1334 μm^2, any

* Foster Findlay Associates Ltd., Newcastle Technopole, Kings Manor, Newcastle upon Tyne, U.K.

object not within these ranges was ignored; the object size ranges were selected by SC1. The lower limit of 13 μm^2 is equivalent to approximately 9 pixels, and SC1 considered it impossible to take accurate image parameter measurements on a pore defined by so few pixels, the upper limit high magnification object was calculated as being the maximum size at which the pores would usually fall entirely within an image. The upper limit in the high magnification data, defined the lower limit of the low magnification data, as the two data sets were taken to represent a continuous set of pore size ranges. The upper limit of the low magnification objects is not set and any object is measured if it does not touch more than one side of the image frame, which in theory could be as large as approximately 1 mm^2.

Phase	Grey Level
Pore (epoxy)	0-50
Clay	51-170
Quartz	171-202
Feldspar	203-220
Carbonate	221-239
Anhydrite	240-249
Iron minerals	250-255

Table 6.1. Grey scale ranges assigned to the seven different mineralogical phases. (*clay*, includes detrital and diagenetic clay as well as artefacts of the software such as grain edge effects.)

6.2.4 Errors associated with the resultant image parameters

Errors associated with SEM images and the image analysis package can only be evaluated qualitatively, which precludes the estimation of meaningful error bars. Errors associated with the data are summarised below:

6.2.4.1 End-trim induced errors

End-trims are taken from core plugs and as such are subjected to the same cleaning processes as the plugs (§5.3.2), thus, the disturbance or removal of clay material may already have occurred. End-trim preparation includes the impregnation of epoxy, and SC1 suggested that the more friable a rock, the more the grains within a plug will spread when the end-trim is prepared. The polishing of the sample may cause edge effects on the minerals where softer minerals will be preferentially thinned, creating an uneven surface, thus hindering the application of an even carbon coating. These topics are difficult to quantify and there is little information available.

Figure 6.3 shows the potential of an image to give unreal values of pore area. The two black regions in the lower portion of the image are not natural pore spaces. It was identified that material was 'plucked out' during the polishing of the end-trims. If this effect was more susceptible within some plugs rather than others, image analysis results would be biased.

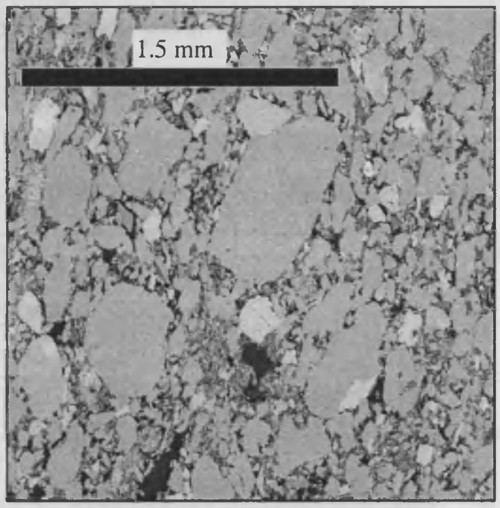

Figure 6.3. Well 1, plug 4a, image 10, the two large black regions are thought to result from end-trim preparation

6.2.4.2 PC_Image errors

The errors in this section are qualitative, they do show however that only carefully selected data can be used for further interpretation. PC_Image has four potential errors:

(i) A scaling error may have been introduced during data transfer between the SEM and the computer for pixel counting exercises.

(ii) The random error associated with the choice of area imaged (§6.2.2).

(iii) Does the software select the various grey levels of the images in a repeatable manner and associated with the 'correct' mineral phase?

(iv) Are the equations (e.g. the area equivalent radius calculation) that the package uses correct?

SC1 have confirmed that the calibration of the SEM image onto the monitor is correct. A variation in grey scale could occur due to instrument conditions, however there is little information available on this topic.

A simple test image of a grid of boxes filled with different percentage grey scale values (Figure 6.4) was designed to examine the reliability of the software's pixel counting and grey scale identification. Each equally sized box gives a 5% increase in grey scale, the boxes were drawn using Aldus Freehand (version 5.5) and therefore, the limitations of this experiment lie within the accuracy of this software. The grid was loaded into PC_Image which allows regions of interest (ROI) to be selected. Twenty boxes were selected and the histogram of results (Figure 6.5) shows that there is an acceptable correlation between the percentage increase in grey level within the image and the even spacing of the histogram peaks from 0 to 256 on the grey level scale. The histogram peaks have a similar height which indicates each box is being counted individually, the exception being the grey level at approximately 110 where two of the boxes in Figure 6.4, were not distinguished by PC_Image. In this study the entire scale range of 51 to 170 is classified as *clay* by the software. The calculation of the histogram from the grey boxes was performed several times selecting different boxes, the same results were always obtained.

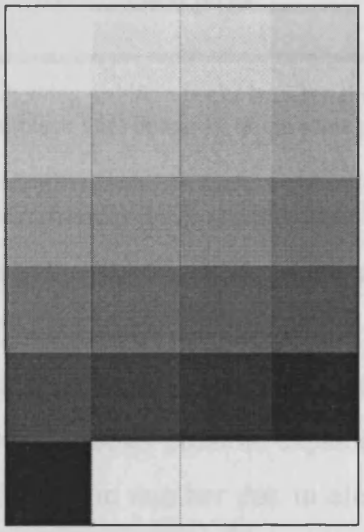

Figure 6.4. Grey level test image.

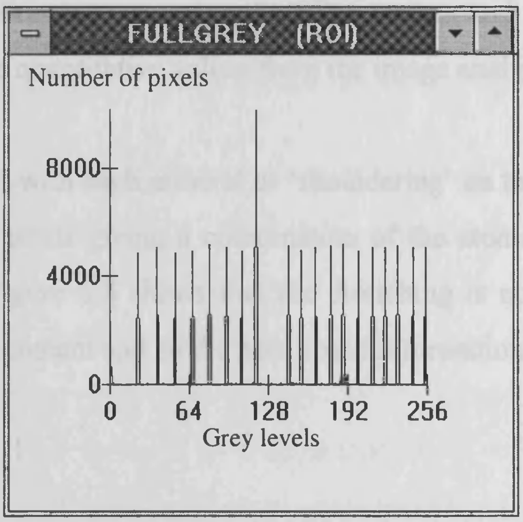

Figure 6.5. A histogram plot of image grey level verses number of pixels on image.

To compare the grey scales allocated to minerals between images, a grey scale histogram of images 5 and 10, from well 1 plug 1a was plotted (Figure 6.6). A difference in peak amplitude was expected as different images were being analysed, but the shift in the three main peaks was not.

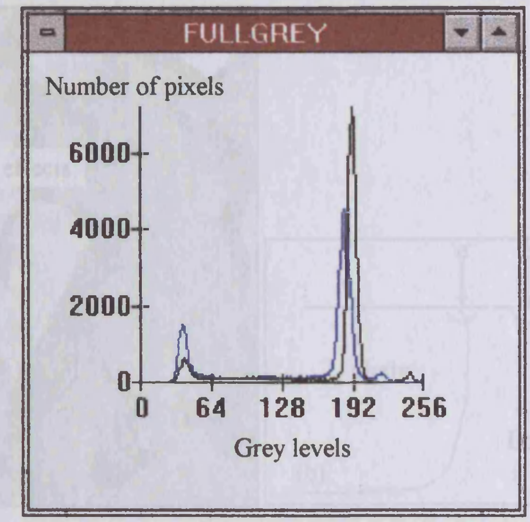

Figure 6.6. A diagram from PC_Image showing a shift in peaks between the high magnification (blue line) image 5 and low magnification (black line) image 10 of the same plug (well 1 plug 1a).

The largest peak (quartz) at approximately 192, should peak at the same value, a shift could be the result of a colour variation in the SEM images, a fault which cannot be altered after the images have been taken. If this is the cause of the error a shift or stretch factor could be applied to each histogram, forcing the epoxy and quartz peaks to a set position, as these should have stable atomic numbers. Another possible explanation of the shift is that some of the minerals may have a variable atomic number due to element substitution in the crystal lattice. For example, feldspar can contain potassium, sodium or calcium. A possible solution to this loss of data resolution is to examine the SEM images and decide what minerals are present and then assign the quantitative values from the image analysis.

The distribution associated with each mineral or 'shouldering' on the peaks is possibly due to an overlapping of two minerals giving a combination of the atomic numbers and a varying grey scale (Figure 6.7). Figure 6.8 shows that the stretching is not always a problem. The epoxy peak is essentially constant and so the pore space information is accepted as reliable.

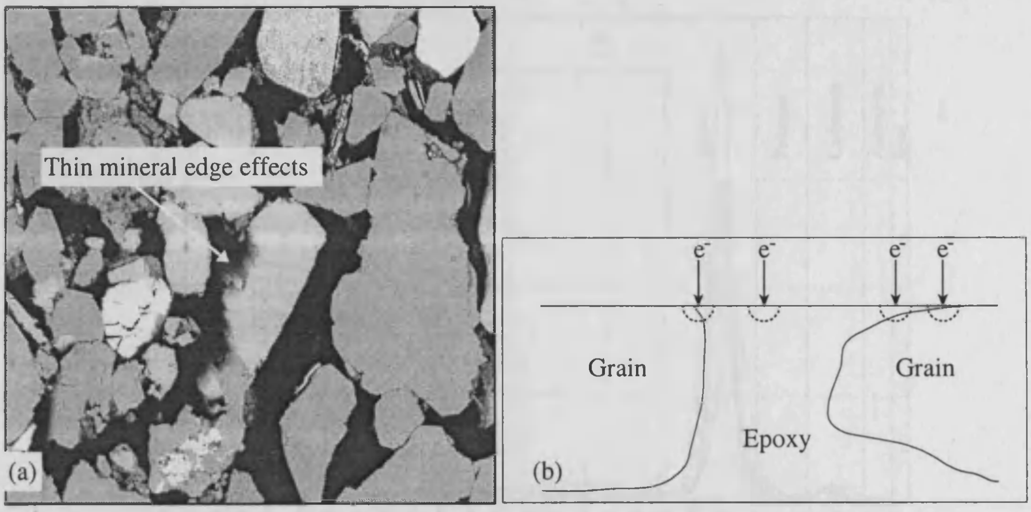

Figure 6.7. (a) Image 2 from plug 20b well 4, showing blurred edges around a mineral grain due to its thinness
(b) Schematic diagram demonstrating the problem of defining pore space from image analysis

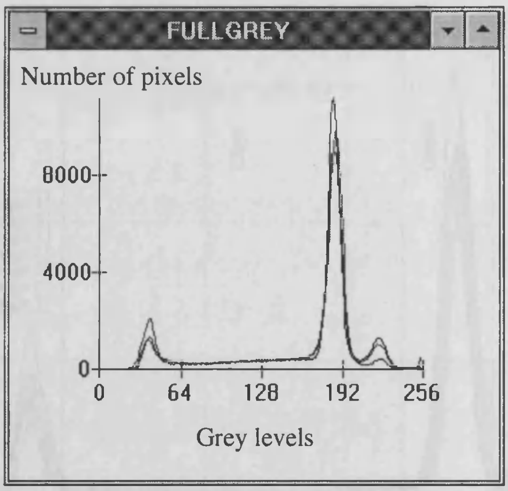

Figure 6.8. Diagram from PC_Image to show matching grey scale peaks for well 3 plug 10b, images 1,10 and 11.

The image grey scale data from well 1 were exported into Excel for further analysis, and are displayed in Figures 6.9 through 6.12. The vertical solid black lines give the grey scale boundaries for each mineral phase (Table 6.1). The mineral peaks for each of the images shown in Figures 6.9 and 6.10 fall in the centre of the expected range. However, in Figures 6.11 and 6.12 there is a distinct shift or variation in values. Occasionally it is difficult to see which mineral phase each peak belongs to. The uncertainty of the data associated with the four mineral phases in the high grey scale range (over 202) has resulted in all of these data being grouped together and called ‘other’. It is noted that detailed chemical analyses can be performed on the end-trims whilst in the SEM using an EDX system thus aiding mineralogical descriptions; unfortunately no such data was received.

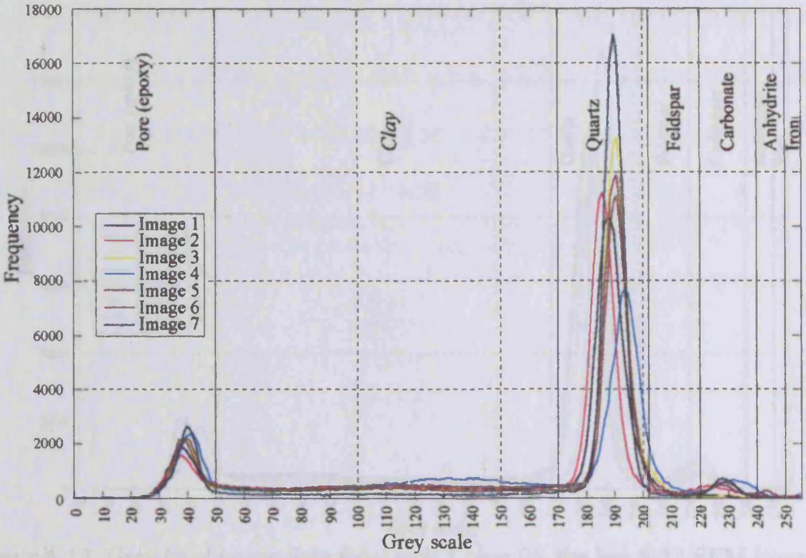

Figure 6.9. Grey level image data from well 1 plug 1a, the first 1-7 SEM images.

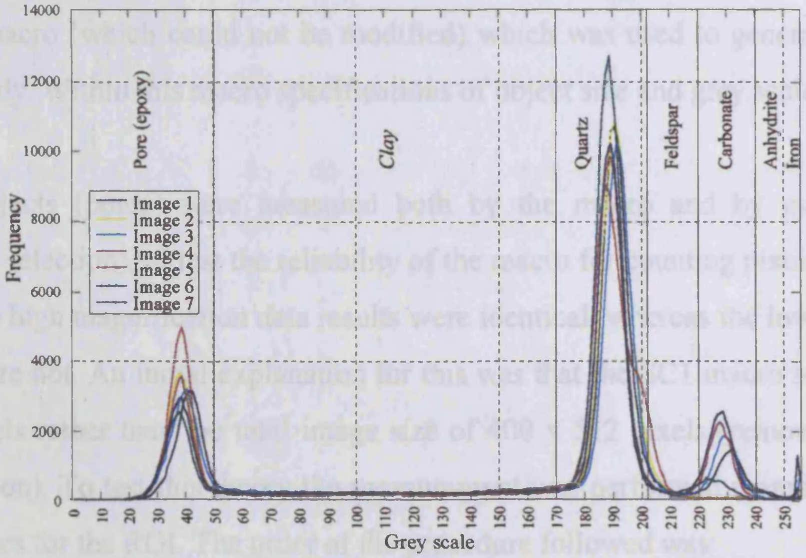

Figure 6.10. Grey level image data from well 1 plug 5c, the first 1-7 SEM images.

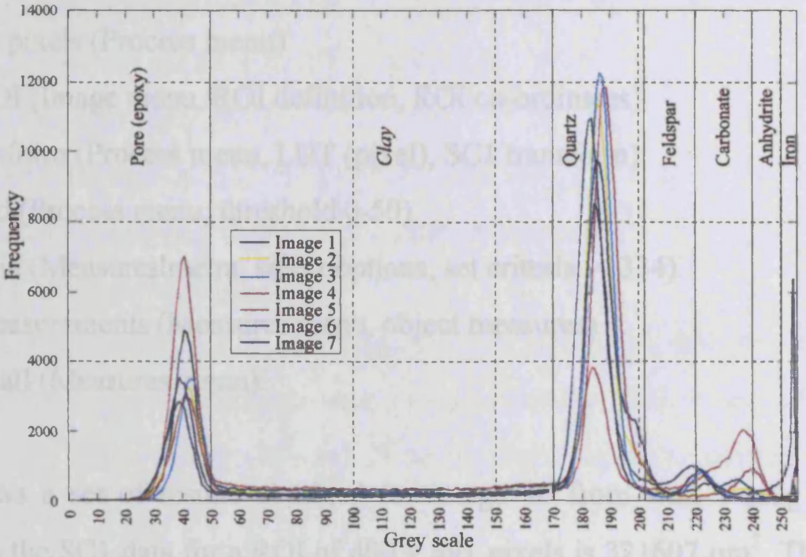

Figure 6.11. Grey level image data from well 1 plug 5a, the first 1-7 SEM images.

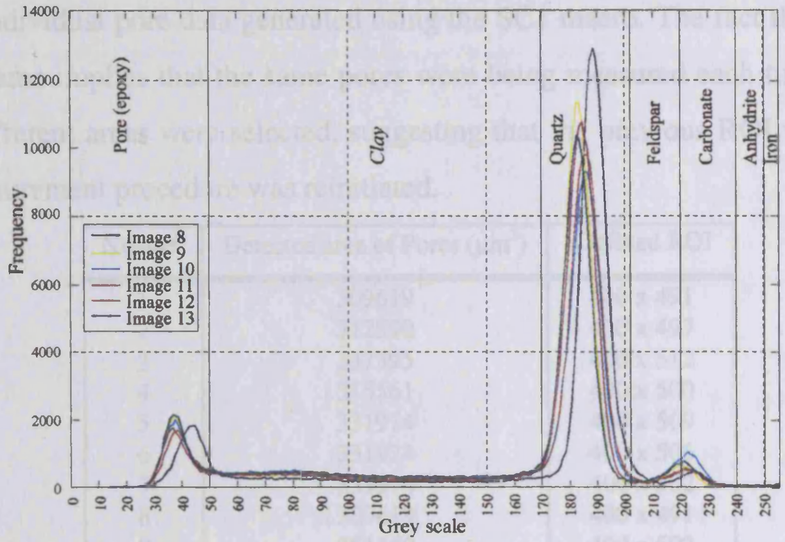

Figure 6.12. Grey level image data from well 1 plug 9a, the last 8-13 SEM images.

SC1 wrote a macro (which could not be modified) which was used to generate the data set used in this study. Within this macro specifications of object size and grey scale were made.

The image objects (pores) were measured both by the macro and by using PC_Image manually (ROI selection), to test the reliability of the macro for counting pixels in a specified size range. The high magnification data results were identical, whereas the low magnification data results were not. An initial explanation for this was that the SC1 macro selects a ROI of 400 x 491 pixels rather than the total image size of 400 x 512 pixels (removing 21 lines of pixel information). To test this theory the measurement was performed manually, stating the new co-ordinates for the ROI. The order of the procedure followed was:

1. Open image
2. Calibrate pixels (Process menu)
3. Select ROI (Image menu, ROI definition, ROI co-ordinates)
4. SC1 transform (Process menu, LUT (pixel), SC1 transform)
5. Threshold (Process menu, threshold 0-50)
6. Set criteria (Measures menu, select options, set criteria >1334)
7. Select measurements (Measures menu, object measures)
8. Measure all (Measures menu).

Table 6.2 shows a set of results obtained for image 10 from well 1 plug 1c. The value generated from the SC1 data for a ROI of 400 x 491 pixels is 321607 μm^2. The results cause concern as the manual measurements are not repeatable, and do not match those generated by summing the individual pore data generated using the SC1 macro. The fact that numbers 5, 6 and 7 are the same implies that the same pores were being measured each time regardless of the fact that different areas were selected, suggesting that the previous ROI were not cleared before the measurement procedure was reinitiated.

Number	Detected area of Pores (μm^2)	Defined ROI
1	309619	400 x 491
2	312590	400 x 497
3	337395	400 x 512
4	315561	400 x 500
5	331974	400 x 509
6	331974	400 x 506
7	331974	400 x 502
8	309619	400 x 491
9	351580	400 x 502
10	133235	400 x 200
11	351580	400 x 502
12	341963	400 x 491

Table 6.2. Detected pore area in various selected ROI for image 10 of well 1 plug 1c

Correspondence with SC1 led to the suggestion that the default file (SC1.set) should be used to select the ROI, rather than typing in ROI co-ordinates. It was suggested that this may give more consistent, though not necessarily improved results.

New measurements were made in the following order:

1. Open image
2. Open SC1.set (Images menu - Open setup.... PPA, programs)
3. Select 400 x 491 from the status box.
4. Calibrate pixels (Process menu x30)
5. SC1 transform (Process menu, LUT (pixel))
6. Threshold (Process menu, 0-50)
7. Set criteria (Measures menu, select options, >1334)
8. Select measurements (Measures menu, object measures)
9. Measure all (Measures menu).

The value generated from the SC1 macro data for a ROI of 400 x 491 pixels is 839100. The value obtained when the co-ordinates were typed in for the ROI of 400 x 491 pixels was 949430. When the entire image (400 x 512 pixels) was manually selected different values were obtained.

Number	Number of pores	Detected area of Pores (μm^2)	Defined ROI
1	377	875720	400 x 491
2	377	875720	400 x 491
3	380	895327	400 x 491
4	377	875720	400 x 491
5	377	875720	400 x 491
6	405	884075	400 x 512

Table 6.3. Detected pore area in various selected ROI for image 10 of well 1 plug 1a, using the SC1.set setup

The results in Table 6.3 are more comparable than the results given in Table 6.2. For this reason the decision was made to calculate an image porosity, for the low magnification images, by summing the previously generated data and divide the supposed used area of 400 x 491 pixels by that value. The assumption is made that the SC1 macro is repeatable.

The addition of extra parameters to the data set could be problematic with the low magnification data. For instance, data such as the length parameter are already available for the area of the images of 400 x 491 pixels, so to add another parameter, for example orientation of an object, for the same pores in this area will be difficult due to the non-repeatability of the area selection. Therefore, as the measuring of an entire image is repeatable, when the default ROI of 400 x 512 pixels is used, it has been decided to ignore the bottom 21 line exclusion and to take future measurements using the entire image.

6.2.4.3 Artefacts

A possible cause of error from the images is the presence of air bubbles. Figure 6.13 shows the effect of a single bubble captured within a high magnification SEM image on the resultant grey level histogram generated by PC_Image, (the blue scatter is the bubble data and the black line is the histogram for the entire image). Examination of the results suggests that even a large bubble has a negligible effect on the peaks within the histograms, but there is a reduced area of epoxy (pore space) given in the histogram. It is concluded that bubbles are not a problem in the data set.

Several concerns with the images and image analysis package have been expressed in this section, and where possible investigated. The data chosen for this study is a direct result of this investigation. It is concluded that the image data is fit for the purpose for which it is used.

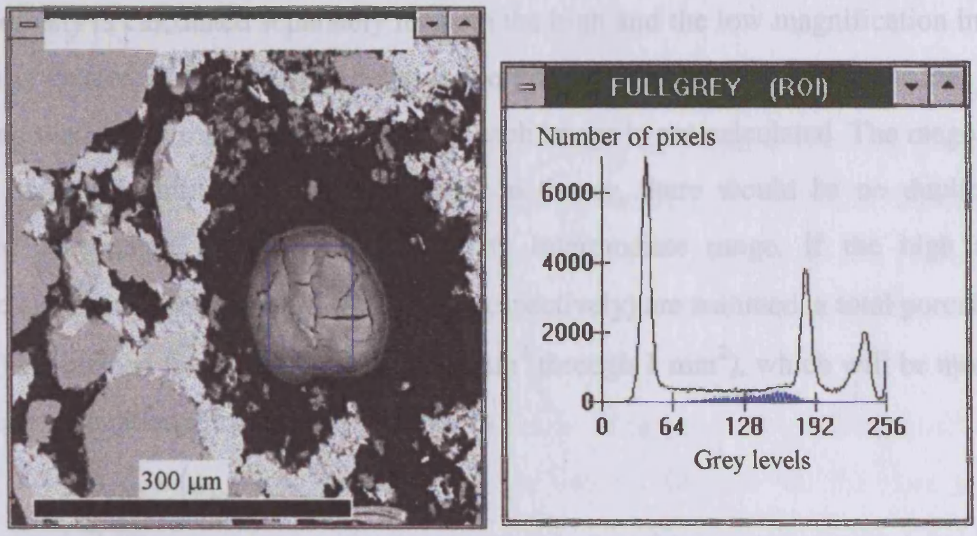

Figure 6.13. Image 5 from well 1 plug 5a, and the associated histogram of grey levels. The black line is the histogram for the entire image, and the blue the histogram of the image within the selected region of interest (shown in the blue rectangle in the image picture), the bubble.

6.2.5 Analysis of the equations used in association with PC_Image

A list of the image parameters calculated by PC_Image used in this study is given in Appendix B. The software manual provides little detail on how the image parameters are calculated. Assumptions had to be made on occasions with regards to the initial equations. These assumptions along with the manual information were used to derive equations to augment this study.

6.2.5.1 Image porosity

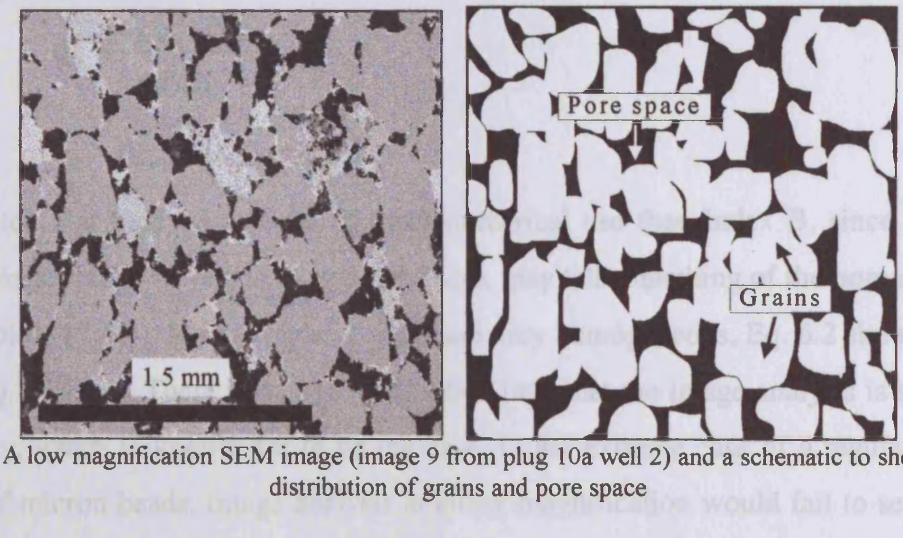

Figure 6.14. A low magnification SEM image (image 9 from plug 10a well 2) and a schematic to show the typical distribution of grains and pore space

Image porosity is defined as the area of detected pores (within a specified size range) divided by the image area. The range in the high magnification images is 13-1334 µm^2 and in the low magnification images 1334 µm^2 to approximately 1 mm^2. A pore space, as recognised in this image analysis process, is any void which has been impregnated with epoxy (Figure 6.14).

Image porosity is calculated separately for both the high and the low magnification images. A problem is created in that the total measurable area of pore space is not measured for each image and therefore a true image porosity for each image is not calculated. The range selected in both of the magnifications was such that in theory, there would be no duplication of measured pore sizes, or the omitting of any intermediate range. If the high and low magnification image porosities (ϕ_{high} and ϕ_{low} respectively) are summed, a total porosity, $\phi_{Total,}$ (Eq. 6.1) is obtained for a specified range (13 μm^2 through 1 mm^2), which will be more useful to compare with other petrophysical parameters.

$$\phi_{Total} = \left(\phi_{high} + \phi_{low}\right) \qquad [6.1]$$

There are errors associated with this method of generating an image porosity. The most fundamental of which is that homogeneity must be assumed within both the high and low magnification images. Also, some pores will inevitably be counted in both magnifications, as any pore (or pore segment) will be measured if it is within the specified size range, and crosses no more than one of the image edges.

A porosity index has been calculated as there is both a total image porosity (within the given pore range) and a plug porosity ϕ_{plug} available. Two examples of such indices (ϕ_A and ϕ_B) are given below,

$$\phi_A = \frac{\phi_{high} + \phi_{low}}{\phi_{plug}} \qquad [6.2]$$

$$\phi_B = \phi_{plug} - \left(\phi_{high} + \phi_{low}\right) \qquad [6.3]$$

It is expected that Index A will be of more numerical use than Index B, since it is a ratio giving a smaller range of values. A porosity index may tell something of the homogeneity of a set of samples (§7.4.4). For example, if plugs are very homogeneous, Eq. 6.2 should approach one and Eq. 6.3 zero. There is a large assumption here that the image analysis is seeing all of the porosity, which is known not to be the case. In the extreme case of a regular bead pack made up of micron beads, image analysis at either magnification would fail to see pores; the sample is totally homogenous but the image analysis experiment, as defined here, is unfit for the purpose.

6.2.5.2 Pore size ranges

Ehrlich et al. (1991b) state that the measurements made in image analysis (e.g. length and breadth) are effective only if the size or shape of the pore varies, but not both. If both pore size and shape vary, such measures would be ambiguous in that objects of diverse sizes and shapes can generate similar values. The pore size distributions of each plug in this study, were therefore divided into a series of ranges, these are used extensively in Chapter 7.

Seven ranges of pore size area were made; no pores less than 13 μm^2 or which touch two sides of the image have been measured and therefore are not included in the pore size range distributions. The pores in the low magnification data could be approximately 1 mm^2, but the largest pore occurring more than once is approximately 110,000 μm^2. The pores are therefore divided into groups for the size range of 13-110,000 μm^2. The high magnification data was split into approximately equal groups of 450 μm^2. The low magnification data was then split into several groups at the smaller end of the pore scale, with one group for the large pores. It is acknowledged with hindsight that these ranges are not optimal, they do however serve a significant purpose in this study.

The pore size ranges used in this study are listed below, all are in μm^2:

13	< Range 1 <	430
430	< Range 2 <	860
860	< Range 3 <	1334
1334	< Range 4 <	2500
2500	< Range 5 <	3500
3500	< Range 6 <	5500
	Range 7 >	5500

6.2.5.3 Pore roughness

Ehrlich et al. (1991a) used the effective technique of erosion and dilation to investigate the relationship of pore roughness, porosity and permeability. It was not possible to use this method and roughness has been defined as follows,

$$R1 = \frac{measured\ pore\ perimeter}{\pi(length * breadth)} \quad [6.4]$$

$$R2 = \frac{measured\ pore\ perimeter}{measured\ pore\ area} \quad [6.5]$$

where $\pi(length*breadth)$ is analogous to elliptical area, and *length* and *breadth* are the average values for each pore size range considered. In quantifying these definitions both R1 and R2 would equal *2/r* for spherical pores of radius *r*, therefore the parameters are size dependent which is why pore size ranges (§6.2.5.2) are used to divide the data before it is used for comparison purposes.

6.2.5.4 Pore aspect ratio

The definition of pore aspect ratio is the harmonic mean average (as the data is skewed) breadth of all the pores within an image, divided by the harmonic mean average length of all the pores within the specified pore size ranges.

6.2.5.5 Image permeability

Kozeny (1927) derived one of the most fundamental relationships expressing permeability as a function of porosity and specific surface area (§2.2.4). In this section image permeability will be expressed in terms of image porosity and specific area pore using the same model as Kozeny.

Consider a porous rock sample of cross-sectional area *A* and length *L*, as being made up of a number *n*, of straight capillary tubes in parallel, with the spaces between the tubes sealed by a cementing material. If the capillary tubes are all the same radius *r* (cm) and length (cm), the flow rate *q* (cm^3/s) through this bundle of tubes according to Poiseuille's equation is,

$$q = \left(\frac{n\pi r^4}{8\mu} \right) \frac{\Delta p}{L} \qquad [6.6]$$

where the pressure loss Δp over length is expressed in dynes/cm^2.

The flow of fluids through these *n* capillaries can also be approximated by Darcy's law as,

$$q = \left(\frac{kA_c}{\mu} \right) \frac{\Delta p}{L} \qquad [6.7]$$

Equating Eq. 6.6 and 6.7 and solving for *k* gives,

$$k = \frac{n\pi r^4}{8A} \qquad [6.8]$$

Now consider a cross-section of that plug and calculate an image porosity (Eq. 6.9) and compare with the plug porosity (Eq. 6.10);

Image porosity ϕ_{img},

$$\phi_{img} = \frac{Area\ pore}{Total\ area\ of\ image} = \frac{n\pi r^2}{A} \tag{6.9}$$

Plug porosity ϕ_{plug},

$$\phi_{plug} = \frac{V_p}{V_b} = \frac{n\pi r^2 L}{AL} = \frac{n\pi r^2}{A} \tag{6.10}$$

Thus image porosity equals plug porosity.

Substituting $A = n\pi r^2/\phi_{img}$ from Eq. 6.9 into Eq. 6.8 the simplest relationship between the image permeability and image porosity for pores of the same size and radii is obtained,

$$k_{img} = \frac{\phi_{img} r^2}{8} \tag{6.11}$$

where k_{img} is in cm^2 (1 cm^2 = 1.013x10^8 Darcys) or in μm^2 (1mD = 9.871 x 10^{-4} μm^2) and ϕ_{img} is a fraction. Let the specific area pore S_{Ap}, be the pore perimeter per unit of pore area, where the pore perimeter P_p, for n capillary tubes is $n(2\pi r)$ and the pore area A_p is $n(\pi r^2)$. Therefore,

$$S_{Ap} = \frac{P_p}{A_p} = \frac{n(2\pi r)}{n(\pi r^2)} = \frac{2}{r} \tag{6.12}$$

Let S_{Pgr} be the pore perimeter per unit of grain area. The total area exposed is A and the grain area A_{gr}, is equal to $A(1-\phi_{img})$ for a slice through a bundle of capillary tubes, (from $\phi_{img} = \frac{(A - A_{gr})}{A}$), thus,

$$S_{Pgr} = \frac{n(2\pi r)}{A(1-\phi_{img})} = \frac{n\pi r^2}{A}\left(\frac{2}{r}\right)\left(\frac{1}{1-\phi_{img}}\right) \tag{6.13}$$

Combining Eq. 6.9, 6.12 and 6.13gives,

$$S_{Pgr} = S_{Ap}\left(\frac{\phi_{img}}{1-\phi_{img}}\right) \tag{6.14}$$

Eq. 6.11 can be expressed as,

$$k_{img} = \left(\frac{\phi_{img}}{2}\right)\frac{1}{(2/r)^2} = \left(\frac{1}{2A_p^{\ 2}}\right)\phi_{img} \tag{6.15}$$

Substituting for S_{Ap} from Eq. 6.14 yields,

$$k_{img} = \left(\frac{1}{2S_{Pgr}^{\ 2}}\right)\frac{\phi_{img}^{\ 3}}{\left(1-\phi_{img}\right)^2} \qquad [6.16]$$

See Section 6.5.2 for the results of this image permeability calculation.

6.3 Condensing the Image analysis data

In order to use the image analysis data 2,400,000 pixels of information must first be reduced to values comparable to a single core plug measurement. Twelve image parameters were chosen: perimeter, length, breadth, area pore, area equivalent radius, minimum radius, maximum radius, mean radius, minimum feret, maximum feret, mean feret (a feret is the diameter of an object as seen from a defined direction) and boundary count (the grey scale value associated with each pixel on the pore edges). The boundary count data was not used as the resolution of the data was low after the summing of grey scales over 202 into one group; called 'other' (§6.2.4.2). These twelve measurements were made on each pore (in the specified size range) within each image. A histogram was visually checked to examine whether the distributions were uni-model for every image parameter of each image in well 1. The majority of the 1620 histograms were strongly positively skewed and uni-modal (Figure 6.15).

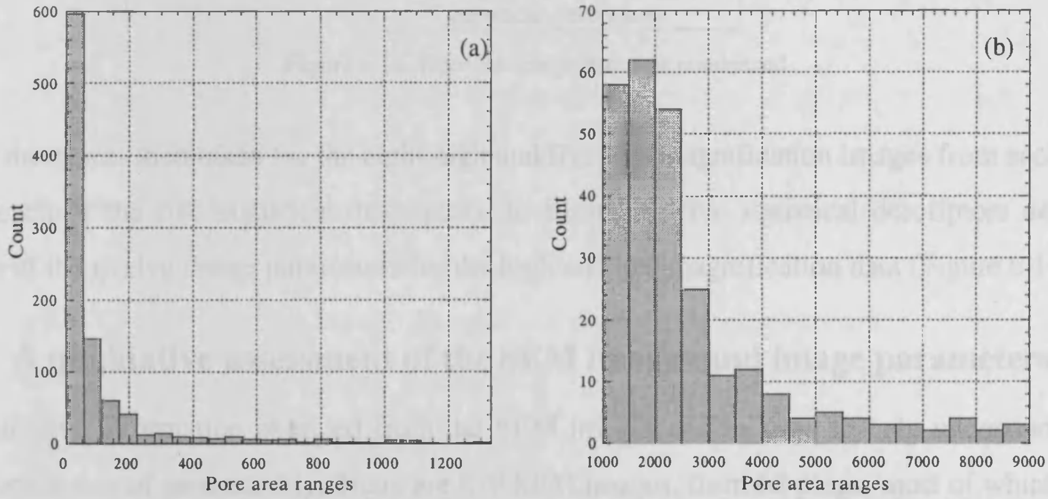

Figure 6.15. A plot giving an example of how the data is positively skewed and uni-modal for well 1 plug 4a data (a) high magnification and (b) low magnification. Note different vertical scales

Various statistical descriptors were investigated to describe the data, from the preliminary plots of the parameters. Ultimately five statistical descriptors were chosen, as they contained all the important information held within each set of image data:

(i) Harmonic mean, as it is close to the modal value of the histogram.

(ii) Skew.

(iii) Standard deviation, to provide an estimate of spread in the data.

(iv) Interquartile range divided by the median, to give an intermediate estimation of the variation in the data.

(v) Interquartile ranges which may be added to data in the form of an error bar to give an extra descriptor to the data.

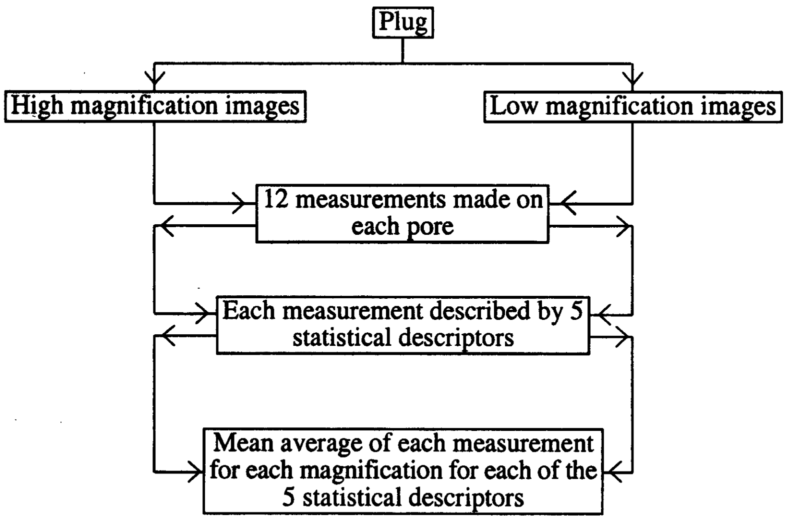

Figure 6.16. How the image data was condensed

The mean was then taken for the eight high and five low magnification images from each plug for each of the five statistical descriptors. In summary, five statistical descriptors describe each of the twelve image parameters for the high and low magnification data (Figure 6.16).

6.4 A qualitative assessment of the SEM images and image parameters

Qualitative information obtained from the SEM images can be used to help understand and aid prediction of permeability. There are 819 SEM images, from 63 plugs, most of which have associated core analysis measurements (Chapter 5). These images are split into 315 low magnification (x30) and 504 high magnification (x150) images. Each plug, as previously mentioned, has five low and eight high magnification images taken on its end-trim (Figure 6.2). Each image was assessed and any distinctive features which may bias the PC_Image measurements noted. Examples of such features are, air bubbles, image distortion and large grains or pores (Appendix B). During this qualitative assessment of the images any mineralogy that was found particularly interesting (e.g. large, rare or unusual mineral growths) was also noted, in case it could be useful in later analysis (Appendix B).

In Section 6.4.1 mineral recognition is discussed. In Section 6.4.2 the qualitative understanding of the images is used to investigate whether the images could be visually linked to gas expansion porosity (§5.3.3) and gas permeability measurements (§5.3.5). The second qualitative approach was to characterise the low magnification images by grain size, anisotropy, pore cleanness (i.e. presence of *clay* scattered throughout epoxy), grain closeness and presence of excessively large pores or grains (§6.4.3). It was necessary to produce hard copies to interpret and compare the 819 images.

6.4.1 Image interpretation

A selection of images (Figure 6.17) were examined to start the image interpretation. Figure 2.14 in Chapter 2 provides schematics of how clays can infill pore space and may prove useful whilst looking at the following figures:

Figure 6.17A. The scattered material which has a grey scale between the quartz and epoxy is thought to be phyllosilicates, which in this image is difficult to identify further. The phyllosilicates will probably contain micro-porosity which has not been impregnated with epoxy and will therefore not be measured as pore space in the images, and its scattered distribution has potential for blocking pores and decreasing a plug's permeability. The feldspar grain has begun to alter and shows the remnants of twinning.

Figure 6.17B. The kaolinite has replaced an original detrital feldspar grain, thus producing secondary porosity, some of which may be too small to be measured as image porosity.

Figure 6.17C. The siderite is blocking pore throats and has a micro-porosity.

Figure 6.17D. The fibrous mineral in the lower right hand corner is probably chlorite, but in the absence of detailed XRD information or the use of the EDX system at the time of image production no conclusive identifications can be drawn. The white specks seen in the figure are identified as iron pyrites, because of their brightness which would be due to the high atomic number of iron, and secondly because of the square shape (assumed to be cubic in 3D) of a particular grain (circled).

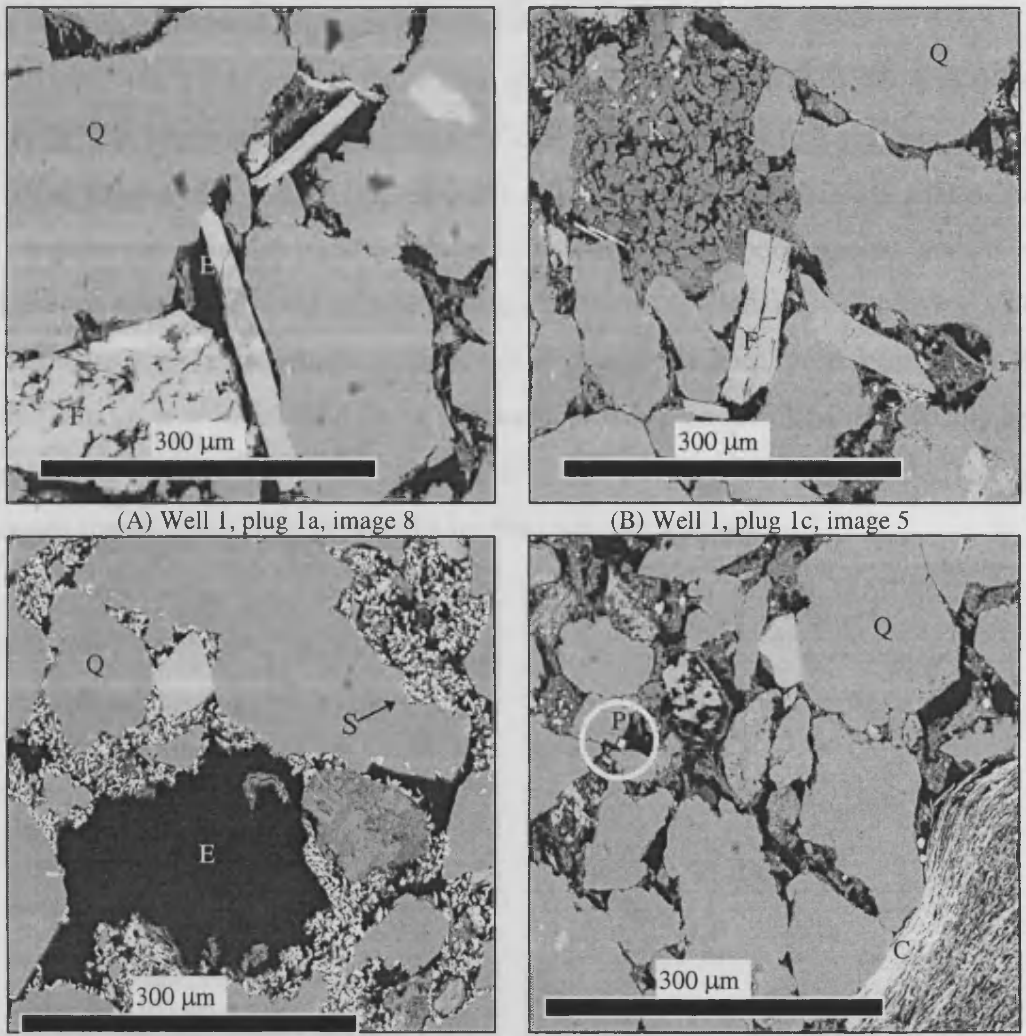

(A) Well 1, plug 1a, image 8 (B) Well 1, plug 1c, image 5

(C) Well 1, plug 5a, image 1 (D) Well 2, plug 1a, image 4

Figure 6.17. Four selected high magnification SEM images. Key: Q = quartz, E = epoxy, F = feldspar, K = kaolinite, M = mica, P = iron pyrites, S = siderite and C = chlorite.

6.4.2 Comparing the images with porosity and permeability

Permeability and porosity values of each plug were noted against each associated set of SEM images to investigate the presence of any relationship between the plug parameters and the images. Six plugs which had a wide range of permeability values were chosen to be investigated further (Table 6.4). The most representative image from the five associated low magnification images, are shown in this section. The descriptive terms are for qualitative purposes only, and quantities of minerals or pore space expressed in these terms are made relative to the other images within the data base.

Well	Plug	Permeability range	Gas permeability (mD)	Plug porosity (%)
2	9b	High	1200	27.7
2	10a	High	1600	24.2
1	6a	Intermediate	250	23.9
3	5a	Intermediate	450	25.3
2	1a	Low	17.9	26.9
1	4a	Low	11.5	26.2

Table 6.4. Six plugs from three wells used for comparison of plug parameters and low magnification images

Images with an associated high gas permeability value

Plugs 9b and 10a from well 2 have high permeability values of 1200 and 1600 mD respectively. The low magnification images of each were examined to investigate if there was a visual link between the images (Figure 6.18) and the high gas permeability values. Plug 9b, shows regions of loosely packed grains with very clear pore space, and a visible heterogeneous zone (illustrated by line). Plug 10a shows a similar loose packing of coarse grains but there is no heterogeneity. In both sets of images the pore space is unusually clear of *clay*, plug 10a has a white mineral lining the pores, possibly siderite. The relationship between the images and permeability is logical, as the grains are generally coarse and well spaced, which gives the assumed large flow paths for the high permeability.

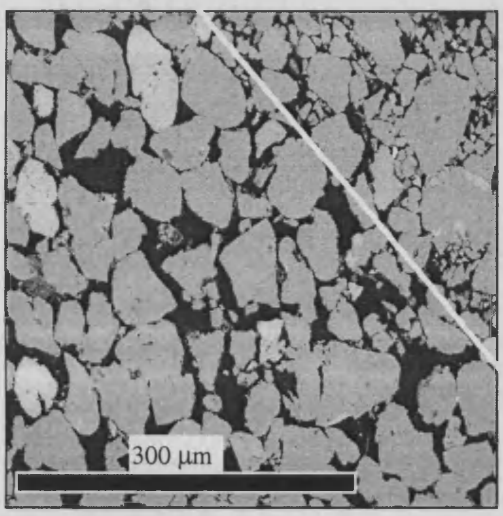

Well 2, plug 9b, image 9. $\phi = 27.7$ and k = 1200.

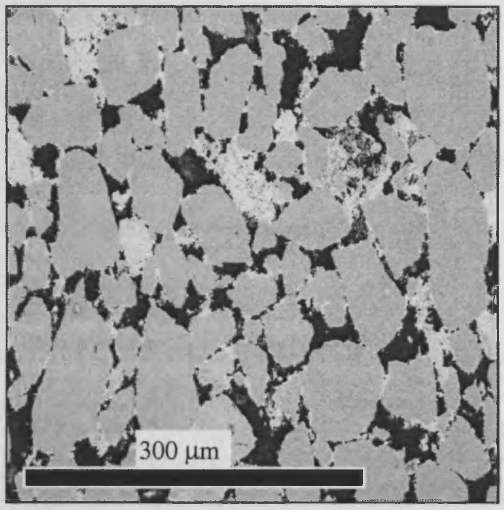

Well 2, plug 10a, image 9. $\phi = 24.2$ and k = 1600.

Figure 6.18. Two low magnification images associated with high permeability plugs

The main difference observed between plugs 9b and 10a is the heterogeneity in plug 9b, which could be a section through a lamination. Figure 6.19a demonstrates that if whole-core is laminated and the core plug sliced parallel to these laminations the end of the plug will show laminations but the permeability of the plug is not hindered (i.e. flow paths are not disrupted as the laminations do not cut across the plug). If a core plug is not taken parallel to laminations (Figure 6.19b) permeability may be hindered. Plug 9b has a higher porosity than 10a but a lower permeability, which may be caused by laminations off parallel to the length of the plug (i.e. the direction of the permeability measurement), impeding flow. A plug taken perpendicular to the laminations would not reveal laminations in the images, but fluid flow may be obstructed, decreasing the permeability value.

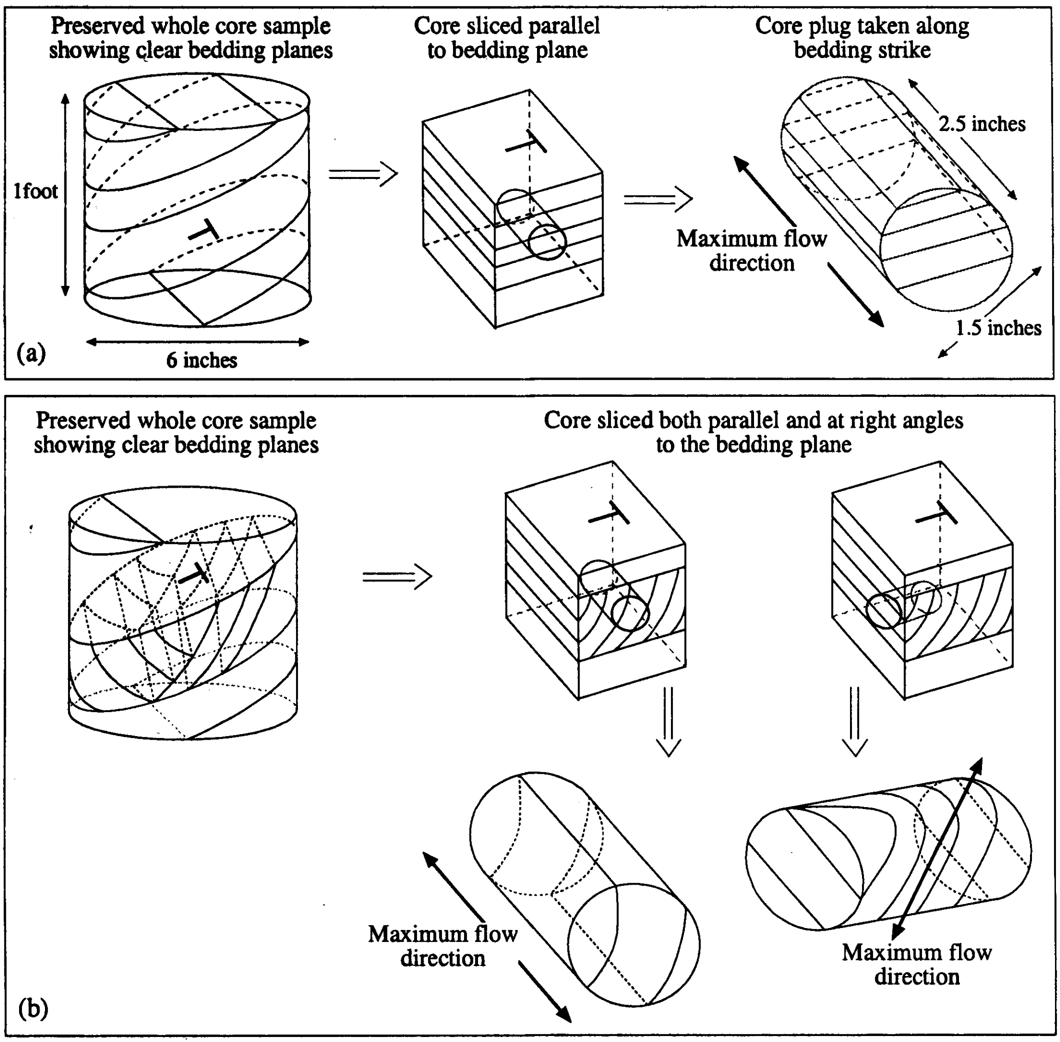

Figure 6.19. Diagrammatic representation of how fabric or bedding within the whole core could be important to the final values of permeability obtained (not to scale)

Images with an associated intermediate gas permeability value

Plug 6a from well 1 and plug 5a from well 3 have intermediate values of gas permeability (250 and 450 mD respectively). The comparison of images of these plugs (Figure 6.20) with Figure 6.18 demonstrates that within the lower permeability plugs, the average pore size has decreased, and the grains are smaller and less sorted. A decrease in pore size with decreasing permeability is expected, as pores are assumed to be interconnected and a reduced flow path will give a reduced permeability. Plugs 6a and 5a have the same amounts of area *clay* (13% and 14% respectively) and area pore space (17% and 16% respectively). On close inspection of the images it was observed that the *clay* in plug 5a has discrete regions of grain aggregate (detrital clays and lithics), whereas 6a has a diffuse distribution (more likely diagenetic and hence pore-lining and throat bridging). The subtle difference between plug 6a permeability (250 mD) and plug 5a (450 mD) may be a result of the diffuse clay obstructing the fluid flow more effectively than the large regions of grain aggregate.

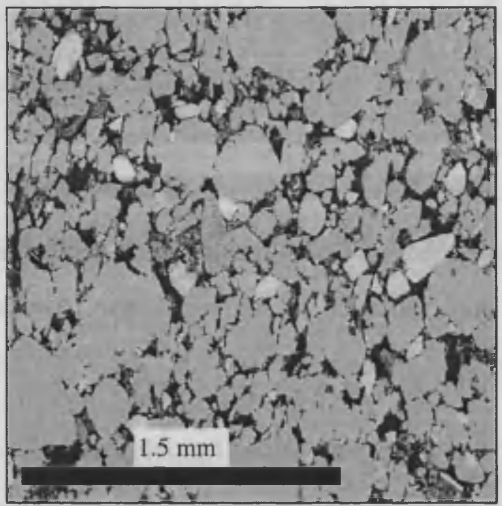

Well 1, plug 6a, image 9. $\phi = 23.9$ and k = 250.

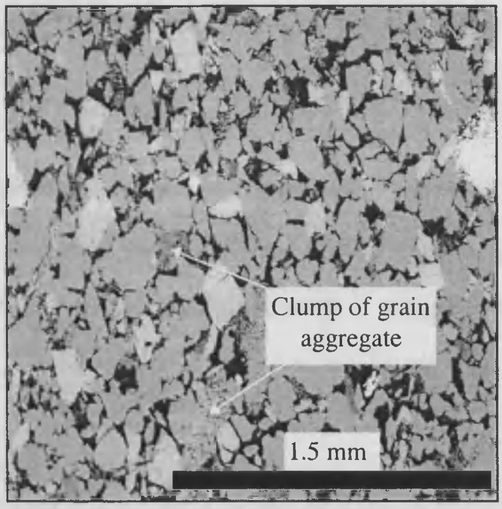

Well 3, plug 5a, image 13. $\phi = 25.3$ and k = 450.

Figure 6.20. Two low magnification images associated with intermediate permeability plugs

Images with an associated low gas permeability value

Plug 1a from well 2 and plug 4a from well 1 have lower values of permeability (17.9 and 11.5 mD respectively). The two plugs have a high area *clay* of 26% (Figure 6.21), which appears to be more diffuse or widely distributed in plug 4a. The subtle difference in permeability values between the two plugs may be attributed to the more diffuse distribution of clay in plug 4a. Plug 4a also has less pore area at 7% compared with plug 1a at 9%.

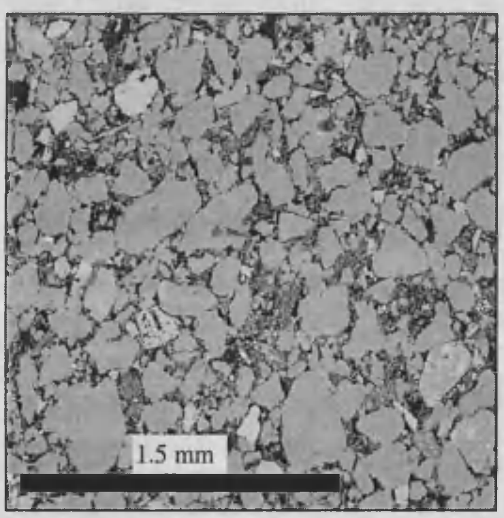

Well 2, plug 1a, image 11. $\phi = 26.9$ and k = 17.9.

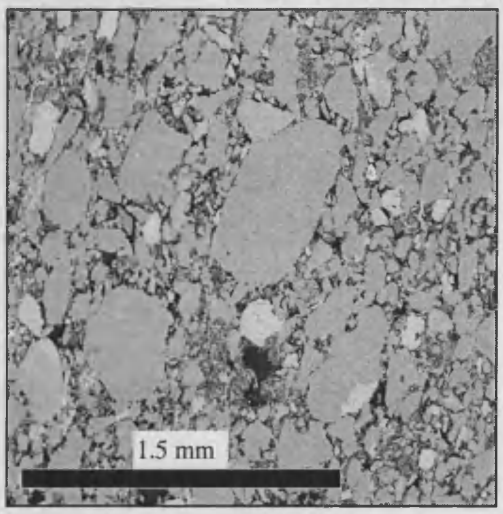

Well 1, plug 4a, image 10. $\phi = 26.2$ and k = 11.5.

Figure 6.21. Two low magnification images associated with low permeability plugs

The comparison of all three sets of permeability ranges (Figures 6.18, 6.20 and 6.21) reveals that the quantity of diffuse *clay* increases with decreasing permeability. The low permeability plugs in Figure 6.21 have a higher plug porosity than plug 10a from well 2, which has a high permeability of 1600 mD. This is a single example from a data set which has many examples of the poor linear porosity-permeability relationship for the prediction of permeability within this reservoir (Figure 5.23, Chapter 5).

The information which is not available from the plug porosity to understand permeability is present within the images, often in the grain size and sorting. Well sorted coarse grained images have higher permeability values than poorly sorted samples, even if plug porosity is the same.

6.4.3 Characterising the images

To characterise the images they were described and categorised at the two magnifications in their respective numbers of eight and five for each plug. The character information from the low magnification images only, was used in subsequent studies as they were seen as the major control. Therefore, only definitions for the low magnification data are given. The measurements were taken on A4 paper size hard copies of the images, and therefore size measurements are in millimetres not micrometres. All the images were compared on the same day to reduce the errors which may occur due to the qualitative nature of this assessment. The characters were chosen as they are the main features present within the images. In Section 7.4.1 these image characteristics are used to aid understanding of the permeability-porosity plot for this reservoir. The defined characteristics are as follows:

Grain size

Fine < 10 mm

Medium 10-50 mm

Coarse > 50 mm

Grain size ranges

Grain size ranges were split into four groups and given numerical keys:

0.5 = single sized grains

1 = fine to medium grained

2 = fine to coarse grained

3 = medium to coarse grained

Ranges 1 and 3 have a similar sorting which is different to 0.5 and 2.

Anisotropy

Anisotropy is defined by the visual presence of grain alignment and/or grading of the grains.

Pore cleanness

Pore cleanness is a descriptive term which describes how clean the epoxy (pore space) of each set of images is relative to the other images. It is not just a measure of the quantity of *clay* present, but whether that *clay* is scattered (possible authigenic clay) making the image appear more dirty.

Grain packing

Grain packing is defined by the number of grains touching each grain on average seen within the images. The ranges are 0-2, 3-5 and >5 touching grains.

Presence of large pores and large amounts of clay

In this category if the images contained one or mores pores >50 mm in diameter it was recorded, as was the presence of large (>50 mm) aggregates of *clay*.

A series of characteristics are now defined for each plug (listed in Appendix B). It was proposed that a set of (image) petrophysical facies be generated using these characteristics. The image facies could then be used in Chapter 7 for comparison with the previous facies descriptions given in Internal Report 1 (§4.4), and used to constrain the permeability-porosity plot. In order to group the plugs into a series of petrophysical facies, a cross plot was made using two of the parameters and then three more parameters were included within the plot by using different plot symbols, colours and sizes for each parameter, thus creating a multi-dimensional plot in 2D. Unfortunately it was not possible to group the data sufficiently to create facies types. However, by using the same technique and only looking at three parameters, subtle relationships became apparent (Figure 6.22). Cluster analysis was not used due to the small number of samples and large number of variables.

Figure 6.22 shows three scatter plots of pore cleanness against the number of touching grains (grain packing), with a different third parameter added in each plot. The data from plugs 8a from well 8, and plugs 4a and 8a from well 6, have not been used due to their poor sorting and large grain size range. The plots from Figure 6.22 are described below:

Figure 6.22a. The majority of images which show large pores have few touching grains and are considered clean. Eighteen plugs have no large pores present, are moderately clean and contain on average 3-5 touching grains.

Figure 6.22b. Anisotropy is generally associated with moderately clean pore spaces and 3-5 touching grains.

Figure 6.22c. Coarse grains are only present in images with clean pores. Small grains occur more in images with more tightly packed grains.

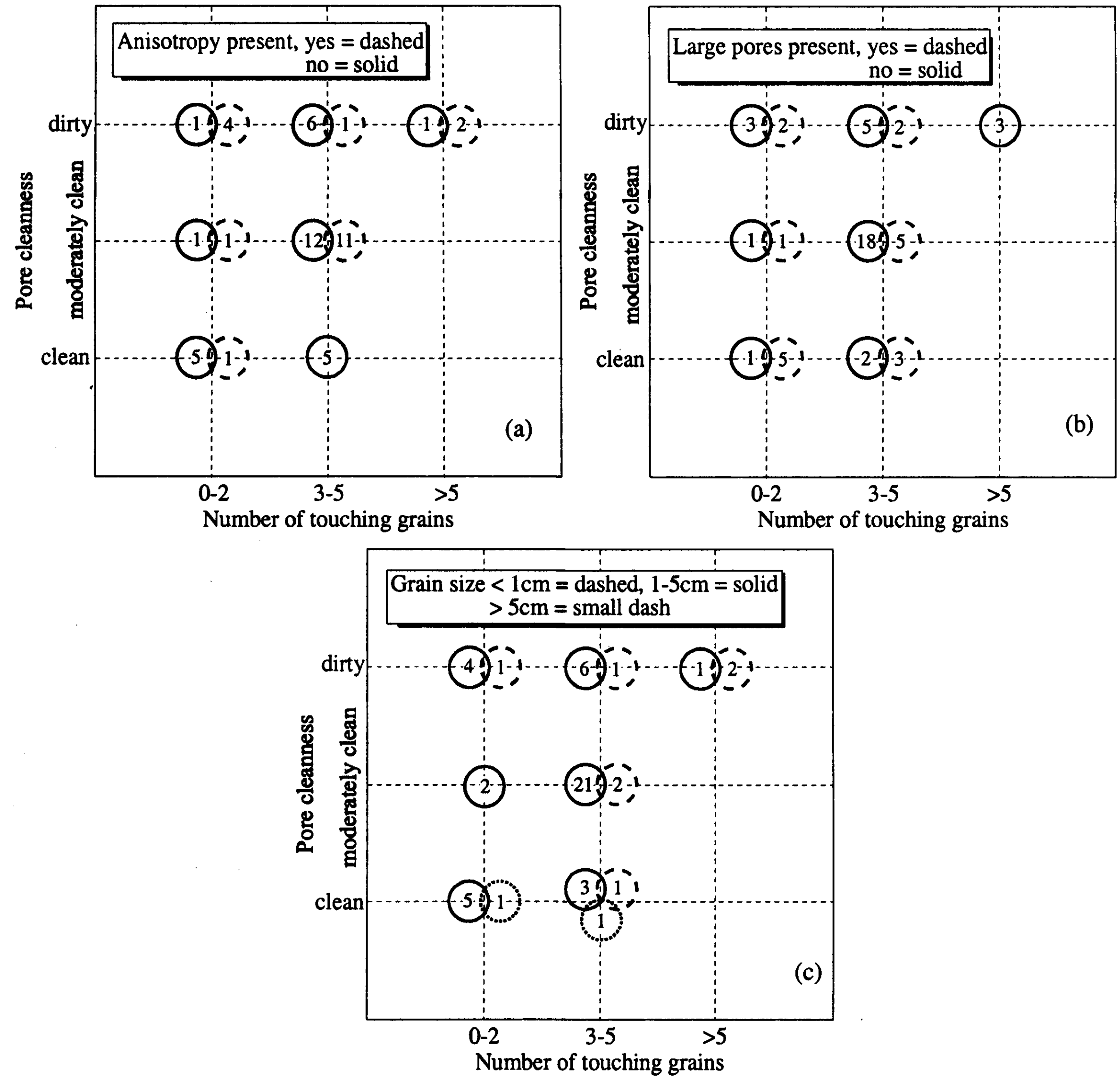

Figure 6.22. Plots to show the relationships between the qualitative image parameters

6.5 A quantitative assessment of the SEM images and image parameters

Nine quantifiable image parameters were calculated: pore roughness, pore aspect ratio, image porosity, image porosity indexes, image permeability and areas pore, *clay*, quartz and 'other'. The parameters are mainly used in Chapter 7 to aid core plug data interpretation, but a selection are discussed below.

6.5.1 Area *clay* against area pore

All combinations of areas pore, *clay*, quartz and 'other' were plotted, a significant* correlation was only present between area *clay* and area pore (r=-0.65, Figure 6.23). The significant relationship suggests a fixed quantity of void space between the detrital quartz and feldspar grains exists which is filled by *clay* or pore. Therefore, the presence of *clay* in the void space will lead to a decrease in the area pore present to be detected in the image analysis. The plug porosity range (20-35%) is approximately the same as the range for the sum of area pore and area *clay*. There is an apparent relationship between plug porosity and areas *clay* and pore, this hypothesis is discussed and substantiated in Chapter 7 (§7.3.5).

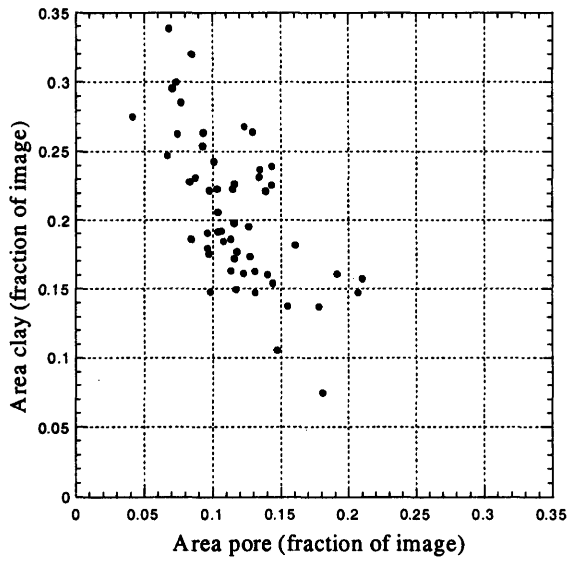

Figure 6.23. Plot of area clay versus area pore

6.5.2 Image permeability and image porosity

The methods of calculating image porosity and image permeability are given in Sections 6.2.5.1 and 6.2.5.5 respectively. Image permeability is derived from image porosity, and therefore not surprisingly a cross plot between the two parameters (Figure 6.24) reveals a strong relationship.

* Unless otherwise stated the significance of the correlation coefficient r, has been tested at a probability level of 0.05.

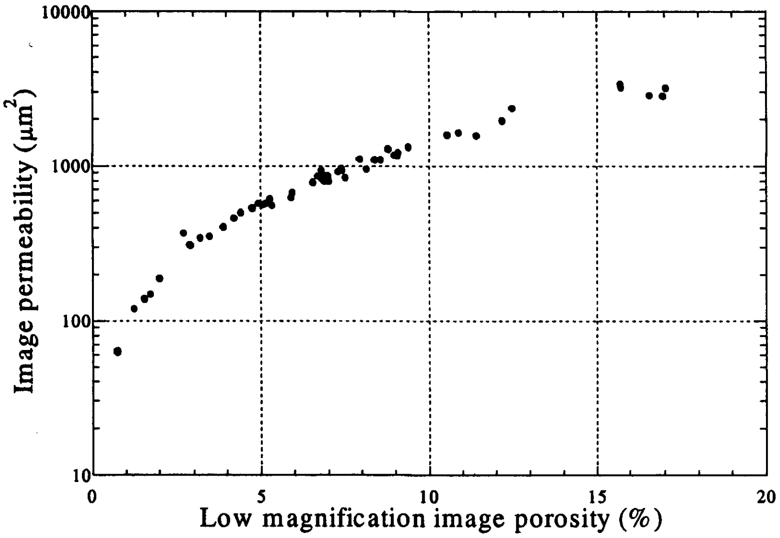

Figure 6.24. Calculated image permeability against measured low magnification image porosity for all 54 plugs

To test whether the derived image permeability is a good estimation of gas permeability (§5.3.5) these two parameters are cross plotted (Figure 6.25a), a significant relationship exists (r=0.79, in linear space). The relationship is not 1:1, and if image permeability were converted to mD (dividing by 0.9871) the difference between the two parameters is increased further. It is observed that the image permeability systematically calculates higher values of permeability than is measured on the plugs. The relationship between image porosity and gas permeability (Figure 6.25b) is stronger (r=0.84) than the image permeability-gas permeability relationship for the purposes of gas permeability prediction within this reservoir.

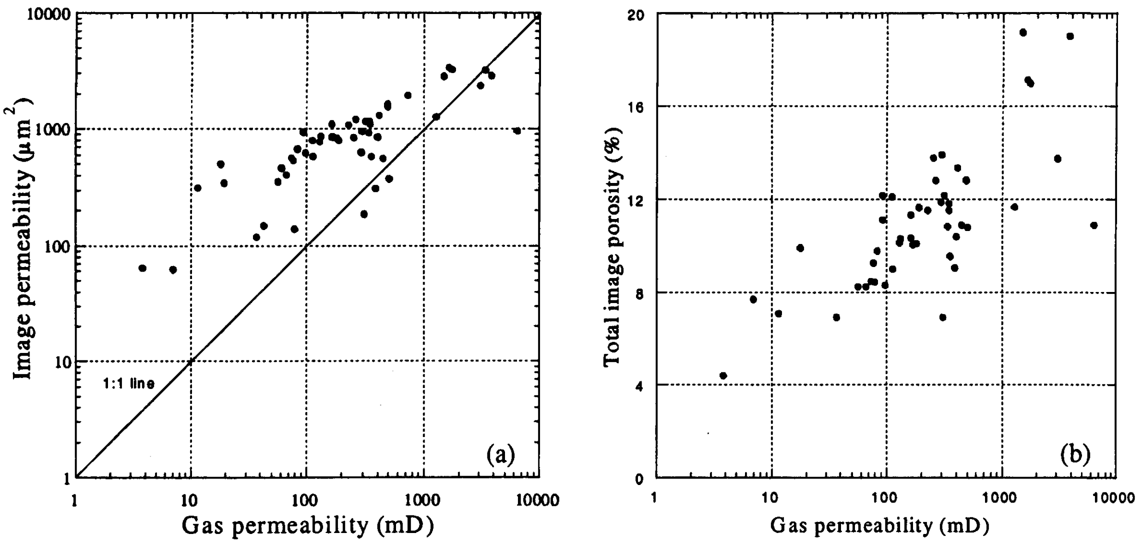

Figure 6.25. Calculated image permeability against plug gas permeability

6.6 Summary

The basic requirement for electron microscopy to be used in quantitative analysis, is to produce an image which can be segmented into pore and grain phases. It has been established in this study that the pore space can be accurately identified. The mineral phases were not so easily identified, which has led to the grouping of data for all minerals with a grey scale value greater than 202. A possible solution to this loss of data resolution would be to visually examine the SEM images, identify mineralogy and assign the quantitative values from the image analysis. The variation in the grey scale peak present in several of the minerals is attributed to element substitution within the minerals adjusting the atomic number. It is proposed that the spread of each mineral peak is related to overlapping minerals, end-trim polishing and the depth of penetration of the electrons. The presence of bubbles within the images does not introduce problematic errors. There was a repeatability problem with the measurement of pore area. The limitations of the SEM images and image analysis package have been investigated and it is concluded that the image data is fit for the purpose for which it is used.

The choice of image magnification was x30 and x150, which strikes a balance between data resolution and data volume. The images provide 2,662,400 pixels of information for each plug; this data is condensed and represented by five statistical descriptors. The question of whether these pixels are representative of plug fabric when they have been averaged is beyond the scope of this study, due to time and data considerations. However, some of the image parameters have a significant relationship with the core plug measurements, suggesting the averaged pixels are representative of the plug. A method of investigating the relationship between the high and low magnification data, could be by comparison of the high magnification images 1, 8, 4 and 5 with their respective low magnification images 12, 11, 13 and 9 (Figure 6.2).

Image porosity was calculated, the main potential for errors being that homogeneity must be assumed within both the high and low magnification images, and that these images are considered representative of the core plug. A secondary error is the duplication of pores measured. Porosity indexes are calculated using total image porosity and plug porosity, which may reflect the homogeneity of a set of samples. Image permeability has been expressed in terms of image porosity and specific area pore. The image permeability has a significantly strong relationship with gas permeability, demonstrating the potential for calculating 3D parameters from 2D data.

The images were characterised both quantitatively and qualitatively. Pore roughness and aspect ratio parameters were calculated from image analysis data. The data for each plug was divided into seven groups of specific pore size ranges, as pore shape parameters are only effective if pore size is considered. The low magnification images were categorised according to six qualitative image characters, with the aim to generate petrophysical facies.

The non-linear core plug porosity-permeability relationship which is poor for permeability prediction purposes within this reservoir can often be understood from examination of the images. It is seen from the images that permeability decreases as the amount of diffuse *clay* within an image increases, and as grain size and sorting decreases. There is an apparent relationship between plug porosity and areas of *clay* and pore; the plug porosity range is approximately the same as the range for the sum of areas pore and *clay*.

CHAPTER SEVEN

A comparison of image analysis and core data

7.1 Introduction

The understanding and interpretation of core analysis and image data obtained in Chapters 5 and 6 are combined in this chapter, to gain a greater comprehension of plug pore morphology and fluid flow which relates to porosity and permeability.

Chapter 7 is divided into five sections:

7.1 Introduction.
7.2 Comparison of image and plug data.
7.3 Comparison of permeability, plug and image porosities.
7.4 Examination other qualitative and quantitative image data discussed in Chapter 6 and their relationship with permeability and porosity.
7.5 Summary.

7.2 Comparison of image and plug data

Figures 7.1 and 7.2 compare image data (area pore, area *clay**, area quartz and area 'other', Chapter 6) and plug data (permeability §5.3.5 and porosity §5.4.3) for wells 1 and 2. The points have been joined for pictorial representation and not to demonstrate variability with depth. The plots illustrate trends and not rigid relationships between the six parameters. For example, area pore (image porosity) has a relationship with permeability (see §7.3.5).

* The term *clay* is defined as a specific grey scale range within the SEM images and it includes detrital and diagenetic clay as well as software artefacts such as grain edge effects (§6.2.4.2).

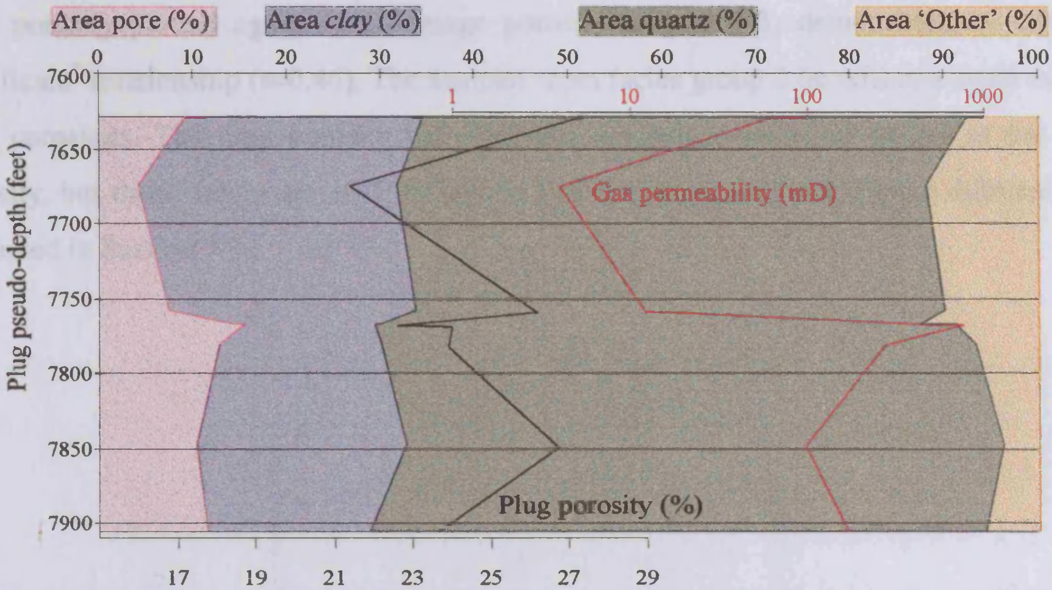

Figure 7.1. Well 1, percentage areas from images and plug porosity and permeability, nine data points

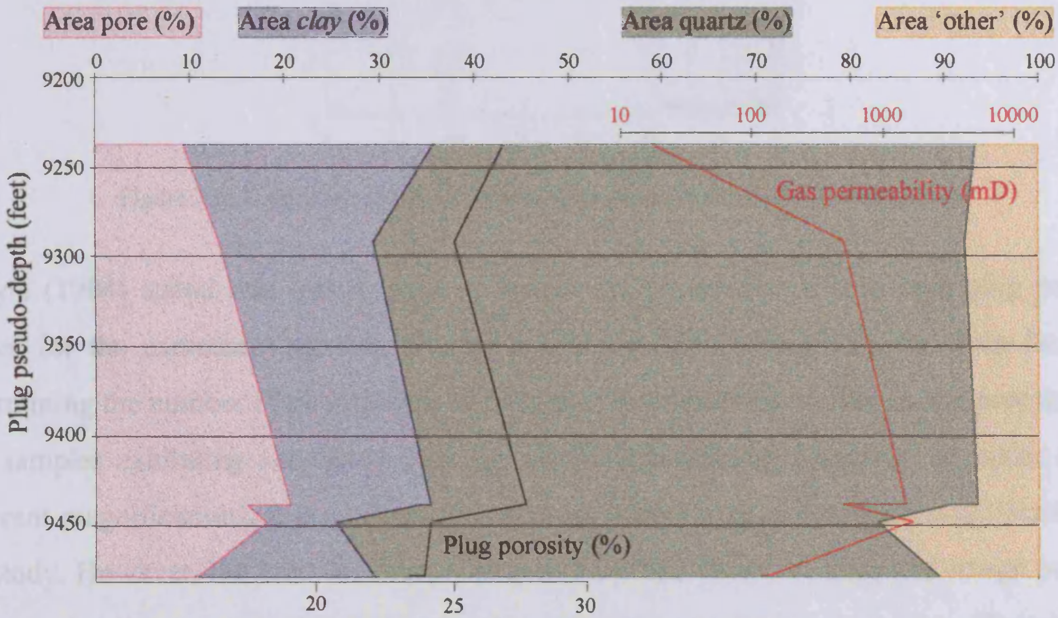

Figure 7.2. Well 2, percentage areas from images and plug porosity and permeability, six data points

7.2.1 A comparison of image and plug porosity

Image porosities are not simply the total area pore space divided by the area of the image, but the sum of pore areas that fall within a specified size range (13-1334 μm^2 for high magnification images and 1334 μm^2 to 1 mm^2 for low magnification images), divided by the area of the entire image (§6.2.5.1). Theoretically there is no duplication of measured pores, which is why, if homogeneity is assumed, the two porosities may be summed and total image porosity generated.

Plug porosity plotted against total image porosity (Figure 7.3) demonstrates a weak but significant* relationship (r=0.46). The samples from facies group 2 lie within a small range of plug porosities. The plug porosity has a similar percentage range of values as the image porosity, but those values are 10-15% higher. Possible explanations for these differences are discussed in Section 7.3.

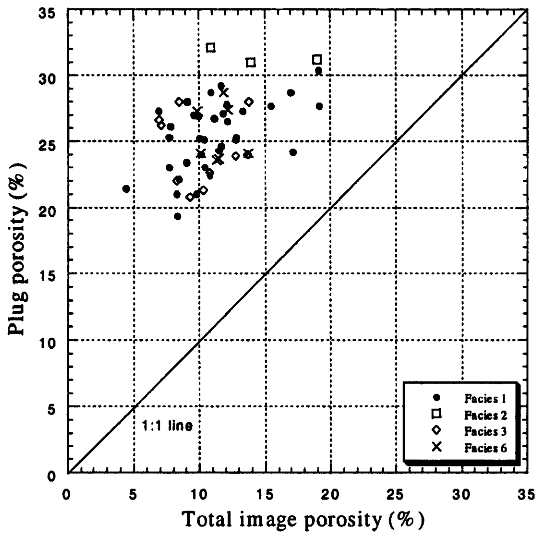

Figure 7.3. Total image porosity against plug porosity with facies distinguished.

Ruzyla (1984) stated that image porosity values are in agreement with core plug porosity values for the carbonate samples. Ruzyla concluded that pore size is the main factor in determining the number of photographs to be taken on an end-trim to capture the porosity, and that samples exhibiting very wide pore size distribution require images to be taken at two different magnifications. It is assumed that Ruzyla (1984) used one or two magnifications in his study. However, the fact that Ruzyla acquired similar values of plug and image porosity suggests that the pore size distributions in his carbonate samples was not large. Ehrlich et al. (1991b) found that plug porosity was greater than image porosity, and concluded that this was due to some of the micro-porosity not being counted in the image porosity calculation. This was evaluated by adding higher magnification images to the data set until the missing image porosity was captured and was equal to plug porosity.

Assuming that the measurement of plug porosity is accurate in this study, it can be concluded that image porosity does not capture all the interconnected porosity within a plug. The

* Unless otherwise stated the significance of the correlation coefficient r, has been tested at a probability level of 0.05.

porosity being excluded probably exists in the pores which fall outside of the measured pore sizes (13 μm^2 to approximately 1 mm^2). Heterogeneity at the image scale is also thought to contribute to the differences, since it is hypothesised that *clay* seen in the images (§6.2) is a source of micro-porosity (pores <13 μm^2) which is not included in the image porosity calculation.

The plots of high and low magnification image porosity data against plug porosity (Figure 7.4) reveal that the high magnification image data has a smaller range of porosity than the plug porosity. The narrow range is attributed to the size of the pores being small. A provisional conclusion which can be drawn from Figure 7.4 is that facies 2 is homogeneous at the plug scale, which is suggested by the stable plug porosity, but heterogeneous at the image scale, due to a large image porosity range both in the low and high magnification data.

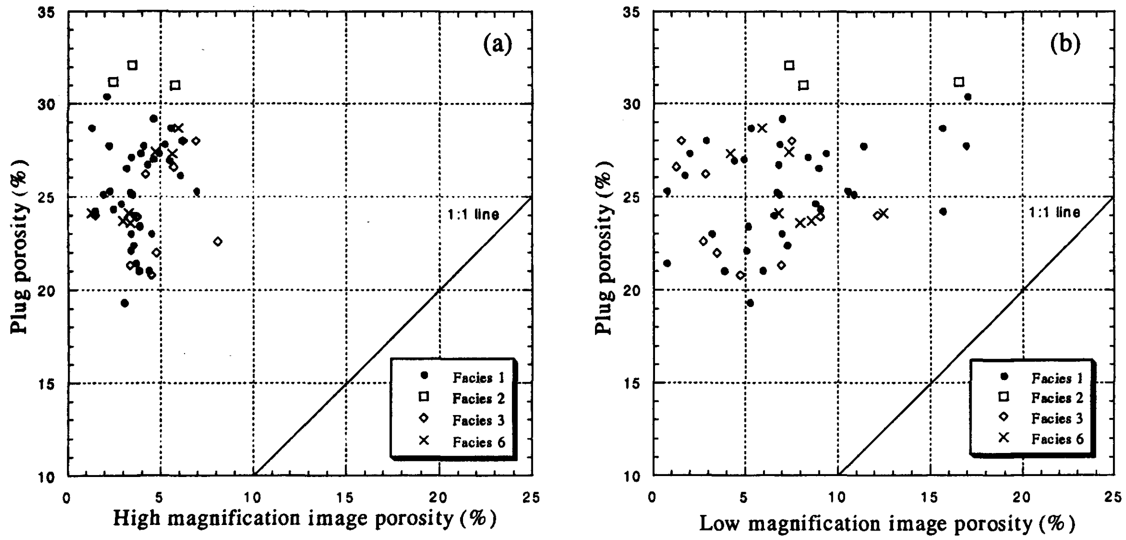

Figure 7.4. Plug porosity against image porosity, with facies distinguished, for (a) high magnification data (b) low magnification data.

7.3 Permeability, plug and image porosities

7.3.1 Setting the scene

The relationship between porosity and permeability is traditionally used in the hydrocarbon industry to assist in reservoir flow prediction. A simple linear relationship is not observed for the data set used in this study and consequently, image analysis has been used to try and understand the nature of the plug porosity-permeability plot. All of the gas permeability and plug porosity values are plotted (199 points, r=0.32 in log:lin space, Figure 7.5a) and compared with a subset of data which has associated image data (54 points, r=0.43 in log:lin space, Figure 7.5b), both relationships are significant. The purpose of these two plots is to verify whether the results obtained for the image-plug data set, are representative of the entire data set (i.e. is the subset a representative sample of the variability seen within the parent data set). A multivariate Hotelling T^2 test confirms that the subset in Figure 7.5b is representative of the parent data set.

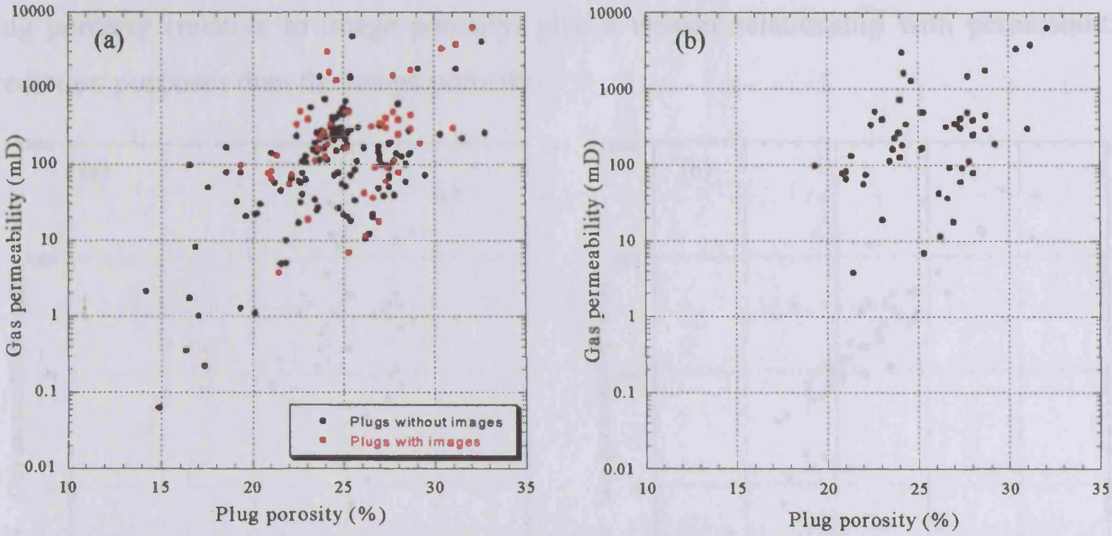

Figure 7.5. Permeability against plug porosity for (a) the entire data set and (b) the plugs which have associated image data

Factor analysis was used (Appendix D) to study the interrelationship of thirteen parameters: gas permeability, Klinkenberg permeability, plug porosity, total, low and high magnification image porosities, formation resistivity factor, sum of pore area in the low magnification data, the *b*-factor calculated by Service Company 2 (SC2), average perimeter divided by the sum of pore area in the low magnification data, sum of area *clay*, sum of area *clay* plus area pore and, average perimeter divided by area equivalent radius for the low magnification data (see Chapters 5 and 6 for parameter definitions). The data are numerical ranges with no ordinal (e.g. grain size) or nominal (e.g. facies) data. The computer package 'Statistica' (Version 4.1) was used to perform the factor analysis calculations. It was observed from the eigenvalues after performing factor analysis, that 90% of the variance was contained within the first four factors, which was a massive reduction in data. It was therefore concluded that the data are strongly interrelated.

7.3.2 Data comparison

The plug porosity and image porosity are plotted against gas permeability (Figure 7.6). The image porosity clearly has a more significant relationship (r=0.84, in linear space with the permeability values logged) with permeability than plug porosity (r=0.41, in the same space). The image porosity-permeability plot would therefore be more useful for the prediction of permeability within this reservoir. Internal Report 3 states that a poor relationship between permeability and porosity has been noticed previously in many reservoirs and it is a well accepted fact that plug porosity values are normally greater than the pore volume utilised by permeability. The examination of Figure 7.6 supports this statement, as the high values of plug porosity (relative to image porosity) give a weaker relationship with permeability for prediction purposes than the image porosity.

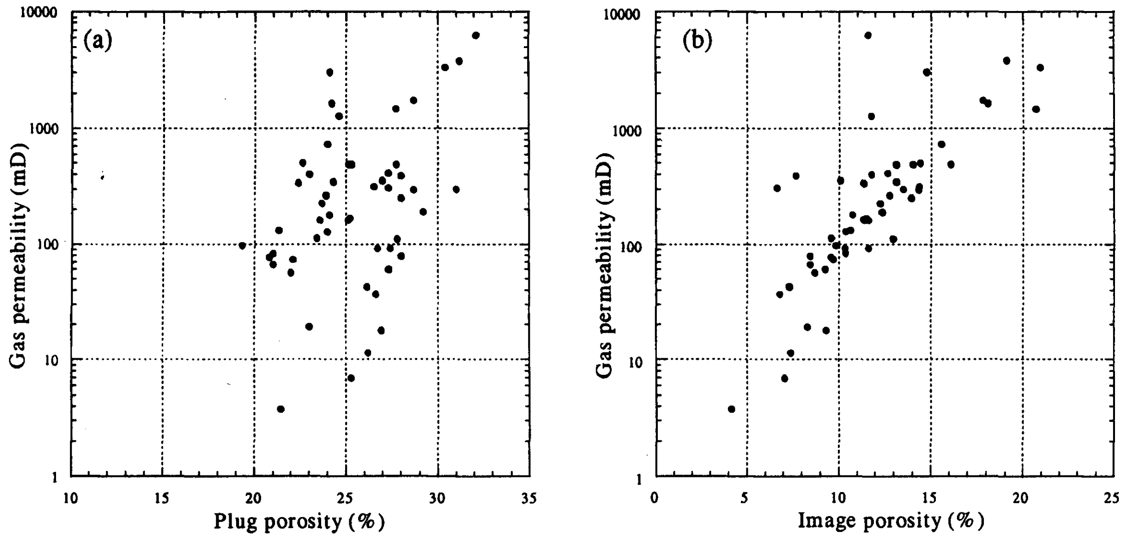

Figure 7.6. Permeability against (a) plug porosity (r=0.41), (b) total image porosity (r=0.84). (Note the shift in the x-axis scale)

The question which is attempted to be answered in Section 7.3 is, *"Why does the 2D image porosity show a stronger relationship with permeability than plug porosity?"*

There are several facts about the data sets which need to be considered before this problem is investigated. Pores less than 13 μm^2 (9 pixels) are not measured and therefore, in the calculation of image porosity, micro-porosity is ignored. These micro pores may be counted as part of their surrounding solid, or at a grey level in-between the epoxy and the surrounding pore. The SEM images are taken at right angles to the direction of the permeability measurement and therefore image porosity is also generated at right angles. The image porosity gives consistently lower values than the plug porosity (§7.2.1). The thirteen images taken on both the end-trims and the sides of seven cubic plugs were not positioned exactly according to the grid shown in Figure 6.2, since images were not taken where excessively large pores or grains were present to avoid biasing.

Four hypotheses have been investigated in an attempt to solve the problem of why image porosity has a stronger relationship with permeability than plug porosity.

Hypothesis 1; *Small pores do not contribute to permeability.*

Hypothesis 2; *Fixed orientation of the permeability measurement with respect to image porosity helps to constrain this relationship, (i.e. plug anisotropy is important).*

Hypothesis 3; *The relationship between permeability and plug porosity is affected by the clay content.*

Hypothesis 4; *Large pores are present within the plugs which are not captured with image analysis and do not contribute to permeability, but increase the value of plug porosity.*

Sections 7.3.3 through 7.3.6 will test, within the limits of the data set, the validity of these four hypotheses.

7.3.3 Hypothesis 1

"Small pores do not contribute to permeability."

Plugs 4a and 9c from well 2 (Figure 7.7) have the same permeability (491 and 490 mD respectively) but different image porosity values (12.8% and 15.5% respectively). There are several possible explanations for these discrepancies, not all of which can be tested: plug laminations biasing of the calculated image porosities, gas bypass (§5.3.5) increasing the permeability of plug 4a, pore tortuosity differences (§2.3.4), grain size, grain sorting, clay, fractures, or the presence of pores in plug 9c which do not contribute to fluid flow.

To investigate the possibility of a non-effective flow porosity, the distribution of high and low magnification image porosity were compared for plugs 4a and 9c. It was observed that the plugs have a similar low magnification image porosity (10.9% and 11.4%), and different high magnification image porosity values (1.9% and 4.1%). It is hypothesised from this observation that the low magnification porosity has a stronger influence on permeability than high magnification image porosity.

It is observed that plugs 1a and 11a (Figure 7.7) have approximately the same total image porosity values (9.9% and 10.1% respectively) but an order of magnitude difference in permeability (17.9 and 128 mD). In plug 11a 64% of the image porosity was attributed to the low magnification data and in plug 1a 44%. Again, the low magnification image porosity is seen to contribute more strongly to the permeability.

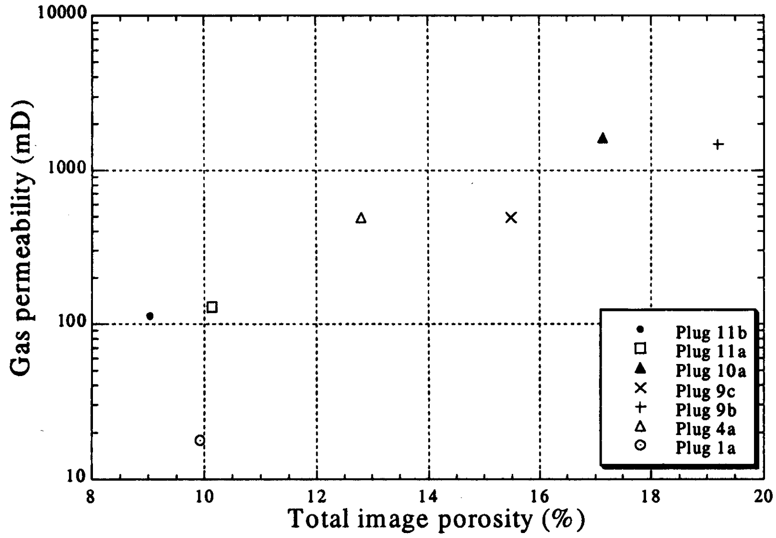

Figure 7.7. Gas permeability against total image porosity, for well 2

To investigate whether the low magnification porosity always has a stronger influence on permeability than the high magnification image porosity, the two porosities have been plotted against permeability. The low magnification image porosity data (Figure 7.8a) and the high magnification data (Figure 7.8b) have a positive and negative trend respectively. The different trends are interpreted as demonstrating that as the area of small pores increases (measured in the high magnification data), the permeability decreases, due to the assumed corresponding decrease in large pores, (this assumption is collaborated in Figure 7.9). It is therefore concluded that small pores do not contribute as significantly to fluid flow as large pores, which substantiates the conclusions drawn from Figure 7.7. Facies do not constrain the data plots.

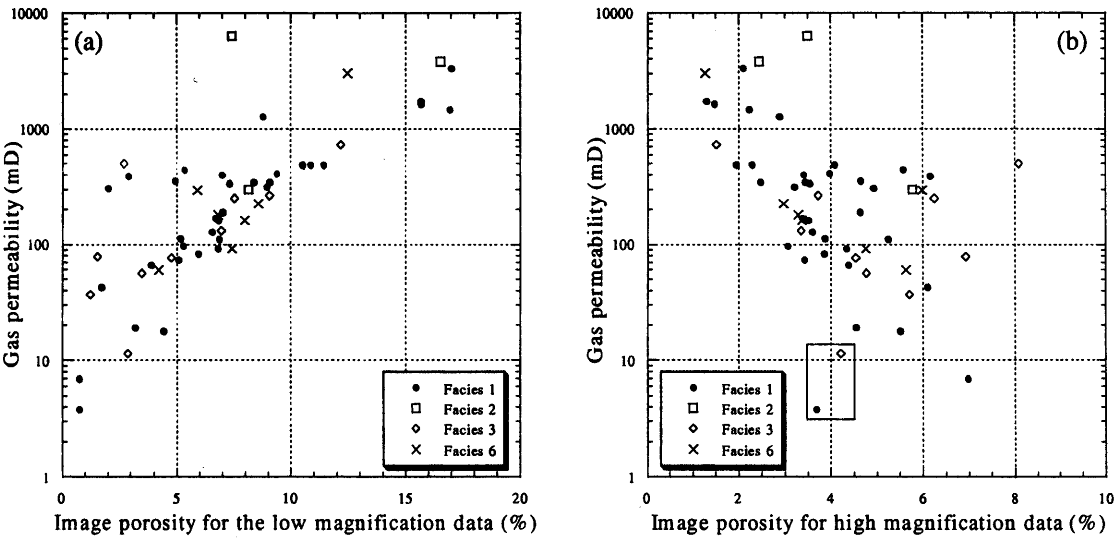

Figure 7.8. Gas permeability versus image porosity, with facies distinguished for (a) low magnification data and (b) high magnification data, (box indicates data outliers)

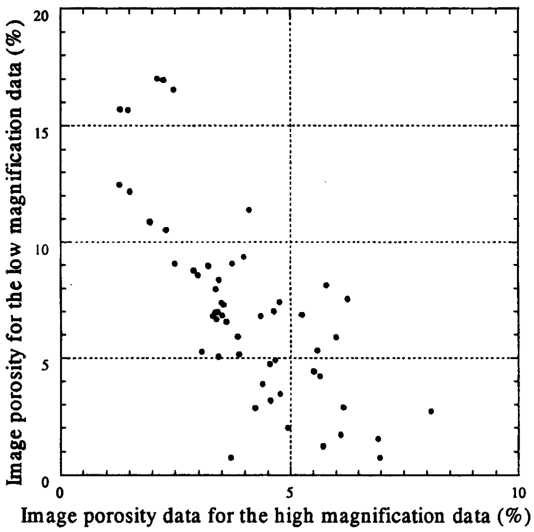

Figure 7.9. Low magnification image porosity against high magnification image porosity

The examination of the SEM images from the lower outliers (boxed in Figure 7.8b), revealed large amounts of clay and/or cement, this prompted a plot of permeability against image porosity distinguishing which plugs contained clay and/or cement was present within the plugs (Figure 7.10). The presence of clay or cement was determined from visual examination of the core plugs by SC2 and was recorded in the core plug descriptions (§3.2). Additionally, SC4 stated that 'Ferroan calcite cement is apparently the strongest control over permeability distribution [for this data set], but on editing out concretionary cemented samples the main controls are mud, indeterminate authigenic clays, cement and grain size.' It is concluded that as a general result, plugs which had a similar image porosity but no clay (Figure 7.10a), had higher permeabilities than those with clay, and plugs containing no cement tended to be within a restricted range of image porosities (Figure 7.10b).

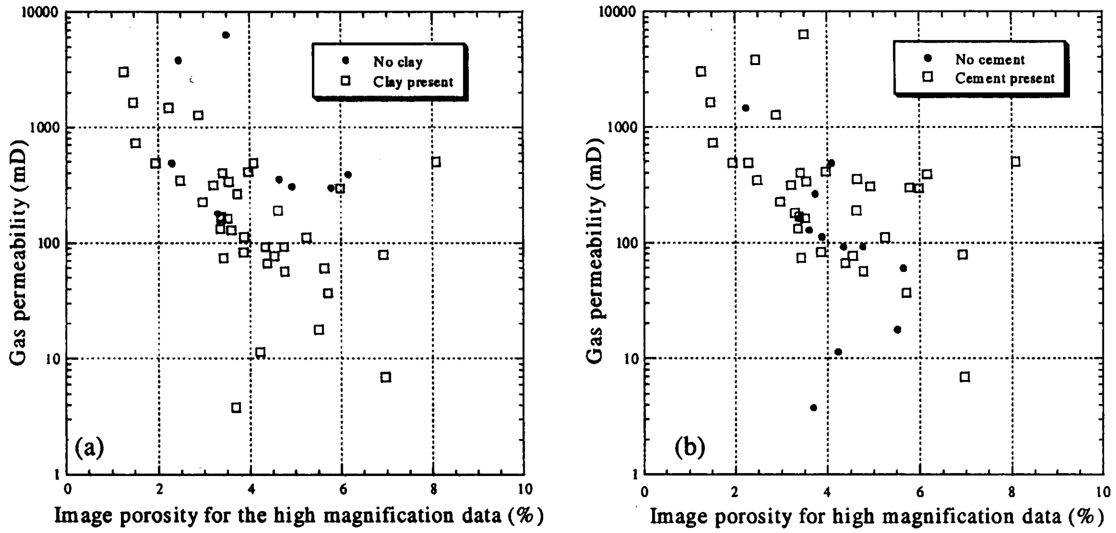

Figure 7.10. Gas permeability against image porosity for the high magnification data showing (a) whether clay is present in the samples (b) whether cement is present in the samples.

The average pore size calculated from the high and low magnification images was plotted against plug porosity to test for a relationship; there was none. To investigate further the affect of pore sizes on permeability, pore size distributions (§6.2.5.2) were used. Gas permeability is plotted against image porosity for image porosity ranges 1, 3 and 7 (Figure 7.11). Range 1 (small pores) has a negative gradient (gradient m =-0.84 and r=-0.63, all three values of r were generated in log:lin space), range 7 (largest pores) has a positive gradient (m = 4.45 and r=0.76) and range 3, an intermediate range, shows no preferred orientation (m = -0.13 and r=-0.27). All three data sets have significant relationships, although the data from the intermediate range is border-line.

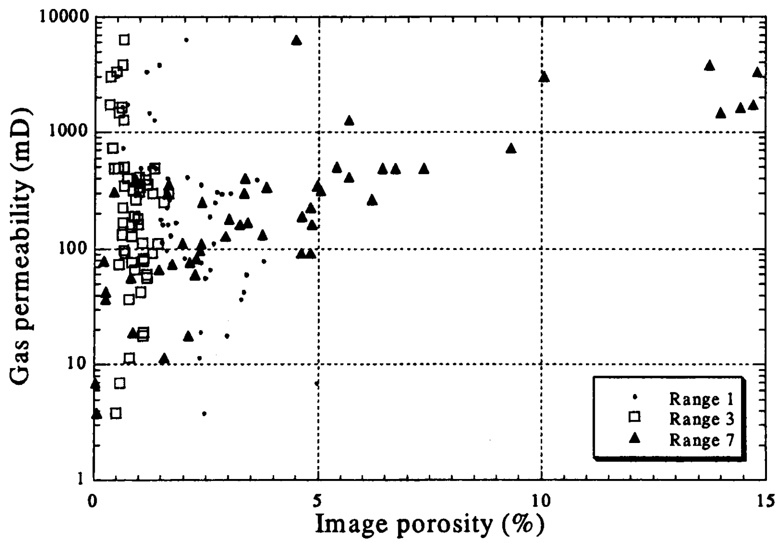

Figure 7.11. Gas permeability against image porosity for three selected ranges of image porosity taken from the same 54 plugs

To investigate the distribution of pore size ranges with permeability, pore size ranges were plotted against the pore size range as a percentage of the entire image porosity calculated for individual plugs. Two plugs were chosen for each plot, with each plot representing either low (7 & 12 mD), medium (97 & 112 mD), high (490 & 491 mD) or very high (3343 & 3057 mD) permeability plugs (Figure 7.12). To reduce sampling biases, such as localised depositional environments, the two plugs used in each plot were taken from different wells, where practical. The four plots in Figure 7.12 demonstrate that that there is a direct relationship between pore size distribution and permeability, with the percentage of small pores decreasing and the sum of the area of large pores increasing with increasing permeability.

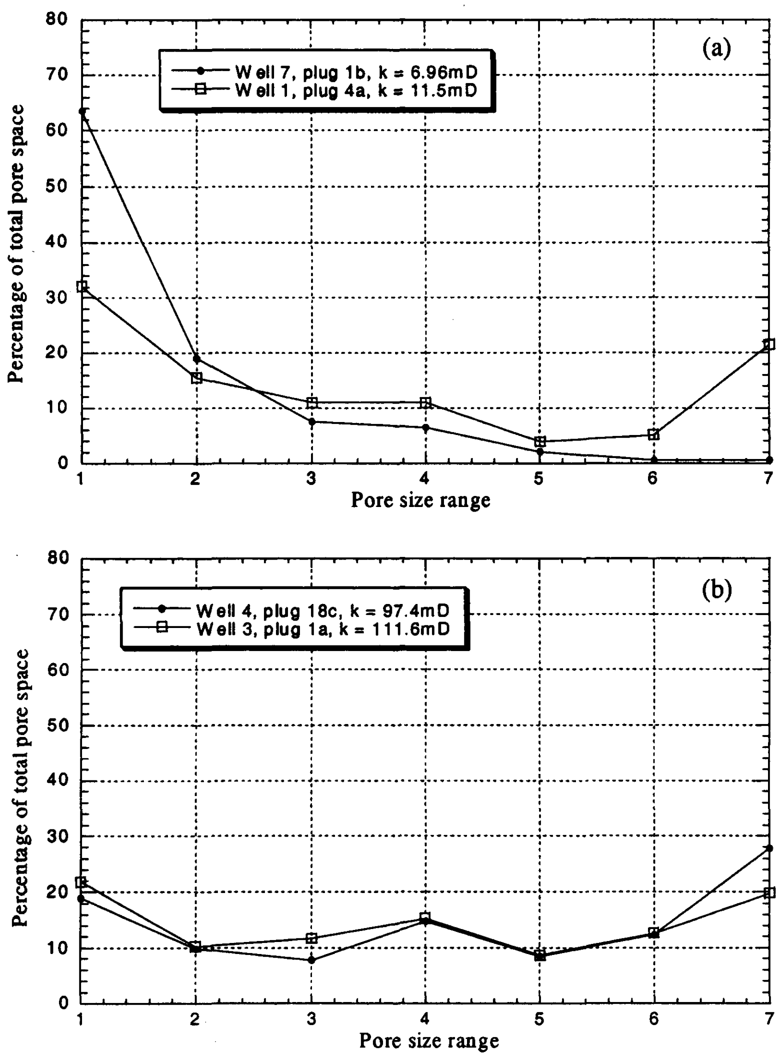

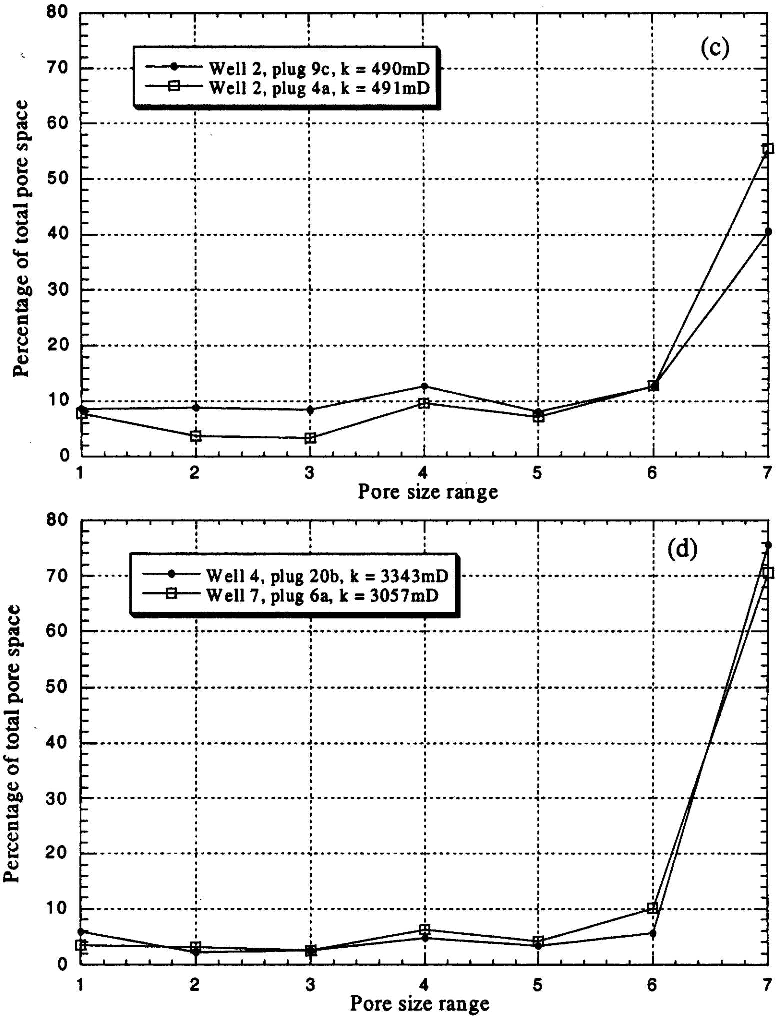

Figure 7.12. Pore size range as a percentage of the entire image porosity against the seven pore size ranges. Each plot consists of data from two plugs within a specified range of permeability. (a) Low (7 & 12 mD), (b) medium (97 & 112 mD), (c) high (490 & 491 mD) and (d) very high (3343 & 3057 mD) permeability plugs.

To quantify the relationship observed for the eight plugs in Figure 7.12 for the entire data set, a ratio of pore size range 7 to pore size range 1 was made and plotted against permeability (Figure 7.13). A significant trend (r=0.78, in linear space using logged values) was observed, which would be good for permeability prediction purposes.

The outlier ringed in Figure 7.13 is plug 6a from well 6. This plug only has a small low magnification porosity (3.5%) and large high magnification image porosity (7.4%), and a large associated permeability (6368 mD), which is contradictory to the conclusion drawn from Hypothesis 1. The permeability value, however, is not believed to be real as it is large for the reservoir and so it is proposed that the plug is fractured.

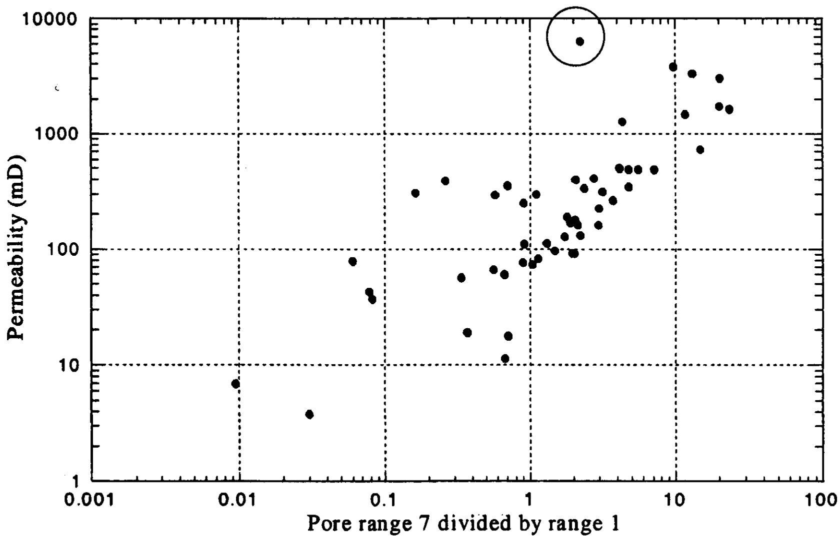

Figure 7.13. Gas permeability against pore range 7 divided by range 1 (ringed is an outlier plug 6a from well 6)

Plugs with a low porosity generally have more large pores than plugs with the same permeability but larger porosity values (Figure 7.14). Archie (1950) noticed the same parallel trend for different formations in a permeability-porosity plot.

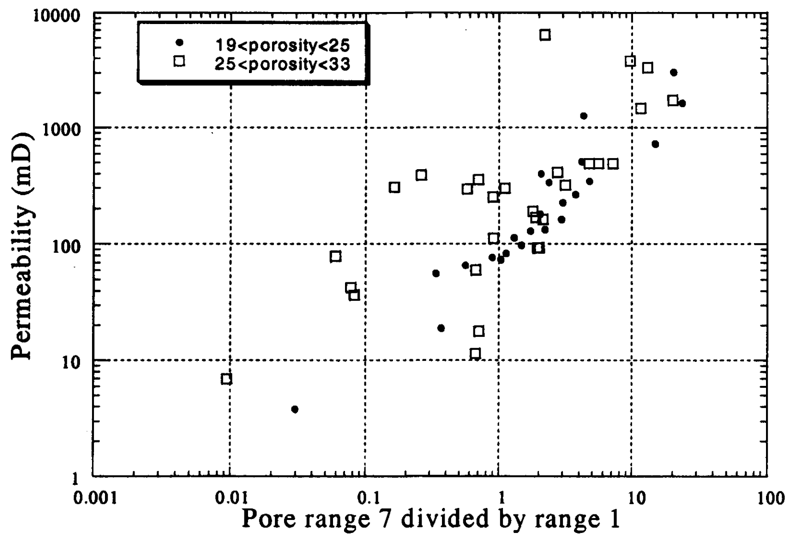

Figure 7.14. Gas permeability against pore range 7 divided by range 1 with two plug porosity ranges distinguished

There are several other methods of evaluating pore size distributions (PSD) within the plugs for comparative purposes with the image data. These include S_{wi}, (initial water saturation, §2.5.2), mercury injection capillary pressure (MICP) curves and NMR (nuclear magnetic resonance). Basan et al. (1997) have compared PSD results from images, MICP curves and NMR and concluded that the PSD from images is not usually comparable to the entire spread of MICP pressure points or NMR relaxation times.

7.3.4 Hypothesis 2

"Fixed orientation of the permeability measurement with respect to image porosity helps to constrain the image porosity-permeability relationship, (i.e. plug anisotropy is important)."

Hypothesis 2 was tested by using seven cubic sandstone plugs from the reservoir. These plugs had permeability measurements made on them from all six sides (Figure 7.15). Plug porosity was also measured and SEM images taken on three orthogonal faces (where possible) using the same grid system as on the cylindrical plug end-trims (Figure 6.2). Together these provided a data set to investigate plug anisotropy and the effects on permeability.

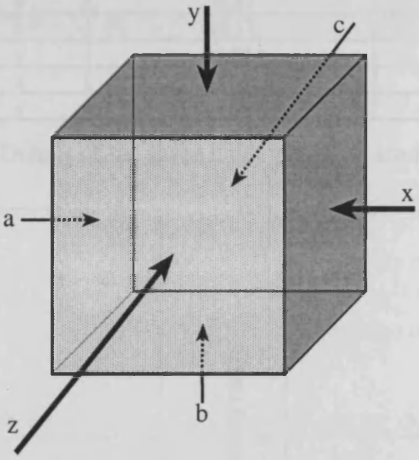

Figure 7.15. Schematic of a cubic plug with its faces labelled

The permeabilities were measured by SC5 using a gas permeameter with a special cubic core holder. The confining pressure (300 psig) and the mean pressure applied across the plug was equal in all directions, and therefore the permeability data through all cube faces are comparable. Sample 1 was finely laminated (mm sand-silt scale) and samples 2-7 were medium grained sandstones. Only sample 1 showed visible laminations (pers. comm., SC5), Table 7.1 gives details of the eight cubic plugs.

To investigate plug anisotropy the permeability and image porosity data were coupled, such that the permeability through plug 1 face x was coupled with the image porosity calculated on face x. A plot of permeability against image porosity (Figure 7.16a) was then performed using this coupled data. This plot of coupled data has a significant relationship of r=0.79. To test if this plot had a strong relationship due to the directional coupling of the data, the plot was reproduced with the direction constraint removed by de-coupling the data. For example, by plotting permeability from plug 1 face x with the image porosity measured on face y. This second permeability-image porosity plot (Figure 7.16b) again had a significant relationship (r=0.76).

Plug number	Plug face	Total image porosity (%)	Permeability (mD)
1	x	5.40	18.131
1	y	7.95	17.989
2	b	11.68	118.82
2	c	12.17	109.016
2	x	10.94	137.464
3	b	10.72	196.231
3	x	11.23	202.49
3	z	10.73	222.43
4	x	8.37	83.162
4	y	6.13	72.385
4	z	5.76	27.848
5	x	13.78	470.468
5	z	12.79	500.177
6	x	10.81	275.328
6	z	10.17	227.578
7	c	8.59	69.395
7	x	8.31	108.555
7	y	8.30	108.784

Table 7.1. Details of the seven cubic plugs, all are from well 1

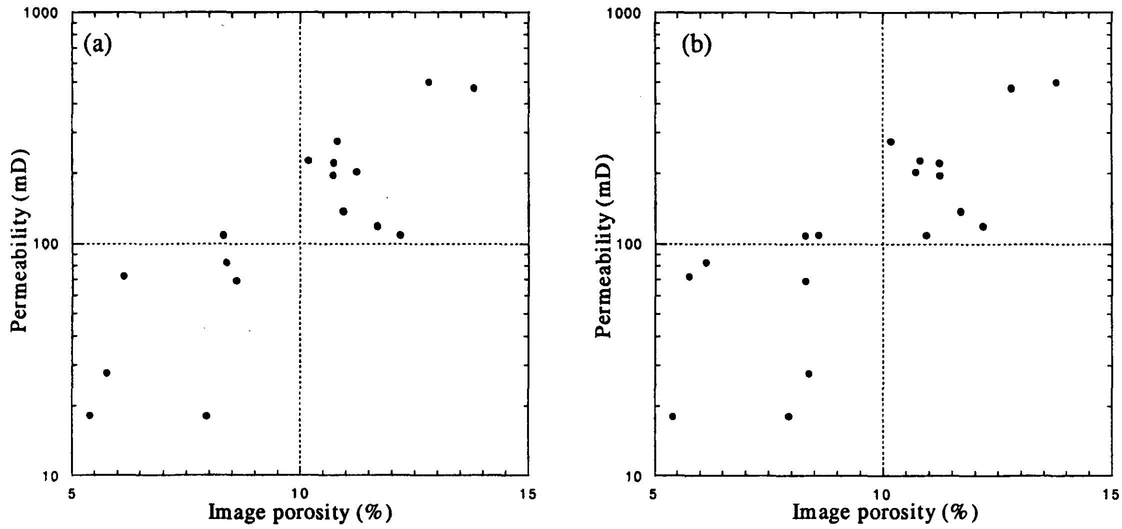

Figure 7.16. Gas permeability versus total image porosity for (a) the coupled data (r=0.79) (b) the de-coupled data (r=0.76)

The change of 0.03 in the correlation coefficient between Figures 7.16a and b is not statistically significant. It is therefore concluded, that plug anisotropy at this scale does not play a significant role. However, these results are not conclusive as if the rocks were homogeneous the differences seen in Figure 7.16 could be due to experimental error. If however, the rocks were heterogeneous, the image porosity would be expected to have little correlation with permeability. Therefore, two assumptions have to be made for the conclusions to be considered valid: (i) the rocks are not homogeneous at the image scale and (ii) image porosity is representative of the pore morphology. These results are important as they demonstrate that the acquisition of orientated plugs would not improve the permeability-porosity relationship, therefore saving time and expense.

Cubic plug sample 7 was chosen to investigate plug anisotropy at the pore scale. It has similar permeabilities on two pairs of orthogonal faces (percentage difference of 108.68 ± 0.25 mD for all four values), and a different value of permeability on the third pair of faces (68.82 ± 0.58 mD, Table 7.3). In order to test whether there was significant pore orientation on any plug face the mean resultant $\overline{\mathbf{R}}$, which is a measure of dispersion, was computed (Table 7.2) for the pore orientation data set, and tested for significance using the Reyleigh test of uniformity (Mardia, 1972). The orientation values are not significant and therefore, could not be compared between plug faces or with the anisotropic permeability values of the plug.

Plug face	Magnification	$\overline{R}$
c	High	0.06
c	Low	0.08
x	High	0.06
x	Low	0.06
y	High	0.11
y	Low	0.12

Table 7.2. Orientation data of cubic plug 7 for the high and low magnification data on side c, x and y

It is proposed that preferential flow paths through the plugs do exist, since the permeability measured through opposite faces are similar (Table 7.3, relative error of ± 1.7%) and often one or two of the paired faces have distinctly different permeability values from the other paired faces. It is therefore likely that the latter differences are real. Figure 7.17 shows two conceptual models for cubic plug samples with planar fabric which may be an explanation for the differences in permeability. Figure 7.17a shows simple vertical planar fabric, which could be a model for samples 1, 7 and 8, where the y-and x-directions have a similar permeability which is greater than the z-direction. Figure 7.17b shows dipping planar fabric, a possible model for sample 6, where the dipping fabric is such that the z-direction would have the lowest permeability, the y-direction an intermediate, leaving the x-direction with the easiest flow path, or highest permeability. The orientation of the plugs in real space is unknown.

Plug face	x	y	z	a	b	c
Sample number	Gas permeability through each face (mD)					
1	18.131	17.989	1.055	18.14	18.008	1.055
2	137.464	118.211	111.602	137.243	118.82	109.016
3	202.49	194.072	222.438	204.009	196.231	173.339
4	83.162	72.385	27.848	78.944	72.447	27.659
5	470.468	527.344	500.177	469.694	522.01	504.703
6	275.328	258.876	227.578	275.948	257.228	227.578
7	108.555	108.784	68.235	108.932	108.454	69.395
8	0.298	0.289	0.108	0.298	0.29	0.11

Table 7.3. A table showing the permeabilities in different directions form the cubic plugs

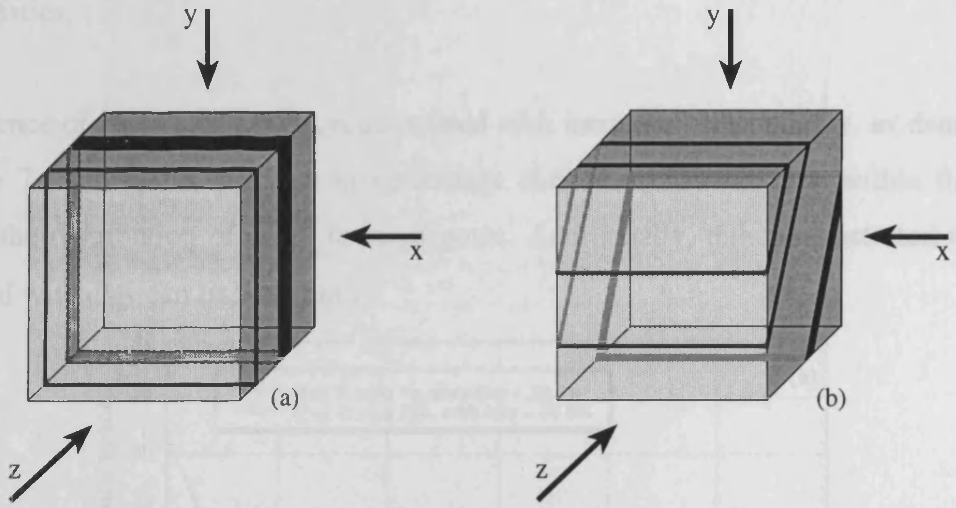

Figure 7.17. Conceptual model of possible anisotropy within cubic plug samples (a) 1, 7 and 8 and (b) 6

7.3.5 Hypothesis 3

"The relationship between permeability and plug porosity is affected by the clay content."

Archie (1950) foresaw that the type of clay minerals present within a reservoir would play a greater role in future studies, which has been substantiated by many later papers (see §2.4). It was suspected that *clay* was providing unrealistically high estimates of diagenetic and detrital clay. Enterprise Oil have substantiated this error from XRD measurements; SC4 calculated 0-9% kaolinite (the main clay mineral in the reservoir) and 0-32% detrital clay in the reservoir (§4.6). The approximate amount of *clay* calculated in the reservoir from image analysis is 15-30% (implying clay is always ≥15% of the rock).

Internal report 4 concluded that micro-pores are associated with detrital and authigenic clays, altered grains, mudstone pellets and clasts. The report states that micro-porosity tends to be highest in the argillaceous sandstones with floating mudstone clasts facies defined by SC4, which is most comparable with Internal Report 1 defined facies 3 (§4.4). Therefore, it would be expected that the most depressed values of permeability would be associated with facies group 3, however Figure 7.8 reveals there is no evidence for this. Pallatt et al. (1984) demonstrated how the flow properties of two fields in the North Sea are similar, although one has a rock consisting of 10% filamentous illite and the other 0.5%. This paper also demonstrates how fluid flow characteristics cannot be predicted from the quantity of illite present. It was not noted however that both fields have the same amount of total (defined as illite, smectite, chlorite and kaolinite) clay present, which may explain the similar flow characteristics.

The presence of many small pores is associated with increased areas of *clay*, as demonstrated in Figure 7.18, where a decrease in percentage *clay* from 30% to 13% within the images reverses the distribution of small to large pores. Additionally, this demonstrated that pores associated with *clay* can be > 13 μm^2.

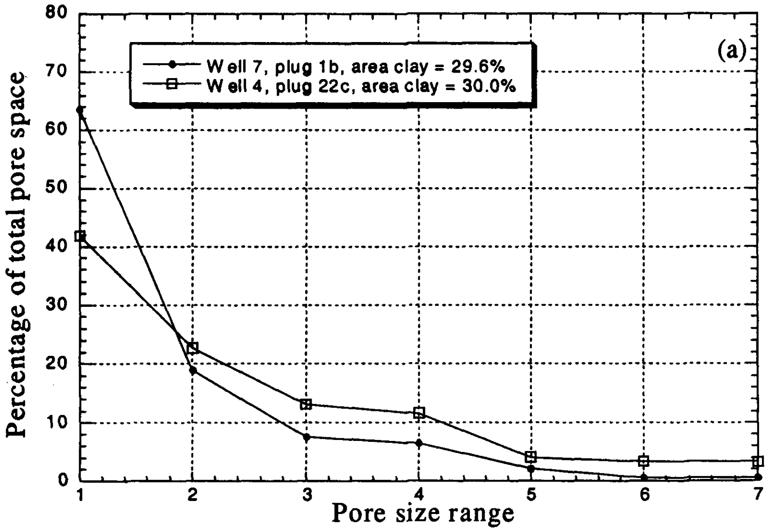

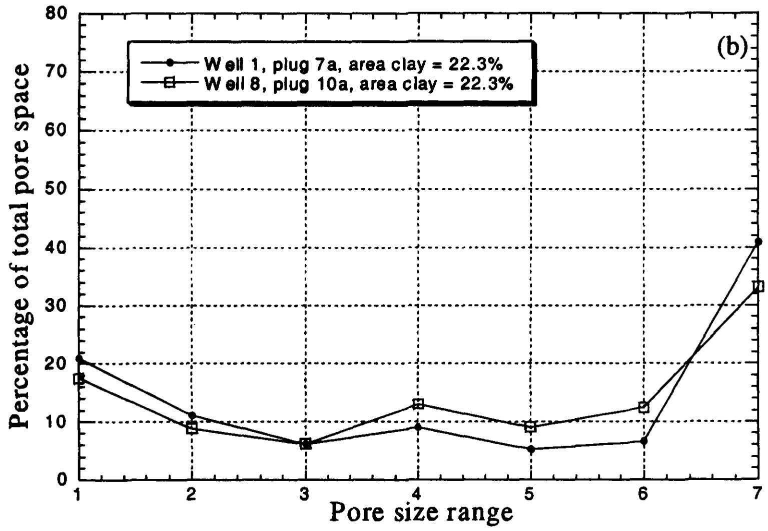

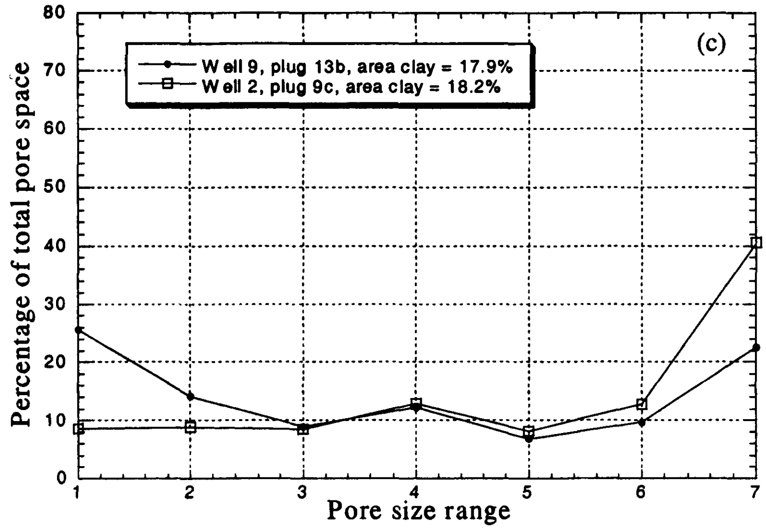

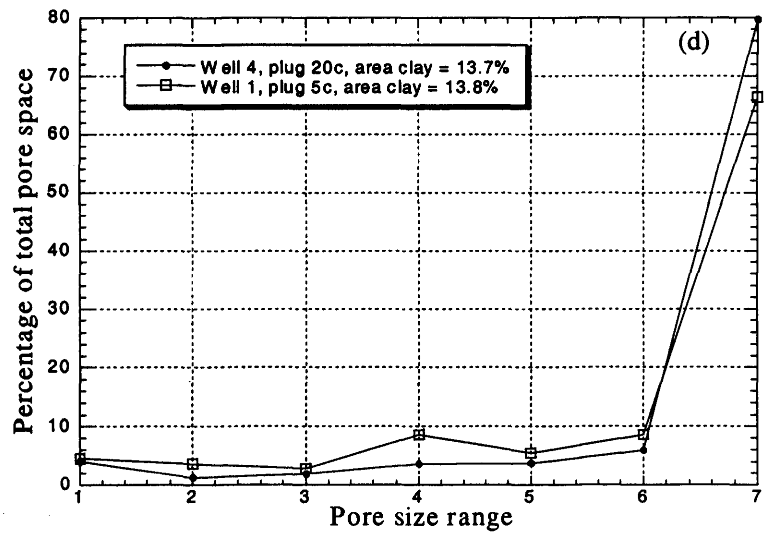

Figure 7.18. Pore size range as a percentage of the entire image porosity against the seven pore size ranges. Each plot consists of data from two plugs within a specified range of area *clay*. (a) Very high, (b) high, (c) medium and (d) low area *clay* percentages

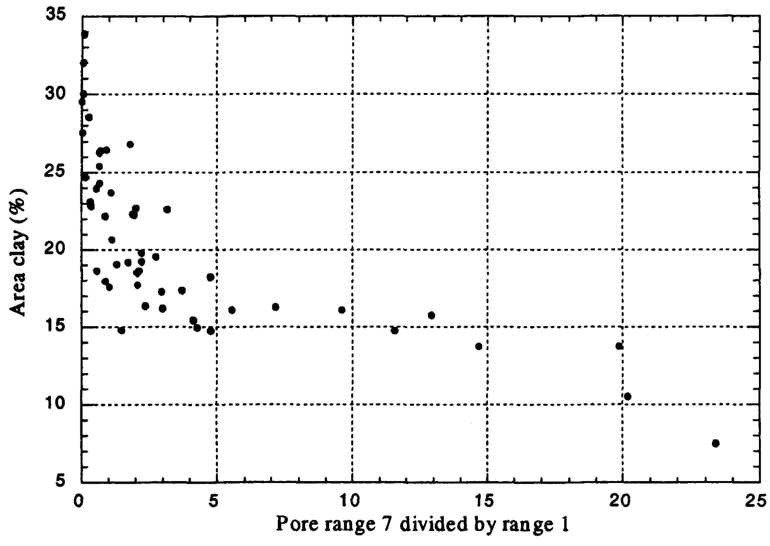

Figure 7.19. Fraction area *clay* versus pore range seven divided by pore range one

To quantify this relationship a plot of area *clay* against a ratio of pore size range 7 to pore size range 1 was made (Figure 7.19), this gives a significant non-linear relationship (r=-0.85, with abscissa axis logged).

There is a positive relationship between permeability and image porosity (Figure 7.6b), and a negative relationship between area *clay* and area pore (Chapter 6, Figure 6.23), therefore an expected negative relationship between permeability and area *clay* (Figure 7.20).

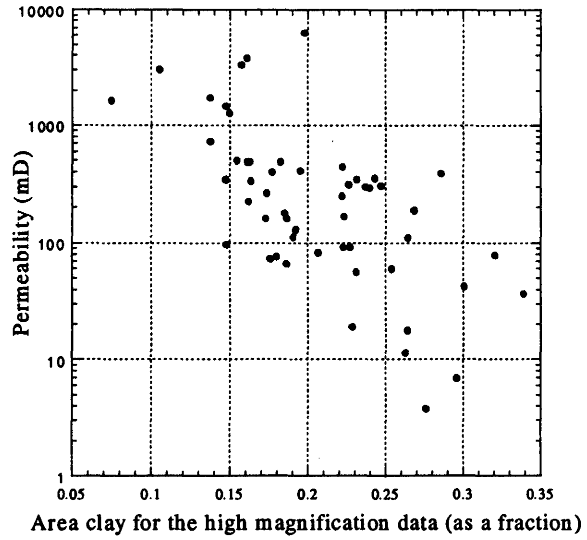

Figure 7.20. Gas permeability against high magnification area *clay*

A question arises from these observations; "what will the difference in permeability be between two plugs, both of which have the same plug porosity, but different amounts of area *clay*?" To answer this question the plug porosity values were split into three groups of increasing value and each of the three groups subdivided into plugs containing low (Group A) and high (Group B) percentages of area *clay* (Table 7.4). Gas permeability was then plotted against plug porosity for each of the three groups distinguishing high and low area *clay* (Figure 7.21).

The plugs in Figure 7.21 with approximately the same porosity are compared in terms of high and low amounts of *clay*. It is observed that the plugs with more *clay* (B groups) generally have a lower permeability. It is therefore suggested that *clay* has an important role to play in the understanding of permeability. It is proposed that image porosity gives a strong relationship with permeability because it does not measure the micro-porosity associated with area *clay* that plug porosity measures.

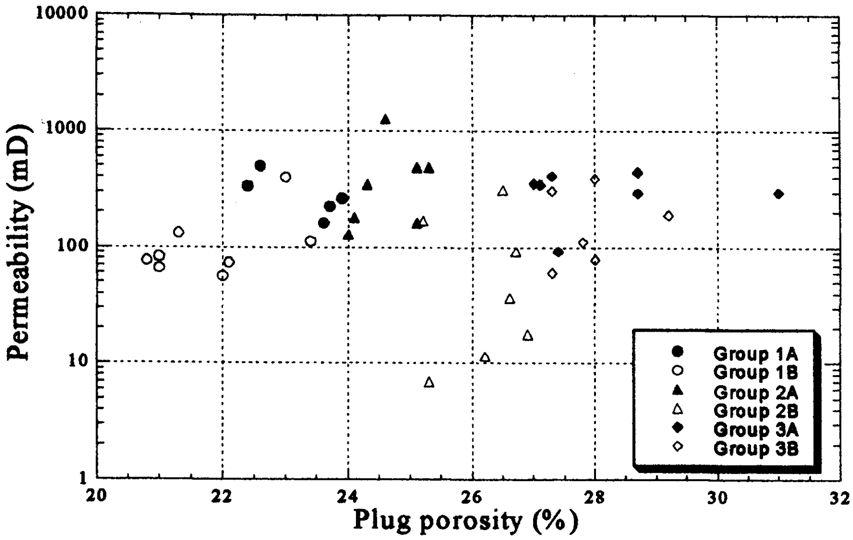

Figure 7.21. Gas permeability against plug porosity for the six groups given in Table 7.4

Well / plug code	Plug porosity (%)	Group	Area *clay* Low %	Area *clay* High %	Gas permeability (mD)
1/5a	22.6		15		505
9/14b	22.4	Group	16		337
7/3a	23.7	1A	16		226
1/9a	23.6		17		162
1/6a	23.9		17		263
9/13b	20.8			18	76.3
3/10b	22.1			18	73.09
9/14a	23			18	400
9/13a	21	Group		19	65.9
9/11b	21.3	1B		19	132
2/11b	23.4			19	113
9/11a	21			21	82.4
8/7a	22			23	56.1
3/8b	24.3		15		344.3
8/8a	24.6		15		1280
2/4a	25.1	Group	16		491
3/5a	25.3	2A	16		489.4
3/11b	24.1		18		180.8
2/11a	24		19		128
3/14c	25.1		19		162.2
8/10a	25.2			22	168
1/7a	26.7			22	91.9
9/12b	26.5	Group		23	317
1/4a	26.2	2B		26	11.5
2/1a	26.9			26	17.9
7/1b	25.3			30	6.96
7/5a	26.6			34	36.7
8/9a	27.3		20		410
6/2a	28.7		22		447
9/12a	27.1		23		347
1/1a	27.4	Group	23		92.7
6/7a	27	3A	24		355
7/4a	28.7		24		294
6/5a	31		24		297
6/4a	27.3			25	307
1/1c	27.3			25	60
3/1a	27.8	Group		26	111.6
7/2a	29.2	3B		27	189
6/8a	28			29	388
7/5b	28			32	78.7

Table 7.4. A table showing plug porosity split into three groups of increasing value and then subdivided into plugs containing low (Group A) and high (Group B) percentages of area *clay*

If it is assumed that the plug porosity measurement includes the micro-porosity within the *clay* and the image porosity does not, it is logical that an image porosity which was generated from the sum of area *clay* plus area pore, would give values and a distribution closer to that of the plug porosity. To investigate this, permeability was plotted against porosity for a single well and compared with permeability against area *clay* plus area pore (Figure 7.22).

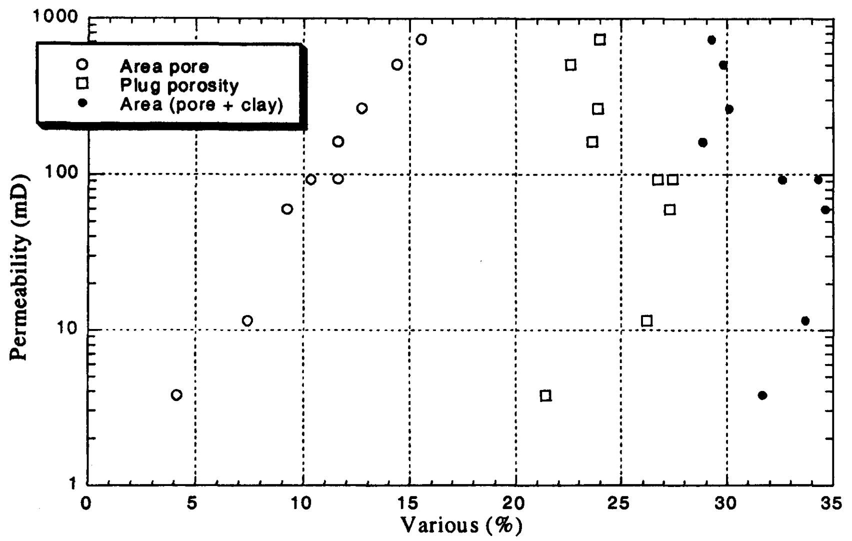

Figure 7.22. Gas permeability against area pore, plug porosity and the sum of area *clay* and area pore, for well 1

The first data set in Figure 7.22 is the total area of pore space as a percentage of the image, and is very linear. The second data set is plug porosity, which gives higher values of porosity than image porosity (area pore) and does not have a linear relationship with permeability. The third data set is percentage area pore plus the percentage area *clay* from the images; it matches the pattern of the plug porosity very clearly. The third data set is not a shifted replica of the second, as the data sets are more widely spaced at the bottom than at the top. The area pore plus *clay* data set has higher values than the plug porosity, which is logical as area *clay* is the sum of *clay* micro-porosity (unable to be measured by the image analysis process) and the actual solid *clay*. It is suggested that the image porosity (or percentage area pore) is estimating the flowing porosity, or effective porosity, which contributes to the permeability. Whereas the plug porosity measures all the interconnected pore space, including the micro-porosity (contained in the *clay*) which does not contribute to fluid flow.

There is no method for calculating a transferable micro-porosity value for authigenic clay minerals and detrital clays, but estimations have been made. Hurst and Nadeau (1995) have performed micro-porosity measurements on diagenetic clays (§2.4.2). They have calculated average porosities of 51% and 43% for chlorite and kaolinites respectively, both clays are present within this reservoir. The average of chlorine and kaolinite porosity value (47%) is used as a first approximation of the average micro-porosity present within the area *clay*. To calculate a second estimation of plug porosity, 53% of the value of *clay* has been subtracted from the sum of area pore plus area *clay*, i.e. the calculation would now be area pore plus 47% area *clay* (considered the porosity). In Figure 7.23 the area pore plus 47% area *clay* is plotted as an overlay on Figure 7.22 (crosses). An improved match (compared with area pore plus *clay*) is seen to the plug porosity, although the amount of micro-porosity present within the *clay* appears to have been generally underestimated. This underestimated porosity is probably due to an incorrect estimation of the micro-porosity associated with the *clay* or other porosity not measured in the image analysis process (e.g. grain edge effects, §6.2.4).

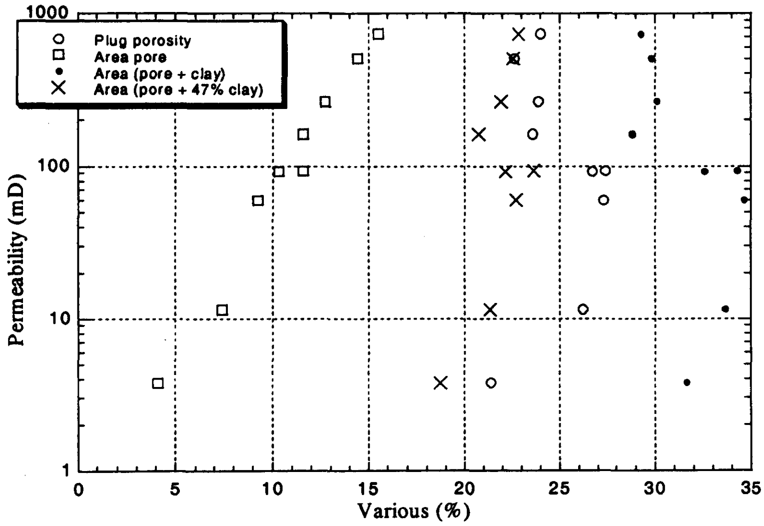

Figure 7.23. Image analysis parameters and plug porosity against permeability, for well 1

Assuming the porosity in the *clays* was underestimated in Figure 7.23 an optimal micro-porosity was calculated, for the entire data set. The optimal value was generated from,

$$micro\ porosity = \frac{(plug\ porosity - image\ porosity)}{Area\ clay}$$

The optimal micro-porosity associated with the *clay* is calculated as 67%. The data set of area pore plus *clay* for well 1 is then re-plotted using this optimal value (Figure 7.24) and an improved relationship is observed. Figures 7.25 and 7.26 are similar plots for wells 4 and 7 respectively, and substantiate the results seen for well 1.

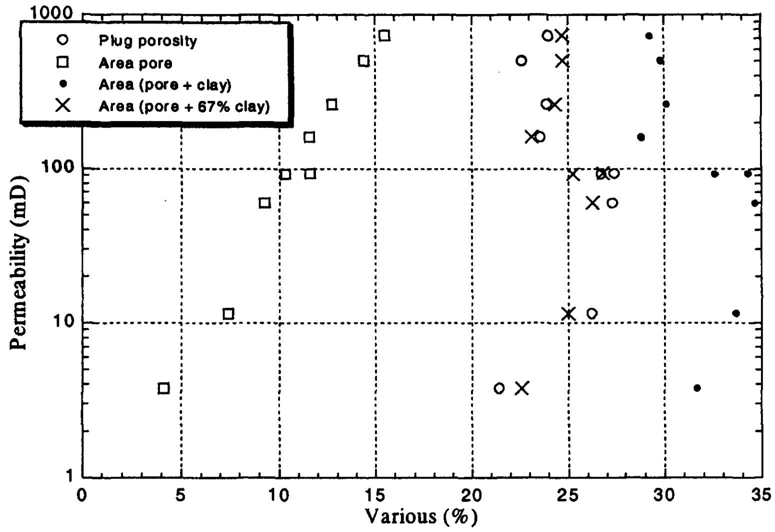

Figure 7.24. Image analysis parameters and plug porosity against permeability, for well 1

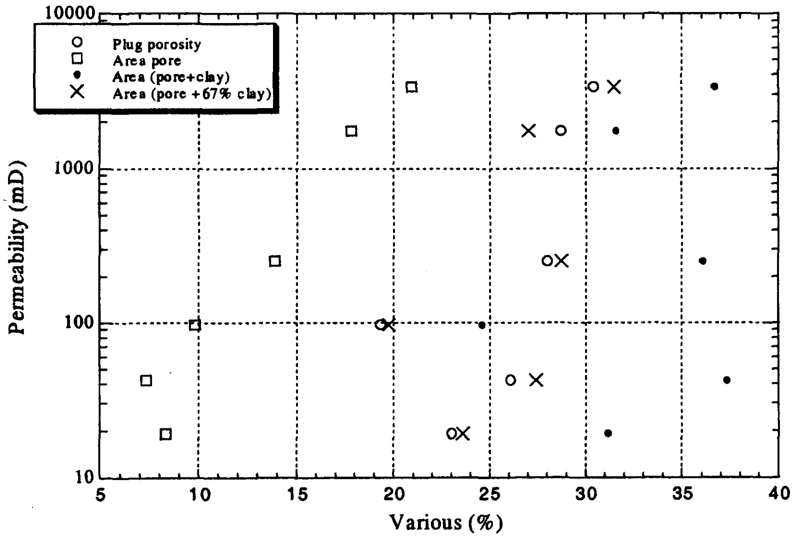

Figure 7.25. Image analysis parameters and plug porosity against permeability, for well 4

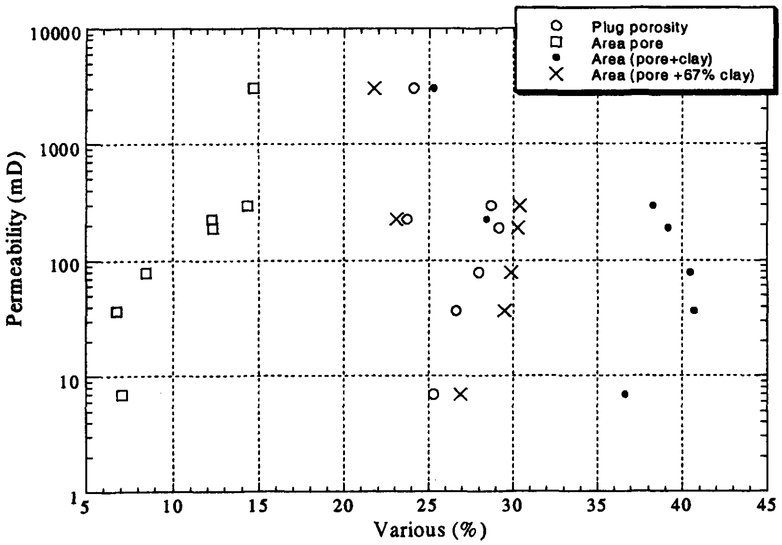

Figure 7.26. Image analysis parameters and plug porosity against permeability, for well 7

The cross-plot of plug porosity against area pore plus 67% area *clay* for all the data (Figure 7.27) demonstrates a significant relationship (r=0.83).

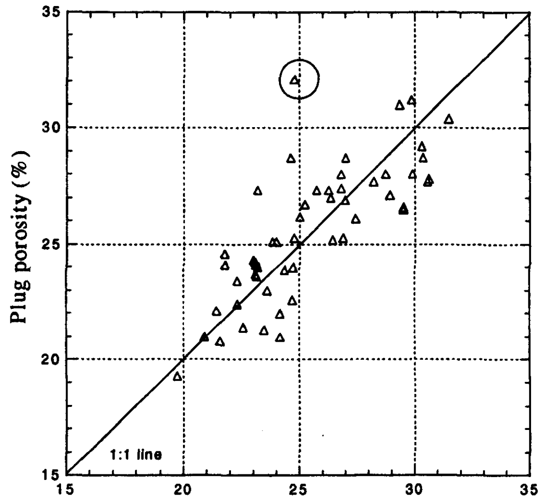

Figure 7.27. A plot of plug porosity versus area pore summed with 67% area clay for all well data. r=0.83 (The ringed outlier is plug 6a from well 6, and was excluded from the calculation of r)

Therefore plug porosity can be calculated from the images. Also, an understanding of the image porosity as an effective flowing porosity, and the plug porosity as a total interconnected porosity has been obtained. If plug porosity is now redefined as plug porosity minus the micro-porosity (67% of the area *clay* value), it is expected to have an improved linear relationship with permeability. Figure 7.28 demonstrates that the redefined plug porosity gives a significantly stronger linear relationship with permeability than the actual core plug porosity.

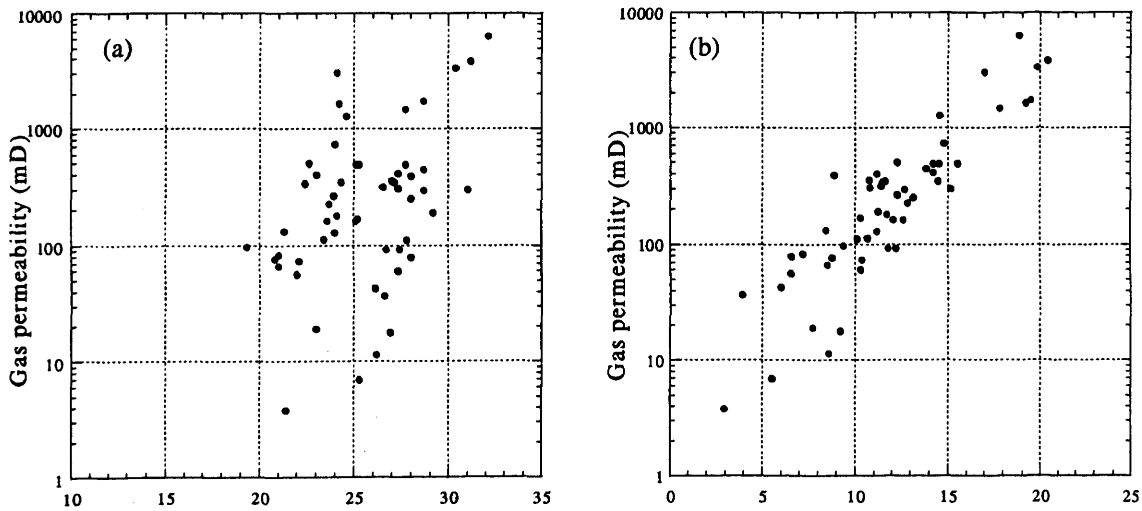

Figure 7.28. Gas permeability against (a) measured plug porosity (r=0.41) (b) the redefined plug porosity (r=0.89)

7.3.6 Hypothesis 4

"Large pores are present within the plugs which are not captured with image analysis and do not contribute to permeability, but increase the value of plug porosity."

Only a range of pore sizes could be captured with the two image magnifications used in this study. This is common practice in image analysis studies as a representative distribution, in petrophysical terms, does not require having all possible pore sizes, or even the absolute largest and smallest pore sizes; rather a distribution that has a significant relationship to the magnitude of known reservoir properties (Internal Report 3). Stereological theory also states that the probability of obtaining extreme ends of the 3D distribution tend to zero.

There are several ways in which Hypothesis 4 could be tested: *(i)* collection of SEM images at a lower magnification and observe whether there are large pores which have been ignored, *(ii)* use capillary pressure curves and *(iii)*, use nuclear magnetic resonance (NMR). Both *(ii)* and *(iii)* produce pore size distribution information, however due to limitations in time and resources, method *(i)* has been used to test this hypothesis.

The end-trims from the reservoir which have been used in this study were requested from SC1 for further analysis (Table 7.5).

Well/ plug code	Plug porosity (%)	Gas permeability (mD)	Low magnification image porosity (%)
1/1a	27.4	92.7	7.41
1/2a	21.4	3.79	0.72
1/5a	22.6	505	2.71
1/5c	24.0	728	12.17
1/7a	26.7	91.9	6.81
2/4a	25.1	491	10.87
2/9c	27.7	490	11.40

Table 7.5. The seven end-trims received from SC1

Four SEM images were taken on two plugs (1a and 7a from well 1) at x20 magnification. The images were taken so that they would overlap to ensure that a continuous image would be captured (Figure 7.29). The two plugs were selected as they have lower image porosity values than average compared with the plug porosity values. If large pores are present which were not captured in the low magnification images (x30) they would have to be less than about 25% of the image at x30 which is 1 mm^2. From Figure 7.29 there are no obvious pores >1 mm^2 within plug 1a. Pores >1 mm^2 were not present in plug 7a either, but it cannot be concluded from two plugs that large pores are not present in other plugs. It is suggested, however, that it would be unlikely due to the size of pore required for it not to be visible in the low magnification images.

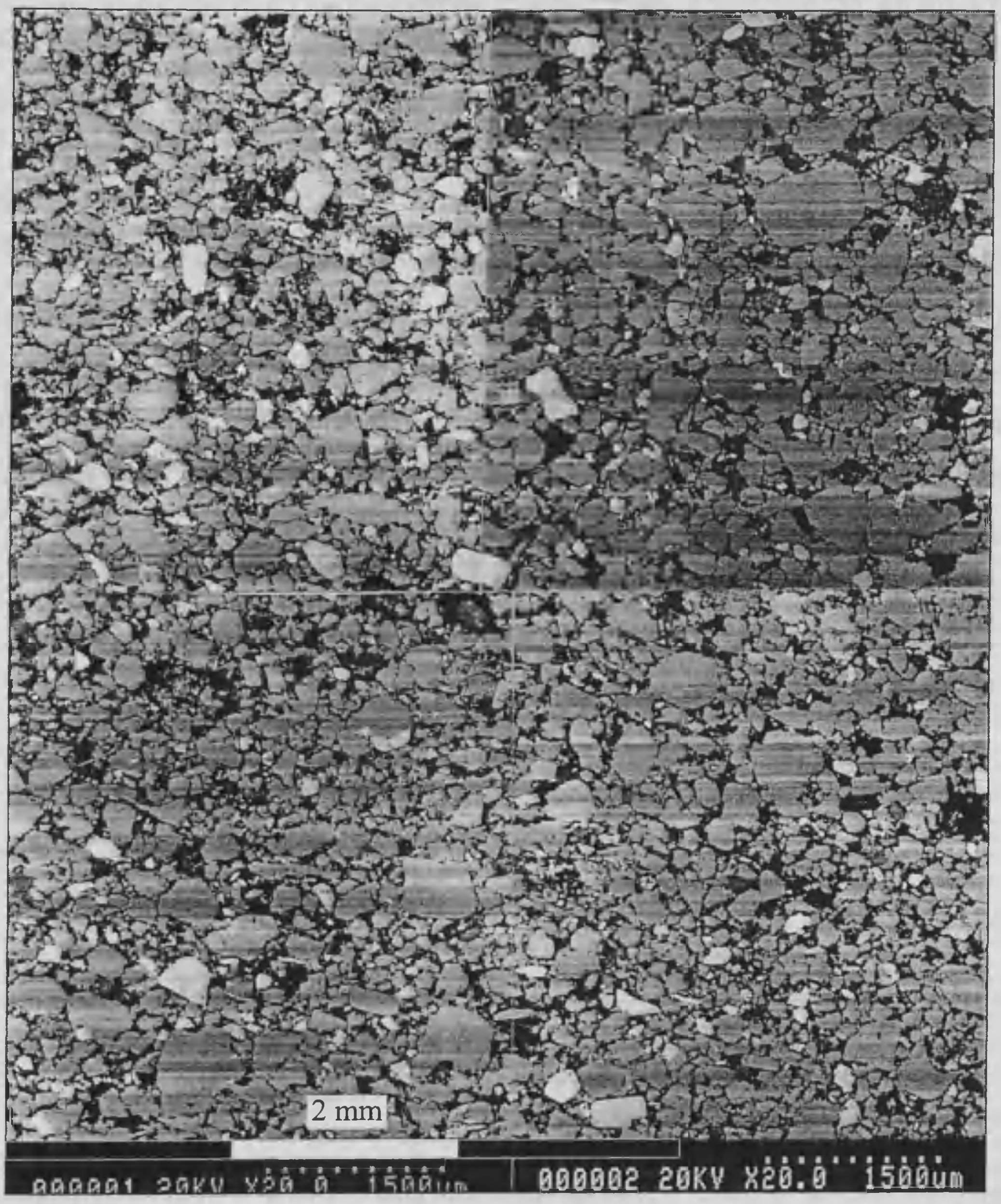

Figure 7.29. Four x20 SEM images from plug 1a from well 1, joined to check for large pores

7.4 Image analysis and core analysis data

This section compares qualitative and quantitative image parameters (defined in Chapter 6) against core plug data (Chapter 5), with the aim of improving the understanding of permeability and porosity.

7.4.1 Qualitative image parameters

Section 6.4.3 defines five qualitative image parameters (grain size, anisotropy, pore cleanness, grain packing and presence of large pores or aggregates of *clay*), these are compared with porosity or permeability to observe and interpret relationships.

Grain size

Figure 7.30 examines the average grain size seen within the images. It is revealed that the large grained images have a high permeability (>1000 mD), but only a medium (≈24%) plug porosity. The fine grained images are associated with high values of plug porosity (25-29%) and lower permeability plugs (3< permeability <200 mD). The fine grained images also exhibit a significant linear trend (r=0.80). The majority (78%) of the points are medium grained plugs and cover the entire range of permeability (1-10,000 mD) and porosity (18-34%) shown in this plot.

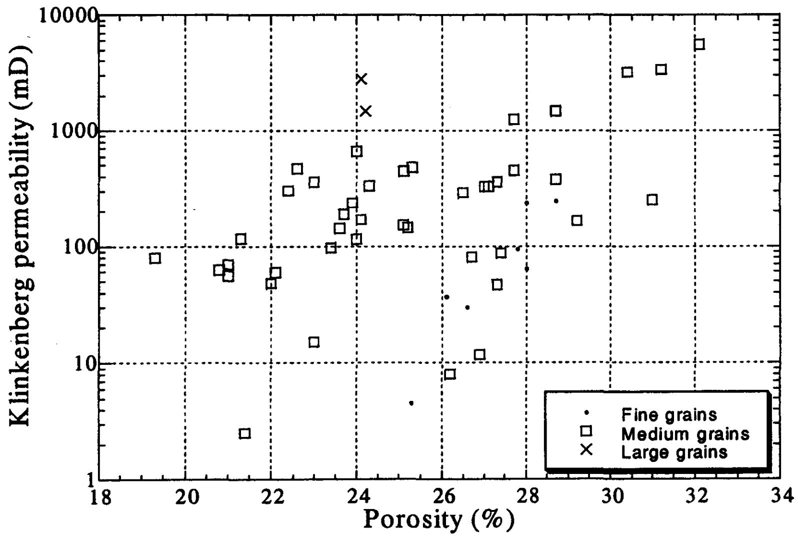

Figure 7.30. Klinkenberg permeability against plug porosity with grain size defined, for the low magnification SEM images. Where fine = 0-10 mm, medium = 10-50 mm and large = >50 mm on the image hard copies

From Figure 7.31 it is evident that grain sorting does not constrain the permeability-porosity relationship. This result is similar to those obtained in Chapter 5 (§5.4.3), where grain size ranges from the plug descriptions were used to understand the permeability-porosity plot.

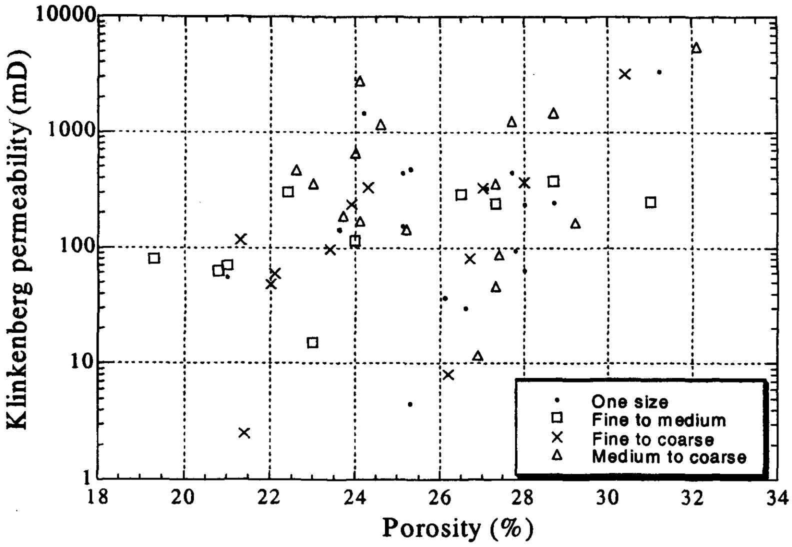

Figure 7.31. Klinkenberg permeability against plug porosity with grain sorting defined from the low magnification SEM images. Where fine = 0-10 mm, medium = 10-50 mm and large = >50 mm in the paper A4 print out of these images)

Anisotropy

Anisotropy (visual presence of grain alignment and/or grading of the grains) was observed in 61% of plug images. The anisotropic and isotropic plugs are plotted in Figure 7.32, and no obvious separation in the data is observed.

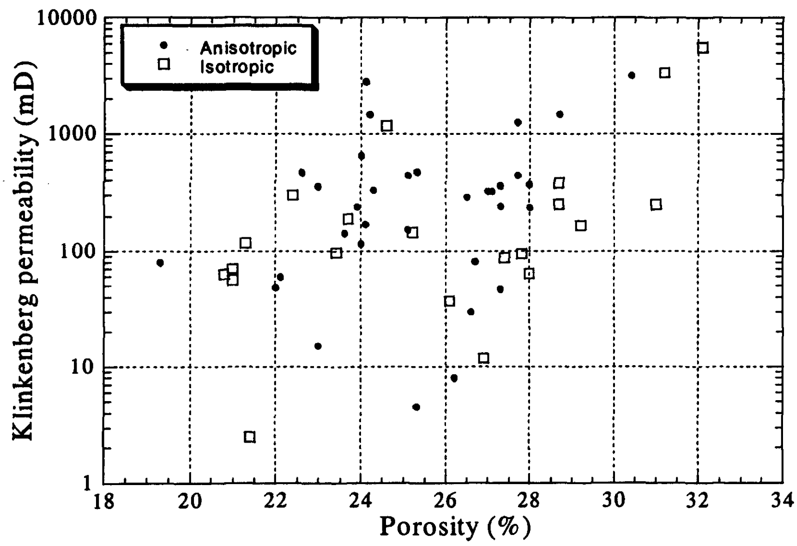

Figure 7.32. Klinkenberg permeability against plug porosity with the presence of anisotropy or not (seen in the low magnification SEM images) distinguished

Pore cleanness

Figure 7.33 examines three different states of pore cleanness (presence of *clay*, specifically scattered *clay* making the image appear more dirty) and the relationship with permeability and porosity. Porosity is not affected by the pore cleanness, but the permeability is split into three distinct groups, with the cleanest pores associated with higher permeability values than the dirty pores. The 'dirt' as it is called, is a qualitative estimation of the amount of pore filling material which in general is clay, so this suggests that the more clay occurring in a plug sample the lower its permeability, almost irrespective of porosity.

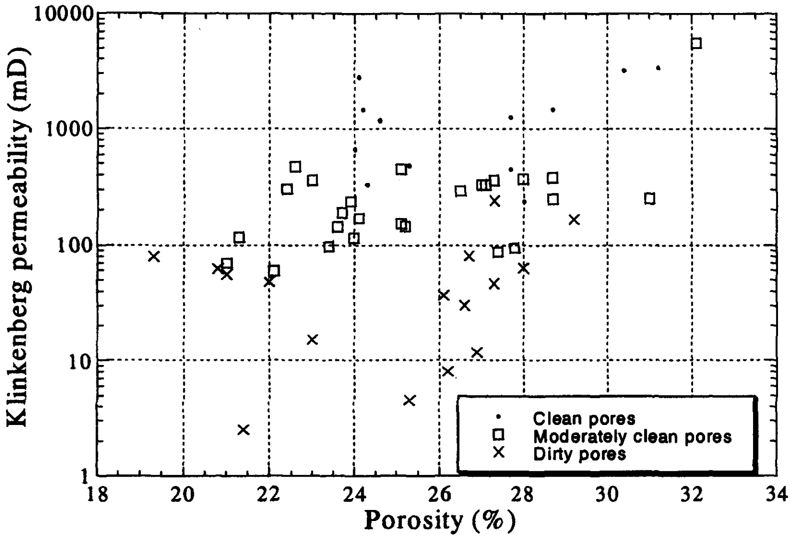

Figure 7.33. Klinkenberg permeability against plug porosity with pore cleanness (as seen in the low magnification SEM images) distinguished

Grain packing

Figure 7.34 examines packing (the average number of grains touching each grain, as seen within the images). Pettijohn (1975) observed that any change in packing that increases the porosity will increase the permeability, therefore the loosely packed grains (0-2 touching grains) which predominantly have a high porosity were expected to have a high permeability value as well. However, a clear decrease in permeability with decreasing porosity, observing changes in packing is not apparent.

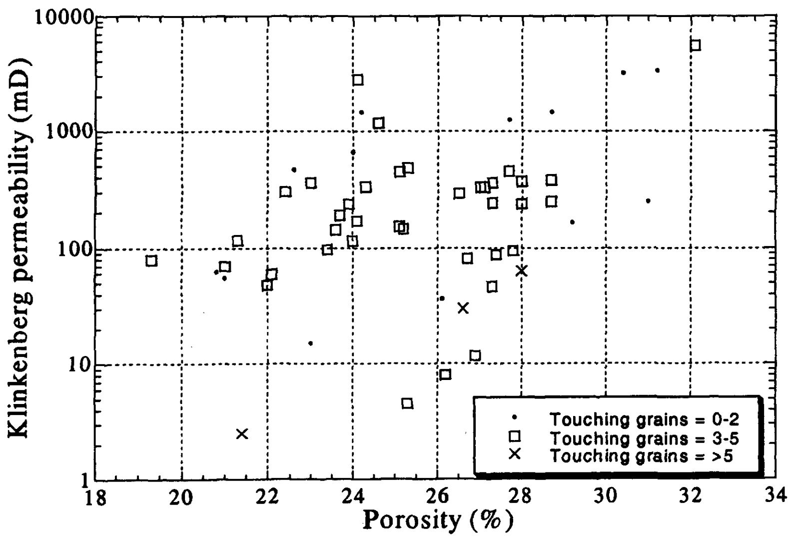

Figure 7.34. Klinkenberg permeability against plug porosity with the number of touching grains (as seen in the low magnification SEM images) distinguished

Large pores or large aggregates of clay

Large pores are observed to be present in the higher (>80 mD) rather than lower permeability ranges (Figure 7.35).

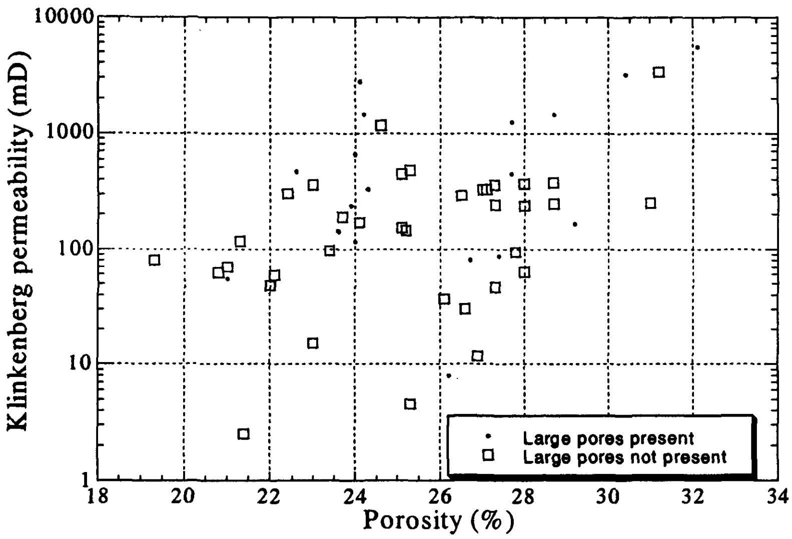

Figure 7.35. Klinkenberg permeability against plug porosity with the presence of large (>50 mm) pores or not (as seen in the low magnification SEM images) distinguished

Distinct, isolated aggregates of clay observed within the images are distinguished in Figure 7.36, and they show no clear relationship with permeability or porosity.

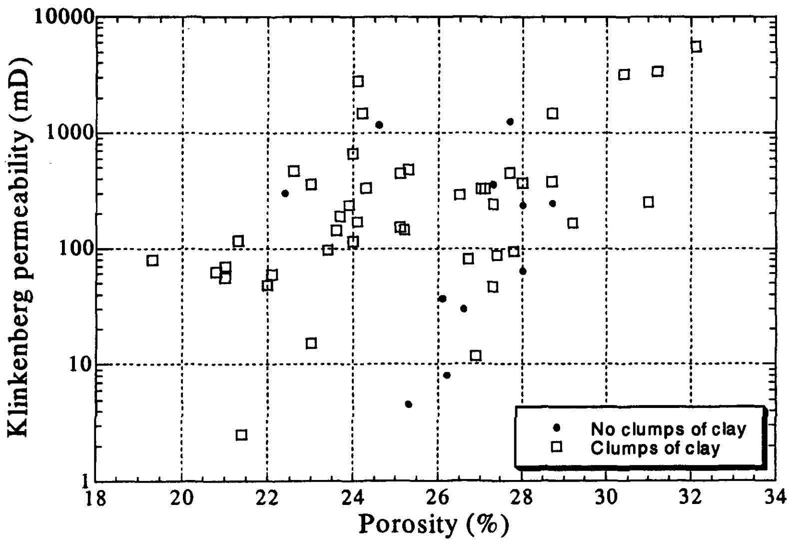

Figure 7.36. Klinkenberg permeability against plug porosity with the presence of large amounts of clay or not (as seen in the low magnification SEM images) distinguished

7.4.2 Aspect ratio

Several authors (Ruzyla, 1984; Ehrlich et al., 1991a; Ehrlich et al. 1991b; Basan et al., 1997) have investigated the effects of changes in pore shape with porosity and permeability and all concluded that the shape of pores can aid understanding of these parameters.

Pore aspect ratio (defined in §6.2.5.4) has no correlation with permeability or porosity (Figures 7.37a and b) even if pore size ranges are used to subdivide the data. It is hypothesised that the absence of correlation between these parameters is either due to the small size of the area investigated with the five low magnification images, or that the magnification itself is not optimal for this investigation.

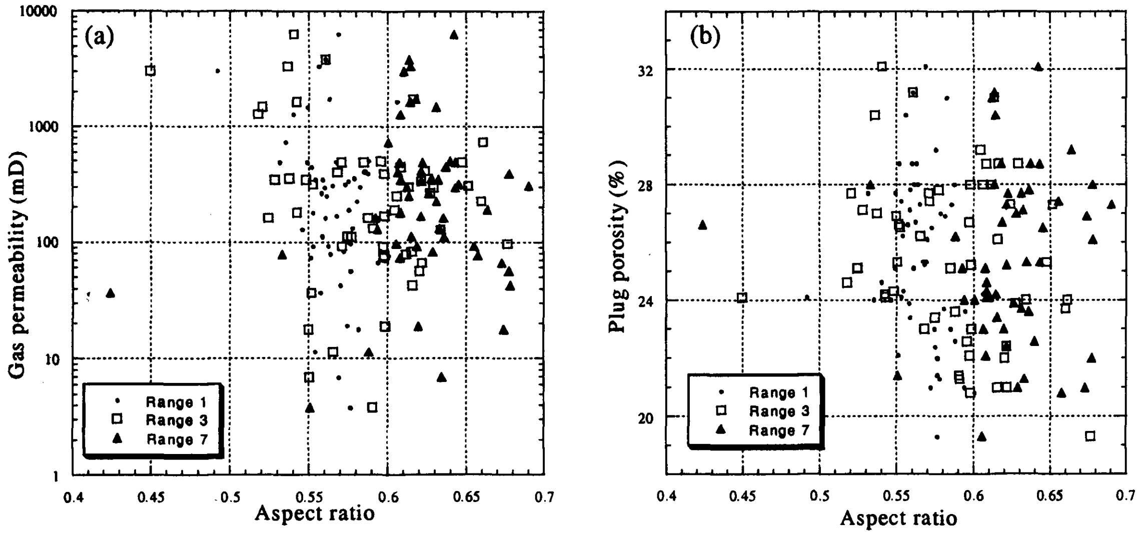

Figure 7.37. (a) Gas permeability versus the aspect ratio for 3 pore size ranges
(b) Plug porosity versus the aspect ratio for 3 pore size ranges
(Increasing aspect ratio correlates with increasing sphericity. Note that each set of plug images are split into 7 ranges of associated pore sizes, so in these plots each plug has three pore size ranges associated with it.)

7.4.3 Pore roughness

Roughness (see §6.2.5.3) is defined as,

$$R1 = \frac{measured\ pore\ perimeter}{\pi(length * breadth)} \qquad [7.1]$$

$$R2 = \frac{measured\ pore\ perimeter}{measured\ pore\ area} \qquad [7.2]$$

The roughness parameters were each plotted against plug porosity and permeability. It was expected that roughness would decrease with increasing pore size for R1 and R2 because of the division by pore area in the equations (Figure 7.38a and b). There are no obvious relationships between porosity and roughness, at the scale shown in Figure 7.38b, and none of the plots have a significant relationship at a probability level of 0.01.

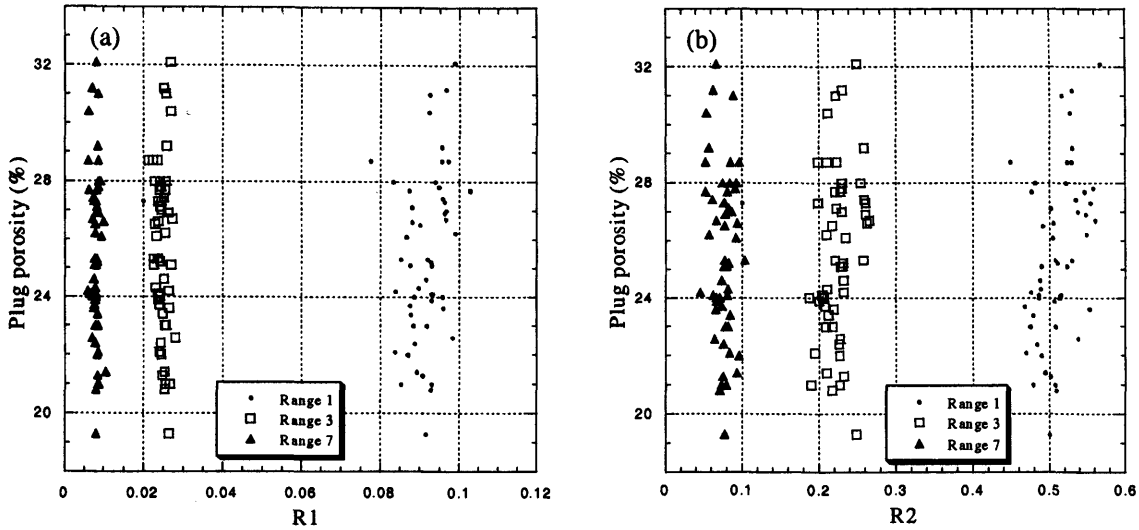

Figure 7.38. A plot of plug porosity against (a) R1, (b) R2, for three pore size ranges. (as the pore roughness parameters increase so does the roughness of the pores). The separation of the three data sets in each plot is due to the division by pore area in the equations.

The roughness is examined at the pixel scale, which suggests that variation in pore shape and pore roughness will be expressed by the equations. An increase in grain angularity may increase porosity and permeability (Pettijohn, 1975), but an increase in clay clinging to the perimeter of a pore could decrease permeability. Permeability is plotted against R1 for (a) pore size range 7 data, and (b) the low magnification data (Figure 7.39). They both have a significant relationship (r=-0.49 and -0.55 respectively), but these are not significantly different values. A suggestion for the increase in roughness with decreasing permeability is that roughness may lead to an enhanced frictional drag on the gas molecules. At a larger scale another possibility is that increased roughness (grain angularity) may create pockets in which flow is disrupted and becomes more turbulent therefore decreasing permeability.

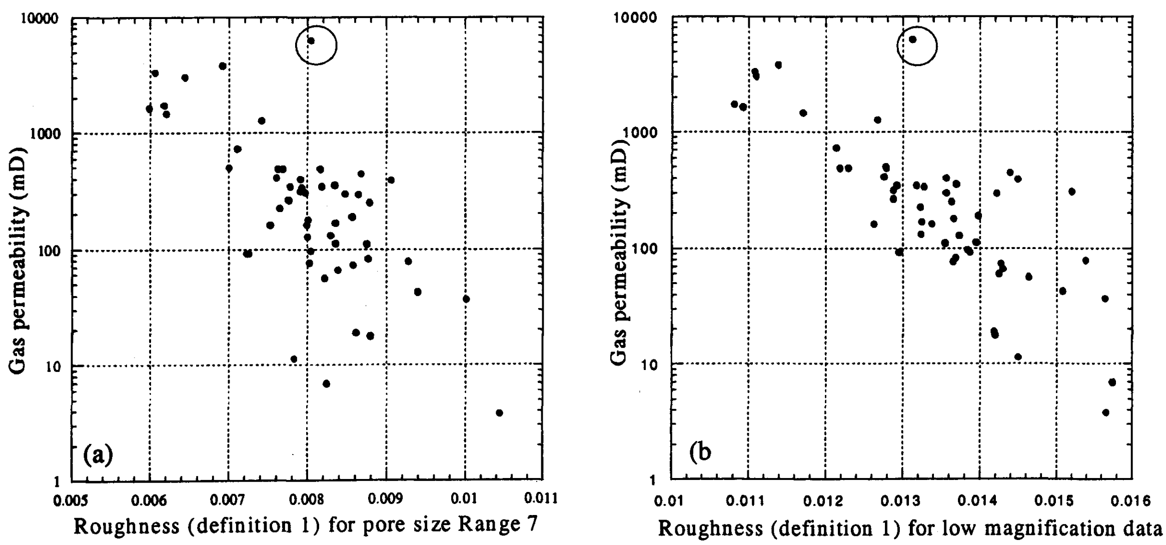

Figure 7.39. Gas permeability against R1 for (a) pore size Range 7 (b) the low magnification data. (the single high permeability outlier (ringed) is again plug 6a from well 6)

7.4.4 Gas permeability against the image porosity index

A porosity index (§6.2.5.1) may be used to examine homogeneity of a plug. Index A will tend to one and Index B will tend to zero as a plug approaches homogeneity if the following assumptions are correct: *(i)* image porosity and plug porosity measure the same pore space (i.e. the two methods are using the same resolution) and, *(ii)* image porosity is capturing all of the necessary pore size ranges (i.e. enough magnifications of SEM images have been taken, this is already known not to be the case, §7.2).

Index A (Figure 7.40a) shows a significant positive relationship (r=0.58) with permeability. Index B (Figure 7.40b) shows a significant negative relationship (r=-0.46). It could be assumed therefore that the plugs are approaching homogeneity with increasing permeability. However, the indexes are calculated using image porosity and it is suggested that this is the primary control on the observed relationship.

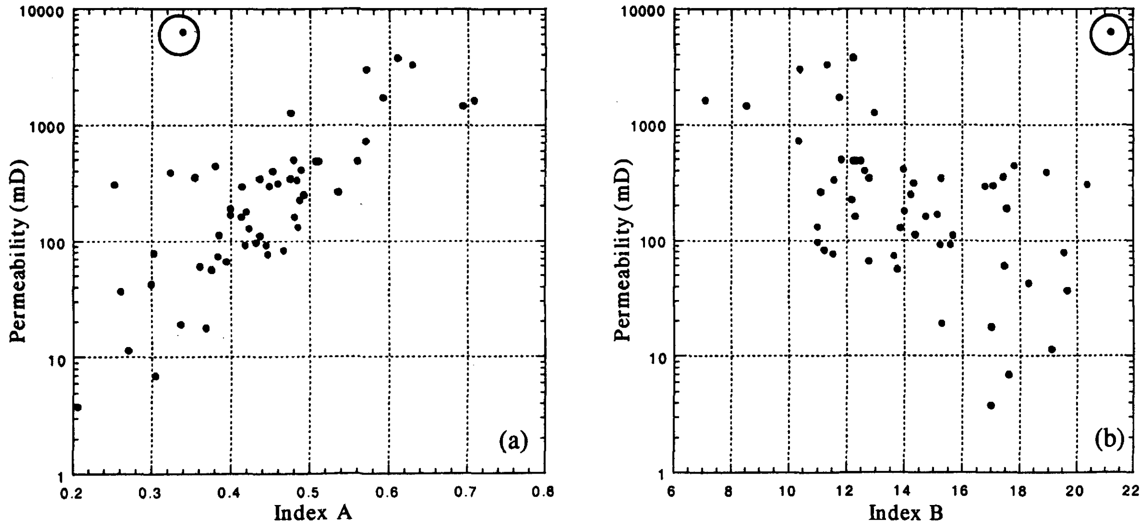

Figure 7.40. Permeability against porosity for (a) Index A (b) Index B, in both plots the ringed outlier, plug 6a from well 6, is excluded form the calculations of r

7.4.5 Formation resistivity factor

Formation resistivity factor *F*, like permeability, is a flow parameter in sedimentary rocks. Although, rather than being the ease with which a fluid flows though a rock it is controlled by the fluid inter-connectivity and measures the transport capacity of the rock to electrically charged species (pers. comm. Peter Whattler, §2.5). *Clay* has been observed to influence both permeability and plug porosity (§7.3.5), this section aims to use *F* to investigate further into *clay* and its effects.

7.4.5.1 Formation resistivity factor, gas permeability, plug porosity and image porosity

Gas permeability and *F* were compared (§5.4.4) and subdivided using facies. It was concluded that facies are not a controlling variable on the permeability-*F* relationship. Figure 7.41 however, demonstrates that the amount of *clay* does impact permeability-*F* relationships (for each area *clay* range in decreasing value, r=-0.76, -0.64, -0.82 and -0.75, in linear space with permeability logged). These significant correlations are in contrast with the entire data set in Figure 7.41 which has a correlation coefficient of r=-0.53.

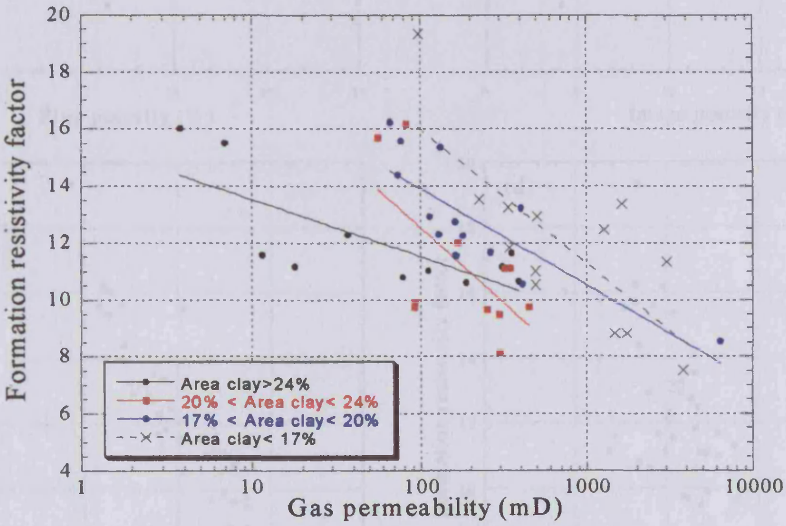

Figure 7.41. *F* against gas permeability with percentage area *clay* ranges distinguished

A comparison of gas permeability and *F* with both image and plug porosity (Figure 7.42) reveals that permeability has a stronger relationship with image porosity than plug porosity, but *F* has a stronger relationship with plug porosity than image porosity. From this simple observation it is concluded that *F* has a greater insensitivity to pore morphology than permeability.

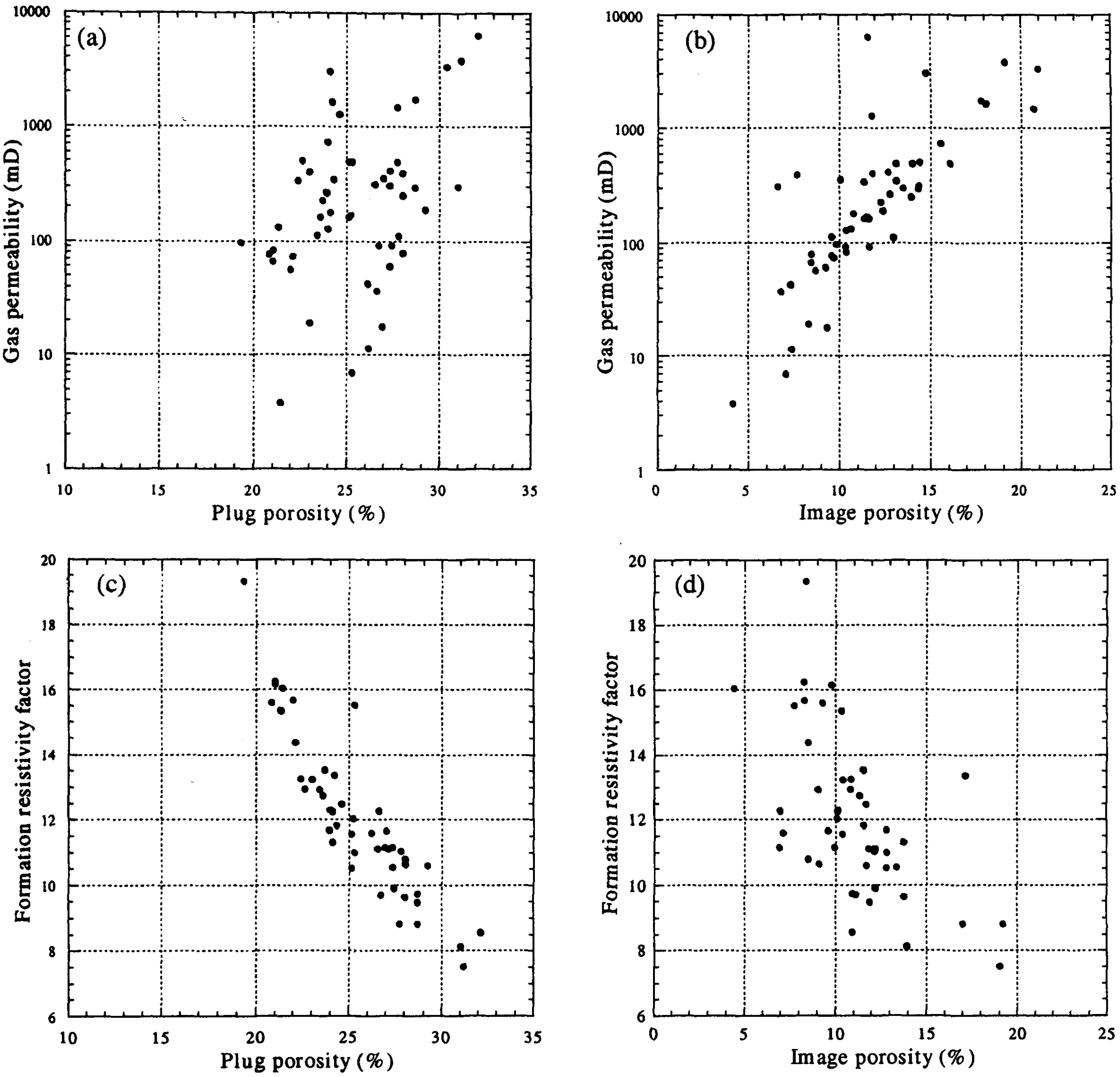

Figure 7.42. (a) Gas permeability against plug porosity, (b) gas permeability against image porosity, (c) F against plug porosity and (d) F against image porosity

The results obtained from plotting F against pore size ranges are not as logical to explain as the permeability plots (Figure 7.12). The very conductive rocks (low F) seen in Figure 7.43a have many pores >5500 μm^2 (pore size range 7), but there is not a simple progression from many large pores to many small pores with decreasing conductivity. The second group of most conductive plugs (Figure 7.43b) have a higher percentage of small pores than the least conductive plugs seen in Figure 7.43d. A possible explanation is that as many small pores (13 to 430 μm^2) are observed to be associated with increases in *clay* (Figure 7.18), the clay may be contributing in a significant manner to the conductivity of the rock (§2.5.1.1).

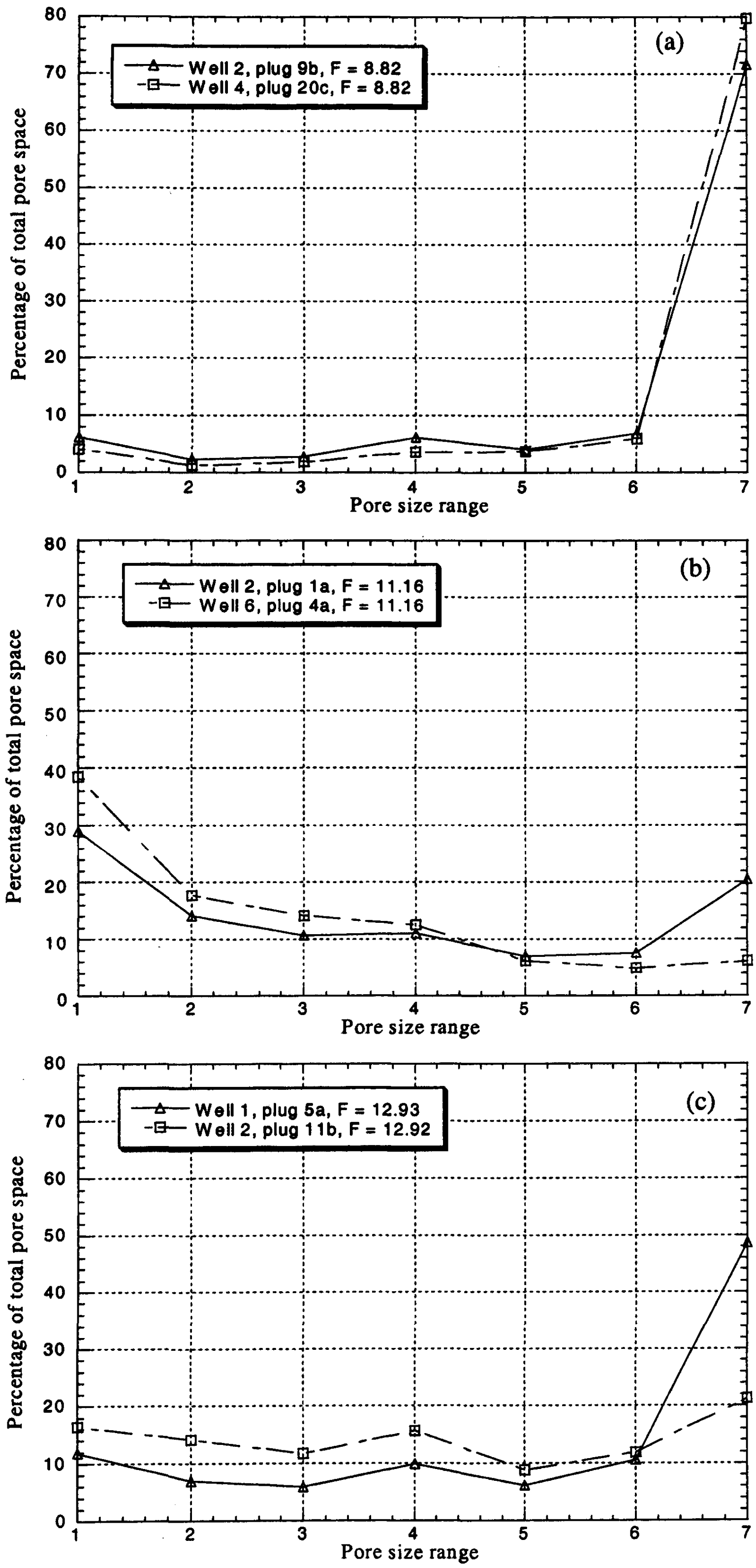
(a)
Well 2, plug 9b, F = 8.82
Well 4, plug 20c, F = 8.82
Percentage of total pore space
Pore size range
(b)
Well 2, plug 1a, F = 11.16
Well 6, plug 4a, F = 11.16
Percentage of total pore space
Pore size range
(c)
Well 1, plug 5a, F = 12.93
Well 2, plug 11b, F = 12.92
Percentage of total pore space
Pore size range

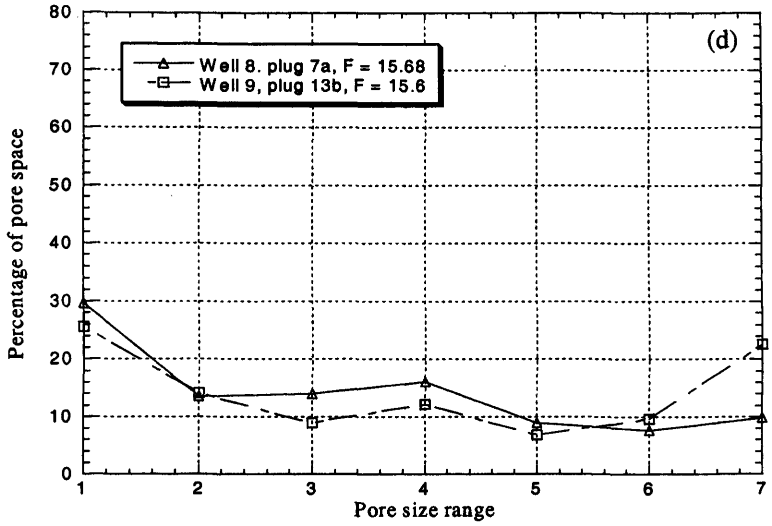

Figure 7.43. Pore size range as a percentage of the entire image porosity against the seven pore size ranges. Each plot consists of data from two plugs within a specified range of *F*. (a) Low (8.82), (b) medium (11.16), (c) high (12.93 & 12.92) and (d) very high (15.68& 15.6)

The relationship between the pore size ranges and permeability was quantified by dividing pore size range 7 by pore size range 1 (Figure 7.13), the same has been done here for the *F* pore size distribution relationship (Figure 7.44). However, the relationship is border-line as to whether it is significant or not (r=-0.33), suggesting that *F* is not related to pore size distributions but more to the total porosity (Figure 7.42c, r=0.90).

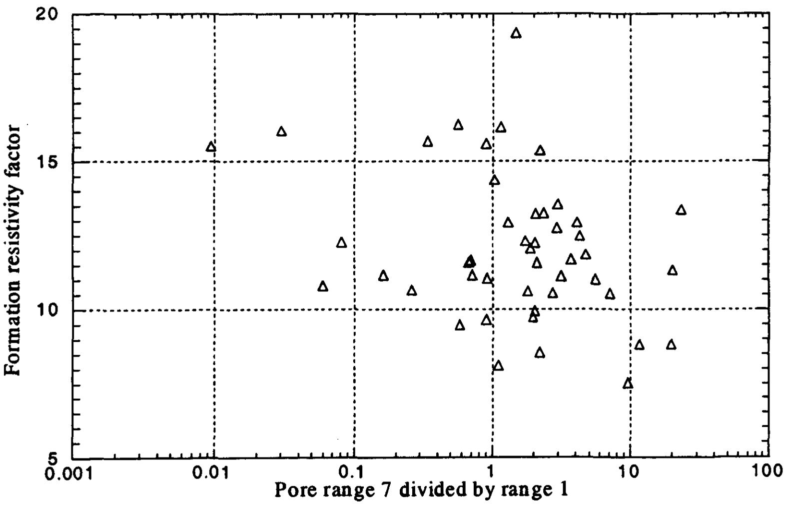

Figure 7.44. *F* versus pore range 7 divided by pore range 1

F is plotted against image porosity with percentage area *clay* ranges distinguished (Figure 7.45). It is observed that area *clay* gives definite grouping to the plot with the groups in order of increasing amounts of *clay* having correlation coefficients of -0.65, -0.82, -0.65 and -0.78 respectively.

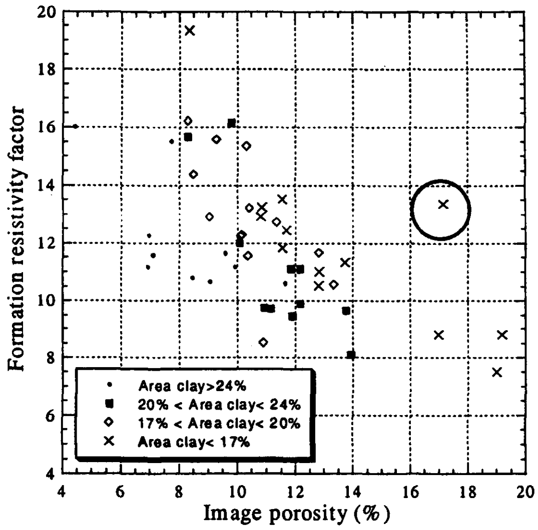

Figure 7.45. *F* versus fraction total image porosity with area *clay* defined. The ringed outlier (Plug 10a well 2) is conspicuous because of its low value of area *clay* 7.5% which is 3% lower than the next lowest value

7.5 Summary

Image porosity was noted as having a stronger relationship with permeability than plug porosity; four hypotheses were investigated in an attempt to understand this observation.

Hypothesis 1; Small pores do not contribute to permeability.

Hypothesis 1 was accepted; permeability is higher in plugs which have larger pores. In reaching this conclusion it was proposed that image porosity does not capture all the interconnected porosity within a plug. It was observed that plug porosity has a similar percentage range of values as the image porosity, but those values are 10-15% higher.

Hypothesis 2; Fixed orientation of the permeability measurement with respect to image porosity helps to constrain this relationship, (i.e. plug anisotropy is important).

Hypothesis 2 was rejected. It was concluded that neither pore orientation nor image porosity measured at the resolution used in this study contain sufficient information to understand the anisotropic permeability values. Anisotropy was investigated at the plug scale and two conceptual planar fabric models were hypothesised as the control on the anisotropic permeability values.

Hypothesis 3; The relationship between permeability and plug porosity is affected by clay.

Hypothesis 3 was accepted. It was observed that the plugs with more *clay* generally had a lower permeability, and that many small pores are associated with increased areas of *clay*.

From the evidence provided in this chapter it is concluded for the current data set, that image porosity is less than plug porosity and has a stronger linear relationship with permeability; this is a result of micro-porosity being included in the measurement of plug porosity but not in the image porosity calculation. It was concluded that the sum of area *clay* plus area pore would give values and a distribution closer to that of the plug porosity, than just area pore. Therefore, image porosity is estimating the flowing, or effective porosity, and plug porosity is a measure of total interconnected pore space.

The optimal micro-porosity associated with the *clay* is calculated from the entire data set as 67%. The plug porosity is modified as plug porosity minus the micro-porosity (67% of the area *clay* value), and had a stronger linear relationship with permeability than the plug porosity.

Hypothesis 4; Large pores are present within the plugs which are not captured with image analysis and do not contribute to permeability, but increase the value of plug porosity.
Hypothesis 4 was rejected; due to the large size (1 mm^2) of pore that would be required for it not to show in the low magnification images.

Other image analysis data used to constrain the permeability-porosity relationship
Several relationships between image parameters and the permeability-porosity relationship were examined. The conclusions which were drawn are:

(i) Fine grained images have a strong positive linear trend, and large grained images have a high permeability (>1000 mD) but only a medium (≈24%) plug porosity.

(ii) Pore cleanness split the permeability values into a series of bands with permeability values increasing with each increase in pore cleanness.

(iii) Loosely packed grains predominantly had a high porosity and permeability value, however, a clear decrease in permeability with decreasing porosity, observing changes in packing was not apparent.

(iv) Large pores are observed to be present in the higher (>80 mD) rather than lower permeability ranges.

(v) Aggregates of clay, grain sorting and anisotropy did not have an obvious relationship with permeability or porosity.

(vi) Facies 2 is suggested as being homogeneous at the plug scale but heterogeneous at the image scale, due to a narrow plug porosity range and the large image porosity range.

(vii) Pore aspect ratio had no correlation with permeability or porosity and it is proposed that this was either due to the small area of investigation, or that the magnification itself was not optimal.

(viii) Permeability decreases with increasing roughness, it was suggested that the roughness may cause an enhanced frictional drag on the gas molecules or increased pore angularity may create pockets in which flow is disrupted and becomes more turbulent, therefore decreasing permeability.

(ix) The porosity indices have a significant relationship with permeability and it could be assumed therefore that the plugs are approaching homogeneity with increasing permeability. However, the indices are calculated using image porosity and it is suggested that this is the primary control on the observed relationship.

Percentage ranges of area *clay* created linear trends in the poorly correlated gas permeability-F cross-plot and the F-image porosity plot, demonstrating the importance of clay to the F value. It is observed that very conductive rocks (low F) have many large pores, but there is not a simple progression from many large pores to many small pores with decreasing conductivity. The second group of most conductive plugs have a higher percentage of small pores than the least conductive plugs. A possible explanation is that as many small pores (13 to 430 μm^2) are observed to be associated with increases in *clay*, the clay may be contributing in a significant manner to the conductivity of the rock.

A comparison of gas permeability and F with both image and plug porosity revealed that permeability had a more significant relationship with image porosity than plug porosity. However, F has a stronger relationship with plug porosity than image porosity. It was concluded from this simple observation that F has a greater insensitivity to pore morphology than permeability.

Conclusions and suggestions for further work

8.1 Conclusions

The aim of this study is stated in Chapter 1 as; 'A simple, linear permeability-porosity relationship is often inaccurate but the oil industry use it for the prediction of reservoir permeability from wireline logs. Can pore morphology data obtained from SEM images help to constrain this relationship?'

The aim of the study has been accomplished for the reservoir investigated. The use of image data led to an understanding of the controls on permeability and porosity. This understanding was achieved by the demonstration that micro-porosity is an ineffective porosity in terms of fluid flow. Micro-porosity is identified as pores <13 μm^2 and mostly occurs within *clay**. It is observed that many small pores (13-430 μm^2) are associated with increased areas of *clay*. Image porosity is less than plug porosity and has a stronger linear relationship with permeability, which is a result of micro-porosity being included in the measurement of plug porosity but not in the image porosity calculation.

The knowledge of the relationship between plug porosity, image porosity and *clay*, enables the estimation of plug porosity from the image data as (image porosity + *clay* micro-porosity) the latter being taken as 67% of the area *clay* value. Hence, a modified plug porosity value consisting of plug porosity minus the area *clay* micro-porosity can be calculated for each plug from the images. The reduced plug porosity gives a stronger linear relationship with permeability than the core plug porosity.

---

* The term *clay* is defined as a specific grey scale range (50-170) on the SEM images, it includes detrital and diagenetic clays, as well as software artefacts such as grain edge effects.

Further conclusions arose from the work discussed in this thesis, including the following:

8.1.1 Image data

1. The image data was generated from thirteen SEM images (five at x30 and eight at x150, captured as 256 grey scales) taken on the end-trims of 63 sandstone plugs. The data was found to be adequate for distinguishing between the matrix and pore space, and for pore shape measurements. Limitations with the data were found:
   - The main potential for errors with the image data are the necessary assumptions that both the high and low magnification images are homogenous, and also that these images are considered representative of the core plug. It was demonstrated that image parameters have strong relationships with core plug measurements, which is a positive indication that the image parameters are representative of the core plugs bulk properties.
   - There was partial loss of image data resolution. All minerals with grey scale values greater than 202 (feldspar, carbonate, anhydrite and iron minerals) were grouped, as a result of non-consistency in the grey scale peaks.
   - The 'shouldering' effect seen in the grey scale curves has been adequately compensated for by the use of a grey scale range associated with each mineral phase, rather than a single grey scale value.
   - Grain edge effects within the images contribute to the fact that image porosity is less than plug porosity.

2. Image permeability was significantly correlated with gas permeability, demonstrating the potential for estimating 3D parameters from 2D data.

3. A qualitative comparison of plug porosity and gas permeability with the SEM images demonstrated that high permeability plugs are associated with coarse, well spaced, well sorted grains with clean* pore space.

4. Neither pore orientation nor image porosity measured at the resolution used in this study contain sufficient information to enable interpretation of the anisotropic plug permeability values associated with the cubic plugs; this result may be a function of the scale of description and/or resolution.

* The term pore cleanness relates to the amount of *clay* scattered throughout the epoxy phase

5. Permeability decreases with increasing pore roughness and it is postulated that this is either due to frictional drag of the gas molecules, or that increased roughness creates pockets in which flow is disrupted and becomes more turbulent.

6. Two porosity indices were derived from the image and plug porosities and used to investigate plug homogeneity. They both gave a significant relationship with permeability and it could be proposed that the plugs are approaching homogeneity with increasing permeability. However, it is suggested that image porosity is the primary control on the observed relationships.

7. Aggregates of clay, grain sorting, pore aspect ratio and anisotropy observed within the images do not show a significant relationship with either permeability or porosity.

8.1.2 Klinkenberg permeability

1. Three data sets of gas permeability measured at different inverse mean pressures were collected on the same suite of plugs in two laboratories (SC2 and SC3), to investigate potential errors associated with Klinkenberg permeabilities. The results demonstrated that:
   - The relationship between gas permeability and inverse mean pressure was frequently non-linear resulting in inaccurate Klinkenberg permeability calculations. The three data sets did not duplicate extrapolated Klinkenberg permeability values or curve shape.
   - The majority of curves if seen alone, however, would look convincing due to their smooth curve shape, even though the measured values can be incorrect; this inaccuracy is suspected as being the result of insufficient time allowed for gas flow to stabilise.

2. The main control on the non-linear relationship is concluded to be back pressure. Additionally, the lack of back pressure control, other than orifice size, for the measurements made at SC3 is suggested as being responsible for the extreme curvature associated with this data set.
   - Gas slippage is suggested as a secondary reason for the increased values of permeability at low mean pressures. A possible optimum value may occur at the plateaued region of the curve, where permeability does not decrease with increasing pressure. Turbulent flow is then thought to occur and there is a rapid decrease of permeability with increasing pressure. The fact that the kink or plateau in the Klinkenberg curves moves to

lower pressures in higher permeability plugs implies that turbulent flow occurs at lower pressures in higher permeability plugs.

- SC2 increased the linearity of the relationship by using a net confining pressure rather than a constant confining pressure (as used by SC3). Hence, false high permeability values due to gas bypass with increasing mean pressures were reduced. The increased confining pressure, however, gave reduced Klinkenberg permeability values and therefore with the effective decrease in confining pressure with increasing mean pressure in the SC2 data, the curve shape should be flattened; maybe the cause of the plateau?
- The curve shape was not due to the movement of pore fines as results at SC3 were repeatable. The curve shape is emphasised in the high permeability plugs.
- The repeatability of some curves was poor and is likely to be a result of instrumentation quality, user error or small upstream and downstream pressure differences.

8.1.3 Formation resistivity factor *(F)*

1. The relationship of the formation resistivity factor with *clay* was investigated. It is proposed that *F* has a greater insensitivity to pore morphology than permeability and it is suggested that clay surface conduction contributes to plug conduction.
    - The evidence for *F* using micro-porosity is taken from a comparison of gas permeability and *F* against both image and plug porosity, which revealed that permeability has a stronger relationship with image porosity than plug porosity (demonstrating a sensitivity to pore morphology), but *F* has a stronger relationship with plug porosity than image porosity (demonstrating an insensitivity to pore morphology).
    - The evidence for surface conductance is from the analysis of pore size ranges. It is observed that very conductive rocks (low *F*) have many large pores, but there is not a simple progression from many large pores to many small pores with decreasing conductivity (increasing resistivity). The second group of most conductive plugs have a higher percentage of small pores than the least conductive plugs. A possible explanation is that as many small pores (13 to 430 μm^2) are observed to be associated with increases in *clay*, the clay may be contributing in a significant manner to the conductivity of the rock.

- Attempts to make use of facies in characterising the permeability, porosity and formation resistivity factor were of limited success, unlike area *clay* ranges which split the F-gas permeability and F-porosity relationship into a series of linear trends.

8.2 Further work

The conclusions above leave a number of unsolved problems and generate several interesting possibilities for future studies.

The first line of recommended further work is quantitative clay analysis of the plugs to substantiate the conclusions.

The image analysis pore size ranges could be validated by comparison with the nuclear magnetic resonance (NMR) pore size distribution data. If the NMR data are directly related to the pore size distributions obtained from image analysis, which are in turn significantly correlated with permeability, NMR could be used to predict permeability where images cannot be taken. For example, in unconsolidated rocks which are extremely difficult to core. Also, downhole NMR logs could be used as a permeability prediction tool, which is already routinely done by some oil companies but the data are rarely used. Perhaps if the relationship between permeability and the pore size ranges was enhanced, the results would be more widely applied.

A recommended piece of further work would be the comparison of the pore size distribution data obtained from the SEM images, with the pore size distributions obtained from mercury injection capillary pressure curves.

Image analysis described in this work could be directly applied to drill cuttings or side wall plugs. These samples can be large enough to put into an SEM and therefore an image porosity calculated. The sample location within the borehole can be estimated at the time of drilling. A pore size distribution could be calculated from these samples and used to predict permeability. Obviously, all samples would have to be tested for fracturing which if present would give misleading results, this may rule out percussion side wall cores. If the samples were fractured an estimate of *clay* micro-porosity could still be calculated, this value could be subtracted from downhole porosity, calculated from logs, which may give a value of effective porosity which has a stronger relationship with the permeability.

Many interesting questions have been raised in relation to the Klinkenberg results, but to answer these more data are required. The ideal data set would be sedimentary plugs deposited under different environments with different sedimentological and petrophysical properties, on which repeated measurements could be made. These plugs would be subjected to different cleaning and drying processes as well as various experimental analysis before gas permeability measurements were made, enabling the effect of different rock properties (e.g. clay content) to be investigated. The plug curve shapes could then be investigated and their response under different experimental situations examined.

Some gas permeability measurements were found to be less repeatable than others, which may be an indication of multiple pore sizes not allowing the gas pressure to stabilise within the plug. The pore size distribution information could be used to test this theory.

Nomenclature

A.1 Introduction

This appendix lists all of the nomenclature used in this study under four sections; Latin letters (A-2-1); Greek letters (§A.2.2); symbols (§A.2.3) and units (§A.2.4).

A.2 Nomenclature

A.2.1 Latin letters

a	Empirical constant
A	Cross sectional area; angle used in capillary pressure curves
A_a	Internal surface area
A_c	Cross sectional area, specific to the Kozeny correlation
A_{gr}	Grain area
A_p	Pore area
AP	Total area pore
API	American Petroleum Institute
At. Pr.	Atmospheric pressure
A_s	Effective pore surface area
b	Slip-factor; number of pore branches
Bp	Atmospheric pressure
c	Constant
clay	An image analysis term for minerals in the grey scale range of 51-170.
C	Connectivity
C.E.	Cation exchange
CP	Capillary pressure
d	Diameter
d.d.	Drillers depth
e^-	Electron
EDX	Energy dispersion X-ray system
f	Fischmeister shape factor
F	Formation resistivity factor
F_{tube}	Formation resistivity in tube
F_{sheet}	Formation resistivity in sheet
g	Conductance as a function of throat geometry alone
$g_e(d)$	Effective electrical conductance
$g_h(d)$	Hydraulic conductance
G	Genus; molar flow rate
GEX	Gas expansion
H_g	Mercury injection
I_R	Resistivity index
k	Permeability
k_0	Permeability at zero inverse mean pressure
k_1	Permeability at an inverse mean pressure of 1 atm
k_A	Absolute permeability
k_{brine}	Brine permeability
k_g	Gas permeability
$k_{g/o}$	Relative permeability measurement of gas to oil
k_{img}	Image permeability
k_{Klink}	Klinkenberg permeability
k_l	Liquid permeability
k_s	Specific permeability
k_{sheet}	Sheet permeability
k_{tube}	Tube permeability
$k_{w/o}$	Relative permeability measurement of water to oil
KDS	Klinkenberg data set
l	Length of pore; lithologic factor
l_c	Characteristic length
l_o	Constant length of pore
L	Length

L_a	Length of pore tube; capillary length
L_f	Length in macroscopic flow direction
LUT	Look up table
m	'Archie's m' or mass
m.d.	Measured depth
MICP	Mercury injection capillary pressure
n	Number of nodes; saturation exponent; no. of capillaries
N	Number of separate networks within a pore structure
NBP	No back pressure
NGR	Natural gamma radiation
NMR	Nuclear magnetic resonance
OB	Overburden
p	Effective pressure
P_1	Initial pressure; upstream pressure
P_2	Final pressure; downstream pressure
P_c	Capillary pressure
P_{cb}	Breakthrough capillary pressure
$P^`_{cb}$	Reduced breakthrough capillary pressure
P_m	$(P_1+P_2)/2$
P_P	Pore perimeter
PSD	Pore size distribution
ΔP	$\equiv(P_1-P_2)$ - the hydrostatic pressure drop
q	Volumetric flow rate
q_b	Flow rate at atmospheric pressure
Q_f	Flux
Q_{tot}	Total flux
r	Radius; correlation coefficient
r_o	Distance of zero from the axis of the capillary
R	Resistance
R_1	Roughness definition 1
R_2	Roughness definition 2
$\bar{R}$	Mean resultant
R_o	Resistivity of rock saturated with brine
ROI	Region of interest
R_t	True resistivity
R_w	Resistivity of brine
S	Specific surface/unit mass
S_{Ap}	Specific area pore
SC	Service company
SCAL	Special core analysis laboratory
SEM	Scanning electron microscope
S_o	Specific surface/unit solid volume
S_{Pgr}	Pore perimeter/unit grain area
S_v	Specific surface/unit bulk volume
S_{Vgr}	Specific surface area/grain volume
S_{Vp}	internal surface area/pore volume
S_w	Water saturation
S_{wi}	Initial water saturation
∂t	Acoustic travel time
∂t_{liq}	Acoustic travel time in liquid
∂t_{ma}	Acoustic travel time in rock matrix
t	Mean temperature of gas
t_b	Gas temperature at atmospheric pressure
T	Absolute temperature
TOP	Total optical porosity
$\bar{U}_m$	Mean molecular speed
v	Fluid velocity
v_2	Volumetric flow rate/cross sectional area
V_a	Volume of vessel
V_b	Volume of evacuated vessel
V_B	Bulk volume
V_{gr}	Grain volume
V_p	Pore volume
V_s	Volume of solids
V_V	Volume fraction
XRD	X-ray diffraction
z	Mean gas compressibility

A.2.2 Greek Letters

β	Inertial resistance (Forchheimer) factor
ϕ	Porosity
ϕ_A	Porosity index A
ϕ_B	Porosity index B
ϕ_c	Core measure porosity
ϕ_{fc}	Fraction of core porosity
ϕ_{high}	High magnification image porosity
ϕ_{img}	Image porosity
ϕ_{low}	Low magnification image porosity
ϕ_{node}	Porosity in node
ϕ_{plug}	Plug porosity
ϕ_{sheet}	Porosity in sheet
ϕ_{Total}	Total image porosity
ϕ_{tube}	Porosity in tube
λ	Mean-free path

μ	Viscosity
θ	Contact angle
ρ	Gas density; resistivity
ρ_B	Bulk density
ρ_{liq}	Liquid density
ρ_{ma}	Matrix density
ρ_o	Resistivity of non-shaley formation saturated with brine
ρ_b	Resistivity of brine
ρ_s	Density of solids
σ	Rock conductivity
σ_b	Brine conductivity
σ_f	Surface tension;fluid conductivity
τ	Pore tortuosity

A.2.3 Symbols

$\Re$	Universal gas constant
§	Section in a chapter

A.2.4 Units

IRHD	International rubber hardness
psi	Pounds per square inch
psia	Pounds per square inch (absolute)
psig	Pounds per square inch (gauge, it is used to indicate that the zero of the gauge relates to atmospheric pressure)

APPENDIX B

Image analysis information

B.1 Introduction

Appendix B is related to the SEM images and the image analysis package, and is referenced in Chapter 6. Section B.2 lists all of the measurements which were initially made (using the PC_Image software) for this study. Section B.3 is a brief record of minerals or features observed within the SEM images used in the coarse of this study. Section B.4 gives a table showing the numerical key assigned to the qualitative character of the images.

B.2 Image parameters measured by PC_Image for this study:

Voids: Weighted Number of Measured Pores
FieldArea: Total Field Area
DetArea: Detected Pore Area
Apore: Area Fraction Pore Phase (grey levels 0-50)
Ashale: Area Fraction Shale Phase (grey levels 51-170)
Aqtz: Area Fraction Quartz Phase (grey levels 171-202)
Afeld: Area Fraction Feldspar Phase (grey levels 203-220)
Acarb: Area Fraction Carbonate Phase (grey levels 221-239)
Aanhy: Area Fraction Anhydrite Phase (grey levels 240-249)
Airon: Area Fraction Iron Phase (grey levels 250-255)
Perimeter: Perimeter (microns)
Length: Length (microns)
Breadth: Breadth (microns)
PoreArea: Pore Area (sq. microns)
AER: Area Equivalent Radius - The radius of a circle with the same area as the measured object. (microns)
AER = Sqrt(pore area/pi)
MinRad: Minimum Radius (microns)
MaxRad: Maximum Radius (microns)
MeanRad: Mean Radius (microns)
MeanFer: Mean Feret (microns)
MinFer: Minimum Feret (microns)
MaxFer: Maximum Feret (microns)
Bpore: Boundary Fraction undetermined

Bshale: Boundary Fraction Shale

Bqtz: Boundary Fraction Quartz

Bfeld: Boundary Fraction Feldspar

Bcarb: Boundary Fraction Carbonate

Banhy: Boundary Fraction Anhydrite

Biron: Boundary Fraction Iron

HydDia: Hydraulic Diameter = 4(Pore Area/Pore Perimeter) (microns)

M: M = (Length/Breadth)

Ssurface: Specific Surface = 4(Pore Perimeter/pi * Pore Area)

AspRatio: Aspect Ratio = (Breadth/Length)

DeltP: Delta Pore = Length-Breadth (microns)

Sort: Weighted STD of Mean Feret

PHI: PHI = (Pore Area/Field Area)

Density: (Pore Area/Field Area)*10e+8

GMvol: Geometric Mean Volume of a sphere based on the mean diameter (microns cubed)

GMdia: Diameter derived from the Geometric Mean Volume (microns)

Ccarb: Total Boundary Count Carbonate Phase

Ciron: Total Boundary Count Iron Phase

MedAvgD: Median Average Diameter (microns)

MedMinD: Median Minimum Diameter (microns)

MedMaxD: Median Maximum Diameter (microns)

Field: The Image Field from which the data was taken

Weight: Area weight used to calculate weighted mean values. The Area Weight for high magnification images is 15. The Area Weight for low magnification images is 1.

B.3 Distinctive features observed in the images

Well-plug	Image	Visual observations
1/14	1	[illegible] oval grains touching another grain. 30% of grains have clean edges, these edges seem comparatively smoother than the other 70%.
	2	3 large grains dominate the image and go over the edge of the image. Classic example of platy clays. A smooth oval grain is present which does not look like the standard quartz grains.
	3	10% of edges of grains show distinct fracturing. Mica like mineral assemblages in the top RHS of image.
	4	Transparent, woven type mineral in the shape of an angular, highly irregular shape. There seems to be something wrong with this image, as though there has been a processing problem.
	5	Picture dominated by large singular quartz grains. Noticed that a film appears around the 'white' grains (possibly feldspar) more frequently than the grey quartz grains.
	6	Untidy image. Would not believe that this image was taken from the same core as the previous 5. There is an inclusion within 2 separate grains. 5% of the image being covered with 'floating' clays.
	7	Quartz grains appear to be polygonal in shape. Very smooth sides to grains, which seem to slot together like a puzzle.
	8	There is a classic example of some mineral tabular in shape, possibly feldspar? Also, a feldspar grain showing twinning.
	9	It can be seen in this low mag image how the clays tend to form or gel together, due to the obvious regions of epoxy infill and clay infill.
	10	As above.
	11	As above.
	12	As above,
	13	Very strange: 3 'grain' surrounded by epoxy, where as the rest of the image shows no such wide spaces. There is a possible explanation that during the polishing the softer material was somehow lost.

1/1c	1	Can see the clay 'clinging' to the roughness of the grains.
[redacted]		
	3	1 major grain on the bottom LHS actually appears wobbly in its appearance, much pore filling.
[redacted]		
	5	A clearer view of the 'rice' mentioned earlier in the core 1A above. A mass of about a fifth of the image.
[redacted]		
	7	Nothing spectacular in this.
[redacted]		
	9	Maybe 2% of image actually shows epoxy, at this scale most of the pores seem to be blocked.
[redacted]		
	11	An apparent mass of grains, clay and other minerals, different textures in the minerals are becoming more apparent to me now.
[redacted]		
	13	As above
[redacted]		
	2	Dark grey smudges, also possibly 2 bubbles. There is a very solid pore filling mineral present.
[redacted]		
	4	A visible E-W direction trend.
[redacted]		
	6	A third of this image is covered by a grain, not the usual quartz colour, with an obvious orientation of fractures. These smudges are still present and may affect the analysis of grey levels.
[redacted]		
	8	Large band of wispy clayey material through the centre of image. In the top centre of the image, there is a bent grain. Is this a tectonic indicator?
[redacted]		
	10	Diffuse clays present
[redacted]		
	12	Untidy image
[redacted]		
1/4a	1	Only 5% epoxy spaces, swirling clays.
[redacted]		
	3	1 huge grain taking up 50% of the image. On the top RHS there is a region where the clays seem to form their own organised system.
[redacted]		
	5	As above
[redacted]		
	7	The grains in this PLUG seem less compressed than the last core set.
[redacted]		
	9	Looking at 9 and 10 together you would never believe that they were from the same image! On the central LHS there seems to be a large mass of clay minerals.
[redacted]		
	11	A clayey sandstone with pores
[redacted]		
	13	3 more of those assemblages of mineral surrounded by epoxy.
[redacted]		
	2	Again a very clear sample, looks like HC would flood through, this time some of the 'rice' clays appear to be grey. The same attracted to, but not sticking to grains affect is observed as in the previous image.
[redacted]		
	4	Clumps of white material clinging together, but the pores crystal clear yet again.
[redacted]		
	6	Large grain at the top of the image, which appears to be wafer thin as little dot of epoxy appear throughout it.
[redacted]		
	8	Some of the wispyness is again observed but the 'rice' are abundant and as usually they appear to be attracted to the grains but are not sticking to them.
[redacted]		
	10	Has the appearance of a clean porous sandstone.
[redacted]		
	12	As above.
[redacted]		

1/5c	1	Large connected void space, but the epoxy isn't quite black, definitely blurred in places. Well the whole image has this kind of blurred photo look.
[redacted]		
	3	There is a large grain which is approx. eighth of the screen which has a definite grain shape but it lacks colour consistency. Actually it has a considerable inclusion (?) of epoxy. Maybe mineral is very soft and the result is just an effect of processing
[redacted]		
	5	The image is very clean with hardly 1% clay content. 1 grain extends from top to bottom of the image.
[redacted]		
	7	Floating 'rice'. A grain on the top LHS seems to have a band running through it. Still there is a lack of fine, wispy clays.
[redacted]		
	9	At this lower magnification it becomes visible how clean this sample is, it shows 3 main clumps of clays, but none of the wispy kind.
[redacted]		
	11	Image is still clear but there is much pore blockage by groups of clay minerals.
[redacted]		
	13	Just an ordinary mixed image
[redacted]		
	2	Bottom LHS layers of platy clays or possibly mica?
[redacted]		
	4	Large grain dominates 50% of image. Some sticking wispy clay now around.
[redacted]		
	6	On upper RHS there is a clump of what looks like small quartz pieces surrounded, and connected, by some sort of clay.
[redacted]		
	8	The clay observed here still has that very interesting smooth globule type tendency.
[redacted]		
	10	No comment
[redacted]		
	12	No comment
[redacted]		
1/7a	1	Large grain covering 40% of screen, in bottom half of image sand grains have spikes!
[redacted]		
	3	Grey 'rice' are present
[redacted]		
	5	Again debris.
[redacted]		
	7	Debris.
[redacted]		
	9	No comment
[redacted]		
	11	Debris
[redacted]		
	13	Debris
[redacted]		
	2	The quartz grains are larger than in the previous image, and there is a lack of the 'other' grain. clay is as above.
[redacted]		
	4	In the centre of the image there appears to be a water mark! maybe it really is.
[redacted]		
	6	In the centre right of the image at a glance there seemed to be more of the blurred grains seen earlier.
[redacted]		
	8	Third of image is dominated by a large quartz grain. Brown 'rice' are present, and also a tabular pale grain, (feldspar?)
[redacted]		
	10	A combination of everything.
[redacted]		
	12	As above. There is a large void in this image but it has been invaded by clays or other material, this implies that it is not the size of the void that decides whether clays remain.
[redacted]		
2/1a	1	A mess, different sized grains. Brown 'rice', very fine clay, bent white mineral, it's all here.
[redacted]		

	3	A quarter of the image is a single mass of brown 'rice'
	4	[illegible] fibres of something, seen previously, [illegible]
	5	Grains seem to be touching in pairs, a spreading of brown 'rice' can be seen!
	6	[illegible] clear pore in the centre of the image, maybe it was totally sealed before it was cut.
	7	7 and 8 are entirely different images. This image contains a large very strangely weathered, 'curvy' type grain. There seems to be some sort of imaging problem, because a grain suddenly changes colour for no apparent reason. (Unless it is alteration of some sort)
	8	Lots of debris and some platy stacked minerals
	9	Small pocket of epoxy
	10	[illegible] clearly. Some white minerals can be seen centrally.
	11	Debris
	12	[illegible]
	13	Interesting conglomeration of fibrous material in the centre of the image.
[illegible]	1	[illegible] the previous core has [illegible] reasonably smooth grains, with the majority of infill being the larger [illegible]
	2	An unusual grain at the centre bottom of the image in that it looks like a solid object, and yet on its upper LHS *there seems to be a fraying of the grain itself.*
	3	Infill [illegible] seems to be squashed into a little space.
	4	1 grain dominates 50% of the image.
	5	[illegible] conglomerate grains, very well fitted close contact quartz [illegible] epoxy.
	6	There appears be a gap between every quartz grain, just like they have all been pulled apart.
	7	A very clear example of grain contact, and some peculiar fibrous material at the base of the image.
	8	Fibres actually seems to spray out from a confined space into a larger pore, as though it 'grew' floating.
	9	A combination of very clean quartz grains and areas totally infilled with a single mineral.
	10	As above
	11	[illegible]
	12	As above
	13	As above
2/9b	1	Looks like one of the grains is rotting on the central RHS. I would say there is almost up to 40% void space and it is very clean space.
	2	As above without the [illegible] grains
	3	There is a film around the grains which appears to be a fine debris.
	4	[illegible] grains dominate the image and also an excellent example of the fibrous material. One of the grains is [illegible]
	5	6 grains dominate the image, air bubble and some clustering of clays.
	6	50% of image is covered with this huge globule of interlocking fibrous material.
	7	A clear image with apparently little blockage.
	8	As above
	9	Amazingly spaced and clean.
	10	[illegible]
	11	Amazingly spaced
	12	Amazingly spaced [illegible]
	13	Amazingly spaced
2/9c	1	Very clean image with feathery mineral at the top of the image. Air bubble at the base.
	2	A very spaced rock.
	3	A brown rice example again, but otherwise very clean and clear.
	4	No comment
	5	Good example of the platy yet fibrous material, lots of little solid bits of mineral.
	6	A central grain, about an eighth of the image, seem to have a mineral vein running through it.
	7	4 large grains with some little grains around them
	8	none of the orientation which was present in earlier cores is seen here
	9	Generally clean with many voids, some areas of solid clay infill.
	10	As above
	11	As above
	12	Very clean.
	13	[illegible] with visible conglomerate grains
2/ 10a	1	8 well spaced grains dominate the image. There is a white mineral touching 30% of the grain. There's <1% other material.
	2	As above but with 3 grains dominating the image and there is an air bubble, and a certain grain has a thick rim of the white mineral.
	3	The quartz grains, as in the last 2 images as well, are much cleaner/clearer, there seem to be no black processing marks.
	4	These quartz grains aren't as clear but the epoxy is black, not sure if this is a better set of processed images than [illegible] or whether it is a lack of resolution compared to the last.
	5	As previous images, with air bubble.
	6	Also has an air bubble, I'm beginning to get suspicious that these air bubbles are air bubble or that they might be a mineral.
	7	3 large grains contain a mass of the above mentioned white mineral. One of the grains is different than the normal quartz and has a shearing fracture across it. This fracture looks fresh.

[redacted]		
	9	Grains appear to be evenly spaces and have a frosted effect from the surrounding white mineral.
[redacted]		
	11	As above.
[redacted]		
	13	Bottom LHS there looks to be a lump of sandstone, quite a confusing sight at a glance!
[redacted]		
	2	Mineral in the centre of the image appears to be in layers.
[redacted]		
	4	'rice' and fibrous material are all intertwined. There is also some wispy clay around some of the quartz grains.
[redacted]		
	6	A clean sandstone possibly showing some orientation of the grains, in a N-S direction as observed before.
[redacted]		
	8	Air bubble in the top LH corner.
[redacted]		
	10	As above, but the blockages are less regular but more condensed.
[redacted]		
	12	As above, well maybe not such condensed blockages.
[redacted]		
2/ 11b	1	Mass of 'rice' blocking a large pore space. In bottom RH corner there is some finer material sticking to the quartz grains.
[redacted]		
	3	On top of one of the quartz grains there is something that looks like a film or mesh of a white mineral, an air bubble in the top RH corner.
[redacted]		
	5	Interesting fractured grain in the top LH corner. Seem to be a wide, third of image, diagonal band going across the image, which is a conglomeration of all sorts of odds and sods.
[redacted]		
	7	More of two-toned grains (altering?).
[redacted]		
	9	Just another SEM image of a sandstone showing clear pores trapped pores and the occasional mass of a fibrous mineral.
[redacted]		
	11	As above.
[redacted]		
	13	As above.
[redacted]		
	2	Brown 'rice', a long tabular grain which has been squashed between 3 quartz grains and has bent accordingly.
[redacted]		
	4	Something wispy in the centre of the image, is it a processing fault?
[redacted]		
	6	All the infill appears to be pretty weak.
[redacted]		
	8	Large scattering of white material
[redacted]		
	10	As above.
[redacted]		
	12	As above.
[redacted]		
3/5a	1	lots of 'rice' and also 2 grains which were possibly one at some stage, which seem to be separated by a total blockage, which is different from the rest of the image.
[redacted]		
	3	The different grains are obvious but they none the less seem welded together.
[redacted]		
	5	Strange swirled grain in the bottom RH corner, lots of large black holes.
[redacted]		
	7	an epoxy film around a quartz grain, where the pore filling minerals don't enter.
[redacted]		
	9	Is there orientation in these sandstones, surly one of the measurements will be able to tell me that.
[redacted]		
	11	As above.
[redacted]		
	13	As above.
[redacted]		
	2	The wispy clay is back again, sticking mainly to the white grains.
[redacted]		
	4	Very thin mineral images appearing in the top RH corner, they almost look 3D. There is a lump of messy material

		about a sixth of the image.
	5	[illegible]
	6	No comment
	7	[illegible]
	8	debris.
	9	[illegible]
	10	Narrow but long grain, third length of image, pore space. This pore space is strange because the clay has formed a grain skeleton structure (kaolinite altered feldspar?).
	11	[illegible]
	12	Clear voids, only small patches of clay
	13	[illegible]
3/ 10b	1	Skeleton like picture of grains formed again in clay. pore filling clay, and tabular like crystal growth on the RHS of the image.
	2	[illegible]
	3	Highly fracture grain on the RHS of the image. The pore space is very clean. No wispy clay is present,
	4	[illegible]
	5	No apparent order in any direction or any preferences to any minerals.
	6	[illegible]
	7	Central quartz grain looks like it is splitting. Clear pores.
	8	[illegible]
	9	Very irregular grain sizes, all pore spaces small.
	10	[illegible]
	11	As above.
	12	[illegible]
	13	As above.
3/11b	1	[illegible]
	2	White grain in top LH corner has had its edges smoothed by the sticking of clay particles. A grain at the bottom of the image looks like it has been sheared by an intruding tabular grain.
	3	[illegible]
	4	No comment.
	5	[illegible]
	6	Air bubble. Lots of clear pore space
	7	[illegible]
	8	1 grain covers half of the image. In the bottom LH corner there is a most peculiar white grain in a quartz grain.
	9	[illegible]
	10	Very obvious large lumps of clay.
	11	[illegible]
	12	As above.
	13	[illegible]
3/14c	1	The whole image looks a bit hazy, but the pores themselves are very clear.
	2	[illegible]
	3	All the debris seems to be confined to the edges of the pores, there is a large range of grain sizes.
	4	[illegible]
	5	Feather mineral again in the centre of the image, and also an air bubble.
	6	[illegible]
	7	As above
	8	[illegible]
	9	4 groups of a mineral all together. Also a large mass of wispy white material.
	10	[illegible]
	11	As above.
	12	[illegible]
	13	As above.
4/16c	1	[illegible]
	2	These white spots are in this image to. The quartz grains seem to be similarly shaped and sized, compared to the contrasts I have already seen.
	3	[illegible]
	4	Where have all the wispy clays gone?
	5	[illegible]
	6	Definitely a direction N-S trend of all grains.
	7	[illegible]
	8	White spots back. Although there is some pore filling the image has some order due to the fact that it looks clean
	9	[illegible]
	10	As above.
	11	[illegible]
	12	As above.
	13	[illegible]
4/18c	1	No comment
	2	[illegible]
	3	RHS small air bubble. Large pitted grain on LHS of image which also has a segment of white in it.

[illegible]	[illegible]	[illegible]
	5	Debris
[illegible]	[illegible]	[illegible]
	7	On LS of image there is a very strange pitted mottled grain.
[illegible]	[illegible]	[illegible]
	9	There are clear pores, but there is also fibrous (clay?) material.
[illegible]	[illegible]	[illegible]
	11	As above, but less white infill
[illegible]	[illegible]	[illegible]
	13	As above.
[illegible]	[illegible]	[illegible]
	2	Some very clean pore spaces, but why is the grain so smudged on its LHS?
[illegible]	[illegible]	[illegible]
	4	2 air bubbles. Rhombus shaped white grain.
[illegible]	[illegible]	[illegible]
	6	Clear spacious pores
[illegible]	[illegible]	[illegible]
	8	Air bubble? top LH corner. Again large clear pore spaces although there is more grey 'rice' infill. Strange grain in the bottom of the image which almost looks like a thick mesh of fibres rather than a solid grain.
[illegible]	[illegible]	[illegible]
	10	Clear, even better spaced grains.
[illegible]	[illegible]	[illegible]
	12	Clear in places as stated above, but there seem to be 2 bands of finer material running in a diagonal direction.
[illegible]	[illegible]	[illegible]
4/20c	1	lovely clear pore spaces, 30% at least of the image must be pore space.
[illegible]	[illegible]	[illegible]
	3	A large grain covering 50% of the image, there is also a huge pore space of 20% of the image.
[illegible]	[illegible]	[illegible]
	5	Large clear voids are back.
[illegible]	[illegible]	[illegible]
	7	Large grain covering 60% of image, peculiar meshed grain to the left of the huge quartz grain.
[illegible]	[illegible]	[illegible]
	9	Large clear voids.
[illegible]	[illegible]	[illegible]
	11	Large clear voids. One of these diagonal bands I saw in the last core of finer material, going in the same direction.
[illegible]	[illegible]	[illegible]
	13	As above.
[illegible]	[illegible]	[illegible]
	2	Only small clusters of grey 'rice', in gaps between the tightly packed pores.
[illegible]	[illegible]	[illegible]
	4	No comment
[illegible]	[illegible]	[illegible]
	6	In RH corner the pore spaces are totally filled.
[illegible]	[illegible]	[illegible]
	8	Lump of fibrous material at the bottom of the image.
[illegible]	[illegible]	[illegible]
	10	As above, although the clay does seem to have stuck a little more together.
[illegible]	[illegible]	[illegible]
	12	Highly filled
[illegible]	[illegible]	[illegible]
4/22c	1	An image full of mess and chaos.
[illegible]	[illegible]	[illegible]
	3	As above.
[illegible]	[illegible]	[illegible]
	5	Lots of different kinds and sized particles but still clear pore spaces.
[illegible]	[illegible]	[illegible]
	7	No comment
[illegible]	[illegible]	[illegible]
	9	9 and 10 are totally different. Clear voids with lumps of clay.
[illegible]	[illegible]	[illegible]
	11	Even more full of clay.
[illegible]	[illegible]	[illegible]
	13	Some bits have lots of clay and others do not.
[illegible]	[illegible]	[illegible]
	2	Same as above, but some smaller grains have come into the image as well as a little clay.
[illegible]	[illegible]	[illegible]
	4	Lots of clear pore space and a very white grain in the centre of the image.
[illegible]	[illegible]	[illegible]
	6	In the top RH corner is an exaggerated example of what has been called grey 'rice'.

	7	Still clear pore spaces, [illegible]
	8	Pore space has been invaded by grey 'rice'.
	9	Very clear pores and grains are freely spaced.
	10	As above
	11	As above but with lumps of grey 'rice' clearly seen.
	12	Clear
	13	[illegible]
6/2a	1	There are pore spaces, but debris infill as well
	2	Lumps of clay and conglomerate stuff, interesting fractured, pale grey grain at the bottom of the image.
	3	Mixture of grain sizes, and a bit of clay.
	4	Large grain taking up about a third of the image. A clump of 'rice' both grey and white. Some of the grains do have [illegible]
	5	No comment.
	6	No comment.
	7	Altering huge grain, approx. third of image, with a bent platy mineral next to it.
	8	LH corner is pale mottled grain with small white 'rice' around the edge, which appear to be corroding the rock.
	9	Clear pore space
	10	A strong clay presence.
	11	Irregular grain size, clays present.
	12	As above.
	13	As above
6/4a	1	Range in size of grains causing much pore infill, plenty of large clay to add to this infill.
	2	As above.
	3	As above without bubble and long platy clay.
	4	Debris. All of these four images have had black smudges.
	5	Thick white cement type infill, also clay.
	6	Hardly a pore in site for all the clay and debris around.
	7	[illegible] 60% of the image, the rest of the image is still cluttered but not as packed as the previous images.
	8	As above, without the huge grain.
	9	Range in grain sizes and lots of infill in the few pores there are.
	10	As above
	11	As above, but a space or void has formed around a bubble.
	12	As above (without the bubble).
	13	As above [illegible]
6/5a	1	There are pores and they are clear apart from scattered, large pieced of clay mineral.
	2	[illegible] filling of clay minerals, but mostly as above.
	3	Reasonably clear, but there is a degree of clay pore filling.
	4	As above [illegible]
	5	As above
	6	As above but there is a altering grain in the top LH corner.
	7	As above
	8	No comment.
	9	Pores are visible, and lumps of clay.
	10	Few lumps of clay and one lump in the top LH corner goes over a quartz grain and changes colour.
	11	As above without the clay
	12	As above [illegible]
	13	As above, once again an a bubble has caused a ring of epoxy around itself.
[illegible]	1	Grains are few and well spaced, there is pore filling material. Fibrous mineral in the bottom RH corner.
	2	Grains are well spaced, but there is a lot of material clinging to the outside of the grains. A variety of grains are present, quartz, pitted, strange eroded object at the bottom of the image.
	3	85% of image is a single grain, will image analysis be possible on this? There is an object enclosed in this large grain.
	4	45% of image is a single grain. This grain is fairly central an assortment of grains and debris can be seen around its edge.
	5	25% of image is a single grain. The remaining grains are very well spaced but there is a large amount of infill.
	6	Large white shattered grain. Lots of debris infill.
	7	A grain is 55% of image, spacing and infill is as above.
	8	Pore space has to be a third of the image, but only if we are excluding the large amount of infill due to clays.
	9	Large grain dominated sandstone, creating large pore spaces, lots of associated clay infill.
	10	As above.
	11	As above.
	12	As above.
	13	As above.
6/7a	1	Lots of grains all together. 'rice' infill, both white and grey, long tabular mineral.
	2	Lots of void space, bright white mineral in the bottom of the image, debris.
	3	The clay minerals are very consolidated in their little groups. Still no sign of the wispy clay.
	4	Much grain contact.
	5	Grains seem to have suddenly shrunk, loads of pore space, but much of it infilled with brown 'rice'.
	6	Conglomerate grains, and assortment of others, debris infill.
	7	In the centre of the image there are circles of a pale mineral, why has it formed like this?
	8	Bright white spot again, on the RHS. Lots of debris infill.

	9	A mixture of grain sizes but not extremes as seen previously. Pore filling clay visible.
	10	[illegible]
	11	As above.
	12	As above, it is very noticeable in this image that the quartz grains all have black spots on them. Is this a processing [illegible]
	13	As above, black dots even seen of the white grains.
[illegible]	1	Image looks washy [illegible] of debris [illegible]
	2	Conglomerate grain. In the bottom of the image, there seem to be an almost foamy sheeted mineral. is everywhere.
	3	Excellent accumulation of clay mineral [illegible] of image which seems to have a flow channel through it.
	4	Air bubble top RH corner, Barely a clean void in sight.
	5	[illegible] much attraction between the clay material and the quartz grains [illegible]
	6	As above
	7	[illegible]
	8	Debris.
	9	Debris [illegible]
	10	A few more clear voids.
	11	As above, at the top of this image there are grains which have epoxy surrounding them. Why is this?
	12	Abundant clay.
	13	Debris with some interesting clay deposits.
7/1b	1	Many tightly packed grains, and brown 'rice' infill, bright white spots. Bent tabular minerals. Little pore space,
	2	As above. In this image that there is more pore space but it is filled with clays.
	3	Majority of clays are disappeared, but the grains seem to be more compact.
	4	Clean inter pore spaces [illegible]
	5	Good example of sheared grains.
	6	Some of the grains seem to be totally sealed together, whereas others seem to be floating, some tabular minerals [illegible]
	7	Lots of debris and clays back.
	8	As above [illegible]
	9	Very fine sandstone with random pore filling.
	10	As above
	11	As above
	12	As above [illegible]
	13	As above but more clay infill.
7/2a	1	Bubble X 3? Pore space visible, but there is a lot of debris infill.
	2	Some of those white circle mineral deposits that I spotted earlier, debris.
	3	More of those fibrous mineral and debris
	4	Large bubble. Some more clay but not so much debris. Most peculiar sort of a skeleton of a sheeted mineral
	5	Large bubble. Some totally clean voids, some filled with clay.
	6	90% of image covered by a single grain, clean pore space is surrounding it.
	7	Again a quartz in the image and looks like a collage of lots of clays and minerals.
	8	Bubble or 2? Lots of debris, which is mainly associated with the grains.
	9	Mixture of grain sizes and a true void, lots of clay infill.
	10	As above, including the void.
	11	As above without the large [illegible]
	12	As above.
	13	As above [illegible]
7/3a	1	Even distribution of grains, pore space and clay.
	2	As above [illegible]
	3	Looks like a bi-modal pore size distribution, with lots of infill, mostly clay.
	4	Top half and bottom half of the image is totally different, the bottom is much more crowded with different, more sort of 'rice' clay. In the top of the image there is only fibrous clay and it is all consolidated.
	5	Clear pore space only a small amount of clay infill.
	6?	One two toned grain, small amount of clay infill.
	7	As the other images really.
	8	Bright white grain. Otherwise as above.
	9	Grains appear loosely packed and there is a lot of clear pore space.
[illegible]	10	As above but with more clay infill [illegible]
	11	As above without the clay.
	12	As above [illegible]
	13	As above, there is an interesting clay lump
7/4a	1	Very spaced clean sandstone. Even the clay has formed in tidy masses!
	2	Bubble X 3? As above
	3	As above with only the one air bubble, [illegible]
	4	More clay infill and the grains are closer together. Problem, something looks like grains, but logically they are epoxy with a thin rim of white mineral.
	5	Bubble. Grains are reasonably space, but more clay infill.
	6	spaced grains and very clean pore space.
	7	Bubble [illegible] as above
	8	As above but without the bubbles

	9	[illegible]
	10	As above, bit more clay infill.
	11	As above without the extra clay infill.
	12	As above.
	13	As above.
7/5a	1	Some of the quartz grains are spaced others are very much together. Minerals seem to be forced into a bent fibrous pattern due to the grain compaction. Lot of fine clay infill.
	2	[illegible]
	3	As above.
	4	As above.
	5	As above. With some bright white spots, seems to be more clear pore space.
	6	As above with even more bright spots, possibly showing a N-S trend.
	7	Clarity of pores has gone, as a lot of debris has come into the image.
	8	As above [illegible]
	9	Fine grained, showing surprisingly few clear pores.
	10	[illegible]
	11	Regions of clear pores have virtually gone.
	12	As above.
	13	Regions of clear pores that are visible are elongated in a N-S direction.
7/5b	1	[illegible]
	2	As above but with more conglomerate infill.
	3	[illegible] mass of clays and grains without any clear pore space.
	4	As above
	5	[illegible] there are some clear pores, but there are still regions of total infill.
	6	Mush clearer, the long clay fibres have disappeared.
	7	[illegible] have come back!
	8	Long fibrous clay has gone but there is debris dispersed in most regions.
	9	Fine grained, some regions of clear pore spaces, but not many.
	10	As above.
	11	As above [illegible]
	12	As above.
	13	As above [illegible]
7/6a	1	2 grains dominate the image, the spaces around them are clear.
	2	2 large grains, with very clear pore space in between.
	3	Smaller grains, still very clear although some clay has come into the image.
	4	As above, although little clay.
	5	4 Grains, very clear image.
	6	A slight variation in grain size and a minimal amount of clay.
	7	Not quite as clear as the previous images as there seems to be a clay gathering around some of the grains.
	8	[illegible]
	9	Much larger grained than the previous cores, as expected, a very clear image.
	10	As above.
	11	As above, with a contained lump of clay.
	12	Some smaller grains have crept into the image, still very clear.
	13	Almost a bi-modal pore size distribution.
8/7a	1	[illegible]
	2	Bright white spots, and fibrous minerals with the debris
	3	[illegible]
	4	Bubble, plus debris.
	5	Bubble, debris, there are clear pores but there are also fibrous minerals.
	6	Bit of everything.
	7	Debris.
	8	Grains have spaced out, causing a thinning of infill material.
	9	Grain size variation, there is more epoxy visible than I would have expected.
	10	As above
	11	As above
	12	As above
	13	As above
8/8a	1	Wide range of grain sizes, small amount of clay infill, otherwise the infill is due to smaller grains blocking the voids.
	2	2 air bubbles, 3 white bright spots, debris filling some of the void spaces.
	3	Bubble. Little infill.
	4	50% of image covered by white grain showing lineations, various other grains and debris surrounding it.
	5	Bubble X 2. Various grain, not much debris.
	6	[illegible]
	7	50% of image is a single quartz grain, to its left there is just a mess of various minerals.
	8	Just another messy quartz/clay sandstone.
	9	Range of grain sizes, visible epoxy.
	10	As above.
	11	As above.
	12	As above.
	13	As above.

[redacted]		
	2	Bubble. As above.
[redacted]		
	4	Spacing out again.
[redacted]		
	6	As compact but with more clay infill.
[redacted]		
	8	Bubble? large grains clear pore spaces.
[redacted]		
	10	As above.
[redacted]		
	12	As above.
[redacted]		
8/10a	1	Most of the image is infill of clay and debris, seems to stick together quite nicely , leaving clean pore space available.
[redacted]		
	3	Bubble. Small grains, wispy clays now present.
[redacted]		
	5	Mass of grains. 50% of pore space is filled with some mineral or another.
[redacted]		
	7	As above, even with the bubble.
[redacted]		
	9	Range of grain sizes. 6 or more regions of clay lumpy infill.
[redacted]		
	11	As above.
[redacted]		
	13	As above.
[redacted]		
	2	Some obvious black spots on the quartz grains. much debris in the pore space.
[redacted]		
	4	The grains are only few, but those here, large and small are welded together.
[redacted]		
	6	A lot of scattered debris. Large white grain.
[redacted]		
	8	Grains are very compact. There is little void space and what is there is 50% filled with clays.
[redacted]		
	10	As above.
[redacted]		
	12	As above
[redacted]		
9/11av	1	Range of grain sizes, with clear pore spaces, only 5% pore filling.
[redacted]		
	3	Pore filling has decreased to 5%, there is much void space in the image, comparatively few grains are touching.
[redacted]		
	5	Debris but the grains are more spaced.
[redacted]		
	7	30% of image covered by large white grain, central mottled grain, and a decrease in infill.
[redacted]		
	9	Range of grain sizes, regions of varying infill.
[redacted]		
	11	As above.
[redacted]		
	13	As above, but there is a specifically more clear region.
[redacted]		
	2	Grains are smaller and there is more pore infill.
[redacted]		
	4	Large grains have returned, but there is now 50% pore infill.
[redacted]		
	6	Fifth of image, is filled with a large flow channel (?) which is filled with lineated clay and debris.
[redacted]		
	8	As above, but there are 2 noticeably large pores.
[redacted]		
	10	As above.
[redacted]		
	12	As above.
[redacted]		
9/12a	1	Lots of clear void space, a mixture of grain shapes and sizes, also clay mixture.
[redacted]		
	3	As above

	[illegible]	Clays in general have [illegible], some smaller grains are filling the void space.
	5	There is some solid clay flowing type infill in regions as well as 'rice'.
	6	[illegible] grains are closer now.
	7	Range of grain sizes and clays
	8	As above, there [illegible] spaces [illegible] and clays.
	9	Regions of very clear voids and others of spaces filled with large lumps of clays.
	10	As above [illegible]
	11	As above.
	12	As above [illegible]
	13	As above.
9/12b	1	Mottled grains, clays and spaces.
	2	Some solid pore infill, and some reasonably clear voids, debris.
	3	Pore spaces are clear [illegible] of the grains look very welded together.
	4	As above
	5	No welding of grains, the clays are sticking very solidly together in these images.
	6	As above, but there is some welding of grains.
	7	As above, [illegible]
	8	Everything is more condensed in this image.
	9	Regions of clear voids and regions of clay compacted pores.
	10	As above
	11	As above [illegible]
	12	As above
	13	As above [illegible]
9/13a	1	50:50 on the quartz:white grain ratio, with grey floating 'rice' around.
	2	As above, with the image [illegible] compact and there are different clays [illegible]
	3	As above
	4	As above
	5	As above, white 'rice' present as well.
	6	Mixture of grey 'rice' and a cut down in white grains.
	7	Back to 50:50 with only white and grey 'rice'.
	8	As above
	9	As above, just at a lower magnification. There is a comparatively large clear void though.
	10	As above, without the void
	11	As above
	12	As above
	13	As above
9/13a[illegible]	1	50:50 white/quartz, with a mixture of both coloured 'rice'.
	2	As above
	3	As above
	4	As above
	5	There is a larger variety of grains in this image, a pitted quartz and a mottled white grain.
	6	More space in this image, not so many blocky white grains.
	7	More compact this time, with 50:50 on the mixture of white and quartz.
	8	Just quartz and white again.
	9	50:50, can only really make out the white and quartz, there is still a mixture of white and grey 'rice'.
	10	As above
	11	As above
	12	As above
	13	As above
9/13b	1	1/3 of grains are white grains, grains are spaced and there are several types of clay infill.
	2	As above, but there is more clay infill. The two 'rice' colours.
	3	As above.
	4	Some of the clay has gone.
	5	As above.
	6	As above, the main of the clay that is in this image is concentrated into a single region.
	7	Not sure is some of the white mineral being seen is some sort of cement and is different from the previous images.
	8	A white cement infill.
	9	A 1/3 of grains are white and there are regions of clear pores and regions of clay infill.
	10	As above.
	11	As above.
	12	As above.
	13	As above.
9/14a	1	10% of grains are white, grains are well spaced, voids are mostly clear.
	2	As above, but a conglomerate grain in the top of the image.
	3	As above, but the grain is in the bottom of the image.
	4	60% of image a single quartz grain, the rest of the image contains several grains and a lump of clay.
	5	Spaced grains, only 3 white grains, minimal clay infill.
	6	Grains are still spaced in the top part of the image, but there is a mass of debris in the bottom of the image.
	7	2 grains dominate the image, with well spaced grains in-between, minimal clay infill.
	8	As above, with more clay infill.
	9	Range of grain sizes, obvious lumps of clay, and some very clear regions of pores.

	10	As above.
	11	As above, but the clays do stick together.
	12	Grains seem to be more spaced, still regions of clay.
	13	Grains have become more compact [illegible]
9/14av	1	1/5 of grains are white, grains are spaced and there is only 20% pore infill. Infill is debris and clays.
	2	[illegible] surrounded by debris.
	3	Assortment of grains, with large amount of void space, some debris infill.
	4	As above.
	5	Grains have become more compact, platy mineral infill. Long thin smudge mark of some kind.
	6	Grains have now spread out and the infill has decreased.
	7	Range of grains, mostly touching another grain, minimal infill.
	8	As above.
	9	Range of grain sizes, some areas of compacting others of clear spacing.
	10	As above.
	11	As above.
	12	As above, with a huge, eighth of image, white grain.
	13	As above, without the white grain.
[illegible]	1	Third of image covered by single large grain, much debris filling the void space, also a large mottled grain.
	2	As above.
	3	[illegible] grains dominate the image, there are some clear voids, but small grains are not allowing for much void space.
	4	Some spacing of the grains, allowing more void space.
	5	Grains are far more spaced, there is some interesting grey, rice infill.
	6	Some grains welded some grains well spaced, more debris has come back into the image.
	7	No welded grains, mixture of infill, some well weathered tatty grains.
	8	Some clays holding small quartz grains together, forming a kind of conglomerate.
	9	Large distribution of grain sizes, some clear regions and some clay filled regions.
	10	As above.
	11	As above.
	12	As above.
	13	As above.

Table B.1. Distinctive features observed in the SEM images

B.4 Qualitative character description of SEM images

This data was defined in Chapter 6 (§6.4) and used in Chapter 7 (§7.4.1). A brief summary of the key used in this table follows:

(i) Anisotropy, large pores and large mass of material. 1=present and 2=not present.

(ii) Grain size is split into three groups where 1=fine, 2=medium and 3=coarse grained.

(iii) Grain size range is split into four groups where 0.5=single sized grains, 1=fine to medium grained, 2=fine to coarse grained and 3= medium to coarse grained.

(iv) Pore cleanness is based on how clean the epoxy (pore space) of each set of images is relative to the other images, 1=clean, 2=moderately clean, 3=dirty.

(v) Number of touching grains or packing is the average number of grains touching each grain, where 1= 0-2, 2=3-5 and 3= >5 touching grains.

Well no./ plug code	Anisotropy	Grain size	Grain size range	Pore cleanness	No. of touching grains	Large pores (>50mm)	Aggregates of *clay* (>50mm)
1/1a	2	2	3	2	2	1	1
1/1c	1	2	3	3	2	2	1
1/2a	2	2	2	3	3	2	1
1/4a	1	2	2	3	2	1	2
1/5a	1	2	3	2	1	1	1
1/5c	1	2	3	1	1	1	1
1/6a	1	2	2	2	2	1	1
1/7a	1	2	2	3	2	1	1
1/9a	1	2	0.5	2	2	1	1

2/10a	1	3	0.5	1	1	1	1
2/11a	1	2	1	2	2	1	1
2/11b	2	2	2	2	2	2	1
2/1a	2	2	3	3	2	2	1
2/4a	1	2	0.5	2	2	2	1
2/9b	1	2	3	1	1	1	2
2/9c	1	2	0.5	1	2	1	1
3/10b	1	2	2	2	2	2	1
3/11b	1	2	3	2	2	2	1
3/14c	1	2	0.5	2	2	2	1
3/1a	2	1	0.5	2	2	2	1
3/5a	1	2	0.5	1	2	2	1
3/8b	1	2	2	1	2	1	1
4/16c	1	1	0.5	1	2	2	2
4/18c	1	2	1	3	2	2	1
4/20b	1	2	2	1	1	1	1
4/20c	1	2	3	1	1	1	1
4/21b	1	2	1	3	1	2	1
4/22c	2	1	0.5	3	1	2	2
6/1a	2	2	0.5	1	1	2	1
6/2a	2	2	1	2	2	2	1
6/5a	2	2	1	2	1	2	1
6/6a	2	2	3	2	2	1	1
6/7a	1	2	2	2	2	2	1
7/1b	1	1	0.5	3	2	2	2
7/2a	2	2	3	3	1	1	1
7/3a	2	2	3	2	2	2	1
7/4a	2	1	0.5	2	2	2	2
7/5a	1	1	0.5	3	3	2	2
7/5b	2	1	0.5	3	3	2	2
7/6a	1	3	3	1	2	1	1
8/10a	2	2	3	2	2	2	1
8/7a	1	2	2	3	2	2	1
8/9a	1	2	3	2	2	2	2
9/11a	2	2	1	2	2	2	1
9/11b	2	2	2	2	2	2	1
9/12a	1	2	0.5	2	2	2	1
9/12b	1	2	1	2	2	2	1
9/13a	2	2	0.5	3	1	1	1
9/13b	2	2	1	3	1	2	1
9/14a	1	2	3	2	2	2	1
9/14b	2	2	1	2	2	2	2
6/4a	1	1 and 2	1	3	2	2	1
6/8a	1	1,2 and 3	2	2	2	2	1
8/8a	2	2 and 3	3	1	2	2	2

Table B.2. Qualitative image descriptions for 54 plugs, the lowest three plugs were not used in the qualitative image study because of their very poor sorting (large grain size variation).

Klinkenberg theory and data collected at Service Company 1 and 2

C.1 Introduction

The following sections are all based on work associated with Klinkenberg theory or data, all of the following sections have been referenced in Chapter 5 (§5.3.6).

C.2 Klinkenberg theory of slip

C.2.1 Flow of gas through a straight capillary

Warburg (1870) applied the effect of slip to the flow of gas through a capillary whose radius is large compared with the mean free path. Klinkenberg (1941) extended Warburg's work to derive an equation to explain the flow of gas through a straight capillary,

$$q = \left(\frac{\pi r_o^4}{8\mu L_a}\right)(P_1 - P_2)P_m\left(1 + \frac{4c\lambda}{r_o}\right) \qquad \text{[C-1]}$$

where q is the volumetric flow rate, r_o a distance of zero from the axis of the capillary, μ the fluid viscosity, L_a the length of the capillary, P_1 and P_2 are the upstream and downstream pressures respectively, P_m the mean pressure, c a constant and λ the mean free path of the molecules at mean pressure. Eq. C-1 is reduced to Poiseuille's equation (Eq. C-2) if there is no slipping of the fluid in contact with the capillary wall.

C.2.2 Flow of a gas through an idealised porous medium

The simplest picture which can be formed of the laminar flow of fluids through a porous medium is that in which all the capillaries in the material are of the same diameter and are oriented at random through the solid material. Consider a cube of the material with an edge of

1 cm; the direction of flow is perpendicular to one of the planes of the cube, and let there be n capillaries of radius r (Klinkenberg, 1941).

The amount of liquid flowing (v) through per unit time (t) is found by applying Poiseuille's law;

$$\frac{v}{t}=\frac{1}{2}\left(\frac{n\pi r^4}{8\mu}\right)(P_1-P_2) \quad \text{[C-2]}$$

According to Darcy's law, the amount of liquid passing through a 1 cm cube is given by,

$$\frac{v}{t}=\left(\frac{k}{\mu}\right)(P_1-P_2) \quad \text{[C-3]}$$

in which k is the permeability constant. Combing Eq. C-2 and C-3 gives,

$$k=\frac{1}{2}\left(\frac{n\pi r^4}{8}\right) \quad \text{[C-4]}$$

For a gas, if slipping of the gas in contact with the wall is taken into account (See Eq. C-1),

$$q=\frac{1}{2}\left(\frac{n\pi r^4}{8\mu}\right)(P_1-P_2)P_m\left(1+\frac{4c\lambda}{r}\right) \quad \text{[C-5]}$$

Or combined with Eq. C-4;

$$q=\frac{k}{\mu}(P_1-P_2)P_m\left(1+\frac{4c\lambda}{r}\right) \quad \text{[C-6]}$$

Darcy's law gives, for the flow of gas through a porous medium of the above dimensions,

$$q=\frac{k_g}{\mu}(P_1-P_2)P_m \quad \text{[C-7]}$$

where k_g is the permeability to gas. Eq. C-6 and C-7 lead to,

$$k_g=k\left(1+\frac{4c\lambda}{r}\right) \quad \text{[C-8]}$$

As the mean free path is inversely proportional to the pressure, we may write,

$$\frac{4c\lambda}{r}=\frac{b}{P_m} \quad \text{[C-9]}$$

in which b is a constant. This substituted in Eq. C-8 gives k_g,

$$k_g=k\left(1+\frac{b}{P_m}\right) \quad \text{[C-10]}$$

a relation between the apparent and true permeability of an idealised porous system to gas.

C.3 Details on the plugs used in the Klinkenberg study

Twelve plugs were supplied by Service company 2 (SC2) (Table C-1), and as time was limited a select number of plugs were chosen which were the same size and had a range of permeabilities. Unfortunately none of the plugs have associated image analysis data.

	Sample No.	Well	Porosity (%)	k_g (mD)
* ^	1b	3	27.7	109
* ^	9b	3	23.6	26.9
^	3c	3	25.2	20.4
^	14b	3	24.6	150
* ^	17b	4	23.1	166
	23b	4	25.6	34
	18a	4	17.5	50
	5c	6	31.5	220
* ^	8c	6	25.4	18.1
	1c	6	32.9	1385
	2c	6	26.9	147
	7c	6	27.1	99.3

* the plugs used for KDS2 ^ the plugs used for KDS3

Table C-1. The plugs supplied by SC2 for further measurements

C.4 Klinkenberg data collected at SC3, in January 1997

C.4.1 Method

Taking gas permeability measurements to obtain a Klinkenberg value is a relatively time consuming process, in six hours fourteen sets of permeability measurements were completed. A 'set' is seven measurements at different mean pressures applied to one plug. The steps followed to obtain these permeability measurements at SC3 were as follows:

(i) Insert the plug into the rubber sleeve of the permeameter. If this is difficult, switch on the vacuum pump and slowly opening the vacuum toggle switch, then load plug easily. When plug is inserted switch off the vacuum and close the toggle switch.

(ii) Secure the plug by closing the base of the holder, and apply a stable downward pressure by twisting the tightening screw at the top of the plug holder.

(iii) Apply a confining pressure to the plug, by slowly lifting the pressure valve toggle, correct the confining pressure so that it is at 250 psi.

(iv) At this stage there is no gas being forced through the plug so an atmospheric pressure reading can be taken through the upstream and downstream pressure valves. These measurements are taken by placing the upper toggle switch in the labelled positions of upstream and downstream. Recorded these values and return the toggle to the upstream position. The atmospheric pressure values are required for correction in the calculation of permeability. Normally these readings will remain constant throughout the day.

(v) The upstream and downstream valves now need to be opened. To do this the four valves marked upstream and downstream must be placed in the open position. (The left two valves were on atmospheric pressure and the right two were on shut).

(vi) Now a pressure can be applied across the plug. This is done by opening the needle valve slowly anticlockwise. It is positioned at the top of the left side panel of the control box. Continue to open this needle valve until a reading on the volt meter of approximately positive one volt is obtained and also a reasonable flow rate, approximately 10-20 cc/minute. Record the upstream and downstream pressures, again by moving the upper toggle switch mentioned in point *(iv)* to the appropriate positions.

(vii) Now open the needle valve to obtain a maximum flow rate through the plug, within the range of the flowmeter which is approximately 500 cc/min, again record the upstream and downstream pressure. The first and seventh point on the permeability verses inverse mean pressure plot have now been measured, five more points need to be obtained evenly distributed between this upper and lower point. All the measurements required of the plug have now been made and recorded, and so the plug can be released.

(viii) To release the plug, shut off the flow rate by closing the needle valve clockwise.

(ix) Close the two valves labelled upstream/SHUT and downstream/SHUT, and then return the remaining two valves to their atmospheric pressure positions.

(x) Now slowly open the exhaust toggle to release the pressure from the plug, close the exhaust toggle. If the plug does not readily fall from the rubber sleeve, switch on the vacuum and open the vacuum toggle, being careful to catch the plug when it falls. Switch off the vacuum and close the toggle.

(xi) The equipment is now ready for another plug and for points *(i)-(x)* to be repeated.

Note; For no known reason the measurements took a long time to stabilise at the lower pressure readings, and values would often continue to creep up at the higher pressure readings.

C.4.2 Results

The permeability of four plugs was measured three times at the start of the day while it remained in the permeameter. At the end of the day plug 17b from well 4 was returned to the permeameter for a further two sets of permeability measurements. The measurements obtained from the voltmeter and flowmeter are as follows (Table C-2):

Sample: Well 4/Plug 17b	Set 1	Atmospheric pressure upstream : - 0.478	Atmospheric pressure Down stream : - 1.367
Run number	Pr (Upstream) mV	Pr (Downstream) mV	Flowrate cc/min
1	1.11	-0.072	26.2
7	4.726	2.986	80.8
6	7.661	5.557	125.9
5	12.197	9.67	202.8
4	18.414	15.444	305.8
3	24.505	21.21	408.8
2	30.25	26.726	507.2

Sample: Well 4/Plug 17b	Set 2	Atmospheric pressure upstream : - 0.478	Atmospheric pressure Down stream : - 1.367
Run number	Pr (Upstream) mV	Pr (Downstream) mV	Flowrate cc/min
1	0.384	-0.675	14.7
2	6.55	4.58	108.9
3	9.8	7.493	161.1
4	14.708	11.981	244.8
5	18.415	15.444	306.4
6	23.827	20.546	397.6
7	29.569	26.056	495.7

Sample: Well 4/Plug 17b	Set 3	Atmospheric pressure upstream : - 0.478	Atmospheric pressure Down stream : - 1.367
Run number	Pr (Upstream) mV	Pr (Downstream) mV	Flowrate cc/min
7	-0.072	-1.041	7.1
6	4.117	2.453	71.9
5	6.335	4.39	105.2
4	14.745	12.017	245.2
3	20.167	17.091	335.4
2	25.539	22.192	426
1	31.152	27.567	524.1

Sample: Well 3/Plug 9b	Set 1	Atmospheric pressure upstream : - 0.476	Atmospheric pressure Down stream : - 1.367
Run number	Pr (Upstream) mV	Pr (Downstream) mV	Flowrate cc/min
1	1.052	-0.732	13.2
7	3.719	0.42	34.9
6	9.501	3.372	87.1
5	20.548	10.12	211.8
4	29.659	16.5	325.1
3	36.078	21.25	411
2	44.065	27.553	523.6

Sample: Well 3/Plug 9b	Set 2	Atmospheric pressure upstream : - 0.476	Atmospheric pressure Down stream : - 1.367
Run number	Pr (Upstream) mV	Pr (Downstream) mV	Flowrate cc/min
1	1.94	-0.362	20.9
2	9.093	3.146	83.6
3	13.481	5.647	127.6
4	19.408	9.361	197.4
5	27.664	15.037	299.2
6	36.295	21.433	413.8
7	44.115	27.57	524.4

Sample: Well 3/Plug 9b	Set 3	Atmospheric pressure upstream : - 0.476	Atmospheric pressure Down stream : - 1.367
Run number	Pr (Upstream) mV	Pr (Downstream) mV	Flowrate cc/min
7	6.208	1.64	56.9
6	11.031	4.226	102.2
5	19.052	9.14	192.6
4	25.132	13.251	265.2
3	31.147	17.582	344.2
2	40.038	24.36	461.9
1	44.384	27.778	528.2

Sample: Well 3/Plug 1b	Set 1	Atmospheric pressure upstream : - 0.474	Atmospheric pressure Down stream : - 1.369
Run number	Pr (Upstream) mV	Pr (Downstream) mV	Flowrate cc/min
1	1.053	-0.247	22.8
7	4.715	2.631	74.9
6	9.43	6.656	144.1
5	14.454	10.937	226.6
4	20.671	16.536	325.7
3	25.744	21.206	409.3
2	32.811	27.850	528.9

Sample: Well 3/Plug 1b	Set 2	Atmospheric pressure upstream : - 0.474	Atmospheric pressure Down stream : - 1.369
Run number	Pr (Upstream) mV	Pr (Downstream) mV	Flowrate cc/min
1	1.731	0.28	32.3
2	6.31	3.936	96.8
3	9.272	6.423	141.9
4	14.881	11.34	234
5	23.653	19.273	374.8
6	28.272	23.557	448.3
7	31.311	26.412	503.3

Sample: Well 3/Plug 1b	Set 3	Atmospheric pressure upstream : - 0.474	Atmospheric pressure Down stream : - 1.369
Run number	Pr (Upstream) mV	Pr (Downstream) mV	Flowrate cc/min
7	3.072	1.326	50.6
6	6.128	3.784	93.7
5	11.093	7.993	169.6
4	14.15	10.664	221.8
3	19.891	15.824	313.1
2	27.169	22.533	431.7
1	32.896	27.904	530.5

Sample: Well 6/Plug 8c	Set 1	Atmospheric pressure upstream : - 0.474	Atmospheric pressure Down stream : - 1.367
Run number	Pr (Upstream) mV	Pr (Downstream) mV	Flowrate cc/min
1	1.24	-0.786	12.2
7	10.991	3.157	83.7
6	21.484	8.589	181.2
5	27.781	12.273	249.7
4	37.201	18.274	356.6
3	41.925	21.463	414.5
2	48.951	26.385	502.9

Sample: Well 6/Plug 8c	Set 2	Atmospheric pressure upstream : - 0.474	Atmospheric pressure Down stream : - 1.367
Run number	Pr (Upstream) mV	Pr (Downstream) mV	Flowrate cc/min
1	4.827	0.52	36.2
2	12.736	3.973	97.6
3	25.404	10.81	224.8
4	33.083	15.527	308.4
5	37.329	18.296	357.2
6	43.446	22.426	430.5
7	49.746	26.863	512.2

Sample: Well 6/Plug 8c	Set 3	Atmospheric pressure upstream : - 0.474	Atmospheric pressure Down stream : - 1.367
Run number	Pr (Upstream) mV	Pr (Downstream) mV	Flowrate cc/min
7	2.78	-0.247	23
6	12.123	3.679	91.9
5	21.244	8.415	177.7
4	28.905	12.915	260.1
3	38.958	19.384	376.7
2	45.12	23.605	449.1
1	49.22	26.482	505

Sample: Well 4/Plug 17b	Set 4	Atmospheric pressure upstream : - 0.475	Atmospheric pressure Down stream : - 1.364
Run number	Pr (Upstream) mV	Pr (Downstream) mV	Flowrate cc/min
1	0.861	-0.277	22.4
7	5.879	3.994	97.6
6	12.082	9.566	200.9
5	14.748	12.028	245.2
4	18.258	15.304	303.4
3	26.15	22.782	435.2
2	31.179	27.614	524.88

Sample: Well 4/Plug 17b	Set 5	Atmospheric pressure upstream : - 0.475	Atmospheric pressure Down stream : - 1.364
Run number	Pr (Upstream) mV	Pr (Downstream) mV	Flowrate cc/min
1	4.142	2.482	72.2
2	8.663	6.468	142.4
3	13.323	10.71	222.7
4	17.839	14.908	296.6
5	21.533	18.381	358.3
6	27.324	23.905	453.8
7	31.086	27.512	523.3

Table C-2. The data collected at SC3

C.5 Klinkenberg data collected at SC2, in May 1997

C.5.1 Apparatus

The permeameter at SC2 has a series of outlet orifices 1, 2, 3 and 4 (not shown in the schematic, Figure 5.1) which decrease in diameter respectively, so the tighter the sandstone the smaller the orifice used so that a back pressure can be created. A back pressure is vital if a range of mean pressures are to be obtained for the Klinkenberg extrapolation, without having to increase flow rate. This procedure hopefully avoids the development of turbulent flow.

The capacities for the four different orifices are briefly described as follows. Their accuracy has been calibrated such that it is desired to keep the downstream pressure between 1-10 mmH_2O (9.68×10^{-5} - 9.68×10^{-4} atmospheres) for each orifice. The respective range of flow rates for orifices 1 through to 4, for the given range in downstream pressures are;

Orifice 1: 185 - 1427 cc/min

Orifice 2: 27.6 - 247 cc/min

Orifice 3: 3.24 - 29.3 cc/min

Orifice 4: 0.39 - 3.42 cc/min

Through personal correspondence with SC2 it was agreed that the following method is identical to the one used by the SC2 staff for the original data set; except that for the original measurements the plugs had been cleaned and then dried in a humidity oven and stored, prior to measurements, in a desiccator with silica gel. The plugs were then used in other experiments including brine permeability tests. It can be assumed that the plugs were not cleaned again after these initial experiments and before these repeated measurements. At least five of the twelve plugs supplied to be re-measured are salt contaminated.

C.5.2 Method used at SC2

(i) Insert the core plug into the rubber sleeve, secure either end by hand tightening the butterfly nuts. There is a plug number written on each core plug record whether this number is located upstream or downstream.

(ii) Supply the loading gas pressure or overburden pressure (OB) by moving the top three way valve from vacuum to vent to OB.

(iii) With the lower three way valve select 50 psi

(iv) Turn the upstream pressure regulator until a pressure of 1 mmH_2O is registered as the downstream pressure reading. Do not go lower than 1 mmH_2O as the instrument is not accurate in this range.

(v) Take the first reading of upstream, downstream and back pressures, in this instance the back pressure is negligible.

(vi) Create a back pressure, using the regulator and take to the limit of the upstream pressure transducer (20 psi). There is now an upper and lower reading, and a range of readings can be taken in between.

When all the measurements are made turn both of the three way valves to vent and then the top valve to vacuum. The plug can now be easily removed and replaced.

C.5.3 Results

Sample 1b - First run - writing upstream

Confining pressure	Upstream pressure	Back pressure	Orifice	Flow rate	k_g	Upstream pressure absolute	Back pressure absolute	1/mean pressure absolute
250	3.5	0.002	1	3.626	107.369	1.228	0.990	0.902
250	7.5	4.000	1	4.323	102.727	1.500	1.262	0.724
250	11.5	8.000	1	5.057	100.385	1.772	1.534	0.605
250	15.5	12.000	1	5.777	98.467	2.044	1.806	0.519
250	19.5	16.000	1	6.485	96.849	2.316	2.078	0.455

Sample 1b - Second run - writing downstream

Confining pressure	Upstream pressure	Back pressure	Orifice	Flow rate	k_g	Upstream pressure absolute	Back pressure absolute	1/mean pressure absolute
250	3	0.001	1	3.050	107.004	1.194	0.990	0.916
250	6	3.000	1	3.544	104.719	1.398	1.194	0.772
250	9	6.000	1	4.003	102.175	1.602	1.398	0.667
250	12	9.000	1	4.428	99.493	1.806	1.602	0.587
250	15	12.000	1	4.875	97.800	2.010	1.806	0.524
250	18	15.000	1	5.393	97.737	2.214	2.010	0.473

Sample 3c - First run - writing upstream

Confining pressure	Upstream pressure	Back pressure	Orifice	Flow rate	k_g	Upstream pressure absolute	Back pressure absolute	1/mean pressure absolute
250	0.25	0.001	3	0.043	19.589	1.013	0.996	0.995
250	0.82	0.004	3	0.150	20.352	1.052	0.996	0.976
250	1.48	0.008	3	0.275	20.217	1.097	0.997	0.955
250	1.99	0.011	3	0.371	19.959	1.131	0.997	0.940
250	2.39	0.013	3	0.447	19.775	1.159	0.997	0.928

Sample 3c - Second run - writing upstream								
Confining pressure	Upstream pressure	Back pressure	Orifice	Flow rate	k_g	Upstream pressure absolute	Back pressure absolute	1/mean pressure absolute
250	2.39	0.001	2	0.464	20.410	1.159	0.996	0.928
250	3.51	0.002	2	0.704	20.387	1.235	0.996	0.896
250	4.71	0.003	2	0.970	20.193	1.317	0.996	0.865
250	6.47	0.005	2	1.390	20.022	1.436	0.996	0.822
250	8.6	0.006	2	1.934	19.777	1.581	0.996	0.776
250	10.52	0.008	2	2.462	19.594	1.712	0.997	0.738
250	12.05	0.010	2	2.918	19.520	1.816	0.997	0.711
250	14.4	0.013	2	3.650	19.335	1.976	0.997	0.673

Sample 3c - Third run - writing upstream								
Confining pressure	Upstream pressure	Back pressure	Orifice	Flow rate	k_g	Upstream pressure absolute	Back pressure absolute	1/mean pressure absolute
250	14.4	0.002	1	3.761	19.911	1.976	0.996	0.673
250	16.02	0.002	1	4.296	19.712	2.086	0.996	0.649
250	18.09	0.002	1	5.005	19.448	2.227	0.996	0.620
250	19.73	0.003	1	5.598	19.277	2.339	0.996	0.600

Sample 3c - Fourth run - writing upstream								
Confining pressure	Upstream pressure	Back pressure	Orifice	Flow rate	k_g	Upstream pressure absolute	Back pressure absolute	1/mean pressure absolute
250	2.49	0.002	2	0.481	20.259	1.165	0.996	0.925
250	6	3.500	2	0.563	19.338	1.404	1.234	0.758
250	9.5	6.990	2	0.649	18.805	1.642	1.472	0.642
250	12.49	10.000	2	0.709	18.301	1.846	1.677	0.568
250	15	12.490	2	0.768	17.945	2.017	1.846	0.518
250	18.01	15.510	2	0.823	17.454	2.222	2.051	0.468

Sample 3c- Fifth run - writing upstream								
Confining pressure	Upstream pressure	Back pressure	Orifice	Flow rate	k_g	Upstream pressure absolute	Back pressure absolute	1/mean pressure absolute
250	3	0.002	2	0.572	19.667	1.200	0.996	0.911
250	5	2.000	2	0.632	19.326	1.336	1.132	0.810
250	8	4.990	2	0.717	18.764	1.540	1.336	0.695
250	11.99	9.010	2	0.823	18.289	1.812	1.609	0.585
250	16.09	12.990	2	0.941	17.317	2.091	1.880	0.504
250	18.99	16.000	2	1.012	17.538	2.288	2.085	0.457

Sample 9b - First run - Writing upstream								
Confining pressure	Upstream pressure	Back pressure	Orifice	Flow rate	k_g	Upstream pressure absolute	Back pressure absolute	1/mean pressure absolute
250	11	0.002	1	3.380	26.160	1.738	0.990	0.733
250	13	2.000	1	3.626	25.510	1.874	1.126	0.667
250	15	4.000	1	3.923	25.302	2.010	1.262	0.611
250	17	6.000	1	4.190	24.950	2.146	1.398	0.564
250	19	8.000	1	4.455	24.636	2.282	1.534	0.524

Sample 9b - Second run - Writing upstream								
Confining pressure	Upstream pressure	Back pressure	Orifice	Flow rate	k_g	Upstream pressure absolute	Back pressure absolute	1/mean pressure absolute
250	6	5	2	0.284	24.156	1.398	1.330	0.733
250	7	5.99	2	0.297	23.854	1.466	1.397	0.699
250	8.02	7.01	2	0.306	23.430	1.535	1.466	0.666
250	10	9	2	0.332	23.591	1.670	1.602	0.611
250	11.99	11	2	0.354	23.461	1.805	1.738	0.564
250	13	12	2	0.354	22.363	1.874	1.806	0.543
250	15	14.01	2	0.394	23.371	2.010	1.943	0.506
250	17	16	2	0.420	23.091	2.146	2.078	0.473
250	19.01	18.01	2	0.455	23.484	2.283	2.215	0.445

Sample 9b - Third run - Writing upstream								
Confining pressure	Upstream pressure	Back pressure	Orifice	Flow rate	k_g	Upstream pressure absolute	Back pressure absolute	1/mean pressure absolute
250	1	0.000669	2	0.221	25.108	1.058	0.990	0.977
250	2	1	2	0.226	24.005	1.126	1.058	0.916
250	2.99	2	2	0.235	23.739	1.193	1.126	0.863
250	3.99	2.99	2	0.262	24.743	1.261	1.193	0.815
250	4.99	4	2	0.270	24.480	1.329	1.262	0.772

Sample 9b - Fourth run - writing Downstream								
Confining pressure	Upstream pressure	Back pressure	Orifice	Flow rate	k_g	Upstream pressure absolute	Back pressure absolute	1/mean pressure absolute
250	10.5	0.001	1	3.271	26.866	1.704	0.990	0.743
250	12.5	2.000	1	3.490	26.032	1.840	1.126	0.674
250	14.51	4.000	1	3.761	25.667	1.977	1.262	0.618
250	16.5	6.000	1	4.030	25.397	2.112	1.398	0.570
250	18.5	8.000	1	4.270	24.972	2.248	1.534	0.529
250	19.5	9.000	1	4.402	24.853	2.316	1.602	0.510

Sample 9b - Fifth run - writing upstream								
Confining pressure	Upstream pressure	Back pressure	Orifice	Flow rate	k_g	Upstream pressure absolute	Back pressure absolute	1/mean pressure absolute
450	2	0.001	2	0.446	24.510	1.126	0.990	0.946
450	5	3.000	2	0.516	23.721	1.330	1.194	0.793
450	7	5.000	2	0.563	23.380	1.466	1.330	0.715
450	8.99	7.010	2	0.610	23.326	1.601	1.466	0.652
450	11	9.000	2	0.662	22.995	1.738	1.602	0.599
450	13	11.000	2	0.704	22.632	1.874	1.738	0.554
450	15	13.000	2	0.759	22.697	2.010	1.874	0.515
450	17	14.990	2	0.806	22.403	2.146	2.009	0.481

Sample 14b - First run - writing upstream								
Confining pressure	Upstream pressure	Back pressure	Orifice	Flow rate	k_g	Upstream pressure absolute	Back pressure absolute	1/mean pressure absolute
250	2.01	0.001	1	3.188	175.044	1.133	0.996	0.939
250	5	3.000	1	3.626	167.805	1.336	1.200	0.788
250	8	6.000	1	4.083	162.776	1.540	1.404	0.679
250	10.99	9.000	1	4.481	157.711	1.744	1.608	0.597
250	13.99	12.010	1	4.875	153.675	1.948	1.813	0.532
250	17	15.000	1	5.264	148.198	2.153	2.017	0.480
250	19	17.020	1	5.521	147.347	2.289	2.154	0.450

Sample 14b - Second run - writing upstream								
Confining pressure	Upstream pressure	Back pressure	Orifice	Flow rate	k_g	Upstream pressure absolute	Back pressure absolute	1/mean pressure absolute
250	2.5	0.002	1	3.842	166.979	1.166	0.996	0.925
250	3.5	1.000	1	4.110	167.938	1.234	1.064	0.870
250	6.49	4.010	1	4.586	160.428	1.438	1.269	0.739
250	9	6.500	1	5.109	157.464	1.608	1.438	0.656
250	12.49	10.010	1	5.726	153.860	1.846	1.677	0.568
250	16	13.510	1	6.410	151.093	2.085	1.915	0.500
250	19.51	16.990	1	7.109	147.985	2.324	2.152	0.447

Sample 14b - Third run - writing downstream								
Confining pressure	Upstream pressure	Back pressure	Orifice	Flow rate	k_g	Upstream pressure absolute	Back pressure absolute	1/mean pressure absolute
250	2	0.001	1	2.994	165.262	1.132	0.996	0.940
250	3.99	1.990	1	3.380	165.418	1.268	1.131	0.834
250	6.49	4.520	1	3.707	161.165	1.438	1.304	0.730
250	9	7.000	1	4.110	156.602	1.608	1.472	0.649
250	12.49	10.490	1	4.586	151.421	1.846	1.710	0.562
250	14.99	13.000	1	4.901	148.378	2.016	1.881	0.513
250	17.49	15.500	1	5.186	144.416	2.186	2.051	0.472
250	19.5	17.500	1	5.470	142.380	2.323	2.187	0.443

Sample 17b - First run - writing upstream								
Confining pressure	Upstream pressure	Back pressure	Orifice	Flow rate	k_g	Upstream pressure absolute	Back pressure absolute	1/mean pressure absolute
250	2	0.001	1	2.883	157.517	1.126	0.990	0.946
250	6	3.990	1	3.490	150.855	1.398	1.261	0.752
250	10	8.000	1	4.137	149.135	1.670	1.534	0.624
250	14	12.000	1	4.770	146.999	1.942	1.806	0.534
250	18	15.990	1	5.393	144.410	2.214	2.078	0.466

Sample 17b - Second run - writing upstream								
Confining pressure	Upstream pressure	Back pressure	Orifice	Flow rate	k_g	Upstream pressure absolute	Back pressure absolute	1/mean pressure absolute
250	2	0.001	1	2.883	157.517	1.126	0.990	0.946
250	5	3.000	1	3.353	153.489	1.330	1.194	0.793
250	6.99	5.000	1	3.599	149.472	1.465	1.330	0.716
250	10	8.000	1	4.056	146.248	1.670	1.534	0.624
250	13	10.990	1	4.455	141.774	1.874	1.737	0.554
250	15.99	14.000	1	4.822	139.269	2.078	1.942	0.498
250	19	17.000	1	5.290	137.962	2.282	2.146	0.452

Sample 17b - Third run - writing downstream								
Confining pressure	Upstream pressure	Back pressure	Orifice	Flow rate	k_g	Upstream pressure absolute	Back pressure absolute	1/mean pressure absolute
250	5	3	1	3.38	154.261	1.334	1.198	0.79
250	7	5.01	1	3.653	151.233	1.47	1.335	0.713
250	10	8	1	4.083	146.866	1.675	1.538	0.622
250	12.99	11	1	4.455	142.909	1.878	1.743	0.552
250	16	14	1	4.848	139.054	2.083	1.947	0.496
250	19	17	1	5.29	137.747	2.287	2.151	0.451

Sample 17b - Fourth run - writing downstream								
Confining pressure	Upstream pressure	Back pressure	Orifice	Flow rate	k_g	Upstream pressure absolute	Back pressure absolute	1/mean pressure absolute
400	1.99	0	1	2.77	151.681	1.129	0.994	0.942
400	6	4	1	3.435	148.829	1.402	1.266	0.749
400	10	8	1	3.949	142.116	1.675	1.538	0.622
400	14	12	1	4.481	137.891	1.947	1.811	0.532
400	18	15.99	1	5.005	133.864	2.219	2.082	0.465
400	19.74	16.75	1	7.75	134.056	2.337	2.134	0.447

Sample 17b - Fifth run - writing downstream								
Confining pressure	Upstream pressure	Back pressure	Orifice	Flow rate	k_g	Upstream pressure absolute	Back pressure absolute	1/mean pressure absolute
250	2	0	1	2.91	158.509	1.13	0.994	0.941
250	4	0	1	5.98	153.049	1.266	0.994	0.885
250	6	0	1	9.324	150.055	1.402	0.994	0.834
250	8	0.01	1	13.086	149.461	1.538	0.995	0.79
250	10.01	0.01	1	17.304	149.861	1.675	0.995	0.749
250	11.99	0.01	1	21.902	150.752	1.81	0.995	0.713

Sample 8c - First run - writing upstream								
Confining pressure	Upstream pressure	Back pressure	Orifice	Flow rate	k_g	Upstream pressure absolute	Back pressure absolute	1/mean pressure absolute
250	2.51	0	2	0.433	16.388	1.166	0.995	0.926
250	4.49	2	2	0.468	15.85	1.3	1.131	0.823
250	7	4.5	2	0.52	15.382	1.471	1.301	0.722
250	10	7.5	2	0.572	14.74	1.675	1.505	0.629
250	13	10.5	2	0.627	14.337	1.879	1.709	0.557
250	15.98	13.5	2	0.674	13.954	2.082	1.913	0.501
250	19	16.51	2	0.73	13.637	2.288	2.118	0.454

Sample 8c - Second run - writing upstream								
Confining pressure	Upstream pressure	Back pressure	Orifice	Flow rate	k_g	Upstream pressure absolute	Back pressure absolute	1/mean pressure absolute
250	3	0	2	0.516	16.09	1.199	0.995	0.912
250	5	0	2	0.912	16.05	1.335	0.995	0.858
250	7	0	2	1.332	15.831	1.471	0.995	0.811
250	9	0.01	2	1.787	15.656	1.607	0.995	0.769
250	11	0.01	2	2.273	15.483	1.743	0.995	0.73
250	12.99	0.01	2	2.786	15.312	1.879	0.995	0.696
250	14.99	0.01	2	3.319	15.09	2.015	0.996	0.664

Sample 8c - Third run - writing upstream								
Confining pressure	Upstream pressure	Back pressure	Orifice	Flow rate	k_g	Upstream pressure absolute	Back pressure absolute	1/mean pressure absolute
250	2.5	0	2	0.433	16.478	1.166	0.995	0.926
250	4.5	2	2	0.464	15.655	1.302	1.131	0.822
250	7.49	5	2	0.52	15.097	1.505	1.336	0.704
250	9.99	7.49	2	0.567	14.655	1.675	1.505	0.629
250	12.5	10	2	0.615	14.335	1.846	1.676	0.568
250	15	12.49	2	0.662	14.019	2.016	1.845	0.518
250	17.99	15.5	2	0.704	13.604	2.22	2.05	0.468
250	19.51	17.01	2	0.734	13.472	2.323	2.153	0.447

Sample 8c - Fourth run - writing downstream								
Confining pressure	Upstream pressure	Back pressure	Orifice	Flow rate	k_g	Upstream pressure absolute	Back pressure absolute	1/mean pressure absolute
250	2	0.001	2	0.328	15.864	1.145	1.009	0.929
250	5	3.000	2	0.376	15.295	1.349	1.213	0.781
250	8	6.000	2	0.420	14.724	1.553	1.417	0.673
250	11	9.000	2	0.459	14.151	1.757	1.621	0.592
250	14	12.000	2	0.498	13.698	1.961	1.825	0.528
250	16.99	15.010	2	0.537	13.464	2.165	2.030	0.477
250	19.49	17.500	2	0.567	13.088	2.335	2.199	0.441

Sample 8c - Fifth run - writing downstream								
Confining pressure	Upstream pressure	Back pressure	Orifice	Flow rate	k_g	Upstream pressure absolute	Back pressure absolute	1/mean pressure absolute
250	19.62	0	1	4.692	14.848	2.344	1.009	0.597
250	15.9	0	1	3.599	15.202	2.09	1.009	0.645
250	12.14	0	1	2.601	15.686	1.835	1.009	0.703
250	13.68	0	1	2.994	15.454	1.939	1.009	0.678
250	14.66	0	1	3.271	15.405	2.006	1.009	0.663

Sample 8c - Sixth run - writing downstream								
Confining pressure	Upstream pressure	Back pressure	Orifice	Flow rate	k_g	Upstream pressure absolute	Back pressure absolute	1/mean pressure absolute
250	0.33	0.000	3	0.049	15.312	1.031	1.009	0.981
250	0.63	0.000	3	0.1	16.109	1.051	1.009	0.971
250	0.99	0.000	3	0.159	16.09	1.076	1.009	0.959
250	1.56	0.010	3	0.253	15.96	1.115	1.009	0.942
250	2.2	0.010	3	0.359	15.768	1.158	1.009	0.923
250	2.55	0.010	3	0.417	15.615	1.182	1.009	0.913
250	2.87	0.010	3	0.471	15.521	1.204	1.01	0.904

Table C-3. The raw data collected from SC2

C.6 Error analysis

Errors associated with the Klinkenberg measurements from the second SC2 data set are calculated and compared with SC2's own estimations of error.

Eq. C-11 is the equation used by SC2 and SC3 for the calculation of gas permeability over a range of mean pressures. Eq. C-12 is the expanded equation as used by SC2, from which the errors associated with each term can be assessed.

SC2 and SC3 equation,

$$k_g = \frac{1000(At.Pr.)q\mu L}{P_m(P_1 - P_2)A} \qquad \text{[C-11]}$$

SC3 equation,

$$k_g = \frac{2000\left(\frac{B_p}{760}\right)q\mu L}{\left[\left(\frac{P_1}{14.696} + \frac{B_p}{760}\right)^2 - \left(\frac{P_2}{10332.203} + \frac{B_p}{760}\right)^2\right]A} \qquad \text{[C-12]}$$

where k_g is the gas permeability, q the flow rate (cm^3/sec), L the length of the plug (cm), A the cross-sectional area of the plug (cm^2), μ the gas viscosity, P_2 the downstream pressure, P_1 the upstream pressure, B_p the atmospheric pressure (mmHg), therefore $B_p/760$ is converting the atmospheric pressure in mmHg into atmospheres. *At. Pr.* is atmospheric pressure in atmospheres, 1 atmosphere is equal to 14.6959 psi, therefore the $P_1/14.696$ is converting the upstream pressure in psi into atmospheres, $P_2/10332.203$ is converting the downstream pressure in mmH_2O into atmospheres and P_m is mean pressure and equals $(P_1\text{-}P_2)/2$.

Tables C-4 and C-5 below give the percentage errors of the plug lengths and diameters, which were measured using callipers. The cross-sectional area error could be calculated from the diameter error. The errors associated with flow rate, upstream and downstream pressures could not be accurately calculated, as these are errors associated with the transducers, orifices and regulators. The barometric pressure was read from a meter within the laboratory, this was considered true atmospheric pressure and had an associated error of ± 1 mmHg, giving a percentage error of approximately 0.13%.

Well / plug number	Length (cm)					
	1	2	3	4	Average	% Error
3/3c	4.962	4.968	4.958	4.968	4.964 ±0.006	0.12
3/9b	4.988	4.99	5	4.988	4.9915 ±0.0085	0.17
3/1b	5.01	4.994	5	5.008	5.003 ±0.009	0.18
3/14b	4.994	5.006	5.018	5.014	5.008 ±0.014	0.23
4/17b	5.086	5.08	5.082	5.08	5.082 ±0.004	0.08
6/8c	5.04	4.99	4.99	4.99	5.0025 ±0.0375	0.75

Table C-4. The plug length percentage errors, measured by the author.

Well / plug number	Diameter (cm)					
	1	2	3	4	Average	% Error
3/3c	3.774	3.784	3.78	3.788	3.7815 ±0.0075	0.20
3/9b	3.736	3.736	3.728	3.732	3.733 ±0.005	0.13
3/1b	3.766	3.75	3.755	3.762	3.7583 ±0.0083	0.22
3/14b	3.732	3.736	3.722	3.736	3.7315 ±0.0095	0.25
4/17b	3.774	3.778	3.78	3.776	3.777 ±0.003	0.08
6/8c	3.98	3.98	4	3.97	3.9825 ±0.0175	0.44

Table C-5. The plug diameter percentage errors, measured by the author.

The errors supplied by SC2 were given as percentage errors, no error was provided with the permeameter at SC3. The method used by SC2 of calculating percentage errors is unavailable and so the most simple method of calculating a relative percentage error has been used (Table C-6).

Parameter	Unit	SC2 quoted error ± (%)	Authors estimated error ± (%)
q	cm/sec	0.29	0.29*
μ		Unknown	Unknown
L	cm	0.31	0.75
A	cm^2	0.11	0.88
P_2	mmH_2O	0.1	0.1*
P_1	psi	0.1	0.1*
Bp	mmHg	Unknown	0.13
Diameter	cm	0.05	0.44
ka	mD	1.51	3.45

*Quoted by SC2 as the error associated with the transducers and orifices

Table C-6. Percentage errors associated with Klinkenberg permeability measurements.

The gas permeability error was calculated from summing the errors of Eq. C-11;

$$\begin{aligned} \text{Error } k_g &= eBp + eq + e\mu + eL + e2P_1 + e\,P_1 + eBp + e2Bp + e2P_2 + eP_2 + e\,P_1 + eBp + eA \\ &= 0.13 + 0.29 + ? + 0.75 + 0.2 + 0.1 + 0.13 + 0.26 + 0.2 + 0.1 + 0.1 + 0.13 + 0.88 \\ &= \pm 3.27\% \end{aligned}$$

The calculated error of ± 3.27% is over twice as large as that supplied by SC2. This is not, however, a large error, and it is noticeable that the increase in error size is a result of the length and area measurements (Table C-6). To estimate the highest possible error associated with the permeability measurements, the largest of the plug parameter errors were chosen from Tables C-4 and C-5.

Appendix D

Factor analysis

D.1 Introduction

'A central aim of factor analysis is the 'orderly simplification' of a number of interrelated measures' (Child, 1970). It is stated that when a group of variables has, for some reason, a great deal in common a factor is said to exist. Factor determination is based on the assumption that correlations are derived form scores bearing linear relationships and therefore, relationships of a serious curvilinear kind are not suitable for factor analysis.

D.1.1 Data on which factor analysis was performed

The data were chosen, on which to perform factor analysis, by examining cross plots of the core and image data, and recording which parameters had a linear relation in any plot. The data were numerical ranges and not scales or keys, i.e. no ordinal (grain size) or nominal (facies) data. The following is a list of the thirteen selected parameters:

(i) Gas permeability
(ii) Klinkenberg permeability
(iii) Plug porosity
(iv) Image porosity (total magnification)
(v) Image porosity (low magnification)
(vi) Image porosity (high magnification)
(vii) Formation resistivity factor
(viii) Area pore (low magnification)
(ix) *b*-factor
(x) Pore perimeter/Pore area (low magnification)
(xi) Area shale (low magnification)
(xii) Area pore + area *clay* (total magnification)
(xiii) Perimeter/ area equivalent radius (low magnification)

These thirteen parameters were tested using factor analysis to establish whether they were interrelated. The analysis was performed using the software Statistica (Version 4.1) on the forty-five plugs. From the eigenvalue results it was revealed that 90% of the variance within the thirteen parameters was contained within the first 4 factors. This was a massive reduction in data, and means that the data is strongly related.

Brine concentrations

E.1 Brine concentrations

Wells 1, 2, 3, 4, 5 and 6 used the same simulated formation brine, based on typical water analysis of the reservoir formation brine from well 1. Wells 7, 8 and 9 used the same formation brine which was based on water from well 4 (Table E.1). Well 12 brine, used in the brine permeability versus throughput experiment (§5.3.4.2), is the same as well 1.

Wells	1, 2, 3, 5 and 6	4, 7, 8 and 9
Cations		
Sodium	33000	31683
Calcium	3950	5003
Magnesium	500	732
Potassium	2700	643
Barium	210	265
Iron	170	<35
Strontium		751
Anions		
Chlorine	58500	
Chloride		61158
Bicarbonate	450	105
Sulphate		<10
R_W (ohm-m)	0.0797 @ 70°F	0.081 @ 70°F
pH	7.2	
Sg	1.0688 @ 70°F	1.070 @ 70°F

Table E.1. Showing the brine concentrations of each well, where R_W is the brine resistivity and Sg the specific gravity

References

Aase, N. E., Bjorkum, P. A. & Nadeau, P. H. (1996). The effect of grain-coating microquartz on preservation of reservoir porosity. *Bulletin of the American Association of Petroleum Geologists* **80**(10), 1654-1673.

Ali, L. (1993). Evaluation of starch based biopolymers for improved oil recovery. Texas A and M University.

Ali, L. & Barrufet, M. A. (1995). Study of pore structure modification using environmental scanning electron microscopy. *Journal of Petroleum Science and Engineering* **12**, p. 323-338.

Anderson, W. G. (1986). Effect of wettability on the electrical properties of porous media. *Society of Petroleum Engineers Journal of Petrology Technology*. (December), p. 1371-1378.

API. (1998). *Recommended practice for core analysis*. API Publishing Services, Washington D. C.

Archie, G. E. (1942). The electrical resistivity log as an aid in determining some reservoir characteristics. *Petroleum Technology* (January), p. 4-13.

Archie, G. E. (1947). Electrical resistivity; an aid in core-analysis interpretation. *Bulletin of the American Association of Petroleum Geologists* **30**(2), p. 350-366.

Archie, G. E. (1950). Introduction to petrophysics of reservoir rocks. *Bulletin of the American Association of Petroleum Geologists* **34**(5), p. 943-961.

Baldwin, B. A. (1994). Immobile water determination in shaly sandstone. *The Log Analyst* **35**(3), p. 31-37.

Banavar, J. R. & Johnson, D. L. (1987). Characteristic pore sizes and transport in porous media. *Physical Review B* **35**(13), p. 7283-7286.

Barrett, P. J. (1980). The shape of rock particles, a critical review. *Sedimentology* **27**, p. 291-303.

Basan, P. B., Lowden, B. D., Whattler, P. R. & Attard, J. J. (1997). Pore-size data in petrophyics: a perspecive on the measurement of pore geometry. *Geological Society Special Publication* (122), p. 47-67.

Beard, D. C. & Weyl, P. K. (1973). Influence of texture on porosity and permeability of unconsolidated sand. *The American Association of Petroleum Geologists Bulletin* **57**(2), p. 349-369.

Berg, C. R. (1995). A simple, effective-medium model for water saturation in porous rocks. *Geophysics* **60**(4), p. 1070-1080.

Bergosh, J. L. & Lord, G. D. (1987). New developments in the analysis of cores from naturally fractured reservoirs. (SPE paper 16805), p. 57-64

Bernabe, Y. (1991). Pore geometry and pressure dependence of the transport properties in sandstone. *Geophysics* **56**(4), p. 436-446.

Best, A. I. & McCann, C. (1995). Seismic attenuation and pore-fluid viscosity in clay rich reservoir sandstones. *Geophysics* **60**(5), p. 1386-1397.

Blatt, Middleton & Murray. (1972). Sedimentary textures, In: *Origin of sedimentary rocks*. Prentice-Hall publ.

Bliefnick, D. M. & Kaldi, J. G. (1996). Pore geometry: control on reservoir properties, Walker Creek Field, Columbia and Lafayette Counties, Arkansas. *Bulletin of the American Association of Petroleum Geologists* **80**(7), p. 1027-1044.

Bloch, S. & Helmold, K. P. (1995). Approaches to predicting reservoir quality in sandstones. *Bulletin of the American Association of Petroleum Geologists* **79**(1), p. 97-115.

Boon, J. D., Evans, D. A. & Hennigar, H. F. (1982). Spectral information from Fourier Analysis of digitised quartz grain profiles. *Mathematical Geology* **14**, p. 589-605.

Bowers, M. C., Ehrilich, R. & Clark, R. A. (1994). Determination of petrographic factors controlling permeability using petrographic image analysis and core data, Satun Field, Pattani basin, Gulf of Thailand. *Marine and Petroleum Geology* **11**(2), p. 148-156.

Burdine, N. T., Gournay, L. S. & Reichertz, P. P. (1950). Pore size distribution of petroleum reservoir rocks. *Petroleum Transactions, AIME* **189**, p. 195-204.

Bloch, S. (1991). Empirical prediction of porosity and permeability in sandstones. *Bulletin of the American Association of Petroleum Geologists* **75**(7), p. 1145-1160.

Cade, C. A., Evans, I. J. & Bryant, S. L. (1994). Analysis of permeability controls: a new approach. *Clay Minerals* **29**, p. 491-501.

Child, D. (1970). *The essentials of factor analysis*. Holt, Rinehart and Winston, London, New York.

Chilingar, G. V. & Yen, T. F. (1983). Some notes on wettability and relative permeabilities of carbonate rocks, II. *Energy sources* **7**(1), p. 67-75.

Chilingarian, G. V. (1963). Relationship between porosity, permeability and grain size distribution of sands and sandstones. In: *Deltaic and shallow marine deposites* (edited by Van Straaten, J. U.). Elsevier science publ. Co., New York, Amsterdam, p. 71-75.

Clark, M. W. (1981). Quantitative shape analysis: A review. *Journal Int. Association of Mathematical Geologists*. **13**, p. 303-320.

Clennell, M. B. (1997). *Tortuosity: a guide through the maze*. In: *Developments in petrophysics* (edited by Lovell, M. A. & Harvey, P. K.). Geological Society publ. London, p. 299-345.

Collins, R. E. (1961). Flow of fluids through porous materials. In: *Von Nostrand-Reinhold,*, Princeton, New Jersey.

Cooper, M. R. & Hunter, R. H. (1995). Precision serial lapping, imaging and three-dimensional reconstruction of minus-cement and post-cementation intergranular pore-systems in the Penrith Sandstone of north-western England. *Mineralogical Magazine* **59**(June), p. 213-220.

Cornwall, C. (1990). Core preservation-an alternative approach. In: *Society of Core Analysts European Conference*.

Coskun, S. B. & Wardlaw, N. C. (1995). Influences of pore geometry, porosity and permeability on initial water saturation - An empirical method for estimating initial water saturation by image analysis. *Journal of Petroleum Science and Engineering* **12**, p. 295-308.

Coskun, S. B., Wardlaw, N. C. & Haverslew, B. (1993). Effects of composition, texture and diagenesis on porosity, permeability and oil recovery in a sandstone reservoir. *Journal of Petroleum Science and Engineering* **8**(4), p. 279-292.

Darcy, H. J. (1856). Les fontaines publiques de la ville de Dijon. In: *Libraire de corps imperiaux des pont et chaussees et des mines*, Paris, 590-594.

Davies, D. K. (1990). Image analysis of reservoir pore systems: state of the art in solving problems related to reservoir quality. (SPE paper 19407).

Dawe, R. A. (1973). The slip correction in accurate viscometry. *Rev. Sci. Instrum.* **44**(9), p. 1271-1273.

de Hoff, R. T. (1983). Quantitative serial sectioning analysis: preview. *Journal of microscopy* **131**, p. 259.

Dias, A. & Jing, X.-D. (1996). Permeability estimation from porosity and pore size distribution: comparative case studies from two North Sea fields. *DiaLog* **4**(4), p. 5-7.

Doyen, P. M. (1988). Permeability, conductivity, and pore geometry of sandstone. *Journal of Geophysical Research* **93**(B7), p. 7729-7740.

Dullien, F. A. L. (1992). *Porous media fluid transport and pore structure.* Academic Press Inc.

Dutton, S. P. & Diggs, T. N. (1992). Evolution of porosity and permeability in the Lower Cretaceous Travis Peak Formation, East Texas. *Bulletin of the American Association of Petroleum Geologists* **76**(2), p. 252-269.

Ehrlich, R. (1984). A strong transfer function links thin section data to reservoir physics. *(abs.): Bulletin of the American Association of Petroleum Geologists* **75**(10), p. 1579-1592.

Ehrlich, R., Crabtree, S. J., Horkowitz, K. O. & Horkowitz, J. P. (1991a). Petrography and reservoir physics I: Objective classification of reservoir porosity. *Bulletin of the American Association of Petroleum Geologists* **75**(10), p. 1547-1562.

Ehrlich, R., Etris, E. L., Brumfield, D., Yuan, L. P. & Crabtree, S. J. (1991b). Petrography and reservoir physics III: Physical models for permeability and formation factor. *Bulletin of the American Association of Petroleum Geologists* **75**(10), p. 1579-1592.

Ehrlich, R. & Weinberg, B. (1970). An exact method for characterisation of grain shape. *Journal of Sedimentary Petrology* **40**, p. 205-212.

Ellison, S. P. J. (1958). Origin of porosity and permeability. University of Texas, Austin, TX.

Etris, E. L. (1991). Investigations into the control of pore/throat structure on capillary pressure imbibition, and its relevance to resistivity index and relative permeability in reservoir rocks. University of South Carolina.

Fischmeister, H. F. (1974). Pore structure and properties of porous materials. In: *International symposium RILEM/UPAC* Part II. Academia, Prague, p. C435-C476.

Forchheimer, P. H. (1901). *Z. Ver. Deutsch. Ing.* **45**, p. 1781.

Fraser, H. J. & Graton, L. C. (1935). Systematic packing of spheres with particular relations to porosity and permeability. *Journal of Geology* (Nov-Dec), p. 785-909.

Frost, E., Jr. & Fertl, W. H. (1981). Integrated core and log analysis concepts in shale clastic reservoirs. *The Log Analyst* **22**(2), p. 3-16.

Galloway, W. E. (1979). Diagenetic control of reservoir quality in Arc-derived sandstones: Implications for petroleum exploration. *SEPM special publication* **26**, p. 251-62.

Hagiwara, T. (1984). Archie's m for permeability. In: *59th Annual Technical Conference and Exhibition*, Houston, Texas.

Haralick, R. M. (1979). Statistical and structural approaches to texture. *Proc. IEEE* **69**, p. 786-804.

Haralick, R. M. & Shanmugam, K. (1973). Computer classification of reservoir sandstones. *IEEE Transaction, Geoscience Electronics* (GE-11), p. 171-177.

Hawkins, P. J. (1978). Relationship between diagenesis, porosity reduction and oil emplacement in late Carboniferous sandstone reservoirs, Bothamshall Oilfield, East Midlands. *Journal Geological Society of London* **135**(7), p. 24.

Herrick, D. C. (1988). Conductivity models, pore geometry, and conduction mechanisms. In: *SWWLA 29 Annual logging symposium.*

Herrick, D. C. & Kennedy, W. D. (1994). Electrical efficiency-A pore geometric theory for interpreting the electrical properties of reservoir rocks. *Geophysics* **59**(6), p. 918-927.

Hubbert, M. K. (1956). Darcy's law and the field equations of flow of underground fluids. *Petroleum Transactions, AIME* **207**, p. 222-239.

Hurst, A. & Nadeau, P. H. (1995). Clay microporosity in reservoir sandstones: an application of quantitative electron microscopy in petrophysical evaluation. *Bulletin of the American Association of Petroleum Geologists* **79**(4), p. 563-573.

Ioannidis, M. A. & Chatzis, I. (1993). Network modelling of pore structure and transport properties of porous media. *Chemical Engineering Science* **48**(5), p. 951-972.

Jones, S. C. (1972). A rapid accurate unsteady-state Klinkenberg permeameter. *Society of Petroleum Engineers* (SPE paper 3535), p. 383-397.

Katz, A. J. & Thompson, A. H. (1986). Quantitative prediction of permeability in porous rock. *Physical Review* **34**(11), p. 8179-8181.

Katz, A. J. & Thompson, A. H. (1987). Prediction of rock electrical conductivity from mercury injection measurements. *Journal of Geophysical Research* **92**(B1), p. 599-607.

Kendall, M. G. & Moran, P. A. P. (1963). *Geometrical probability.* Hafner, New York.

Klinkenberg, L. J. (1941). The permeability of porous media to liquids and gases. In: *Eleventh mid-year meeting of the API,* Tulsa, Oklahoma, p. 2-12.

Knudsen, M. (1909). Die Gesetze der Molekularstromung und der inneren Reibungsstronmung der Gase durch Rohren. *Ann. Physik* **28**, p. 75.

Kopaska-Merkel, D. C. (1994). Pore-throat morphology in the Upper Jurassic Smackover Formation of Alabama. *Journal of Sedimentary Research* **A64**(3), p. 524-534.

Koplik, J., Lin, C. & Vermette, M. (1984). Conductivity and permeability from microgeometry. *Journal of Applied Physics* **56**(11), p. 3127-3131.

Kostek, S., Schwartz, L. M. & Johnson, D. L. (1992). Fluid permeability in porous media: comparison of electrical estimates with hydrodynamical calculations. *Physical Review B* **45**(1), p. 186-195.

Kozeny, J. (1927). Uber kapillare Leitung des Wassers im Boden. *Sitzungberichte der Akadamie der Wissenschaftung in Wein Abteilung IIa,* **136**, p. 271-301.

Krumbein, W. C. & Monk, G. D. (1942). Permeability as a function of the size parameters of unconsolidated sand. *Transactions American institute mining metallurgical engineers* (151), p. 153-163.

Kundt, A. & Warburg, E. (1875). *Poggendorfs Ann. Physik* (155), p. 337 and 525.

Lin, C. & Cohen, M. H. (1982). Quantitative methods for microgeometric modelling. *Journal of Applied Physics* **53**, p. 4152.

Liu, K., Boult, P., Painter, S. & Paterson, L. (1996). Outcrop analog for sandy braided stream reservoirs: permeability patterns in the Triassic Hawkesbury Sandstone, Sydney Basin, Australia. *Bulletin of the American Association of Petroleum Geologists* **80**(12), p. 1850-1866.

Lowden, B. (1994). Image analysis: obtaining 3-D data from 2-D. *DiaLog* **2**(4), p. 6-8.

Luffel, D. L., Howard, W. E. & Hunt, E. R. (1989). Relationships of permeanility, porosity, and overburden stress derived from an extensive core analysis data base in the Travis Peak Formation. *Society of Petroleum Engineers* (SPE paper 19008), p. 729-740.

Luo, P. & Machel, H. G. (1995). Pore size and pore throat types in a heterogeneous dolostone reservoir, Devonian Grosmont Formation, Western Canada sedimentary basin. *Bulletin of the American Association of Petroleum Geologists* **79**(11), p. 1698-1720.

MacGowan, D. (1992). Prediction of permeability from a combination of mercury injection and pore image analysis data. In: *Institute of mathematics and its applications* (edited by King, P. R.) **31**. Academic press.

Mardia, K. V. (1972). *Statistics of direction data.* Academic Press, London, New York.

McCreesh, C. A., Ehrlich, R. & Crabtree, S. J. (1991). Petrography and reservoir physics II: Relating thin section porosity to capillary pressure, the association between pore types and throat size. *Bulletin of the American Association of Petroleum Geologists* **75**(10), p. 1563-1578.

McPhee, C. A. (1992). Permeability: conventional core analysis measurements. In: *Society of Professional Well Log Analysts Permeability Seminar.*

McPhee, C. A. & Arthur, K. G. (1991). Klinkenberg permeability: Problems and practical solutions. In: *2nd European Symposium of Society of Core Analysts*, London.

Mowers, T. T. & Budd, D. A. (1996). Quantification of porosity and permeability reduction due to calcite cementation using computer-assisted petrographic image analysis techniques. *Bulletin of the American Association of Petroleum Geologists* **80**(3), p. 309-322.

Mungan, N. (1966). Certain wettability effects in laboratory waterfloods. *Journal of Petroleum Technology* (February), p. 247-252.

Muskat, M. (1937). *The flow of homogeneous fluids through porous media.* McGraw-Hill, New York.

Mutti, E. & Ricci-Lucchi, F. (1972). Le torbiditi dell'Appennino settentrionale: inroduzione all' analisi di facies. *Mem. Soc. Geol. It.* **11**, p. 161-199.

Mutti, E. & Ricci-Lucchi, F. (1975). Turbidite facies and facies associations. In: *Examples of turbidite facies and facies associations from selected formations of the Northern Apennines. IX International Congress on Sedimentology, Nice, A-11*, p. 21-36.

Neasham, J. W. (1977). The morphology of dispersed clay in sandstone reservoirs and its effect on sandstone shaliness, pore space and fluid flow properties. In: *52nd annual fall technology conference* (SPE paper 6858), Denver.

Nelson, P. H. (1994). Permeability-Porosity relationships in sedimentary rocks. *The Log Analyst* **35**(3), p. 38-62.

Nesbitt, G. J., Degroot, A., Fens, T. W. & Bonnie, J. H. M. (1991). Towards validation of porous-media models using NMR imaging. *Journal of Magnetic Resonance Imaging* **9**(5), p. 779-785.

Nieto, J. A., Yale, D. P. & Evans, R. J. (1994). Improved methods for correcting core porosity to reservoir conditions. *The Log Analyst* **35**(3), p. 21-30.

Norman, R. & Kalam, M. Z. (1990). Transition from laminar to non-Darcy flow of gases in porous media. In: *Advances in core evaluation: accuracy and precision in reserves estimation.* (edited by Worthington, P. F.). Gordon and Breach, London, p. 447-462.

Ostensen, R. W. (1983). Microcrack permeability in tight gas sandstone. *Society of Engineers of AIME,* (December), p. 919-927.

Pallatt, N., Wilson, J. & McHardy, B. (1984). The relationship between permeability and the morphology of diagenetic illite in reservoir rocks. *Journal of Petroleum Technology* (December), p. 2225-2227.

Panda, M. N. & Lake, L. W. (1994). Estimation of single-phase permeability from parameters of particle-size distribution. *Bulletin of the American Association of Petroleum Geologists* **78**(7), p. 1028-1039.

Panda, M. N. & Lake, L. W. (1995). A physical model of cementation and its effects on single-phase permeability. *Bulletin of the American Association of Petroleum Geologists* **79**(3), p. 431-443.

Patchett, J. G. (1975). An investigation of shale conductivity. *The Log Analyst* **16**(6), p. 3-20.

Patterson, M. S. (1983). The equivalent channel model for permeability and resistivity in fluid-saturated rock - a re-appraisal. *Mechanics of Materials* **2**, p. 345-352.

Perez-Rosales, C. (1982). On the relationship between formation resistivity factor and porosity. *Society of Petroleum Engineers* (August).

Pettijohn, E. J. (1975). *Sedimentary Rocks*. Harper & Row, publishers, New York.

Rider, M. H. (1986). *The geological interpretation of well logs*. Blackie and Son ltd, Glasgow, UK.

Rink, M. & Schopper, J. R. (1976). Pore structure and physical properties of porous sedimentary rocks. *Geophysics*. **114**, p. 273-284.

Ruth, D. W. & Chen, Z. A. (1995). Measurement and Interpretation of Centrifuge Capillary Pressure Curves - The SCA survey data. *The Log Analyst* **36**(5), p. 21-33.

Ruzyla, K. (1984). Characterization of pore space by quantitative image analysis. In: *59th Annual Technical Conference and Exhibition*. (SPE paper 13133), Houston, Texas.

Sampath, K. & Keighin, C. W. (1982). Factors affecting gas slippage in tight sandstones of Cretaceous Age in the Uinta Basin. *Journal of Petroleum Technology* (November), p. 2715-2720.

Scheidegger, A. E. (1974). *The physics of flow through porous media*. University of Toronto Press, Toronto.

Schlueter, E. M., Cook, N. G. W., Zimmerman, R. W. & Witherspoon, P. A. (1991). Predicting permeability and electrical conductivity of sedimentary rocks from microgeometry. In: *32nd U.S. Symposium on Rock Mechanics*, Rotterdam, p. 355-364.

Schlumberger, Inc. (1972). *Log interpretation-principles*, Houston.

Schwarcz, H. P. & Shane, K. C. (1969). Measurement of particle shape by Fourier Analysis. *Sedimentology* **13**, p. 213-231.

Serra, O. (1984). *Fundamentals of well-log interpretation - the acquisition of logging data*. Elsevier Publ.

Shaw, H. F. (1980). Clay minerals in sediments and sedimentary rocks. In: *Developments in Petroleum Geology*, p. 53-85.

Sinclair, G. & Duguid, S. (1990). Laboratory induced damage-a review of the problem. In: *Society of Core Analysts Conference*.

Smith, F. W. (1970). The behaviour of partially hydrolyzed polyacrylamide solutions in porous media. *Journal of Petroleum Technology* (February), p. 148-156.

Soeder, D. J. & Randolph, P. L. (1987). Porosity, permeability, and pore structure of the tight Mesaverde sandstone, Piceance Basin, Colorado. *Society of Petroleum Engineers Formation Evaluation* (June), p. 129-136.

Szabo, M. T. (1975). Some aspects of polymer retention in porous media using a C^{14}-tagged hydrolyzed polyacrylamide. *Journal of the Society of Petroleum Engineers* (August) 323-337.

Thomas, D. C. & Pugh, V. J. (1989). A statistical analysis of the accuracy and reproducibility of standard core analysis. *The Log Analyst* (March-April), p. 71-76.

Thompson, A. H., Katz, A. J. & Raschke, R. A. (1987). Estimation of absolute permeability from capillary pressure measurements. In: *62nd Annual Technical Conference and Exhibition of the Society of Petroleum Engineers,* Dallas, (SPE paper 16794), p. 475-481.

Tiab, D. & Donaldson, E. C. (1996). *Petrophysics; theory and practice of measuring reservoir rock and fluid transport properties*. Gulf publishing company, Houston, Texas.

Tiss, M. & Evans, R. D. (1989). Measurement and correlation of non-Darcy flow coefficient in consolidated porous media. *Journal of Petroleum Science and Engineering* **3**, p. 19-33.

Underwood, E. E. (1970). *Quantitative stereology*. Addison-Wesley, Reading, Massachusetts.

Wadell, H. (1935). Volume, shape and roundness of quartz particles. *Journal of Geology* **43**, p. 250-280.

Warberg, E. (1870). *Poggendorfs, Ann Physik* (139), p. 399

Wardlaw, N. C. & Taylor, R. P. (1976). Mercury capillary pressure curves and the interpretation of pore structure and capillary behaviour in reservoir rocks. *Bulletin of Canadian Petroleum Geology* **24**(2), p. 225-262.

Weibel, E. R. (1974). Selection of the best methods in stereology. *Journal of Microscopy* **100**, p. 261-269.

Wilson, M. D. (1982). Origin of clays controlling permeability in tight gas sands. *Society of Petroleum Engineers* (December), p. 2871-2876.

Wilson, M. D. & Pittman, E. D. (1977). Authigenic clays in sandstones: recognition and influence on reservoir properties and palaeoenvironmental analysis. *Journal of Sedimentary Petrology* **47**, p. 3-31.

Winsauer, W. A., Shearin, H. M., Masson, P. H. & Williams, M. (1952). Resistivity of brine-saturated sands in relation to pore geometry. *Bulletin of the American Association of Petroleum Geologists* **36**(2), p. 253-277.

Wissler, T. M. (1987). Sandstone pore structure: a quantitative analysis of digital SEM images. Mass. Institute of Technology.

Wong, P. Z., Koplik, J. & Tomanic, J. P. (1984). Conductivity and permeability of rocks. *Physical Review B* **30**(11), p. 6606-6614.

Wyllie, M. R. J. (1963). *The fundamentals of well log interpretation*. Academic Press.

Wyllie, M. R. J. & Spangler, M. B. (1952). Application of electrical resistivity measurements to problem of fluid flow in porous media. *Bulletin of the American Association of Petroleum Geologists* **36**(2), p. 359-403.